Doctoral Thesis

for the academic degree of
Doctor rerum naturalium

written by
Dipl.-Ing. René Hammer

Dynamics of Dirac fermions

supervised by
Univ.-Prof. Dr. Walter Pötz

Institute of Physics - Theoretical Physics
Karl-Franzens-University Graz
Austria

Graz, October 2013

STATUTORY DECLARATION

I declare that I have authored this thesis independently, that I have not used other than the declared sources / resources, and that I have explicitly marked all material which has been quoted either literally or by content from the used sources.

Date René Hammer

ABSTRACT

In the relatively new but extremely fast growing field of topological matter research, this thesis should contribute to the understanding of the behavior of the underlying quasiparticle: the Dirac fermion. For this purpose the reader gets a brief introduction to the emergence of relativistic quantum mechanics in solid state systems. The connection to the topological invariant and its indispensability in giving a unified description of the physics at topological defects like surfaces, domain-walls, and vortices is made. The main focus, however, lies in the description of the dynamical behavior of the Dirac fermion quasiparticle in this non-trivial spatial and, possibly, time dependent potential and mass landscapes. To allow an efficient numerical simulation, a new scheme is developed. Along the way, the famous fermion doubling problem is introduced, and avoided by a special time and space staggering of the numerical finite difference grid. Like in the underlying differential equation, this special discretization of the Dirac equation treats time and space on an equal footing. Schemes for (1+1)D, (2+1)D, and (3+1)D are formulated, and their numerical properties are derived. The important topic of open boundary conditions is discussed and, in the one-dimensional case, perfect absorbing boundary conditions (so-called discrete transparent boundary conditions) are derived. In (2+1)D absorbing boundary conditions, using imaginary potential regions, are introduced. On the applied physics side, the utilization of domain-wall fermions for dissipation-less electric circuits is proposed. Using these principles, an interferometer device which can be controlled by an electrical gate is envisioned and its working principle is shown numerically.

ZUSAMMENFASSUNG

In dem relativ jungen, aber extrem schnell wachsenden, Forschungsfeld der topologischen Materie soll diese Arbeit einen Beitrag zum Verständnis des Verhaltens des zugrundeliegenden Quasiteilchens liefern: dem Dirac Fermion. Einleitend findet der Leser eine kurze Einführung, welche die Emergenz von relativistischer Quantenmechanik im Festkörper demonstriert. Die Verbindung zu der topologischen Invariante und ihrer Unentbehrlichkeit für eine geschlossene, vollständige Beschreibung der Physik an topologischen Defekten wie etwa Oberflächen, Domänenwänden und Vortices wird hergestellt. Der Schwerpunkt der Arbeit liegt jedoch in der Beschreibung und Simulation des dynamischen Verhaltens des Dirac Fermion Quasiteilchens in nichttrivialen örtlich, und nach Möglichkeit auch zeitlich, variierenden Potential- und Masse-Landschaften. Um eine effiziente numerische Simulation zu gewährleisten wurde ein neues numerisches Schema entwickelt. Auf diesem Wege stößt man auf das Fermion-Verdopplungs Problem, welches durch eine Verschachtelung des numerischen Gitters in Ort und Zeit gelöst wird. Wie die zugrundeliegende Differentialgleichung, behandelt diese spezielle Diskretisierung Ort und Zeit gleichwertig. Schemen für (1+1)D, (2+1)D und (3+1)D werden formuliert und ihre numerischen Eigenschaften gezeigt. Das wichtige Thema der Randbedingungen wird diskutiert und im eindimensionalen Fall werden perfekt absorbierende Randbedingung (sogenannte diskrete transparente Randbedingung) hergeleitet. In (2+1)D werden absorbierende Randbedingungen unter Verwendung von imaginären Potential Regionen vorgestellt. Auf der angewandten Seite wird die Verwendung von Domänenwand-Fermionen für verlustfreie, elektrische Schaltungen vorgeschlagen. Mit diesen wird das Prinzip eines Interferometer-Bauteils gezeigt, welches durch ein Gate gesteuert werden kann, und dessen Wirkungsweise numerisch demonstriert.

CONTENTS

Chapter 1

PREFACE

1.1 Motivation

The common worldview in the 18th century was that the general laws in physics had been already found. Everything could be understood within classical Newtonian physics. Max Planck was one of the students of Philipp von Jolly, who advised Max Planck not to go into physics by saying "in this field, almost everything is already discovered, and all that remains is to fill a few unimportant holes." Nevertheless, Max Planck did go into physics and filled an important hole, discovering the quantization of black body radiation. The latter turned out to be decisive in the development of quantum mechanics (QM), which led to a paradigmatic shift in physics and the fundamental understanding of our world.[1] In hindsight, it seems even more surprising that a basic consequence of QM had been overlooked for so long. The phase of the wavefunction, describing a QM system, does not lead to any observable effect. This is known since the early days of QM and is called gauge freedom. But, in addition to a phase from time evolution, an adiabatic change in the parameters of a QM system leads to an additional phase, the geometrical phase. 1928 M. Born and V. Fock [1] stated that independently of the path, which is taken in the parameter-space, one can always find a

---

[1] It is not very likely that non scientists will read this, but for them I want to note: QM is not only a nice toy for theoretical physicists, caught in their ivory towers, but nowadays it has great influence in peoples everyday lives. Without writing down a full list of devices which today would probably not exist without the development of QM let me just give one example, which I would call "condensed quantum physics": *the smartphone*.

suitable gauge leading to a cancellation of the geometrical phase. This was the general belief until 1984, when M. V. Berry [2] investigated a closed path. He found, that in this case, the geometrical phase can not be gauged away. It is now called the Berry phase and is an integer multiple of 2π. As usual, the closed path integral over a vector field can be transformed into an area integral over the curl of the quantity which, in this case, is called the Berry curvature. Since the latter is gauge invariant it leads to measurable effects. In solid state physics the topological invariant is the total Berry flux, the integral over the Berry curvature, in the Brillouin zone. In fact, it was a major breakthrough, which allows for a unified description of the quantum Hall effect (QHE), quantum anomalous Hall effect, valley Hall effect, electric polarization of crystalline solids, adiabatic pumps, etc. [3]. It has lead to a burst of experimental discovering [4, 5, 9, 10, 11, 12, 13] and a theoretical understanding [4, 5, 14, 15, 16, 8, 17] of a new form of matter, *the topological matter*. One is the time-reversal symmetry protected class, being the quantum spin Hall effect and the topological insulator (TI) [5]. Without a claim to completeness, the phenomena which show up are: the emergence of relativistic quasiparticle physics, non-local transport, weak antilocalization, half integer QHE on the surface, quantum spin Hall effect (QSHE), quantum anomalous Hall effect (AHE), the topological magnetoelectric effect (axion electrodynamics), magnetic monopoles, Dyons, and Majorana fermions [5].

In G. E. Voloviks famous Book "The Universe in a Helium Droplet", the universality classes of fermionic vacua can be found. They are quantum vacua having (i) Fermi surfaces, (ii) Fermi points, and (iii) gapped fermionic vacua [18]. In this thesis, we will deal with (ii) and (iii), which can be described with a mathematical structure called the Dirac equation. The latter is also the relativistic description of elementary spin $1/2$ fermions (e.g. the electron) [19]. The conclusion that the low energy sector of discrete microscopic models can resemble (ii), with the emergence of all the properties of continuous space-time, such as Lorenz invariance, might have some interesting philosophical consequences. At least, the standard model could be an effective theory of some, until now, unknown more fundamental microscopic theory [18]. The (3+1)D Dirac equation leads to correction terms which, may have to be incorporated in, non relativistic, microscopic theories. They survive the non-relativistic limit in form of the well-known spin-orbit coupling. The latter, in turn, allows the emergence of topological matter with the Dirac equation, as effective theory, describing the underlying quasiparticles. So, which came first, the chicken or the egg?

Most results from this thesis research have been published or, at least, been submitted for publication. Starting point is an effective model, which describes (2+1)D Dirac fermions on the surface of a three dimensional TI. Exchange coupling of the spin, carried by the Dirac fermion, with magnetic moments of e.g. magnetic impurities or a near by ferromagnetic layer allows one, to tune the mass of the Dirac fermions [5, 7]. Exploiting this principle, one can induce topological defects on the surface of the TI. An example are 1D chiral (one-way) conducting states, living at ferromagnetic domain-walls. These novel states allow dissipation-less current and are related to the QHE edge states. In fact they arise from the half integer QHE showing a non-zero Hall conductivity without applying a magnetic field. The sign of the Hall conductivity depends on the mass of the surface region, encircled by the Hall current. In contrast to the QHE it has spin polarized (chiral) edge channels. Moreover, compared to the QSHE it shows only one propagation direction (one-way transport). This avoids spin-flip scattering and should allow to observe (and exploit) the edge channel transport over a macroscopic length scale (hundreds of μm), like in the recently observed QAHE [20]. Moreover, one can think of utilizing this one-way spin polarized channels together with beam-splitters, given by domain-wall intersections, in order to construct complex networks (see paper reprints in CHAPTER 10 and 11) [22, 23]. These dissipation-less networks could be part of future low power consuming electronic and/or spintronic devices.

To allow numerical simulation, a scheme for solving the dynamics of the Dirac quasiparticle has to be developed. It is a (2+1)D finite-difference scheme with a staggered grid in space and time by which the famous fermion doubling problem can be avoided (paper reprints CHAPTER 9 and 12) [24, 25]. The fully (3+1)D version of this scheme is presented and should be valuable in various other areas where the Dirac equation is used. These are for example particle physics, atomic physics and cosmology. In particular it can provide an efficient numerical algorithm for the simulation of the dynamics of electrons in strong laser fields (paper reprint CHAPTER 12).

1.2 Contents

An introduction to topological matter is given in CHAPTER 1. The Dirac equation is established as an effective equation describing the quasiparticles near Fermi points. Furthermore, an outline of potential device applications is given.

CHAPTER 2 contains a brief introduction to the Dirac equation. The Minkowski space-time and the Lorenz transformation are introduced. The latter together with parity is sufficient for the derivation of the Dirac equation and directly reveals its left-/right-handed structure. The solution for constant coefficients is shown and the simpler two space-dimensional and two component spinor Dirac equation is given.

CHAPTER 3 deals with the emergence of effective relativistic quantum mechanics in a solid state environment. For that purpose simple tight-binding models are used. Topological nontriviality is introduced using the concept of the Chern number. A pedagogical topological nontrivial model is explained, which serves as a demonstration for the emergence of edge channels. With that, a model showing helical states at the surface of the 3D topological insulator is presented.

In CHAPTER 4, the short history of 3D topological insulators is summarized. The focus is given to the challenges with respect to future device applications.

Numerical simulation of the Dirac equation is discussed in CHAPTER 5. Finite difference modeling, its advantages and its problems (e.g. fermion doubling) are discovered pedagogically. Open boundary conditions are discussed.

Numerical simulations of the wave packed dynamics of the Dirac fermion are shown in CHAPTER 6 for various potential and mass textures. Among them are the free propagation, the Klein-step, superlense-focusing, and Landau orbits.

CHAPTER 7 deals with special bound states in mass domain-walls and vortices. For the domain-wall states photoexcitation is discussed. The vortex zero modes are shown for various angular momentum numbers and different magnetic structures, e.g. hedgehog and tilted hedgehog configurations.

In the paper reprint CHAPTER 8, a dispersion and norm preserving leap-frog staggered-grid finite difference scheme for the (1+1)D Dirac equation is introduced [21]. An exactly preserved functional, for the norm, is identified and stability for arbitrary space- and time-dependent mass and potential terms, is proven. Transparent boundary conditions are derived for the continuum equation, as well as for the discretized problem. This gives exact discrete transparent boundary conditions for the numerical problem.

An extension of the scheme to (2+1)D, preserving its continuum properties along the principal coordinate axes, is contained in the paper reprint CHAPTER 9 [24]. As a drawback, this method yields a second Dirac cone at the Brillouin zone boundary. Because of the special properties of the dispersion relation, the scheme performs best for rectangular structures and propagation mainly in the direction of the coordinate axes. This is the case for the interferometer setup shown in CHAPTER 10, were the scheme shows extremely low phase error. Various numerical examples demonstrate the general properties of the scheme, as well as the physics of the (2+1)D Dirac equation.

In the paper reprint CHAPTER 10 a Dirac fermion interferometer on the topological insulator surface is proposed and verified numerically [22]. It is shown, that the interferometer can be controlled by an electrical gate. The interferometer consists of one-way chiral channels located at the domain-walls and their intersections. A realistic model for the mass-texture is obtained by free energy minimization of the magnetic structure. The device should be robust against perturbations because it relies on the stability of the half-integer quantum Hall effect on the surface [5].

In the paper reprint CHAPTER 11, a more systematic numerical investigation of the splitting behavior of ferromagnetic domain-wall intersections is given for various domain-wall parameters [23]. Important parameters are the angle of intersection, the domain-wall width (relative to the confinement width of the wave packet) and the energy of the wave packet relative to the asymptotic gap created by the magnetic domains.

The last paper reprint shows an extension of the (1+1)D scheme to the (2+1)D case and the full four spinor (3+1)D Dirac equation [25]. In contrast to previous finite difference schemes in the literature, it completely avoids the fermion doubling by staggering of the spinor components in space and time. As for the (1+1)D scheme, an exactly preserved functional is identified and stability is proven for arbitrary space- and time-dependent mass and potential terms.

In the last CHAPTER 13 an outlook is given regarding further subjects to be investigated with the numerical schemes, as well as potential extensions of the formalism.

1.3 Acknowledgments

I had a good time during my PhD work at the University Graz, which is steeped in history. Being in the same house, but some time later, with legends like Victor Franz Hess, Ernst Mach, Ludwig Boltzmann and of course Erwin Schrödinger, one can almost feel their spirit. Nowadays, "small but nice" best describes the university and the city of Graz. The same holds for the physics research group. It is a small but very able group of students and experienced researchers. Here, I want to thank them all. In fact, Graz is a great place to live and even more so, to do physics research.

First of all, among the people I want to name and to acknowledge here, is my supervisor Professor Walter Pötz. He is an excellent physicist and his broad knowledge is very impressive. I want to thank him very much for letting me do research like it makes the most fun, namely with the curiosity of a child. He was always giving me the freedom and time to play with physics and to find my own way, often by trial and error. However, if I had lost my way he was always there and gave me the right amount of guidance to get me back on track. Thank you, Walter.

I am also very grateful to Professor Anton Arnold for supporting and supervising me in various mathematical details of my thesis. Much of it would have been not possible without his support.

I was also fortunate that I have been able to work with Christian Ertler, who greatly inspired me in the work with ferromagnetic domain-walls on topological insulators.

I also want to thank two of my best friends and colleges. We had an uncountable number of discussions about physics, but also about the world in general. We have shared many coffees in front of the physics building and sometimes a beer in a pub. Thank you for the inspiring time with you, Ben and Mulla alias Benjamin Stickler and Thomas Obermüller.

I am certain, that I am among the luckiest men alive, because I have found my great love, Sabine. In a few months, we are ten years together. Of course she had always to compete with physics, but she did that without being jealous and supported me always with great patience. Nothing feels better than to come home to our flat and simply knowing and having the feeling of being at home. Thank you, Sabine.

Last but not least, I want to thank my family and my friends for sharing their time with me, but also for being so understanding and supportive, when the latter was rare.

REFERENCES

[1] M. Born and V. Fock, Beweis des Adiabatensatzes, Z. Phys. 51 (1928) 165-180.

[2] M. V. Berry, Quantal Phase Factors Accompanying Adiabatic Changes, Proc. R. Soc. Lond. A 392 (1984) 45-57.

[3] D. Xiao, M. C. Chang, and Q. Niu, Berry Phase Effects on Electronic Properties, Rev. Mod. Phys. 82 (2010) 1959-2007.

[4] M. Z. Hasan, C. L. Kane, Colloquium: Topological Insulators, Rev. Mod. Phys 82 (2010) 3045-3065, and references therein.

[5] X. L. Qi and S. C. Zhang, Topological Insulators and Superconductors, Reviews of Modern Physics 83 (2011) 1057-1110, and references therein.

[6] J. G. Analytis, J. H. Chu, Y. Chen, F. Corredor, R. D. McDonald, Z. X. Shen, and Ian R. Fisher, Bulk Fermi Surface Coexistence with Dirac Surface State in Bi_2Se_3: A comparison of Photoemission and Shubnikov-de Haas Measurements, Phys. Rev. B 81 (2010) 204507-1 - 204507-5.

[7] Y. L. Chen, J. H. Chu, J. G. Analytis, Z. K. Liu, K. Igarashi, H. H. Kuo, X. L. Qi, S. K. Mo, R. G. Moore, D. H. Lu, et al., Massive Dirac Fermion on the Surface of a Magnetically Doped Topological Insulator, Science 329 (2010) 659-662.

[8] Y. Xia, D. Qian, D. Hsieh, L. Wray, A. Pal, H. Lin, A. Bansil, D. Grauer, Y. S. Hor, R. J. Cava, and M. Z. Hasan, Observation of a Large-Gap Topological-Insulator Class with a Single Dirac Cone on the Surface, Nature Physics 5 (2009) 398-402.

[9] J. Chen, H. J. Qin, F. Yang, J. Liu, T. Guan, F. M. Qu, G. H. Zhang, J. R. Shi, X. C. Xie, C. L. Yang, K. H. Wu, Y. Q. Li, and L. Lu, Gate-Voltage Control of Chemical Potential and Weak Antilocalization in Bi_2Se_3, Phys. Rev. Lett. 105 (2010) 176602-1 - 176602-4.

[10] J. G. Checkelsky, Y. S. Hor, R. J. R. J. Cava, and N. P. Ong, Bulk Band Gap and Surface State Conduction Observed in Voltage-Tuned Crystals of the Topological Insulator Bi_2Se_3, Phys. Rev. Lett. 106 (2011) 196801-1 - 196801-4.

[11] F. Xiu, L. He, Y. Wang, L. Cheng, L. T. Chang, M. Lang, G. Huang, X. Kou, Y. Zhou, X. Jiang, Z. Chen, J. Zou, A. Shailos, and K. L. Wang, Manipulating Surface States in Topological Insulator Nanoribbons, Nat. Nanotech. 6 (2011) 216-221.

[12] D. Kim, S. Cho, N. P. Butch, P. Syers, K. Kirshenbaum, S. Adam, J. Paglione, and M. S. Fuhrer, Surface Conduction of Topological Dirac Electrons in Bulk Insulating Bi_2Se_3 Nat. Phys. 8 (2012) 459-463.

[13] Y. Wang, F. Xiu, L. Cheng, L. He, M. Lang, J. Tang, X. Kou, X. Yu, X. Jiang, Z. Chen, J. Zou, and K. L. Wang, Gate-Controlled Surface Conduction in Na-Doped Bi_2Te_3 Topological Insulator Nanoplates, Nano Lett. 12 (2012) 1170-1175.

[14] J. E. Moore and L. Balents, Topological Invariants of Time-Reversal-Invariant Band Structures, Phys. Rev. B 75 (2007) 121306-1 - 121306-6.

[15] L. Fu and C. L. Kane, Topological Insulators with Inversion Symmetry, Phys. Rev. B 76 (2007) 045302-1 - 045302-4.

[16] X. L. Qi, T. L. Hughes, and S. C. Zhang, Topological Field Theory of Time-Reversal Invariant Insulators, Phys. Rev. B 78 (2008) 195424-1 - 195424-43.

[17] D. Hsieh, Y. Xia, D. Qian, L. Wray, F. Meier, J. H. Dil, J. Osterwalder, L. Patthey, A. V. Fedorov, H. Lin, et al., Observation of Time-Reversal-Protected Single-Dirac-Cone Topological-Insulator States in Bi2Te3 and Sb2Te3, Phys. Rev. Lett. 103 (2009) 146401-1 - 146401-4.

[18] G. E. Volovik, The Universe in a Helium Droplet, Oxford University Press (2009).

[19] W. Greiner, Relativistic Quantum Mechanics: Wave Equations, 3rd ed., Springer Berlin (2000).

[20] C. Z. Chang, J. Zhang, X. Feng, J. Shen, Z. Zhang, M. Guo, K. Li, Y. Ou, P. Wei, L. L. Wang, Z. Q Ji, Y. Feng, S. Ji, X. Chen, J. Jia, X. Dai, Z. Fang, S. C. Zhang, K. He, Y. Wang, L. Lu, X. C. Ma, and Q. K. Xue, Experimental Obseration, of the Quantum Anomalous Hall Effect in a Magnetic Topological Insulator, Science 340 (2013) 167-170.

[21] R. Hammer, W. Pötz, and A. Arnold, A Dispersion and Norm Preserving Finite Difference Scheme with Transparent Boundary Conditions for the Dirac Equation in (1+1)D, J. Comp. Phys. 256, 728 (2014), in press, http://dx.doi.org/10.1016/j.jcp.2013.09.022

[22] R. Hammer, C. Ertler, and W. Pötz, Solitonic Dirac Fermion Wave Guide Networks on Topological Insulator Surfaces, Appl. Phys. Lett. 102, (2013) 193514-1 - 193514-4.

[23] R. Hammer and W. Pötz, Dynamics of Domain-Wall Dirac Fermions on a Topological Insulator: A Chiral Fermion Beam Splitter, arXiv:1306.6139

[24] R. Hammer and W. Pötz, Staggered-Grid Leap-Frog Scheme for the (2+1)D Dirac Equation, Comp. Phys. Comm., in press, http://dx.doi.org/10.1016/j.cpc.2013.08.013

[25] R. Hammer, W. Pötz, and A. Arnold, Single-Cone Real-Space Finite Difference Scheme For the Time-Dependent Dirac Equation, submitted to Journal of Computational Physics (2013), preprint available at arXiv:1309.3452

Chapter 2

A BRIEF INTRODUCTION TO THE DIRAC EQUATION

The aim of this chapter is not to expose the theory of the Dirac equation, for which many excellent textbooks exist [1, 2, 3, 4], but to condense the basic facts and to introduce the notations used later in this thesis.

Interestingly the Dirac equation, being the relativistic description of spin $1/2$ particles (e.g. electrons), was found by P. A. M. Dirac only two years after the non-relativistic quantum-mechanical evolution equation was presented by E. Schrödinger [6, 5]. Historically, the Dirac equation is introduced by demanding the fulfillment of the relativistic energy-momentum relation $E = \sqrt{m^2c^4 + |\mathbf{p}|^2c^2}$. The square-root is linearized, by the introduction of Dirac matrices and spinors [1]. As usual $\mathbf{p} = (p_x, p_y, p_z)$ is the 3-momentum, m is the mass and c is the speed of light.
Symmetry principles are among the most beautiful entities of models, which we use to describe nature. Every observer, regardless of his/her state of motion, has to agree with all others about all physical processes in the universe: the principle of relativity [7]. For observers in inertial systems simply moving with constant speed, this postulate is mathematically expressed by invariance under Lorenz transformation [7]. Therefore, perhaps the most elegant way of deriving the relativistic description of the electron is to demand invariance under Lorenz transformation together with parity [3]. This will be shown briefly below.

2.1 Minkowski space-time: 4-vector notation

Under rotation, the distance between two points[1] in Euclidean space has to be invariant $dr^2 := \sum_{j=1}^{3} \mathrm{d}x_j^2 = \mathrm{d}x^2 + \mathrm{d}y^2 + \mathrm{d}z^2 = \text{const}$. Similarly, within Minkowski space, the distance between events (space-time points), in addition, has to be invariant under boosts (transformations between initial systems having different velocity). This is written as

$$ds^2 := \sum_{\mu=0}^{3} \mathrm{d}x_\mu \mathrm{d}x^\mu = c^2\mathrm{d}t^2 - \mathrm{d}x^2 - \mathrm{d}y^2 - \mathrm{d}z^2 = \text{const} \,. \tag{2.1}$$

Einstein summation convention will be used in the following, which means that if an index occurs "twice" in an expression, a summation has to be performed and one can omit the sum sign. E.g. the second expression in the last equation can be simply written as $\mathrm{d}x^\mu \mathrm{d}x_\mu$. Here, as usual, the 4-vectors[2] are introduced in their covariant and contravariant form

$$\begin{aligned} x^\mu &:= (x^0, x^1, x^2, x^3) = (ct, x, y, z) \\ x_\mu &:= (x_0, x_1, x_2, x_3) = (ct, -x, -y, -z) \,. \end{aligned} \tag{2.2}$$

2.2 Lorenz transformation and derivation of the Dirac equation

The Lorenz group includes rotation and boosts (for a more detailed discussion see for example [3]). A boost can be expressed as a rotation in hyperbolic space (Minkowski space) which, e.g., for a boost in x_1 direction can be written as follows

$$\begin{pmatrix} x'_0 \\ x'_1 \\ x'_2 \\ x'_3 \end{pmatrix} = \underbrace{\begin{pmatrix} \cosh\eta_1 & \sinh\eta_1 & 0 & 0 \\ \sinh\eta_1 & \cosh\eta_1 & 0 & 0 \\ 0 & 0 & 1 & 0 \\ 0 & 0 & 0 & 1 \end{pmatrix}}_{B_1} \begin{pmatrix} x_0 \\ x_1 \\ x_2 \\ x_3 \end{pmatrix} \,. \tag{2.3}$$

and analogous for the other spatial directions. Here we have the rapidity $\eta_j = \text{arctanh } v_j/c$. The generators of the Lorenz group form a Lie group

---

[1] The incices for the components of a spatial 3-vector are by convention always written in Latin letters.

[2] The indices for 4-vectors are always expressed by Greek letters.

with the generators

$$K_j = \frac{1}{i}\frac{\partial}{\partial \eta_j} B_j \bigg|_{\eta_j=0} \quad . \tag{2.4}$$

From the rotation matrices R one gets the matrix representation of the known angular momentum operators

$$J_j = \frac{1}{i}\frac{\partial}{\partial \theta_j} R_j \bigg|_{\theta_j=0} \quad . \tag{2.5}$$

One can easily prove, that the boosts alone do not form a group

$$\left[K_i, K_j\right] = -\epsilon_{ijk} J_k \; . \tag{2.6}$$

This means a boost in one direction e.g. x, followed by a boost in an other direction e.g. y and then back in negative x-direction followed by a boost in negative y-direction, brings the object back to the starting point. Surprisingly, (in addition) it has accumulated a rotation around the z-axis. Now comes the interesting step which will lead us to the Dirac equation. One can combine the generators in the following way

$$\mathbf{A} := \frac{1}{2}(\mathbf{J} + i\mathbf{K}) \; , \tag{2.7}$$

$$\mathbf{B} := \frac{1}{2}(\mathbf{J} - i\mathbf{K}) \; . \tag{2.8}$$

Then $\mathbf{A}$ and $\mathbf{B}$ form two commuting subgroups of the Lorenz group in the sense that

$$\begin{aligned} \left[A_i, A_j\right] &= \epsilon_{ijk} A_k \; , \\ \left[B_i, B_j\right] &= \epsilon_{ijk} B_k \; , \\ \left[A_i, B_j\right] &= 0 \; . \end{aligned} \tag{2.9}$$

Both fulfill the algebra of angular momenta forming SU(2) groups. Thus, the "Lorenz group is SU(2) ⊗ SU(2)" and the elements can be labeled by the angular momenta (j_1, j_2). For the case $\mathbf{B} = 0$ $(j, 0)$ one gets $\mathbf{J} = i\mathbf{K}$ and for $\mathbf{A} = 0$ $(0, j)$ one obtains $\mathbf{J} = -i\mathbf{K}$. Using known representations of the generators of the rotation immediately leads to the two following inequivalent representations of the Lorenz transformation

$$\psi_L \rightarrow \exp\left(i\frac{\boldsymbol{\sigma}\cdot\boldsymbol{n}}{2} + \frac{\boldsymbol{\sigma}\cdot\boldsymbol{\eta}}{2}\right)\psi_L \tag{2.10}$$

and

$$\psi_R \to \exp\left(i\frac{\boldsymbol{\sigma}\cdot\boldsymbol{n}}{2} - \frac{\boldsymbol{\sigma}\cdot\boldsymbol{\eta}}{2}\right)\psi_R \; . \tag{2.11}$$

$\boldsymbol{\sigma}$ is the vector of Pauli matrices, $\boldsymbol{n}$ is the vector of the angles of rotation in space and $\boldsymbol{\eta}$ contains the boost parameters. Remark: the behavior under rotation is characteristic for spin-$1/2$ particles, whose wave-function gain a minus sign from rotation by 2π. The velocity and thus the generators of the Lorenz boost change sign $\mathbf{K} \to -\mathbf{K}$ Under the parity operation, whereas the angular momentum does not $\mathbf{J} \to \mathbf{J}$. Therefore, under parity transformation one gets $\psi_L \leftrightarrow \psi_R$. Finally, to combine both within one object, following construction is made (bi-spinor)

$$\psi := \begin{pmatrix} \psi_L \\ \psi_R \end{pmatrix} \; . \tag{2.12}$$

Writing the rapidity in terms of energy and momentum (using $c = 1$) leads to

$$\psi_L(\mathbf{p}) = \frac{E + m + \boldsymbol{\sigma}\cdot\mathbf{p}}{\sqrt{2m(E+m)}}\psi_L(0) \tag{2.13}$$

and

$$\psi_R(\mathbf{p}) = \frac{E + m - \boldsymbol{\sigma}\cdot\mathbf{p}}{\sqrt{2m(E+m)}}\psi_R(0) \; . \tag{2.14}$$

This can be rearranged to

$$\psi_R(\mathbf{p}) = \frac{E + \boldsymbol{\sigma}\cdot\mathbf{p}}{m}\psi_L(\mathbf{p}) \tag{2.15}$$

and

$$\psi_L(\mathbf{p}) = \frac{E - \boldsymbol{\sigma}\cdot\mathbf{p}}{m}\psi_R(\mathbf{p}) \; . \tag{2.16}$$

Using the definitions of the gamma matrices

$$\gamma^0 = \sigma_1 \otimes \mathbb{1}_2 := \begin{pmatrix} 0 & \mathbb{1}_2 \\ \mathbb{1}_2 & 0 \end{pmatrix} \; , \quad \gamma^i = i\sigma_2 \otimes \sigma_i := \begin{pmatrix} 0 & \sigma_i \\ -\sigma_i & 0 \end{pmatrix} \; , \tag{2.17}$$

one arrives at the momentum space representation of the Dirac equation in Weyl, or also called chiral, form

$$(\gamma^\mu p_\mu - m)\psi(\mathbf{p}) = 0 \; , \tag{2.18}$$

and in real-space

$$(i\gamma^\mu \partial_\mu - m)\psi(x_\mu) = 0 \; . \tag{2.19}$$

For $m = 0$, the equation decouples into an equation for the right-handed ψ_R and for the left-handed ψ_L part and is called the Weyl equation. The coupling of the electrically charged Dirac particle $q = -e$) to an electromagnetic external field is established within the minimal coupling prescription

$$p_\mu \to \Pi_\mu = p_\mu + eA_\mu \quad \text{or} \quad \partial_\mu \to D_\mu = \partial_\mu - ieA_\mu, \tag{2.20}$$

with e being the electron charge, the scalar potential $A_0 = \phi$, and the vector potential A_i. There are infinitely many unitary equivalent representations of the Dirac equation. In this manuscript the Schrödinger, or also called standard, representation is used frequently. The transformations from the chiral form are

$$\beta := S\gamma^0 S^{-1} = \begin{pmatrix} \mathbb{1}_2 & 0 \\ 0 & -\mathbb{1}_2 \end{pmatrix} \quad \text{and} \quad \alpha_i := S\gamma^i S^{-1} = \begin{pmatrix} 0 & \sigma_i \\ \sigma_i & 0 \end{pmatrix} , \tag{2.21}$$

using

$$S := \begin{pmatrix} \mathbb{1}_2 & \mathbb{1}_2 \\ \mathbb{1}_2 & -\mathbb{1}_2 \end{pmatrix} . \tag{2.22}$$

Finally using this definitions, the Dirac equation in Schrödinger representation has the form

$$i\hbar \frac{\partial}{\partial t} \psi = H \, \psi , \tag{2.23}$$

with

$$H = -i\hbar c \alpha_i \left(\frac{\partial}{\partial x_i} - i \frac{e}{c\hbar} A_i \right) + \beta mc^2 - e\phi . \tag{2.24}$$

2.3 Solution, observables and interpretation

It follows from Eqs. (2.10) and (2.11) that

$$\bar{\psi}\psi = \psi_L^\dagger \psi_R + \psi_R^\dagger \psi_L \tag{2.25}$$

is invariant under Lorenz transformation, where $\bar{\psi} := \gamma^0 \psi^\dagger$. The later is also invariant under parity transformation and is therefore a true scalar under Lorenz transformation. A useful expression not being Lorenz invariant is

$$j^\mu = \bar{\psi}\gamma^\mu\psi . \tag{2.26}$$

Its zeroth component

$$j^0 = \psi^\dagger \gamma^0 \gamma^0 \psi = \psi^\dagger \psi = \psi_L^\dagger \psi_L + \psi_R^\dagger \psi_R = |\psi_1|^2 + |\psi_2|^2 + |\psi_3|^2 + |\psi_4|^2 , \tag{2.27}$$

is positive definite, allowing the interpretation of a probability density. Then, the other components j^i are the spatial components of the current density. By insertion of the Dirac equation Eq. (2.19) it can be shown that the continuity equation $\partial_\mu j^\mu = 0$ is fulfilled. Mass and charge density deviate from the probability density only in prefactors leading to the conclusion that total mass and charge are conserved.

The solution for the free Dirac equation can be obtained most easily by examining the Schrödinger representation in the rest frame

$$i\frac{\partial}{\partial t}\,\psi = \beta m \psi \, , \tag{2.28}$$

giving

$$\psi_n = w_n(0) e^{-i\epsilon_n m t} \tag{2.29}$$

where $\epsilon_1 = \epsilon_2 = 1,\ \epsilon_3 = \epsilon_4 = -1$ and $w_n(0)$ are 4-component vectors with a 1 at the n-th position and the rest zero. Thus, in the rest frame one can identify the purely positive and negative energy solutions. The general case, having momentum $\mathbf{p} = (p_x, p_y, p_z)$ can be obtained by applying a Lorenz transformation Eqs. (2.13) and (2.14) [3]

$$w_n(\mathbf{p}) = \sqrt{\frac{E+m}{2m}} \begin{pmatrix} 1 & 0 & \frac{p_z}{E+m} & \frac{p_x - ip_y}{E+m} \\ 0 & 1 & \frac{p_x+ip_y}{E+m} & -\frac{p_z}{E+m} \\ \frac{p_z}{E+m} & \frac{p_x-ip_y}{E+m} & 1 & 0 \\ \frac{p_x+ip_y}{E+m} & -\frac{p_z}{E+m} & 0 & 1 \end{pmatrix} w_n(0) \, . \tag{2.30}$$

The eigenvectors are the columns of the matrix in the expression above. The solution including a constant 4-vector potential is obtained by substitution using the minimal coupling prescription Eq. (2.20). Then the eigenvectors of Eq. (11.2) corresponding to positive energy are (using $V = -e\phi$)

$$\psi_1(x_\mu) = \sqrt{\frac{E-V+m}{2m}} \begin{pmatrix} 1 \\ 0 \\ \frac{\Pi_z}{E-V+m} \\ \frac{\Pi_x + i\Pi_y}{E-V+m} \end{pmatrix} e^{-i\Pi^\mu x_\mu} \tag{2.31}$$

and

$$\psi_2(x_\mu) = \sqrt{\frac{E-V+m}{2m}} \begin{pmatrix} 0 \\ 1 \\ \frac{\Pi_x - i\Pi_y}{E-V+m} \\ -\frac{\Pi_z}{E-V+m} \end{pmatrix} e^{-i\Pi^\mu x_\mu} \, . \tag{2.32}$$

The negative energy eigenstates are

$$\psi_3(x_\mu) = \sqrt{\frac{E+V+m}{2m}} \begin{pmatrix} \frac{\Pi_z}{E+V+m} \\ \frac{\Pi_x+i\Pi_y}{E+V+m} \\ 1 \\ 0 \end{pmatrix} e^{i\Pi^\mu x_\mu} \tag{2.33}$$

and

$$\psi_4(x_\mu) = \sqrt{\frac{E+V+m}{2m}} \begin{pmatrix} \frac{\Pi_x-i\Pi_y}{E+V+m} \\ -\frac{\Pi_z}{E+V+m} \\ 0 \\ 1 \end{pmatrix} e^{i\Pi^\mu x_\mu} \; . \tag{2.34}$$

The eigenenergies are

$$\mathcal{E}_\pm = \pm E = \pm\sqrt{\Pi_x^2+\Pi_y^2+\Pi_z^2+m^2} + V \; . \tag{2.35}$$

The spectrum is not bounded from below. This is a major problem for the Klein-Gordon equation, which deals with bosons. An arbitrary number of particles can be in the same quantum state and the system can make a transition to a lower energy state by radiation. In this way it can loose an infinite amount of energy. For fermions, this puzzle can be solved within the particle-hole interpretation. For fermionic systems a quantum state can be only singly occupied (the Pauli principle). Within the particle-hole interpretation one assumes that all the negative energy states are filled (the Dirac sea), preventing the Dirac particle from decaying to lower energy states. Moreover, particle-hole creation can be explained within this construction. An electron, having positive energy, negative charge and spin "up", can be kicked out of the Dirac sea when a minimum energy of $2mc^2$ (being the excitation gap, or in other words, twice the energy corresponding to the rest mass of the electron) is transfered to it by a photon. Then the sea contains a hole, which can be reinterpreted as an antiparticle (the positron) having positive energy, positive charge and spin "down". Within solid state systems such filled bands are natural. This suggests that the Dirac equation and the field theories in general, used in the standard model, may be effective theories of an underlying more fundamental microscopic theory [8].

Analytic solutions of the Dirac equation for external fields with time- and/or space-dependence are rare. Without claim to completeness they include the case of a homogeneous magnetic field [9], the Dirac oscillator [10], an electromagnetic plane wave [11], and the Coulomb potential [12]. In general, the problem has to be treated numerically.

2.4 The Dirac equation in lower dimensions

The Dirac equation in three spatial dimensions requires a minimal dimension for the Dirac matrices of four. The dimension for the Dirac matrices has to be even [1] and one cannot provide four anti-commuting two-dimensional matrices. Things look different in one or two dimensions. Here, one can choose e.g. σ_x for the x-momentum term, σ_y for the y-momentum term and σ_z for the mass term

$$H_D = \sigma_x p_x + \sigma_y p_y + m\sigma_z \; . \tag{2.36}$$

Of course this cannot capture the full particle-hole and spin degree of freedom of a general Dirac particle, but sometimes the spin does not matter. In other cases it is fully locked to the momentum, as in the topological insulator case [13]. Also, one can have translational invariance in one or two directions allowing for a one or two dimensional description. But particles can also be confined to lower dimensions leading to an effective 1D or 2D Dirac Hamiltonian. An example for the 1D situation are the edge channels in the quantum spin Hall effect [13]. The 2D case occours for example in narrow band semiconductors, graphene, and again in topological insulators [13]. More about these issues and how the Dirac equation arises as an effective model will be shown in the next chapter.

REFERENCES

[1] W. Greiner, Relativistic Quantum Mechanics: Wave Equations, 3rd ed., Springer Berlin (2000).

[2] J. J. Sakurai, Advanced Quantum Mechanics, Pearson Education India (2006).

[3] L. H. Ryder, Quantum Field Theory, Cambridge University Press (1996).

[4] B. Thaller, The Dirac Equation, Springer Berlin (1992).

[5] E. Schrödinger, Quantisierung als Eigenwertproblem, Annalen der Physik 385 (1926) 437-490.

[6] P. A. M. Dirac, The Quantum Theory of the Electron, Proc. R. Soc. Lond. A 117 (1928) 610-624.

[7] A. Einstein, Zur Elektrodynamik bewegter Körper. Annalen der Physik und Chemie 17 (1905) 891-921.

[8] G. E. Volovik, The Universe in a Helium Droplet, Oxford University Press (2009).

[9] I. I. Rabi, Das freie Elektron im homogenen Magnetfeld nach der Diracschen Theorie, Z. Phys. 49 (1928) 507-511.

[10] K. Nikolsky, Das Oszillatorproblem nach der Diracschen Theorie, Z. Phys. 62 (1930) 677-681

[11] D. M. Wolkow, Über eine Klasse von Lösungen der Diracschen Gleichung, z. Phys. 94 (1935) 250-260.

[12] H. A. Bethe, E. E. Salpeter, Quantum Mechanics of One- and Two-Electron Atoms, Plenum Publishing Corporation New York (1977) 63-71.

[13] X. L. Qi and S. C. Zhang, Topological Insulators and Superconductors, Reviews of Modern Physics 83 (2011) 1057-1110, and references therein.

Chapter 3

EMERGING "RELATIVISTIC" QUANTUM MECHANICS IN SOLID STATE PHYSICS

In periodic systems, like solids or cold atomic lattices, a linear dispersion relation can occur when energy bands touch. The simplest example for this behavior is the electron in a periodic potential. The Bloch solutions have a degeneracy of two at most and therefore the bands cannot overlap. At a touching point they must have linear dispersion (see e.g. [1]). The behavior of the quasiparticle, near this so-called Dirac-point, can be described by the Dirac equation. In general, topological non-triviality, like emerging symmetry protected surface states, is expressed in form of topological invariants. More precisely, the occurrence/non-occurrence of this protected surface states can be fully classified by these invariants, which themselves are determined by the symmetry of the bulk Hamiltonian [2]. The relevant symmetries are time-reversal symmetry (TRS), particle-hole symmetry (PHS) and sub-lattice (or chiral) symmetry (SLS).

In a QM mechanical system, if parameters are changed adiabatically, the wave function picks up a geometrical phase, the Berry phase [3]. In general the Berry phase can be computed by the Berry vector potential, in analogy to the vector potential in electrodynamics, and is not gauge invariant. In the case of a closed path the phase can not be removed by gauge transformation. The locally defined gauge invariant quantity, corresponding to the magnetic field in electrodynamics, is the Berry curvature [3]. A system can have a conserved quantity, the topological charge (Z_2 or Chern number), which can be computed from the Berry curvature [6]. The latter has singularities at the Dirac-points. They determine the connectedness in the parameter space and thus its topology. For time-reversal invariant systems Dirac points usually exist in pairs. This is called fermion doubling. Topological non-triviality can occur "holographically", leading to the topological insulator (TI) [7]. For this material the time-reversal partners sit on opposite sides of the surface. The computation of topological invariants for "almost" touching bands, will be discussed briefly on hand of a generic two band model (3.1.3). Comments regarding topological triviality/ non-triviality, for the Hamiltonians presented, will be made. For a certain tight-binding model, having a Chern number of one, dimensional reduction reveals the 1D quantum Hall (QH) edge states always lying in the band-gap of the 2D bulk states [8].

First, it will be discussed how linear dispersion relation arises by examining simple tight-binding models. Linear dispersion behavior of touching bands can also be understood within the $k \cdot p$ approach or in general by examining symmetry principles. Here, we will argue with tight-binding models because they are very closely related to finite difference approximations used to develop the numerical scheme. They show common features arising from the lattice, most prominently the periodic band structure and the famous fermion doubling.

3.1 Dirac equation from tight-binding models and the fermion doubling problem

In general, a tight-binding model trivially needs at least two "states" per unit cell to show a two band structure, eventually having touching energy bands with a linear dispersion relation.

3.1.1 1D two atom tight-binding model

Here, the behavior is demonstrated with a simple 1D two atom, nearest neighbor, tight-binding model. Let us call one atom u and the other one v (see Fig. 3.1). The electron has the probability amplitude u sitting on the atom at position j, where we use the notation u_j. It can hop to (one can also say: the atom is coupled to) the atom at position v_j, being in the same unit cell, and to v_{j-1}, which is in the neighbor unit cell. The electron on v_j can undergo a transition to u_j and u_{j+1} respectively. Thus, for the Schrödinger equation in tight-binding representation and matrix form one can write

$$i\frac{\partial}{\partial t}\vec{\psi} = -\begin{pmatrix} 0 & 1+T \\ 1+T^{-1} & 0 \end{pmatrix}\vec{\psi}\,, \tag{3.1}$$

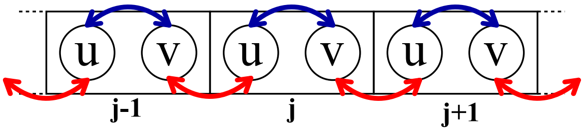

Figure 3.1: 1D two atom tight-binding model.

where $\vec{\psi} = (u, v)$ and T is the translation operator $Tw_j = w_{j+1}$ with $w = u, v$. Then the Fourier transformed Hamiltonian is

$$H = -\begin{pmatrix} 0 & 1 + e^{ik\Delta} \\ 1 + e^{-ik\Delta} & 0 \end{pmatrix} , \tag{3.2}$$

with Δ being the distance between unit cells ($=$ two times the distance between the atoms). The Hamiltonian can be diagonalized giving the eigenvalues

$$E(k) = \pm 2 \cos \frac{k\Delta}{2} \; . \tag{3.3}$$

The domain for k ("Brillouin zone") is $k \in \big(-\frac{\pi}{\Delta}, \frac{\pi}{\Delta}\big]$. One can conclude, that the Hamiltonian (3.2) has one cone at the Brillouin zone boundary. To obtain a model with the cone at $k = 0$ one substitutes $k \to k + \frac{\pi}{\Delta}$ leading to

$$\begin{aligned} H &= -\begin{pmatrix} 0 & 1 + e^{i(k\Delta+\pi)} \\ 1 + e^{-i(k\Delta+\pi)} & 0 \end{pmatrix} \qquad (3.4) \\ &= -\begin{pmatrix} 0 & 1 - e^{ik\Delta} \\ 1 - e^{-ik\Delta} & 0 \end{pmatrix} , \qquad (3.5) \end{aligned}$$

having the dispersion relation

$$E(k) = \pm 2 \sin \frac{k\Delta}{2} \; . \tag{3.6}$$

Note that the shift by a general value $k \to k + A$ corresponds to the Peierls substitution by which a vector potential A can be included [9, 10]. Expansion at the Dirac point gives

$$H_W = \begin{pmatrix} 0 & -ik \\ ik & 0 \end{pmatrix} \quad \to \quad -i \begin{pmatrix} 0 & -i\partial_y \\ i\partial_y & 0 \end{pmatrix} , \tag{3.7}$$

which is the 1D Weyl (massless Dirac) Hamiltonian. Finally a mass term is included by a σ_z term leading to the Dirac Hamiltonian

$$H_D^y = -i\sigma_y \partial_y + m\sigma_z \; . \tag{3.8}$$

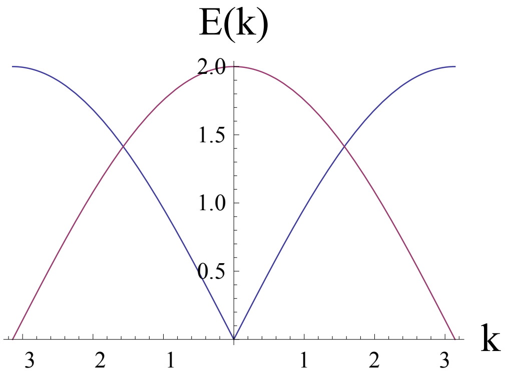

Figure 3.2: Dispersion relation of a 1D two atom tight-binding model. It shows a linear dispersion relation at the Brillouin zone boundary π/Δ. A vector potential $A = \pi/\Delta$ shifts the Dirac cone to the center ($k \to k + A$).

The Pauli matrices fulfill the Lie algebra and a rotation from the 1D representation along the y-axis to the x-axis can be performed by the unitary transformation

$$UH_D^y U^{-1} = H_D^x = -i\sigma_x \partial_x + m\sigma_z \; , \tag{3.9}$$

with

$$U = \exp\big(-i\frac{\alpha}{2}\mathbf{n}\cdot\boldsymbol{\sigma}\big) = \cos\frac{\alpha}{2} - i\,\mathbf{n}\cdot\boldsymbol{\sigma}\sin\frac{\alpha}{2} \; , \tag{3.10}$$

$\boldsymbol{\sigma}$ is the vector of Pauli matrices, $\mathbf{n} = (0, 0, 1)$ is the rotation axis, and $\alpha = \pi/2$ is the angle of rotation.

3.1.2 The 2D Dirac Hamiltonian and the fermion doubling problem

Demanding rotational symmetry in the xy-plane one gets the full 2D Dirac Hamiltonian from Eqs. (3.8) and (3.9)

$$H_D = -i\sigma_x\partial_x - i\sigma_y\partial_y + m\sigma_z \; . \tag{3.11}$$

Here one should note that Eq. (3.5) is the finite difference expression of the differential operator given in Eq. (3.7) using only right- and left-sided finite difference expressions of the first derivative. In 2D (or higher dimensions) it is not possible to construct a local finite difference approximation of the Hamiltonian (3.11), which is Hermitian without using central finite difference expressions instead of one-sided ones. A central finite difference approximation of the first derivative always omits the central point, which in turn can have arbitrary values without changing the value, which the finite difference expression yields. Thus, the constant and the function with the highest possible spatial oscillation frequency, on the grid leads to the value zero and therefore to energy equal zero. This is a special case of what is called the fermion doubling problem [11]. In general, the induced non-monotonic behavior of the dispersion relation leads to additional solutions, propagating with opposite group velocity. The linear dispersion relation can be approximated exactly by the SLAC derivative operator, which includes infinitely many neighbor points [12]. This makes the operator non-local, since even in the limit of vanishing lattice spacing an infinite region in space is included in the approximation. Nielsen and Ninomia stated a no-go theorem for the Dirac-equation. They found that its discretization on a regular grid inevitably leads to additional fermion flavors under the assumptions of translational invariance, locality, and Hermiticity of the Hamiltonian [11].

3.1.3 The Chern number of a general two band Hamiltonian

A general two band model can be written as (see e.g. [7])

$$h(\mathbf{k}) = \boldsymbol{\sigma} \cdot \boldsymbol{d}(\mathbf{k}) + \mathbb{1}\epsilon(\mathbf{k}) \, , \tag{3.12}$$

where $\boldsymbol{d}$ is the vector of spin or pseudospin, depending on the concrete problem. The first Chern number (also called the topological charge), for this system, is defined as [7]

$$C_1 = \frac{1}{4\pi} \int \mathrm{d}k_x \int \mathrm{d}k_y \hat{\boldsymbol{d}} \cdot \frac{\partial \hat{\boldsymbol{d}}}{\partial k_x} \times \frac{\partial \hat{\boldsymbol{d}}}{\partial k_y} \, . \tag{3.13}$$

As an example writing Eq. (3.11) in momentum space gives

$$\hat{\boldsymbol{d}}(\mathbf{k}) = \frac{1}{\sqrt{k_x^2 + k_y^2 + m^2}} \begin{pmatrix} k_x \\ k_y \\ m \end{pmatrix} \, . \tag{3.14}$$

Remark: This vector field is called a meron, for $m > 0$ ($m < 0$) pointing upwards (downwards) in the origin and in-plane at infinity. It is half a skyrmion which also points upwards (downwards) at infinity.

The Chern number of (3.11) gives $C_1 = 1/2$ for $m > 0$ and $C_1 = -1/2$ for $m < 0$. From the Chern number the *Hall conductance* can be calculated by [13]

$$\sigma_{xy} = \frac{e^2}{h} C_1 \, . \tag{3.15}$$

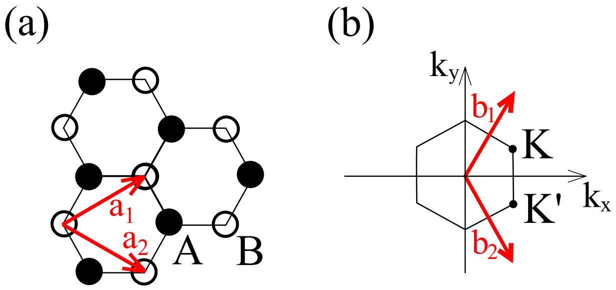

Figure 3.3: (a) Tight-binding model for graphene, consisting of two staggered triangular lattices having the "atoms" A and B respectively. a_1 and a_2 are the lattice vectors. (b) The reciprocal lattice (Brillouin zone) with the reciprocal vectors $\boldsymbol{b}_1$ and $\boldsymbol{b}_2$ and the positions of the Dirac cones at the Brillouin zone corners K and K'.

A general result in topological band and field theory is that a system needs to have either broken time-reversal or inversion symmetry to be topologically non-trivial [13, 7]. Then, what is broken in the 2D Dirac equation (3.11)? It turns out parity (=space inversion symmetry) is violated. [1] With $P = \sigma_x$ being a suitable parity transformation one gets

$$\begin{aligned} PH_D(k_x, -k_y, m)P^{-1} &= \sigma_x\sigma_x\sigma_x k_x - \sigma_x\sigma_y\sigma_x k_y + m\sigma_x\sigma_z\sigma_x \\ &= \sigma_x k_x + \sigma_y k_y - m\sigma_z \\ &= H_D(k_x, k_y, -m)\ , \end{aligned} \tag{3.16}$$

which means that parity is broken by the mass term.

3.1.4 Graphene, topologically trivial

In the 2D honeycomb lattice material graphene time-reversal symmetry and inversion symmetry is preserved, thus fermion doubling has to be expected. Indeed, in graphene one observes two valleys within the Brillouin zone at K and K' [16]. In the low energy limit they resemble two Dirac cones at these points. One transforms into the other under time-reversal and also under inversion. In analogy to real spin this degree of freedom is called pseudospin (compare Kramers theorem [15]). For a tight-binding model consisting of two staggered triangular lattices including atoms A and B (Fig. 3.3)

---

[1] In contrast to 3D parity in 2D inverts only one coordinate e.g. $(x, y) \to (x, -y)$ otherwise it would simply be a rotation.

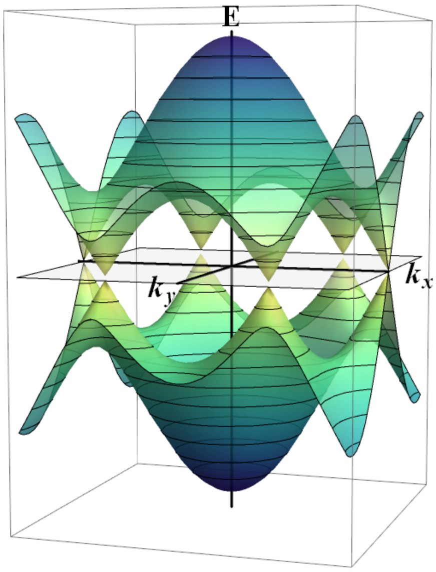

Figure 3.4: Band structure of graphene, showing linear dispersion relation at the Dirac points. It is shown for the simplest tight-binding model [16], allowing only nearest neighbor hopping.

respectively, I refer to a review article [16]. Therefore, a minimal continuum model has to describe electrons and holes together with the two fermion flavors and requires a four-component Dirac spinor. Essentially, the continuum model for Dirac fermions in graphene consists of two copies of the massless 2D Dirac Hamiltonians with opposite parity [16]

$$H_G = k_x(\sigma_z^v \otimes \sigma_x^{ph}) + k_y(\mathbb{1}^v \otimes \sigma_y^{ph}) \ . \tag{3.17}$$

The superscript "v" stands for the valley subspace and the "ph" for the particle-hole subspace. Within this model, graphene is topologically trivial, because the Berry curvature is zero in the whole Brillouin zone (see result for the Dirac equation (3.13) in the case of $m = 0$). Breaking inversion symmetry in graphene leads to a mass term and non vanishing Berry curvature at the Dirac points. In principle, the mass terms at the valleys can have the same (normal case for graphene) or opposite sign. In the former case one has $C_1 = 1/2$ at K and $C_1 = -1/2$ at K' adding to zero. Equal signs for the Chern number at the Dirac points lead to the valley Hall effect [6]. Taking into account the electron spin and therefore spin-orbit coupling leads to a Hamiltonian consisting of two copies of the Haldane Hamiltonian [4] with opposite sign of the Hall conductivity for up and down spin. This results in graphene being a QSHE material, although with a very small gap [5].

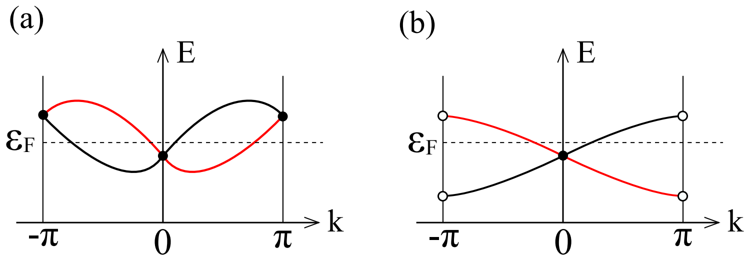

Figure 3.5: Energy dispersion relations of 1D systems. (a) The dispersion relation of an ordinary 1D spin-$1/2$ system always crosses the Fermi-energy four times because at least at $k = 0$ and at $k = \pi$ there are Kramers-degenerate points (shown as filled circles). This is called the fermion doubling (one has two fermion flavors). (b) For a 1D system, emerging "holographically" at the boundary of a 2D time-reversal invariant system, one obtains only one Dirac cone. In this case the time invariant point at $k = \pi$ merges with the dispersion relation of the opposite boundary (not shown).

3.1.5 Systems with half integer spin, Kramers theorem

Fermion doubling also arises in Hamiltonians describing half integer spin systems. Even with spin-orbit coupling (splitting the spin-up/spin-down degeneracy) there exist time-reversal invariant points in the Brillouin zone. These points are always twofold degenerate (Kramers theorem) [15]. This behavior already can be seen in 1D where the time-reversal invariant points are at $k = 0$ and $k = \pi/\Delta$ with Δ being the size of the unit cell. Then the Fermi energy is crossed at least four times, twice as often as it would for a single fermion flavor (see Fig. 3.5(a)). In contrast, for a 1D system emerging "holographically" at the edge of a 2D time-reversal invariant system, one has also Kramers degeneracy, but at $k = \pi/\Delta$ the state of one edge is the Kramers degenerate partner of a state on the other edge Fig. 3.5(b). This circumvents the fermion doubling and allows a single fermion flavor.

3.2 How nature circumvents the fermion doubling problem: The topological insulator

Topological insulators are materials insulating in the bulk (2D or 3D) but having conducting surface states, which cannot be removed by perturbations unless time-reversal symmetry is broken.

3.2.1 Topologically non-trivial 2D tight-binding model and dimensional reduction

A 2D tight-binding model, being topologically non-trivial, was first introduced by Haldane [8]. This was achieved on a honeycomb lattice by using imaginary next nearest neighbor hopping. An also topological non-trivial, but simpler, model on a rectangular grid was introduced in [6]. It shall, along with its topological surface states, be shown here briefly. In the tight-binding Hamiltonian the σ's represent the spin degree of freedom, where the latter is coupled to momentum due to strong spin-orbit coupling and the σ_z corresponds to out of plane ferromagnetic polarization

$$H = \sum_n \left(c_n^\dagger \frac{\sigma_z - i\sigma_x}{2} c_{n+\hat{x}} + c_n^\dagger \frac{\sigma_z - i\sigma_y}{2} c_{n+\hat{y}} + m\, c_n^\dagger \sigma_z c_n + H.c. \right) . \tag{3.18}$$

$\hat{x}$ and $\hat{y}$ are the unit vectors in x- and y-direction respectively. In Fourier space this writes

$$h(\mathbf{k}) = (\sin k_x)\sigma_x + (\sin k_y)\sigma_y + (m + \cos k_x + \cos k_y)\sigma_z \, . \tag{3.19}$$

In the low energy limit this Hamiltonian leads to the 2D Dirac Hamiltonian (3.11) with $m \to m{+}2$. The occurence of additional Dirac cones is avoided in a certain parameter range for m because of the momentum dependent mass (σ_z) terms, which corresponds to the Wilson solution to the fermion doubling problem [17]. Using Eq. (3.13) one computes the first Chern number of the Hamiltonian (3.19) as

$$C_1 = \begin{cases} 1 & \text{for } 0 < m < 2 \\ -1 & \text{for } -2 < m < 0 \\ 0 & \text{otherwise.} \end{cases} \tag{3.20}$$

Thus, in a certain parameter range the Hamiltonian is topologically non-trivial and one has to expect topological surface states on the boundary to a topologically trivial material (e.g. vacuum). This can be shown by *dimensional reduction* and diagonalizing the resulting uncoupled 1D Hamiltonians. Here we merely sketch the idea, details can be read in [6]. Generally, one wraps up (by imposing periodic boundary conditions) one dimension, e.g. y , getting a cylinder in the 2D case. Then, one can apply a partial Fourier transform in y-direction and obtains uncoupled 1D Hamiltonians in the x-direction. The wave number of the Fourier transformed direction k_y then enters as a parameter in the 1D models. From an added vector potential $k_y \to k_y + A_y = k_y + E_y t$, coming from a constant electric field E_y, one can

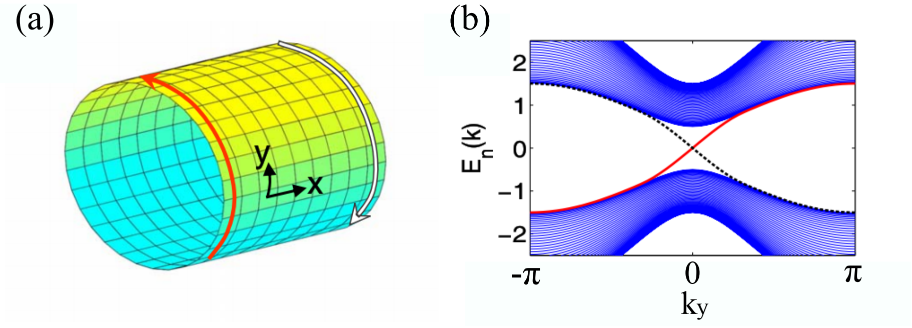

Figure 3.6: (a) Chiral edge states of a topologically non-trivial 2D tight-binding model with periodic boundary conditions in y-direction. (b) 2D bulk states and 1D chiral edge states in the bulk band-gap. Adapted with permission from Qi et al. [7], Copyright (2008) by The American Physical Society.

compute the charge that flows trough the system in one adiabatic cycle of the parameter k_y. Finally, using this result one obtains the Hall response in this model without external magnetic field of the system. Complementary, direct diagonalization of the 1D Hamiltonians reveals the energy spectrum, showing chiral (one-way) propagating states localized in the gap and on opposite ends of the cylinder (see Fig. 3.6 adapted from Qi et al. [7]).

3.2.2 The topological insulator

In contrast to a purely 2D material on the surface of a topological insulator, there can exist a single (or generally an odd number of) Dirac cone, although time-reversal symmetry is preserved. It is also called a "holographic metal", because it exists only due to the topological non-trivial bulk, interfaced with a topological trivial material. In actual experimentally confirmed topological insulators, a single fermion flavor for the quasiparticles on the surface lives on the domain-wall between a spin-orbit driven band inversion within the topological insulator and normal band ordering in vacuum. Conversely, the time-reversal symmetry topological protection of the surface states can be understood by the fact, that a single Dirac cone can not exist in a solely 2D material having time-reversal symmetry (see Kramers theorem [15].

In 1D and 2D, the simple Dirac model (3.11) with mass is topologically non-trivial. With the mass changing sign it shows domain-wall solutions. They will be shown in detail in CHAPTER 7. The same is true for the, slightly more complicated, effective Hamiltonian for the strong spin-orbit coupled states in the bulk of a topological insulator [13]

$$H(\mathbf{k}) = \epsilon_0(\mathbf{k})\mathbb{1}_4 + \begin{pmatrix} \mathcal{M}(\mathbf{k}) & A_1 k_z & 0 & A_2 k_- \\ A_1 k_z & -\mathcal{M}(\mathbf{k}) & A_2 k_- & 0 \\ 0 & A_2 k_+ & \mathcal{M}(\mathbf{k}) & -A_1 k_z \\ A_2 k_+ & 0 & -A_1 k_z & -\mathcal{M}(\mathbf{k}) \end{pmatrix} . \tag{3.21}$$

Here we have $k_\pm = k_x \pm i k_y$, $\epsilon_0(\mathbf{k}) = C + D_1 k_z^2 + D_2 k_\perp^2$, $\mathcal{M}(\mathbf{k}) = M - B_1 k_z^2 - B_2 k_\perp^2$ and $k_\perp = \sqrt{k_x^2 + k_y^2}$. The model has time-reversal symmetry, inversion symmetry, and rotation symmetry around the z-axis. The Hamiltonian is unitary equivalent to a uniaxially anisotropic 3D Dirac Hamiltonian (see Eq. (11.2)) with the difference, that the mass term $\mathcal{M}$ and the potential term $\epsilon_0(\mathbf{k})$ are $\mathbf{k}$ dependent. For the M and B's having the same sign, the bands at $k = 0$ are inverted compared to large k. Under these conditions the Hamiltonian is topologically non-trivial and supports gap-less symmetry protected surface states. One can compute the domain-wall solutions exponentially confined perpendicular to the surface. A projection of the bulk Hamiltonian (3.21) to these surface states gives the effective Hamiltonian [13]

$$H_{surf} = C + A_2(\sigma_x k_y - \sigma_y k_x) . \tag{3.22}$$

Here C is the chemical potential μ and A_2 corresponds to the effective velocity v. The latter, e.g. for Bi_2Se_3, is 6.2×10^5m/s. By a unitary transformation Eq. (3.10) (rotating the spin by $\alpha = \pi/2$) the Hamiltonian can be transformed to the 2D Dirac Hamiltonian in standard form Eq. (3.11). This Hamiltonian is a good approximation for the physics near the Dirac point. It is well confirmed by spin and angle resolved photo emission measurements (SARPES), which are shown in Fig. 3.7 [14]. The data clearly show the surface band structure in the form of a Dirac cone for Bi_2Se_3 and Bi_2Te_3, as well as the spin-momentum locking. In principle, there are also corrections from higher orders of k. E.g. for Bi_2Se_3, one can consider k^3 terms, which break the rotational symmetry around the z-axis. By explicitly breaking time-reversal symmetry in the Hamiltonian a mass term, opening a gap, can be introduced. More details how this actually can be done will be given in CHAPTER 7.

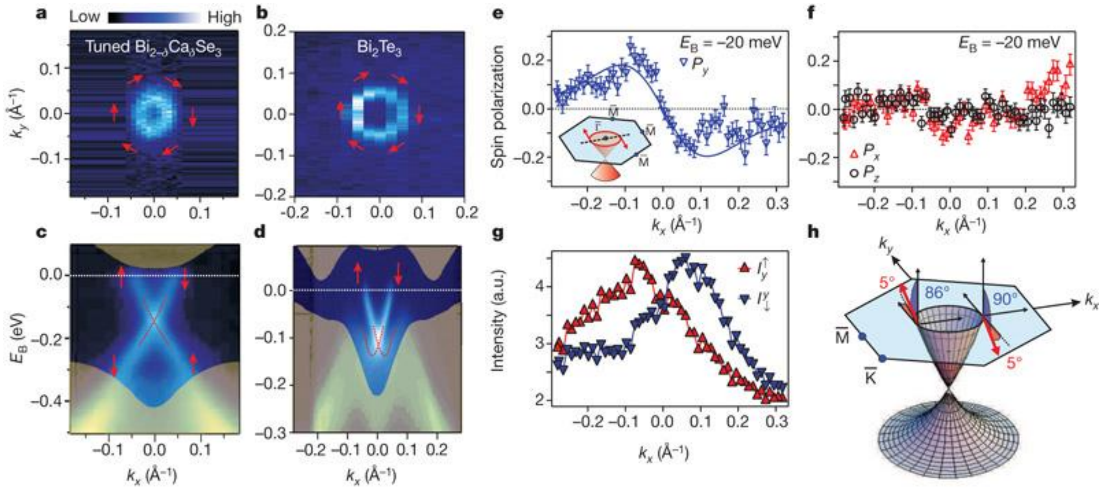

Figure 3.7: ARPES measurements of (a), (c) calcium doped Bi_2Se_3 (for Fermi level tuning) and of (b), (d) Bi_2Te_3. (e) y-component of spin polarization. (f) x-(red triangles) and z-components (black circles) of spin polarization. (g) Spin-resolved spectra from the y-component spin-polarization data. (h) Fitted values, showing the spin polarization of the spin-Dirac cone. With permission, from Hsieh et. al [14]

REFERENCES

[1] W. Pötz, Scattering Theory for Mesoscopic Quantum Systems with Non-Trivial Spatial Asymptotics in One Dimension, J. Math. Phys. 36 (1995) 1707-1741.

[2] A. P. Schnyder, S. Rhyu, A. Furusaki, and W. W. Ludwig, Classification of Topological Insulators and Superconductors in Three Spatial Dimensions, Phys. Rev. B 78.19 (2008) 195125-1 - 195125-22.

[3] M. V. Berry, Quantal Phase Factors Accompanying Adiabatic Changes, Proc. R. Soc. Lond. A 392 (1984) 45-57.

[4] F. D. M. Haldane, Model for a Quantum Hall Effect without Landau Levels: Condensed-Matter Realization of the "Parity Anomaly". Phys. Rev. Lett. 61 (1988) 2015-2018.

[5] M. Z. Hasan, C. L. Kane, Colloquium: Topological Insulators, Rev. Mod. Phys 82 (2010) 3045-3065, and references therein.

[6] D. Xiao, M. C. Chang, and Q. Niu, Berry Phase Effects on Electronic Properties, Rev. Mod. Phys. 82 (2010) 1959-2007.

[7] X. L. Qi, T. L. Hughes, and S. C. Zhang, Topological Field Theory of Time-Reversal Invariant Insulators, Phys. Rev. B 78 (2008) 195424-1 - 195424-43.

[8] X. L. Qi, Y. S. Wu, and S. C. Zhang, Topological Quantization of the Spin Hall Effect in Two-Dimensional Paramagnetic Semiconductors, Phys. Rev. B 74 (2006) 085308-1 - 085308-7.

[9] R. Peierls, Zur Theorie des Diamagnetismus von Leitungselektronen, Z. Phys. 80 (1933) 763-791.

[10] M. Graf and P. Vogl, Electromagnetic Fields and Dielectric Response in Empirical Tight-Binding Theory, Phys. Rev. B 51 (1995) 4940-4949, and references therein.

[11] H. B. Nielsen and M. Ninomiya, A No-Go Theorem for Regularizing Chiral Fermions, Physics Letters B 105 (1981) 219-223.

[12] S. D. Drell, M. Weinstein, and S. Yankielowicz, Strong-Coupling Field Theories. II. Fermions and Gauge Fields on a Lattice, Phys. Rev. D 14 (1976) 1627-1647.

[13] X. L. Qi and S. C. Zhang, Topological Insulators and Superconductors, Reviews of Modern Physics 83 (2011) 1057-1110, and references therein.

[14] D. Hsieh, Y. Xia, D. Qian, L. Wray, J. H. Dil, F. Meier, J. Osterwalder, L. Patthey, J. G. Checkelsky, N. P. Ong, A. V. Fedorov, H. Lin, A. Bansil, D. Grauer, Y. S. Hor, R. J. Cava, and M. Z. Hasan, A Tunable Topological Insulator in the Spin Helical Dirac Transport Regime, Nat. Lett. 460 (2009) 1101-1106.

[15] L. D. Landau, J. M. Lifschitz, Lehrbuch der theoretischen Physik, Akademie-Verlag Berlin (1990).

[16] A. C. Neto, F. Guinea, N. M. R. Peres, K. S. Novoselov, and A. K. Geim, The Electronic Properties of Graphene, Rev. Mod. Phys. 81 (2009) 109-162, and references therein.

[17] P. H. Ginsparg and K. G. Wilson, A Remnant of Chiral Symmetry on the Lattice, Phys. Rev. D 25 (1982) 2649-2657.

Chapter 4

EXPERIMENTAL CHALLENGES AND RECENT PROGRESS WITH TOPOLOGICAL INSULATORS

In this chapter the history of 3D topological insulators (TI) and their promises for future device applications are discussed. The literature has become very extensive due to the booming of TI research. Thus, here we can only give a brief overview with prominent examples from the literature, guiding the reader into this rapidly expanding field. For a recent review article see [4].

The 2D version of the TI, the so-called quantum spin Hall effect QSHE, was found theoretically for graphene (2005) by Kane and Mele [1]. The proposal of HgTe/CdTe quantum-wells as a QSHE material by Bernevig, Hughes and Zhang (2006) was soon followed by an experimental confirmation by König et al. (2007) [2, 3]. After the theoretical generalization of the 2D topological field theory to 3D and the prediction of 3D TIs (2007) [5, 6, 7, 8, 9] the run for experiments, proving the existence of this form of matter, was opened. Because this method is extremely surface-sensitive, rapid progress was made with angle-resolved photo emission spectroscopy measurements (ARPES). The single Dirac cone surface band structure [10, 11, 12, 13] (see Fig. 3.7) was verified already in (2008). Under the most promising materials which were investigated are $Bi_{1-x}Sb_x$ [10], Bi_2Te_3 [11, 12, 29], Bi_2Se_3 [13, 34, 14] and Sb_2Te_3 [12]. Recently, with Kawazulite even a natural TI was found [15]. The theoretically predicted spin texture of the surface states was confirmed experimentally using spin resolved ARPES (SARPES)[16, 17, 12] (see Fig. 3.7). Scanning tunneling spectroscopy (STS) was also used as a surface sensitive probe [18]. In principle this method allows a very good

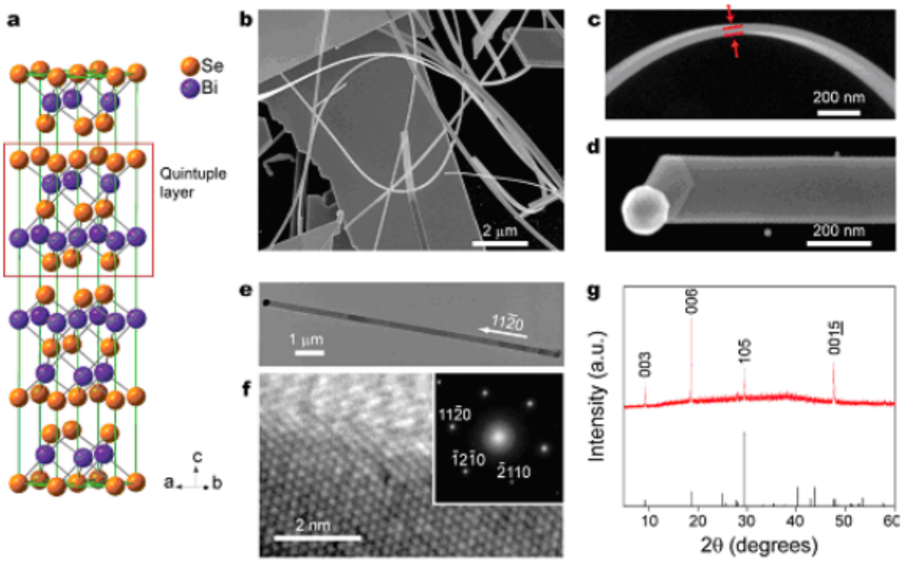

Figure 4.1: Gold-catalyzed vapor-liquid-solid (VLS) grown Bi$_2$Se3 nanoribbons. (a) shows the crystal structure with Se-Bi-Se-Bi-Se quintuple layers which (along c direction) are loosely bonded (by Van-der-Waals interactions) to each other. (b) SEM image of the VLS grown ribbons. (c) SEM image of a 30 nm thick ribbon. SEM image (d) and TEM image (e) of a nanoribbon with the catalyzing gold nanoparticle at the end. (f) high-resolution TEM and electron diffraction figure (inset) confirming the crystalline structure of the ribbon. (g) X-ray powder diffraction pattern. The ribbons can be identified as single crystals, along its length, with a size of the unit cells $a = b = 0.4140$ nm and $c = 2.8636$ nm. With permission, from Peng et. al [33].

spatial resolution and, in contrast to ARPES, can give additional information on hetero-structures, nano-structures, impurities etc.

For transport experiments and possible applications it is crucial to tune the Fermi level into the bulk gap. This was done by bulk doping e.g. with Sn for Bi$_2$Te$_3$ [21] or with Sb [29] or Ca [30] for Bi$_2$Se$_3$. In Bi$_{2-\delta}$Ca$_\delta$Se$_3$, tuning of the Dirac point towards the Fermi level, by NO$_2$ absorption at the surface, was shown (see Fig. 4.2). Despite great efforts the unintended doping, e.g. due to vacancies and antisites, still leads to a large bulk contribution to the electrical transport. In order to reduce the latter, the research direction goes to thin films and nanoribbons [31, 32, 33]. Nanoribbons grown by Peng et al. [33], using gold-catalyzed vapor-liquid-solid (VLS) growth, are shown in Fig. 4.1. Gate control of the chemical potential was shown in [28, 34].

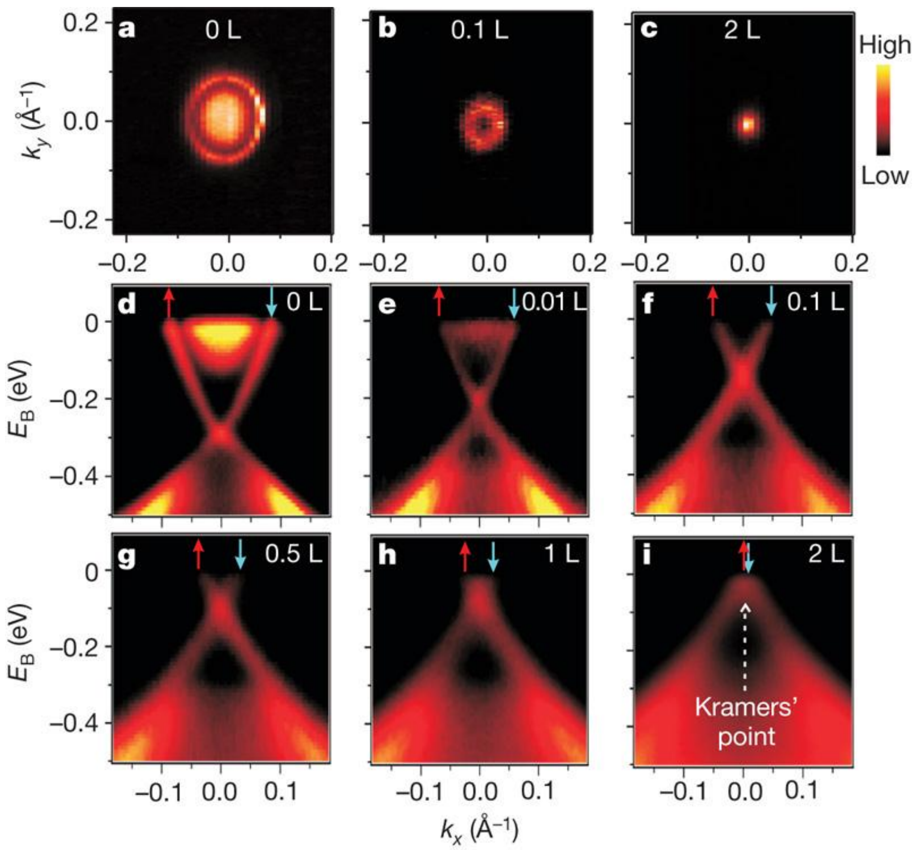

Figure 4.2: ARPES measurements, showing the Dirac point by NO_2 absorption at the surface. The introduction of hole-carriers shifts the Dirac point towards the Fermi energy. With increasing NO_2 absorption the spectrum becomes more diffuse due to surface disorder. With permission, from Hsieh et. al [12].

Massless Dirac fermions cannot be confined (efficiently) by an electrical potential because of Klein tunneling (see CHAPTER 9). Thus, for applications the possibility to open a gap in the surface spectrum is very important. This can be done by breaking time-reversal symmetry using a magnetic field and, more promising, by nearby magnetic layer or magnetic impurities exchange coupled to the surface Dirac fermions [9, 23]. Recently, this was also demonstrated experimentally [22, 23, 24, 25]. For Fe as dopant, in-plane magnetization was reported [24]. Out of plane ferromagnetic order was shown e.g. for Mn doped Bi_2Se_3 thin films [27], or for Cr doped thin films of $(Bi_xSb_{1-x})_2Te_3$ [26]. Doping of Bi_2Se_3 with ferromagnetically ordering Mn impurities, with out of surface-plane magnetization and opening of a gap

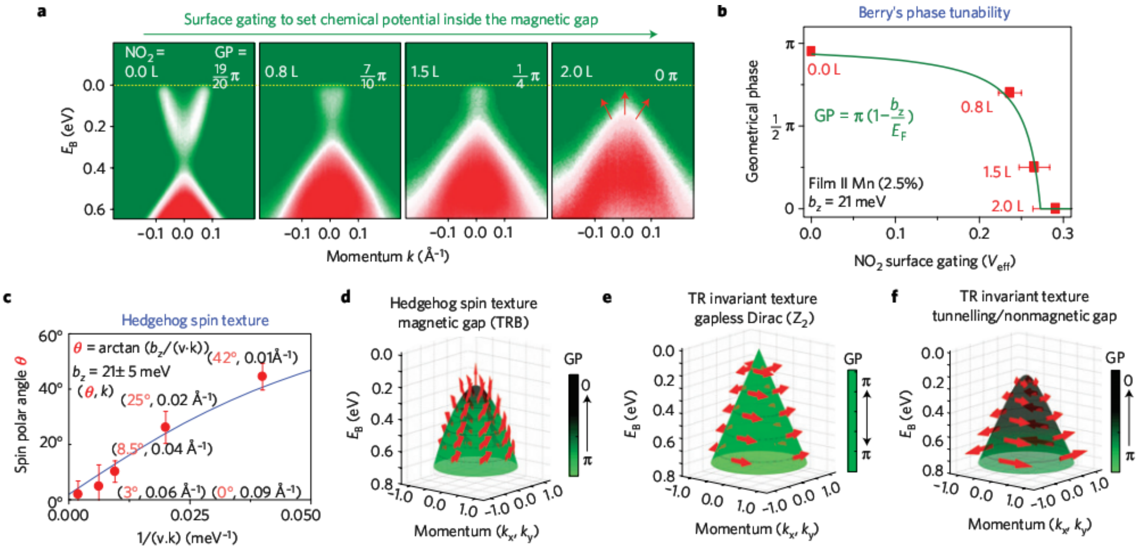

Figure 4.3: Doping of Bi_2Se3 with Mn impurities, showing out of surface-plane magnetization and opening of a gap for the surface states. (a) NO_2 surface doping to set the chemical potential inside the surface gap. (b) Berry phase as a function of the effective gate voltage from NO_2 doping. (d)-(f) schematic spin textures of Bi_2Se3, (d) for Mn doping a gap opens due to time reversal breaking by the ferro-magnetically ordered impurities, (e) time reversal texture for Zn doping, (f) ultrathin-film 3 QL with opened tunneling gap. With permission, from Xu et. al [27].

for the surface states, was shown in [27] (see Fig. 4.3).

Because of the difficulties mentioned above, it was a great experimental challenge to confirm the topological surface states in transport measurements. Clear signals of surface transport were found in nanoribbons showing Aharonov-Bohm oscillations [33, 35, 36] (see Fig. 4.4). Another potentially Nobel Prize worthy experimental breaktrough was the recent confirmation of the quantum anomalous Hall effect in a thin magnetic topological insulator [37]. It combines the robustness and the dissipationless one-way transport of the edge states of the QHE and the spin polarization of the QSHE, without requiring an external magnetic field. This is a very interesting combination for future device applications [37].

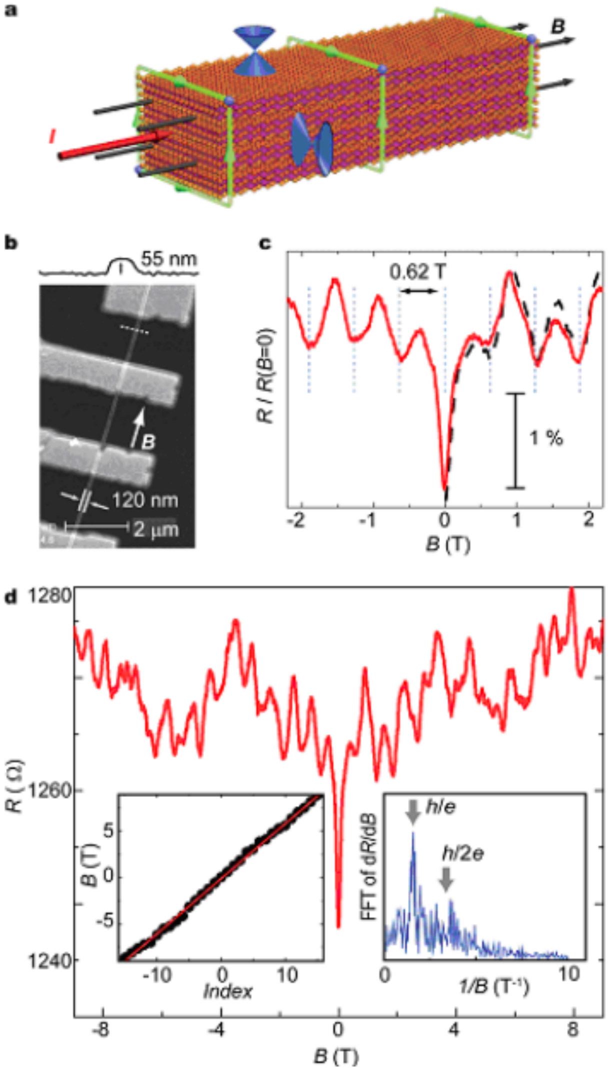

Figure 4.4: Aharonov-Bohm oscillations of the resistance of Bi$_2$Se3 nanoribbons. (a) schematic ribbon with magnetic field along the ribbon axis (black arrows). The red arrow is the current direction and the green arrows show phase coherent paths on the surface encircling the flux quantum. (b) STM image of a Ti/Au contacted 120 nm wide nanoribbon. (c) and (d) Magnetoresistance at 2 K. The magnetic field at the resistance minima is shown in the left inset. The right inset shows the fast Fourier transform of the derivative $\mathrm{d}R/\mathrm{d}B$ with labeling of the flux quantization h/e and $2/2e$. With permission, from Peng et. al [33].

REFERENCES

[1] C. L. Kane and E. J. Mele, Quantum Spin Hall Effect in Graphene, Phys. Rev. Lett. 95 (2005) 226801-1 - 226801-4.

[2] B. A.Bernevig, T. L. Hughes, S. C. Zhang, Quantum Spin Hall Effect and Topological Phase Transition in HgTe Quantum Wells, Science 314 (2006) 1757-1761.

[3] M. König, S. Wiedmann, C. Brüne, A. Roth, H. Buhmann, L. W. Molenkamp, X. L. Qi, S. C. Zhang, Quantum Spin Hall Insulator State in HgTe Quantum Wells, Science 2 (2007) 766-770.

[4] X. L. Qi and S. C. Zhang, Topological Insulators and Superconductors, Reviews of Modern Physics 83 (2011) 1057-1110.

[5] L. Fu, C. L. Kane, and E. J. Mele, Topological Insulators in Three Dimensions, Phys. Rev. Lett. 98 (2007) 106803-1 - 106803-4.

[6] S. Murakami, Phase Transition Between The Quantum Spin Hall and Insulator Phases in 3D: Emergence of a Topological Gapless Phase, New J. Phys. (2007) 356.

[7] L. Fu and C. L. Kane, Topological Insulators with Inversion Symmetry, Phys. Rev. B 76 (2007) 045302-1 - 045302-4.

[8] J. E. Moore and L. Balents, Topological Invariants of Time-Reversal-Invariant Band Structures, Phys. Rev. B 75 (2007) 121306-1 - 121306-6.

[9] X. L. Qi, T. L. Hughes, and S. C. Zhang, Topological Field Theory of Time-Reversal Invariant Insulators, Phys. Rev. B 78 (2008) 195424-1 - 195424-43.

[10] D. Hsieh, D. Qian, L. Wray, Y. Xia, Y. S. Hor, R. J. Cava, and M. Z. Hasan, A topological Dirac Insulator in a Quantum Spin Hall Phase, Nature 452 (2008) 970-974.

[11] H. J. Noh, H. Koh, S. J. Oh, J. H. Park, H. D. Kim, J. D. Rameau, T. Valla, T. E. Kidd, P. D. Johnson, Y. Hu, and Q. Li, Spin-orbit Interaction Effect in the Electronic Structure of Bi2Te3 Observed by Angle-Resolved Photoemission Spectroscopy, Euro Phys. Lett. 81 (2008) 57006-p1 - 57006-p5.

[12] D. Hsieh, Y. Xia, D. Qian, L. Wray, F. Meier, J. H. Dil, J. Osterwalder, L. Patthey, A. V. Fedorov, H. Lin, A. Bansil, D. Grauer, Y. S. Hor, R. J. Cava, and M. Z. Hasan, Observation of Time-Reversal-Protected Single-Dirac-Cone Topological-Insulator States in Bi_2Te_3 and Sb_2Te_3, Phys. Rev. Lett. 103 (2009) 146401-1 146401-4.

[13] Y. Xia, D. Qian, D. Hsieh, L. Wray, A. Pal, H. Lin, A. Bansil, D. Grauer, Y. S. Hor, R. J. Cava, and M. Z. Hasan, Observation of a Large-Gap Topological-Insulator Class with a Single Dirac Cone on the Surface, Nature Physics 5 (2009) 398-402.

[14] Y. S. Hor, A. Richardella, P. Roushan, Y. Xia, J. G. Checkelsky, A. Yazdani, M. Z. Hasan, N. P. Ong, and R. J. Cava, p-type Bi_2Se_3 for Topological Insulator and Low-Temperature Thermoelectric Applications, Phys. Rev. b 79 (2009) 195208-1 - 195208-5.

[15] P. Gehring, H. M. Benia, Y. Weng, R. Dinnebier, C. R. Ast, M. Burghard, and K. Kern, A Natural Topolgical Insulator, Nano Lett. 13 (2013) 1179-1184.

[16] A. Nishide1, A. A. Taskin, Y. Takeichi1, T. Okuda, A. Kakizaki, T. Hirahara, K. Nakatsuji, F. Komori1, Y. Ando, and I. Matsuda, Direct Mapping of the Spin-Filtered Surface Bands of a Three-Dimensional Quantum Spin Hall Insulator, Phys. Rev. B 81 (2010) 041309(R).

[17] Z. H. Pan, E. Vescovo, A. V. Fedorov, D. Gardner, Y. S. Lee, S. Chu, G. D. Gu, and T. Valla, Electronic Structure of the Topological Insulator Bi2Se3 Using Angle-Resolved Photoemission Spectroscopy: Evidence for a Nearly Full Surface Spin Polarization, Phys. Rev. Lett. 106 (2011) 257004-1 - 257004-4.

[18] G. Zhang, H. Qin, J. Teng, J. Guo, Q. Guo, X. Dai, Z. Fang, and K. Wu, Quintuple-Layer Epitaxy of Thin Films of Topological Insulator Bi_2Se_3, Appl. Phys. Lett. 95 (2009) 053114-1 - 053114-4.

[19] Z. Alpichshev, J. G. Analytis, J. H. Chu, I. R. Fisher, Y. L. Chen, Z. X. Shen, A. Fang, and A. Kapitulnik, STM Imaging of Electronic Waves on the Surface of Bi_2Te_3: Topologically Protected Surface States and Hexagonal Warping Effects, Phys. Rev. Lett. 104 (2010) 016401-1 - 016401-4.

[20] D. Hsieh, Y. Xia, D. Qian, L. Wray, J. H. Dil, F. Meier, J. Osterwalder, L. Patthey, J. G. Checkelsky, N. P. Ong, A. V. Fedorov, H. Lin, A. Bansil, D. Grauer, Y. S. Hor, R. J. Cava, and M. Z. Hasan, A Tunable Topological Insulator in the Spin Helical Dirac Transport Regime, Nat. Lett. 460 (2009) 1101-1106.

[21] J. G. Analytis, R. D. McDonald, S. C. Riggs, J. H. Chu, G. S. Boebinger, and I. R. Fisher, Two-Dimensional Surface State in the Quantum Limit of a Topological Insulator, Nat. Phys. 6 (2010) 960-964.

[22] Y. L. Chen, J. H. Chu, J. G. Analytis, Z. K. Liu, K. Igarashi, H. H. Kuo, X. L. Qi, S. K. Mo, R. G. Moore, D. H. Lu, M. Hashimoto, T. Sasagawa, S. C. Zhang, I. R. Fisher, Z. Hussain, and Z. X. Shen, Massive Dirac Fermion on the Surface of a Magnetically Doped Topological Insulator, Science 329 (2010) 659-662.

[23] Q. Liu, C. X. Liu, C. Xu, X. L. Qi, and S. C. Zhang, Magnetic Impurities on the Surface of a Topological Insulator, Phys. Rev. Lett. 102(2009) 156603-1 - 156603-4.

[24] J. Honolka, A. A. Khajetoorians, V. Sessi, T. O. Wehling, S. Stephanow, J. L. Mi, B. B. Iversen, T. Schlenk, J. Wiebe, N. B. Brookes, A. I. Lichtenstein, P. Hofmann, K. Kern, and R. Wiesendanger, In-Plane Magnetic Anisotropy of Fe Atoms on Bi_2Se_3(111), Phys. Rev. Lett. 108 (2012) 256811-1 - 256811-5.

[25] P. Wei, F. Katmis, B. A. Assaf, H. Steinberg, P. Jarillo-Herrero, D. Heiman, and J. S. Moodera, Exchange-Coupling-Induced Symmetry Breaking in Topological Insulators, Phys. Rev. Lett. 110 (2013) 186807-1 - 186807-5.

[26] C. Z. Chang1, J. Zhang, M. Liu, Z. Zhang, X. Feng, K. Li, L. L. Wang, X. Chen, X. Dai, Z. Fang, X. L. Qi, S. C. Zhang, Y. Wang, K. He, X. C. Ma, and Q. K. Xue, Thin Films of Magnetically Doped Topological Insulator with Carrier-Independent Long-Range Ferromagnetic Order, Nat. Adv. Mater. 25 (2013) 1065-1070.

[27] S. Y. Xu, M. Neupane, C. Liu, D. Zhang, A. Richardella, L. A. Wray, N. Alidoust, M. Leandersson, T. Balasubramanian, J. Sánchez-Barriga, O. Rader, G. Landolt, B. Slomski, J. H. Dil, J. Osterwalder, T. R. Chang, H. T. Jeng, H. Lin, A. Bansil, N. Samarth, and M. Z. Hasan, Hedgehog Spin Texture and Berry's Phase Tuning in a Magnetic Topological Insulator, Nat. Phys. 8 (2012) 616-622.

[28] J. Chen, H. J. Qin, F. Yang, J. Liu, T. Guan, F. M. Qu, G. H. Zhang, J. R. Shi, X. C. Xie, C. L. Yang, K. H. Wu, Y. Q. Li, and L. Lu, Gate-Voltage Control of Chemical Potential and Weak Antilocalization in Bi_2Se_3, Phys. Rev. Lett. 105 (2010) 176602-1 - 176602-4.

[29] Y. L. Chen1, J. G. Analytis, J.-H. Chu, Z. K. Liu, S.-K. Mo, ,X. L. Qi, H. J. Zhang, D. H. Lu, X. Dai, Z. Fang, S. C. Zhang, I. R. Fisher, Z. Hussain, and Z.-X. Shen, Experimental Realization of a Three-Dimensional Topological Insulator, Bi_2Te_3, Science 325 (2009) 178-181.

[30] Z. Wang, T. Lin, P. Wei, X. Liu, R. Dumas, K. Liu, and J. Shi, Tuning Carrier Type and Density in Bi_2Se_3 by Ca-Doping, Appl. Phys. Lett. 97 (2010) 042112-1 - 042112-4.

[31] S. S. Hong, W. Kundhikanjana, J. J. Cha, K. Lai, D. Kong, S. Meister, M. A. Kelly, Z. X. Shen, and Y. Cui, Ultrathin Topological Insulator Bi2Se3 Nanoribbons Exfoliated by Atomic Force Microscopy, Nano Lett. 10 (2010) 3118-3122.

[32] D. Kong, J. C. Randel, H. Peng, J. J. Cha, S. Meister, K. Lai, Y. Chen, Z. X. Shen, H. C. Manoharan, and Y. Cui, Topological Insulator Nanowires and Nanoribbons, Nano Lett. 10 (2010) 329-333.

[33] H. Peng, K. Lai, D. Kong, S. Meister, Y. Chen, X. L. Qi, S. C. Zhang, Z. X. Shen, and Y. Cui, Aharonov-Bohm Interference in Topological Insulator Nanoribbons, Nature Materials 9, 225 (2010).

[34] J. G. Checkelsky, Y. S. Hor, R. J. R. J. Cava, and N. P. Ong, Bulk Band Gap and Surface State Conduction Observed in Voltage-Tuned Crystals of the Topological Insulator Bi_2Se_3, Phys. Rev. Lett. 106 (2011) 196801-1 - 196801-4.

[35] F. Xiu, L. He, Y. Wang, L. Cheng, L. T. Chang, M. Lang, G. Huang, X. Kou, Y. Zhou, X. Jiang, Z. Chen, J. Zou, A. Shailos, and K. L. Wang, Manipulating Surface States in Topological Insulator Nanoribbons, Nat. Nanotech. 6 (2011) 216-221.

[36] B. Xia, P. Ren, A. Sulaev, P. Liu, S. Q. Shen, and L. Wang, Indications of Surface-Dominated Transport in Single Crystalline Nanoflake Devices of Topological Insulator $Bi_{1.5}Sb_{0.5}Te_{1.8}Se_{1.2}$, Phys. Rev. B 87 (2013) 085442-1 - 085442-8.

[37] C. Z. Chang, J. Zhang, X. Feng, J. Shen, Z. Zhang, M. Guo, K. Li, Y. Ou, P. Wei,L. L. Wang, Z. Q. Ji, Y. Feng, S. Ji, X. Chen, J. Jia, X. Dai, Z. Fang, S. C. Zhang, K. He, Yayu Wang, L. Lu, X. C. Ma, and Q. K. Xue, Experimental Observation of the Quantum Anomalous Hall Effect in a Magnetic Topological Insulator, Science 314 (2013) 167-170.

Chapter 5

NUMERICAL SIMULATION

Since analytic solutions for the Dirac equation are very rare (see introduction in the paper reprint: CHAPTER 10) efficient numerical algorithms are called for. Their strengths and weaknesses mainly have to do with the discretization. It can be done either in real- or momentum-space, or a combination thereof. Real-space schemes, like finite difference or finite element schemes, allow for an easy implementation of space- and time-dependent mass and potential terms. In addition, real-space schemes avoid the Fourier and inverse Fourier transform, but they are plagued by the so-called fermion doubling problem [1, 2, 3]. Thus, in this chapter we focus on issues which arise when the derivatives in the Dirac equation are approximated by finite difference expressions, especially the fermion doubling problem (see also CHAPTER 3 about tight-binding models, where fermion doubling also arises). The main result not only will be that fermion doubling can be avoided, but the structure of the Dirac equation allows a staggering of the grid in time and space which leads to an efficient explicit method (see paper reprints CHAPTER 8 and 10).

5.1 Finite difference modeling

Finite difference (FD) modeling is the oldest and also the best understood method for the numerical treatment of partial differential equations [4]. One of the advantages of FD is that translation from the underlying partial differential equation to a FD scheme is more or less straightforward. Their accuracy and stability can be proved rigorously. However, it is also a fact that

FD in many fields has been replaced by "more sophisticated" finite element methods, finite volume methods, spectral methods, operator splitting methods etc. Nevertheless, there are also situations where finite difference methods are among the most efficient and widely used ones. The most prominent one is the finite difference time domain (FDTD) method in computational electromagnetics [5]. There, the clever utilization of the special structure of the partial equations at hand, namely the Maxwell equations, makes this finite difference scheme very efficient. The trick is to compute the electric and magnetic field variables in a space and time staggered fashion. Because the time-stepping is explicit no linear algebra is needed in order to evolve the solution. One gets optimal linear scaling, with the number of gridpoints. The FDTD method is used for highly complex engineering problems and excels especially when the simulation region is highly packed with inhomogeneous structures [6]. The ever growing computational resources probably will not reduce its importance because together with them the demands regarding scaling behavior and parallelizability rather grows also.

For the Dirac equation the equal status of time and space suggests to treat them on an equal footing. As will be shown below, this can be achieved by staggering of the spinor components in space and time leading to a simple, explicit, and efficient algorithm.

5.1.1 Finite difference approximation of the first derivative (and its problems)

We use the following notation for the discretization of a function on a regular grid: $u(x_j, t_n) \approx u_j^n$, where $x_j = j\Delta_x$ with $j \in \mathbb{Z}$, and $t_n = n\Delta_t$ with $n \in \mathbb{N}$. For later reference, we introduce the translation operators

$$E_t u_j^n := u_j^{n+1} , \tag{5.1}$$

$$E_x u_j^n := u_{j+1}^n , \tag{5.2}$$

where their inverse are

$$E_t^{-1} u_j^n := u_j^{n-1} , \tag{5.3}$$

$$E_x^{-1} u_j^n := u_{j-1}^n . \tag{5.4}$$

With them, and the identity operator $\mathbb{1}$, one can write the first order accurate, forward/backward difference operators as

$$\delta_t^{\pm} := \pm \frac{(E_t^{\pm 1} - \mathbb{1})}{\Delta_t} , \tag{5.5}$$

$$\delta_x^{\pm} := \pm \frac{(E_x^{\pm 1} - \mathbb{1})}{\Delta_x} \, . \tag{5.6}$$

Analogously, the second order accurate, centered difference operators are defined as

$$\delta_t^0 := \frac{(E_t - E_t^{-1})}{2\Delta_t} \, , \tag{5.7}$$

$$\delta_x^0 := \frac{(E_x - E_x^{-1})}{2\Delta_x} \, . \tag{5.8}$$

For convenience we also introduce arithmetic averaging operators

$$a_t^{\pm} := \frac{(E_t^{\pm 1} + \mathbb{1})}{2} \, , \tag{5.9}$$

$$a_x^{\pm} := \frac{(E_x^{\pm 1} + \mathbb{1})}{2} \, . \tag{5.10}$$

On the grid one can define a discrete translation group where the wave vector (frequency in space) k_x is the creator of the translation

$$u_{j+1}^n = e^{ik_x \Delta_x} u_j^n \, . \tag{5.11}$$

Thus $E_x^{\pm 1}$ corresponds to $e^{\mp i k_x \Delta_x}$. For the translation in time $E_t^{\pm 1}$ one has $e^{\pm i\omega\Delta_t}$, where ω is the frequency in time

$$u_j^{n+1} = e^{-i\omega\Delta_t} u_j^n \, . \tag{5.12}$$

With this, one immediately obtains the action of the operators in Fourier space. The centered approximation leads to

$$\delta_x^0 \to \frac{i}{\Delta_x} \sin k_x \Delta_x \, , \tag{5.13}$$

where $k_x \in (-\frac{k_x}{\Delta_x}, \frac{k_x}{\Delta_x}]$ on the grid. Thus, the difference expression gives zero for a constant function but also for a function, oscillating with the maximal frequency, which can be resolved by the grid. This can lead to additional (spurious) solutions in the finite difference solution of a differential equation (see fermion doubling problem SECTION 3.1.2). In the next section this issue will be demonstrated using the advection equation for a prototypical case. The forward/backward difference operator has the following action in Fourier space

$$\delta_x^{\pm} \to \frac{2i}{\Delta_x} e^{\pm i k_x \Delta_x / 2} \sin \frac{k_x \Delta_x}{2} \, , \tag{5.14}$$

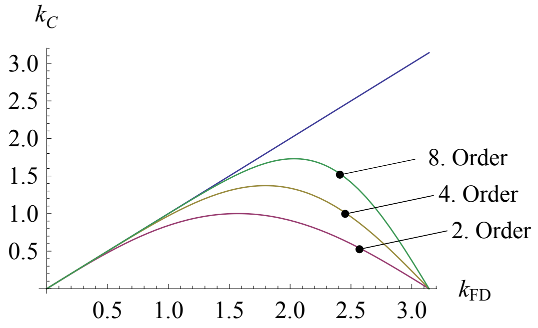

Figure 5.1: The Fourier transform of centered difference operators shown for the 2^{nd} order, 4^{th} order and 2^{th} order accurate approximation and $\Delta = 1$. There is a zero at 0 and π/Δ regardless, of the order of accuracy of the finite difference operator.

$$\delta_t^{\pm} \to \frac{2i}{\Delta_t} e^{\mp i\omega\Delta_t/2} \sin\frac{\omega\Delta_t}{2} \; . \tag{5.15}$$

For completeness, the averaging operator takes on the form

$$a_x^{\pm} \to e^{\pm ik_x\Delta_x/2} \cos\frac{k_x\Delta_x}{2} \; , \tag{5.16}$$

$$a_t^{\pm} \to e^{\mp i\omega\Delta_t/2} \cos\frac{\omega\Delta_t}{2} \; . \tag{5.17}$$

Higher order accurate centered approximations of the first derivative do not solve the problem of having additional spurious solutions, see Fig. 5.1.

5.1.2 Prototypical case: The advection equation

The advection equation (or one-way wave equation) is the simplest transport equation and writes as follows [4]

$$\partial_t u(x,t) = c\partial_x u(x,t) \; , \tag{5.18}$$

with initial conditions $u_0(x) = u(x,0)$ for $x \in \mathbb{R}$. It has the characteristic solution

$$u(x,t) = u_0(x - ct) \; . \tag{5.19}$$

Thus, the function given by the initial condition is simply propagated to the right without changing the shape of the function. In other words it propagates solutions which need not to be smooth or even continuous. It is this behavior which constitutes a challenge in designing accurate numerical schemes for this equation, or hyperbolic equations in general.

Since the forward-in-time and centered-in-space scheme is unconditionally unstable, let us first consider a centered-in-space finite difference operator together with Crank-Nicolson in time

$$\delta_t^+ u_j^n = c a_t^+ \delta_x^0 u_j^n \; , \tag{5.20}$$

or

$$\frac{u_j^{n+1} - u_j^n}{c\Delta_t} = \frac{u_{j+1}^{n+1} - u_{j-1}^{n+1}}{4\Delta_x} + \frac{u_{j+1}^n - u_{j-1}^n}{4\Delta_x} \; . \tag{5.21}$$

For constant coefficients (here the velocity c) and periodic boundary conditions one can use von Neumann (Fourier) analysis to prove stability. One transforms to Fourier space in the spatial variable and obtains the growth of the amplitude of each Fourier mode. One gets $u^{n+1}(k_x) = \lambda u^n(k_x)$, where λ is called the amplification factor. If $|\lambda| \leq 1$, the scheme is stable. For the Crank-Nicolson scheme one gets

$$\lambda = \frac{1 + \frac{c\Delta_t}{2\Delta_x} \sin k_x\Delta_x}{1 - \frac{c\Delta_t}{2\Delta_x} \sin k_x\Delta_x} \; . \tag{5.22}$$

$|\lambda| = 1$ regardless the ratio $r = \frac{c\Delta_t}{\Delta_x}$, which means that the scheme is unconditionally stable. This is a property which only implicit schemes can have. Explicit schemes are always limited in the size of the time step due to the Courant-Friedrichs-Lewy (CFL) condition. A growth factor of $|\lambda| = 1$ also implies that there is no amplitude error (dissipation).

But now comes the dark side of this scheme (arising from the centered-in-space difference operator). Fourier transform in time, or simply using the ansatz $u_{j+1}^{n+1} = e^{i(k_x\Delta_x - \omega\Delta_t)} u^n(k_x)$, leads to the dispersion relation

$$\omega = \frac{2}{\Delta_t} \arctan\left(\frac{c\Delta_t}{2\Delta_x} \sin k_x\Delta_x\right) \approx \frac{c}{\Delta_x} \sin k_x\Delta_x \; . \tag{5.23}$$

It is plotted in Fig. 5.2. For the continuum advection equation (5.18) the *phase velocity*

$$v_{ph} = \frac{\omega}{k} = c \; , \tag{5.24}$$

is equal to the *group velocity*

$$v_g = \frac{\mathrm{d}\omega}{\mathrm{d}k} = c \; . \tag{5.25}$$

Obviously this is not the case for the centered-in-space and Crank-Nicolson in time discretization of the advection equation. For certain wave vectors

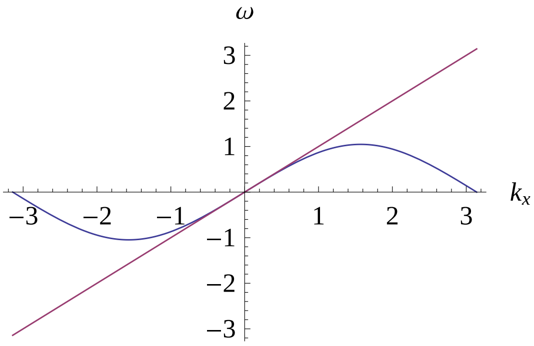

Figure 5.2: Dispersion relation for the Crank-Nicolson in time and centered-in-space discretization of the advection equation, compared to the linear continuum disperison relation. Shown for $c = \Delta_t = \Delta_x = 1$.

the group velocity even is negative, which leads to parts of the solution propagating in the wrong direction $\rightarrow$, typical for spurious solutions (see the fermion doubling problem, SECTION 3.1.2). This kind of errors are known as dispersive errors. Even for smooth initial conditions, having only wave numbers for which the dispersion relation is approximated accurately, high wave numbers are induced by the finite computational precision of the function on each grid point.
One has to be particularly careful when imposing boundary conditions. For the continuum problem one is only allowed to impose boundary conditions at the outgoing boundary. For the discretized case one requires boundary conditions on both boundaries, because of the spurious solutions. In SECTION 5.3 transparent boundary conditions will be derived.

It is not the purpose of this introduction to present all available finite difference schemes for the advection equation. Without claim of completeness further stable methods are: Backward Euler, upwind, Lax-Friedrichs, Lax-Wendroff, MacCormack, Leapfrog, and the Box scheme [4]. Some schemes resemble the analytical characteristic solution without inducing any error for a certain value of $r = \Delta_t/\Delta_x$. The simplest scheme with this property is the upwind scheme

$$\delta_t^+ u_j^n = c\delta_x^- u_j^n \; . \tag{5.26}$$

In one time step the initial condition is shifted one spatial grid spacing to the right, without disturbing its shape. Like in the continuum case, the dispersion relation in this case is $\omega = k_x$.

The next section shows that the Dirac equation can be seen as two coupled advection equations. Further, the occurrence of fermion doubling is demonstrated, again using the example of the Crank-Nicolson scheme. By using the upwind strategy the fermion doubling can be avoided for the 1D chiral form (section 5.1.3). This strategy does not work in higher dimensions. The discretization for the standard form leads to a staggered-grid leap-frog scheme, which avoids fermion doubling and can be generalized to the (2+1)D (paper reprint CHAPTER 9) and (3+1)D (paper reprint CHAPTER 12) case.

5.1.3 1D Dirac equation in chiral form: two advection equations coupled by the mass vs. standard form

By a unitary transformation of the 1D Dirac equation (3.8) it can be transformed to the chiral form

$$U(-i\sigma_x\partial_x + m\sigma_z)U^{-1} = -i\sigma_z\partial_x + m\sigma_x \ , \tag{5.27}$$

where

$$U = \begin{pmatrix} 1 & 1 \\ 1 & -1 \end{pmatrix} . \tag{5.28}$$

This is equivalent to two advection equations which are coupled by the mass

$$\begin{pmatrix} \partial_t - \partial_x & -im \\ -im & \partial_t + \partial_x \end{pmatrix} \begin{pmatrix} u \\ v \end{pmatrix} = 0 \tag{5.29}$$

First let us consider the Crank-Nicolson (CN) in time and centered-in-space discretization

$$\delta_t^+ \psi_j^n - \sigma_z a_t^+ \delta_x^0 \psi_j^n - im\sigma_x a_t^+ \psi_j^n = 0 \ . \tag{5.30}$$

Substitution with Eq. (5.13) and (5.17) gives the dispersion relation

$$\begin{aligned} \omega &= \pm\frac{1}{\Delta_t}\arccos\left[\frac{16\Delta_x^2}{(1-\cos(2k_x\Delta_x))\Delta_t^2 + 2(m^2\Delta_t^2+4)\Delta_x^2} - 1\right] \\ &\approx \pm\frac{1}{\Delta_x}\sin k_x\Delta_x \ , \end{aligned} \tag{5.31}$$

where both the space and time discretization lead to dispersive errors. In the last line the limit $\Delta_t \to 0$ is taken, revealing the error coming solely from the space discretization. Since the domain for the wave vector on the grid is $k_x \in (-\pi/\Delta_x, \pi/\Delta_x]$, this discretization leads to a non monotonic dispersion relation: the so-called fermion doubling. In Fig. 5.4 the dispersion relation is shown for $m = 0$ and $\Delta_t = \Delta_x = 1$. In the SECTION 5.3 we will see that this equation has four different solutions: a right- and a left-going physical and a right- and left-going spurious mode, which all have to be taken into account for the boundary conditions.

Using forward differences for the approximation of the spatial derivatives of the upper spinor component and backward differences for the lower one, solves this problem but leads to an unstable scheme.

$$\begin{pmatrix} \delta_t^+ - a_t^+\delta_x^- & -ia_t^+m \\ -ia_t^+m & \delta_t^+ + a_t^+\delta_x^+ \end{pmatrix} \begin{pmatrix} u_j^n \\ v_j^n \end{pmatrix} = 0 \quad \text{(unstable)} . \tag{5.32}$$

This strategy does work in the standard form of the Dirac equation (compare to the tight-binding chain SECTION 3.1.1)

$$\begin{pmatrix} \delta_t^+ + a_t^+m & a_t^+\delta_x^- \\ a_t^+\delta_x^+ & \delta_t^+ - a_t^+m \end{pmatrix} \begin{pmatrix} u_j^n \\ v_j^n \end{pmatrix} = 0 , \tag{5.33}$$

and gives the dispersion relation [3]

$$\omega \approx \pm\frac{2}{\Delta_x}\sin\frac{k_x\Delta_x}{2} . \tag{5.34}$$

Interestingly in the chiral form, with forward/backward differences in space, the CN time averaging can be omitted

$$\begin{pmatrix} \delta_t^+ - \delta_x^- & -im \\ -im & \delta_t^+ + \delta_x^+ \end{pmatrix} \begin{pmatrix} u_j^n \\ v_j^n \end{pmatrix} = 0 . \tag{5.35}$$

It only leads to a stable explicit scheme for the special value $r = 1$ showing the following dispersion relation

$$\omega = \pm\text{arcsec}\left[\frac{4(1+m^2\Delta_x^2)}{2(2+m^2\Delta_x^2)\cos k_x\Delta_x - \sqrt{2m^4\Delta_x^4(-1-2m^2\Delta_x^2+\cos 2k_x\Delta_x)}}\right] . \tag{5.36}$$

For $m = 0$ this is equivalent to the dispersion relation of the continuum problem $\omega = k_x$. In this case the scheme has the same dispersion relation as the staggered-grid leap-frog scheme (applied to the standard form of the Dirac equation), which will be introduced below. The later is stable for $r \leq 1$ and can be more easily generalized to higher spatial dimension.

5.2 Leap-frog staggered-grid finite difference scheme

We have seen that the centered difference approximation is the reason for fermion doubling in the discretization of the Dirac equation. Because a unitary time evolution is required a forward/backward approximation only is a solution in one spatial dimension. In higher dimensions, one can solve the problem by either incorporating the central point (adding a momentum dependent mass, the Wilson term [7]), or by avoiding the existence of this point (using a staggered grid [8]). The Wilson strategy leads to an implicit scheme. We use the staggering strategy, which leads to an explicit scheme. The u-component of the spinor is defined only on integer grid-points, whereas the v-component is defined only on half-integer points. For the (1+1)D problem, staggering only the space component is equivalent to the forward/backward strategy (see SECTION 5.1.3) [3]. An additional staggering in time improves the dispersion relation. The (1+1)D staggered grid scheme including transparent boundary conditions is presented in the paper reprint CHAPTER 8.[1] For more than one space dimension, staggering in space can be performed in several ways. A scheme showing perfect dispersion along the main axes, but showing a non monotonic dispersion in the diagonal direction, is shown in the paper reprint CHAPTER 9. A (2+1)D scheme and its (3+1)D analogue which completely avoids the fermion doubling problem is presented in CHAPTER 12.

5.3 Open boundary conditions

In a real-space finite difference scheme one has to implement appropriate boundary conditions. Here, absorbing conditions (ABC) or transparent boundary conditions (TBC) are used. They cut the infinite domain of the problem into a finite one by minimizing (ABC) or fully avoiding reflections (TBC) at the boundary. For this purpose there are two main strategies: By wrapping an absorbing layer around the simulation region (leading to ABCs) and feeding the boundary with data which it would have if there was no artificial boundary (TBCs possible). For the derivation of the latter there are again two possible ways. The first one is to get a solution of the partial differential equation on the outer domain analytically. Afterwards, a discretization of this TBCs is necessary [9]. In general this leads to reflections and in some cases to instabilities [10]. The alternative way, which leads directly to discrete TBCs (DTBCs), is to discretize first and match the solutions for the discrete problem [11, 13, 12]. In this section we show the latter strategy on the example of the advection equation and the chiral Dirac equation, both for centered-in-space and Crank-Nicolson in-time discretization. The derivation of TBCs for the leap-frog staggered-grid scheme we refer to the paper reprint shown in CHAPTER 8.

---

[1] A Matlab code is shown in APPENDIX A.2

To simplify the derivation of DTBCs following simplifying assumptions are made

- The initial data $\psi_0(x) = \psi(0, x)$ is compactly supported inside the computational domain.
- In each exterior domain the mass $m(x,t) = m$ and potential $V(x,t) = V$ are constant in t and x.

5.3.1 DTBCs for the 1D advection equation

The 1D advection equation Eq. (5.1.2) with the centered-in-space and Crank-Nicolson approximation in time Eq. (5.21) reads

$$\frac{u_{j+1}^{n+1} - u_{j-1}^{n+1}}{4\Delta x} + \frac{u_{j+1}^{n} - u_{j-1}^{n}}{4\Delta x} - \frac{u_j^{n+1} - u_j^n}{c\Delta t} = 0\ . \tag{5.37}$$

A Z-transformation, $\beta(z) := Z(b_n) = \sum\limits_{n=0}^{\infty} b_n z^{-n}$, in the discrete time domain, use the shifting properties of the Z-transform,
$Z(b_{n+1}) = \sum\limits_{n=0}^{\infty} b_{n+1} z^{-n} = \sum\limits_{n^\prime=1}^{\infty} b_{n^\prime} z^{-n^\prime+1} = z\beta(z) - zb_0\ ,$
and assume $b_0 = 0$ (the initial data are compactly supported on the interior domain), gives

$$(z+1)\frac{\zeta_{j+1}(z) - \zeta_{j-1}(z)}{4\Delta x} - (z-1)\frac{\zeta_j}{c\Delta t}(z) = 0\ . \tag{5.38}$$

This is a simple difference equation of second order:

$$\zeta_{j+1} - \frac{4\Delta x}{c\Delta t}\frac{z-1}{z+1}\zeta_j - \zeta_{j-1} = 0 \tag{5.39}$$

which can be solved with the ansatz:

$$\zeta_{j+1}(z) = \lambda(z)\zeta_j(z)\ , \tag{5.40}$$

and the characteristic polynomial has the solution:

$$\lambda_\pm(z) = \frac{2\Delta x}{c\Delta t}\frac{z-1}{z+1} \pm \sqrt{\left(\frac{2\Delta x}{c\Delta t}\right)^2 \left(\frac{z-1}{z+1}\right)^2 + 1}\ . \tag{5.41}$$

It shows up that there are two solutions which are propagated by the numerical scheme, the physical and the numerical one, due to the fermion doubling. According to this we have to deal with one solution traveling rightward (plus sign in 5.41), which has to be computed by the boundary on the right side and one additional numerical (spurious) mode traveling in the wrong direction which has to be processed on the left boundary. The condition for λ is that the solution of the difference equation has to decay towards infinity in the outside regions. Insertion of the proper solution λ in the Ansatz (5.40) gives us the condition for the left and right boundary

$$\text{left TBC: } \zeta_0(z) = \lambda_+(z)\zeta_1(z) \tag{5.42}$$

$$\text{right TBC: } \zeta_L(z) = \lambda_-(z)\zeta_{L-1}(z) \tag{5.43}$$

All work now remaining is to do the inverse Z-transformation back to the discrete time domain. The product in Z-space leads to a convolution in time. According to this the of the TBC on the right boundary in "Dirichlet form" is

$$u_L^n = \sum_{k=0}^{n} l_{right}^{(n-k)} u_{L-1}^k \tag{5.44}$$

for implementation with the finite difference scheme it can also be written in "von Neumann form":

$$u_L^n - l_{right}^{(0)} u_{L-1}^n = \sum_{k=0}^{n-1} l_{right}^{(n-k)} u_{L-1}^k \tag{5.45}$$

In general, the inverse Z-transformation of λ (eq.: 5.41) can not easily be done because it is a non-rational function in z. The Z-transformed solutions difference equations discussed below will be even more complicated and must be treated numerically. Due to this, no special effort will be made here to find an analytical inverse (or approximation) in this particular case. A series expansion by first replacing z (in eq.: 5.41) by $1/z$ using the symbolic math program Mathematica is a pragmatic and efficient way of getting the desired coefficients. From the numerical point of view (to avoid subtractive cancellation errors) it is preferable to transform $\frac{z+1}{z}\lambda(z)$. This corresponds to the summed coefficients $s^{(n)} := l^{(n)} + l^{(n-1)}$ for $n \geq 1$ and $s^{(0)} := l^{(0)}$. In this case $l^{(n)}$ behaves like $const * (-1)^n$ for large n (this was also done in the Schrödinger case [11]). The decay in discrete time of $s^{(n)}$ can be seen in

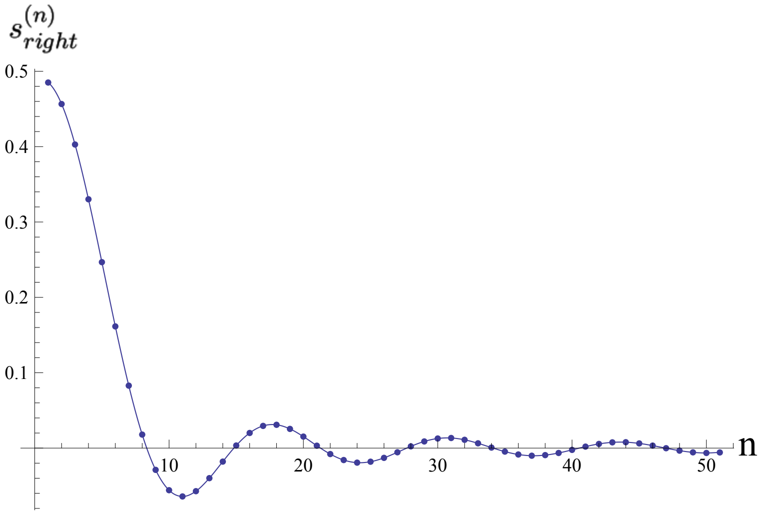

Figure 5.3: Coefficients for the TBC's of the advection equation $s_{right}^{(n)}$ with $\Delta t = 0.005$ and $\Delta x = 0.01$ with centered-in-space and Crank-Nicolson in time discretization.

figure (5.3.1). The coefficients for the left boundary show up to be the same but multiplied with (-1).

5.3.2 DTBCs for the (1+1)D Dirac equation with centered-in-space and Crank-Nicolson in time discretization

One has the same situation as in the prototype case, SECTION 5.3.1, now with two physical and two spurious modes, $V = 0$, and m is arbitrary, but constant. CN discretization in time and Z-transformation in the discrete time variable gives the result

$$\begin{pmatrix} \partial_x u(z,x) \\ \partial_x v(z,x) \end{pmatrix} = \begin{pmatrix} +\frac{2}{\Delta t}\frac{z-1}{z+1} & +im \\ -im & -\frac{2}{\Delta t}\frac{z-1}{z+1} \end{pmatrix} \begin{pmatrix} u(z,x) \\ v(z,x) \end{pmatrix} . \tag{5.46}$$

At this stage of the calculation it would be possible to diagonalize the system and separate the left and right-decaying eigenmodes corresponding to the two eigenvalues. But afterwards one must discretize the continuous TBC´s. This leads to spurious reflections and eventually to stability problems. In our treatment we perform the discretization first. For this purpose we use the centered difference expression of the space derivative $\partial x w \longrightarrow \frac{w_{j+1}-w_{j-1}}{2\Delta t}$.

$$\begin{pmatrix} 1 & 0 \\ 0 & 1 \end{pmatrix} \begin{pmatrix} u_{j+1}(z) \\ v_{j+1}(z) \end{pmatrix} + \begin{pmatrix} -\frac{4\Delta x}{\Delta t}\frac{z-1}{z+1} & -2im\Delta x \\ +2im\Delta x & 4\Delta x\frac{z-1}{z+1} \end{pmatrix} \begin{pmatrix} u_j(z) \\ v_j(z) \end{pmatrix} - \begin{pmatrix} 1 & 0 \\ 0 & 1 \end{pmatrix} \begin{pmatrix} u_{j-1}(z) \\ v_{j-1}(z) \end{pmatrix} = 0\,. \tag{5.47}$$

We can rewrite this system of two difference equations of second order into four difference equations of first order:

$$\begin{pmatrix} u_{j+1}(z) \\ v_{j+1}(z) \\ u_j(z) \\ v_j(z) \end{pmatrix} = \underbrace{\begin{pmatrix} \frac{4\Delta x}{\Delta t}\frac{z-1}{z+1} & 2im\Delta x & 1 & 0 \\ -2im\Delta x & -\frac{4\Delta x}{\Delta t}\frac{z-1}{z+1} & 0 & 1 \\ 1 & 0 & 0 & 0 \\ 0 & 1 & 0 & 0 \end{pmatrix}}_{\mathbf{T}} \begin{pmatrix} u_j(z) \\ v_j(z) \\ u_{j-1}(z) \\ v_{j-1}(z) \end{pmatrix}, \tag{5.48}$$

where $\mathbf{T}$ has the eigenvalues:

$$\lambda_{\pm,\pm} = \pm\frac{1}{\sqrt{2}}\sqrt{F(z) \pm \sqrt{F(z)-4}}\,, \tag{5.49}$$

with

$$F(z) := 2 + 4m^2\Delta x^2 + \left(\frac{4\Delta x}{\Delta t}\right)^2 \left(\frac{z-1}{z+1}\right)^2 . \tag{5.50}$$

Let us think about the meaning of the solutions which correspond to four modes in the numerical simulation. One can easily see that the $\lambda_{-,\pm}$ are highly oscillating in space with the maximum lattice wave-number. They give no smooth physical solution and are therefore called the spurious ones. On the other side the $\lambda_{+,\pm}$ are slowly varying in space and correspond to the physical solution of the continuum problem. The occurrence of this multiple solutions can be understood by looking at the dispersion relation (Fig.: 5.3.2). Furthermore, there are eigenvalues which lead to a solution of the difference equation decaying (growing) in the outside regions, towards infinity. Now we transform to an eigensystem, where we can separate the modes in the numerical scheme

$$\mathbf{U}^{-1}\vec{\zeta}_j = \underbrace{\mathbf{U}^{-1}\mathbf{T}\mathbf{U}}_{\Lambda}\mathbf{U}^{-1}\vec{\zeta}_{j-1}\,, \qquad \mathbf{U} = (\ldots, \vec{v_\nu}, \ldots)\,, \tag{5.51}$$

$$\vec{\vec{\zeta}}_j = \mathbf{\Lambda}\vec{\vec{\zeta}}_{j-1}\,, \qquad \mathbf{\Lambda} = \begin{pmatrix} \lambda_{-,-} & & & \\ & \lambda_{+,-} & & \\ & & \lambda_{-,+} & \\ & & & \lambda_{+,+} \end{pmatrix}. \tag{5.52}$$

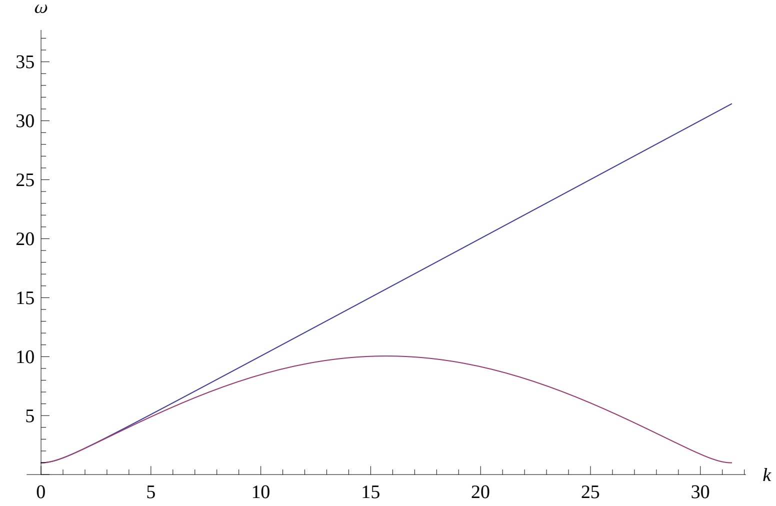

Figure 5.4: Dispersion relation of the centered-in-space and CN in time scheme for the (2+1)D Dirac equation using $V = 0$, $m = 1$ with $\Delta t = 0.1$ and $\Delta x = 0.1$ in comparison to the dispersion of the continuous problem (the dispersion is mirror symmetrical for $k \longrightarrow -k$ and $\omega \longrightarrow -\omega$ so only $k > 0, \omega > 0$ is shown.)

The $\vec{v_\nu}$'s are the eigenvectors of $\mathbf{T}$. The matrix $\mathbf{U}$ represents the unitary matrix which diagonalizes the system. The eigenvalues have the following correspondence to the solutions of the difference equation:

- $\lambda_{-,-}$ …spurious right-decaying
- $\lambda_{+,-}$ …physical right-decaying
- $\lambda_{-,+}$ …spurious left-decaying
- $\lambda_{+,+}$ …physical left-decaying

One allows only right-decaying solutions on the right boundary and, respectively, left-decaying solutions on the left boundary. To accomplish this one projects out the "wrong" solutions to obtain

$$\mathbf{\Lambda}_{\text{left}} = \begin{pmatrix} 0 & & & \\ & 0 & & \\ & & \lambda_{-,+} & \\ & & & \lambda_{+,+} \end{pmatrix}, \qquad \mathbf{\Lambda}_{\text{right}} = \begin{pmatrix} \lambda_{-,-} & & & \\ & \lambda_{+,-} & & \\ & & 0 & \\ & & & 0 \end{pmatrix}. \tag{5.53}$$

Finally, one gets the DTBC´s for the left and right boundary in Z-transformed form

left TBC:

$$\vec{\zeta}_0 = \underbrace{\mathbf{U}^{-1}\mathbf{\Lambda}_{left}^{-1}\mathbf{U}}_{\mathbf{B}_{\text{left}}(z)}\vec{\zeta}_1(z) \,, \tag{5.54}$$

right TBC:

$$\vec{\zeta}_L(z) = \underbrace{\mathbf{U}\mathbf{\Lambda}_{right}\mathbf{U}^{-1}}_{\mathbf{B}_{\text{right}}(z)}\vec{\zeta}_{L-1}(z) \,. \tag{5.55}$$

After inverse Z-transformation one gets the nonlocal-in-time DTBCs in Dirichlet form

$$\begin{aligned}&\left(1 - a_{right}^{(0)}\right) u_L^n - b_{right}^{(0)} v_L^n - c_{right}^{(0)} u_{L-1}^n - d_{right}^{(0)} v_{L-1}^n \\ &= \sum_{k=0}^{n-1} \left(a_{right}^{(n-k)} u_L^k + b_{right}^{(n-k)} v_L^k + c_{right}^{(n-k)} u_{L-1}^k + d_{right}^{(n-k)} v_{L-1}^k \right) \,.\end{aligned} \tag{5.56}$$

The numerical evaluation of the coefficients (again with a series expansion using Mathematica in powers of $1/z$) shows that $b_{right}^{(n)} \equiv 0$. The other ones show a behavior in time which can be seen in the figures (5.3.2–5.3.2).

5.3.3 DTBCs for the (1+1)D Dirac equation with the leap-frog staggered-grid scheme

The derivation of DTBCs for the 1D Dirac equation within the leap-frog staggered-grid discretization is somewhat easier. This is because on the left boundary there is only a coupling of the u-component of the spinor to the outside region. On the right boundary only the v-component couples a point lying outside of the computational domain. The derivation is shown in the paper reprint CHAPTER 8 and a Matlab code can be found in the APPENDIX A.2.

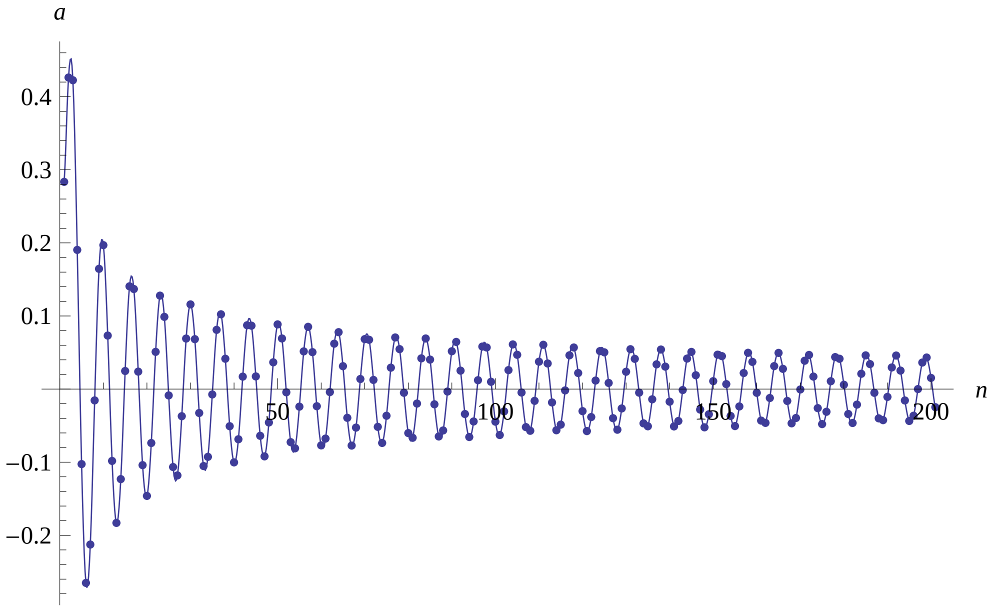

Figure 5.5: Coefficients for DTBC of centered-in-space CN in time scheme of the (2+1)D Dirac equation, using $V = 0$, $m = 1$: $a_{right}^{(n)}$ with $\Delta t = 0.1$ and $\Delta x = 0.1$.

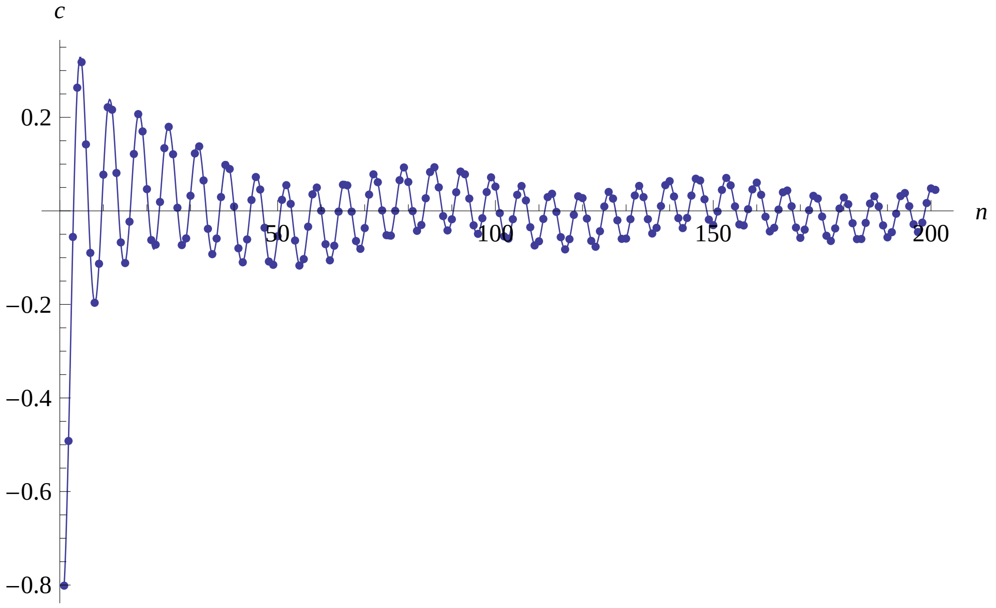

Figure 5.6: Coefficients for DTBC of centered-in-space CN in time scheme of the (2+1)D Dirac equation, using $V = 0$, $m = 1$: $c_{right}^{(n)}$ with $\Delta t = 0.1$ and $\Delta x = 0.1$.

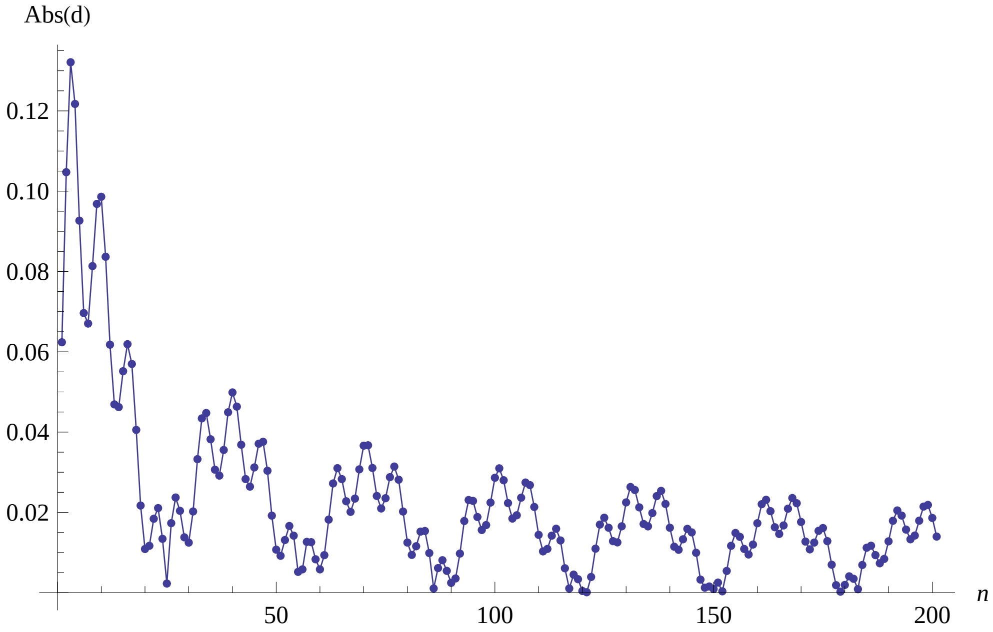

Figure 5.7: Coefficients for DTBC of centered-in-space CN in time scheme of the (2+1)D Dirac equation, using $V = 0$, $m = 1$: $d_{right}^{(n)}$ with $\Delta t = 0.1$ and $\Delta x = 0.1$.

5.3.4 DTBCs for the (2+1)D Dirac equation with the leap-frog staggered-grid scheme

For the physical simulations of the (2+1)D Dirac equation, with the leap-frog staggered-grid scheme as in the paper reprints CHAPTER 10 and 11, we have used absorbing boundary conditions in the form of an absorbing layer. This issue is discussed in detail in the paper reprint CHAPTER 9. Here, extension of the (1+1)D TBCs CHAPTER 8 to higher dimensions is sketched. For a quasi (1+1)D system, having finite size or periodic boundary conditions in one spatial direction, one can apply a Fourier transform in this direction. Then, one obtains uncoupled (1+1)D systems for each transversal wave number. They then can be treated separately with the 1D DTBCs in CHAPTER 8. Here, this procedure is sketched for the scheme presented in CHAPTER 9. Discrete Fourier transform in y-direction gives the scheme for a single transverse mode p

$$\begin{aligned}
&\frac{u^{n+1}_{j,p}-u^{n}_{j,p}}{\Delta t}+i(m-V)\frac{u^{n+1}_{j,p}+u^{n}_{j,p}}{2} \\
&\qquad+\frac{(1+e^{ip\Delta y})(v^{n}_{j,p}-v^{n}_{j-1,p})}{2\Delta x}-i\frac{(1-e^{ip\Delta y})(v^{n}_{j,p}+v^{n}_{j-1,p})}{2\Delta y}=0\,, \\
&\frac{v^{n+1}_{j,p}-v^{n}_{j,p}}{\Delta t}-i(m+V)\frac{v^{n+1}_{j,p}+v^{n}_{j,p}}{2} \\
&\qquad+\frac{(1+e^{-ip\Delta y})(u^{n+1}_{j+1,p}-u^{n+1}_{j,p})}{2\Delta x}+i\frac{(e^{-ip\Delta y}-1)(u^{n+1}_{j+1,p}+u^{n+1}_{j,p})}{2\Delta y}=0\,.
\end{aligned} \tag{5.57}$$

By rearranging we get an equation similar to Fig. (8.23)

$$\begin{aligned}
\frac{u^{n+1}_{j,p}-u^{n}_{j,p}}{\Delta t}+i(m-V)\frac{u^{n+1}_{j,p}+u^{n}_{j,p}}{2}+\frac{f(p)v^{n}_{j,p}-f^{*}(-p)v^{n}_{j-1,p}}{2\Delta x\Delta y}&=0\,, \\
\frac{v^{n+1}_{j,p}-v^{n}_{j,p}}{\Delta t}-i(m+V)\frac{v^{n+1}_{j,p}+v^{n}_{j,p}}{2}+\frac{f(-p)u^{n}_{j+1,p}-f^{*}(p)u^{n}_{j,p}}{2\Delta x\Delta y}&=0\,,
\end{aligned} \tag{5.58}$$

where

$$f(p)=\left[\Delta y-i\Delta x+(\Delta y+i\Delta x)e^{ip\Delta y}\right]\,. \tag{5.59}$$

The steps for the derivation of the DTBCs are analogous to CHAPTER 8.4.

For the fully 2D case one idea is to Fourier transformation only the spinor-data at the boundary like it is sketched in Fig. 5.8. Then one can implement the 1D DTBCs for each transverse Fourier mode at the boundary. In a final step one applies an inverse Fourier transform on the obtained data to supply them to the scheme in real-space.

Here, I want to emphasize that this procedure was not tested numerically or even proven rigorously. It is expected to work perfectly if no data loss in the Fourier transform occurs. Unfortunately this is only the case if the solution, e.g a wave-packet impinges only upon one boundary type, for example the vertical one, at once. If this is not so, the information of the wave packet which has left across the other boundary, in this case the horizontal one, can get lost. In principle it is stored in all the past values of the spinor on the boundary, assuming, for example, constant coefficients in the outside domain.

Another strategy might be to apply a real-space operator-splitting algorithm for the values at the boundary. Such a method was proposed by Gourdeau

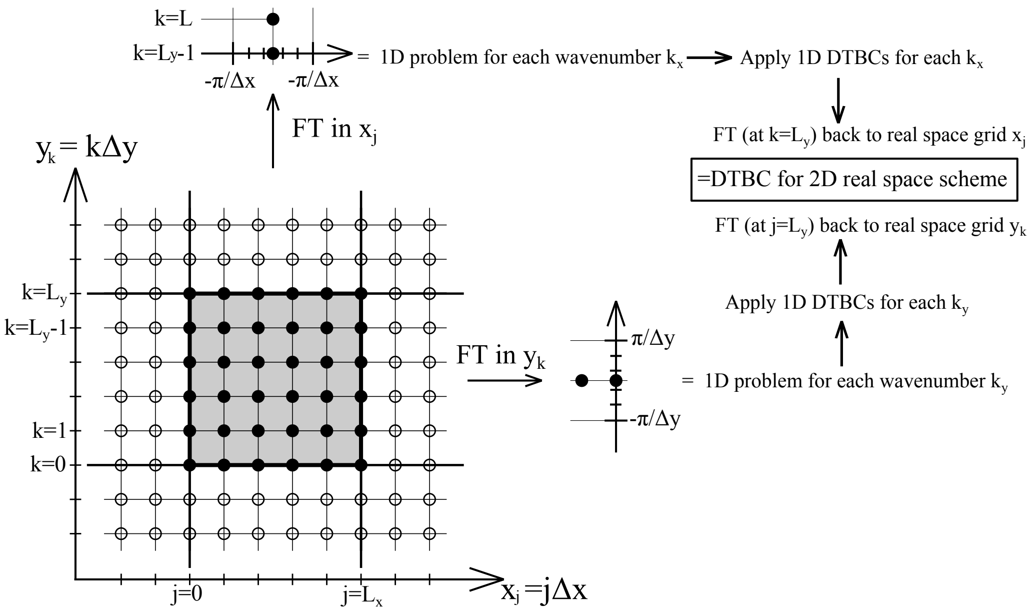

Figure 5.8: The sketch of an idea for the implementation of ABCs into the (2+1)D scheme. In the exterior and on the boundary translational invariance is assumed. Thus, by Fourier transform the problem on the boundaries can be transformed into effective 1D problems for all transverse wave numbers separately. Computing the DTBCs for them and transforming back to real-space gives ABCs for the fully (2+1)D real-space scheme.

et al. [14], where the Dirac equation is transformed into advection equations. Then the method of characteristics can be used for the solution and can be applied one after another in x- and y direction. For the 1D advection equation, using characteristic solutions, the boundary conditions are trivial. E.g. in one time-step one simply shifts the solution one space-step towards the boundary. This operator splitting in x and y induces a second Dirac cone at the Brillouin zone corners. In fact this method has the same dispersion relation as one of our schemes (shown in CHAPTER 9). Thus spurious solutions, traveling in the wrong direction, can occur again when k_x and k_y are both large. One can conclude, that the resulting ABCs are only good for small wave-numbers.

In practice, e.g. for the simulations shown in CHAPTER 9, 10 and 11, an absorbing boundary layer consisting of an imaginary potential, has been found to be sufficient for avoiding spurious back reflection into the simulation domain.

REFERENCES

[1] H. B. Nielsen and M. Ninomiya, A No-Go Theorem for Regularizing Chiral Fermions, Physics Letters B 105 (1981) 219-223.

[2] C. Müller, N. Grün, and W. Scheid, Finite Element Formulation of the Dirac Equation and the Problem of Fermion Doubling, Physics Letters A 242 (1998) 245-250.

[3] R. Stacey, Eliminating Lattice Fermion Doubling, Physical Review D 26, (1982) 468-472.

[4] J. C. Strikwerda, Finite Difference Schemes and Partial Differential Equations, SIAM Philadelphia (2004).

[5] K. S. Yee, Numerical Solution of Initial Boundary Value Problems Involving Maxwell's Equations in Isotropic Media, IEEE Transactions on Antennas and Propagation 14 (1966) 302-307.

[6] A. Taflove and S. C. Hagness, Computational Electrodynamics: The Finite-Difference Time-Domain Method, Artech House Norwood, (2005).

[7] P. H. Ginsparg and K. G. Wilson, A Remnant of Chiral Symmetry on the Lattice, Phys. Rev. D 25 (1982) 2649-2657.

[8] J. Kogut und L. Susskind, Hamilton Formulation of Wilson's Lattice Gauge Theories, Phys. Rev. D 11 (1975) 395-408.

[9] V. A. Baskakov and A.V. Popov, Implementation of Transparent Boundaries for Numerical Solution of the Schrödinger Equation, Wave Motion 14 (1991) 123-128.

[10] B. Mayfield, University of Rhode Island, Providence, Ph.D. thesis (1989).

[11] A. Arnold, M. Ehrhardt, and I. Sofronov, Discrete Transparent Boundary Conditions for the Schrödinger Equation: Fast Calculation, Approximation, and Stability, Communications in Mathematical Sciences 1 (2003) 501-556.

[12] X. Antoine, A. Arnold, C. Besse, M. Ehrhardt, and A. Schädle, A Review of Transparent and Artificial Boundary Conditions Techniques for Linear and Nonlinear Schröodinger Equations, Communications in Computational Physics 4 (2008) 729-796.

[13] A. Zisowsky, A. Arnold, M. Ehrhardt, and T. Koprucki, Discrete Transparent Boundary Conditions for Transient kp-Schrödinger Equations with Application to Quantum Heterostructures, Journal of Applied Mathematics and Mechanics 11 (2005) 793-805.

[14] F. Fillion-Gourdeau, E. Lorin, and A. D. Bandrauk, Numerical Solution of the Time-Dependent Dirac Equation in Coordinate Space without Fermion-Doubling, Comp. Phys. Comm. 183 (2012) 1403-1415.

Chapter 6

THE DYNAMICS OF DIRAC FERMIONS ON TOPOLOGICAL INSULATOR SURFACES

For a trivial metallic 2D electron gas coherent reflection at impurities with increasing disorder strength drives the system towards an Anderson localization [1]. The situation is completely different for quasiparticles on the surface of a TI. Due to spin momentum locking the electrons wave function picks up a Berry phase when it is reflected. If time-reversal symmetry holds, the two possible backscattering paths (clockwise and counterclockwise) interfere destructively. For this reason, such a quasiparticle cannot be localized, as long as the energy gap of the 3D bulk is not closed. This is called the weak antilocalization phenomenon [3]. The coherence length for this quasiparticles is rather large [2]. It should make it possible to exploit coherent phenomena in a hundreds of nm lengthscale. Thus, the TI allows "relativistic physics" in a table-top experiment. As shown in SECTION 3.22, the effective theory for these quasiparticles near the Dirac point is the (2+1)D Dirac equation. Among the rich dynamics, characteristic for these 2D Dirac fermions, presented in this chapter is: the general dynamics of a free 2D Dirac fermion (section 6.2.1), the dynamics in external potentials (e.g. the Klein step and superlens-focusing (SECTION 6.2.2)), and the dynamics under the influence of external magnetization (SECTION 6.2.3). More about the latter and how magnetic texturing can be exploited for a potential device application will be discussed in the CHAPTERS 10 and 11.

For the numerical simulations we have developed two slightly different finite difference schemes, which are shown in the paper reprints CHAPTER

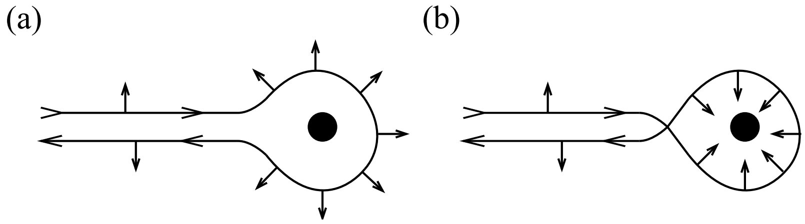

Figure 6.1: Rotation of a spin when an electron on a topological insulator is encircling a magnetic impurity clockwise (a) or anticlockwise (b). The overall phase difference, which their wave function picks up, is π, leading to destructive interference.

9 and 11.

6.1 Special properties of the Dirac fermion on the topological insulator

One essential property of the Dirac fermions on the TI is the *spin momentum locking* (for experimental evidence see [4] and Fig. 4.3). Those who are familiar with condensed matter physics will have recognized the Hamiltonian (3.22) as the Rashba Hamiltonian. In this case, it is the dominant k-dependent term and therefore there is spin-orbit locking

$$H_{SO} = v(\sigma_x k_y - \sigma_y k_x) \ . \tag{6.1}$$

In Eq. (6.1) the Pauli vector $\boldsymbol{\sigma}$ is proportional to the spin and the *spin density* is given by

$$\mathbf{S}(\mathbf{x}) = \psi(\mathbf{x})^\dagger \boldsymbol{\sigma} \psi(\mathbf{x}) \ , \tag{6.2}$$

whereas the momentum density (or respectively the current) is given by

$$\mathbf{j}(\mathbf{x}) = v \mathbf{S}(\mathbf{x}) \times \hat{\mathbf{z}} \ , \tag{6.3}$$

and the probability or charge density is given by

$$\rho(\mathbf{x}) = \psi(\mathbf{x})^\dagger \psi(\mathbf{x}) \ . \tag{6.4}$$

The suppressed backscattering can be understood by simple arguments. Because of spin momentum locking the spin-$1/2$ particle, encircling an impurity 180^o clockwise (counterclockwise), picks up a phase of $\pi/2$ (-$\pi/2$). This gives an overall phase of π (a minus sign for the wave-function) for this time-reversal symmetry related paths. This leads to destructive interference and prohibited backscattering. If time-reversal symmetry is broken, for example by a local magnetic moment, destructive interference no longer occurs.

An external magnetic perturbation with magnetization normal to the surface opens a gap leading to a Dirac Hamiltonian with mass [3, 5]. This issue will be discussed in detail in SECTION 7.2. Inhomogeneous mass textures lead to chiral (one-way) electronic domain-wall channels which can be exploited to utilize complex networks on the surface of the TI (see paper reprints CHAPTERS 10 and 11).
The possibility of introducing a mass texture is of huge importance for wavefunction engineering, since an electric potential cannot confine a Dirac particle (this is one of the major problems in single-layer graphene electronics [6]). A Dirac fermion simply goes trough a potential barrier regardless of its hight by propagating as an electron state on one side of the barrier and as a hole state on the other side. This is known as Klein tunneling and will be shown in SECTION 6.2.2.

6.2 Numerical examples for Dirac wave packet dynamics

In this section, some examples of the Dirac wave packet dynamics on the topological insulator are shown. The simulations are done with the (2+1)D scheme, showing a single Dirac cone, presented in CHAPTER 12.[1] The Fermi velocity is chosen to be $v = 6.2 * 10^5 \mathrm{m/s}$ [3] and the ratio $\Delta_t = \Delta_x/(v\sqrt{2})$.

6.2.1 Dynamics of the free Dirac fermion on the topological insulator

As will be discussed in more detail in the SECTION 6.2.3 a mass term can be introduced for the Dirac fermions on the topological insulator by breaking time-reversal symmetry

$$H_{SO} = v(\sigma_x k_y - \sigma_y k_x) + m\sigma_z \,. \tag{6.5}$$

---

[1] A Matlab code is shown in APPENDIX A.3

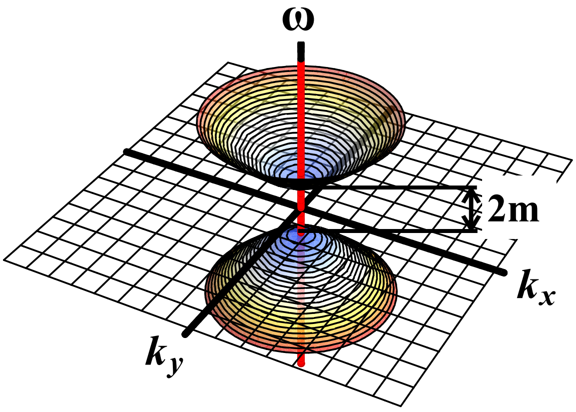

Figure 6.2: Dispersion relation of the 2D Dirac fermion with a gap due to a mass term $m\,\sigma_z$.

Solving the eigenvalue problem gives the dispersion relation

$$\omega(k_x, k_y) = \pm\sqrt{v^2 k_x^2 + v^2 k_y^2 + m^2}\,. \tag{6.6}$$

The phase velocity is

$$v_{ph} = \frac{\omega}{|\boldsymbol{k}|} \tag{6.7}$$

and the group velocity is

$$v_g = \frac{\mathrm{d}\omega}{\mathrm{d}\boldsymbol{k}}\,. \tag{6.8}$$

The mass term opens a gap of $2m$ in the Dirac spectrum, as is shown in Fig. 6.2. Snapshots of a wave packet propagation are shown in Fig. 6.3 and 6.4. The initial wave packet has an upper component which is chosen to be Gaussian and a lower component of the spinor which is zero. This corresponds to a mean value for the wave-number in x- and y-direction of $(k_x, k_y) = (0, 0)$. The mass-less case of the Dirac equation is equivalent to the wave equation (modeling a spring-mass system), which can be seen most easily in the chiral form 5.29. The group velocity is constant and equal to the phase velocity $v_g = v_{ph} = v$. As a consequence, the whole solution leaves the starting point with constant speed (Fig. 6.3). The mass term introduces a coupling of the right- and the left-chiral mode. This results in a group velocity $v_g \leq v$. It can be even zero if there is a component $\boldsymbol{k} = 0$ in the initial condition. Then the amplitude remains finite in the center of the simulation region (see Fig. 6.4).

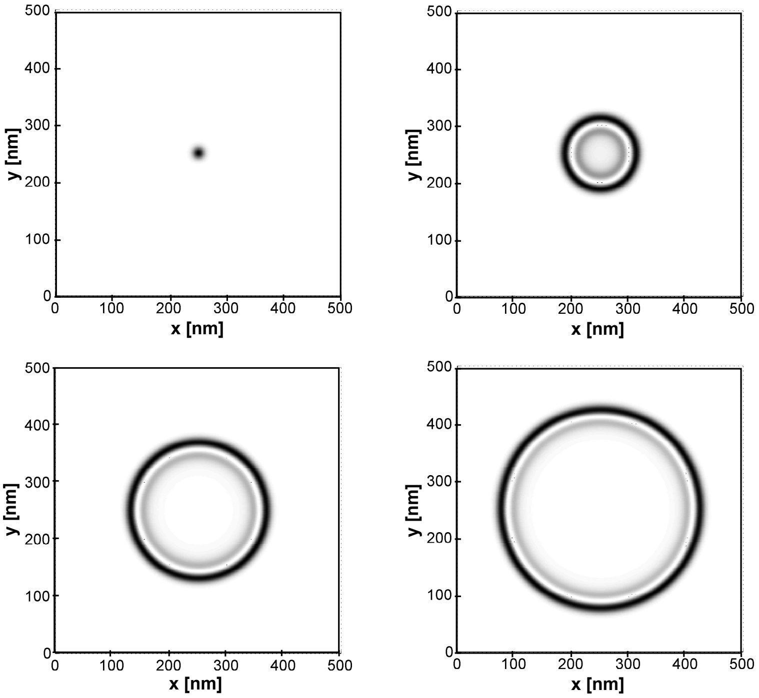

Figure 6.3: Wave packet propagation of an initial wave packet with a Gaussian upper component and a zero lower component of the spinor. In the four successive snapshots at $t_n = 0, 40, 80, 120$ the probability density is shown in gray-scale and $m = 0$.

In general, the a wave packet can have a center wave number $\boldsymbol{k} = (k_x, k_y)$. The shift in the mean wave number is equivalent to a modulation of the initial Gaussian wave packet.

$$\psi_0 = \begin{pmatrix} u \\ v \end{pmatrix} \exp\left[-\frac{(x-x_0)^2}{2b_x^2} - ik_x x \right] \exp\left[-\frac{(y-y_0)^2}{2b_y^2} - ik_y y \right] . \tag{6.9}$$

To reveal this phase information, the following plots show the real part of the upper spinor component by a color/brightness variation, whereas the probability density is shown as a brightness saturation.

6.2.2 Dynamics with external scalar potential: Klein-step and superlens-focusing

Rather unfamiliar behavior of a wave packet occurs at a high potential barrier. In the massless case, at this so-called Klein-step, the wave packet is not

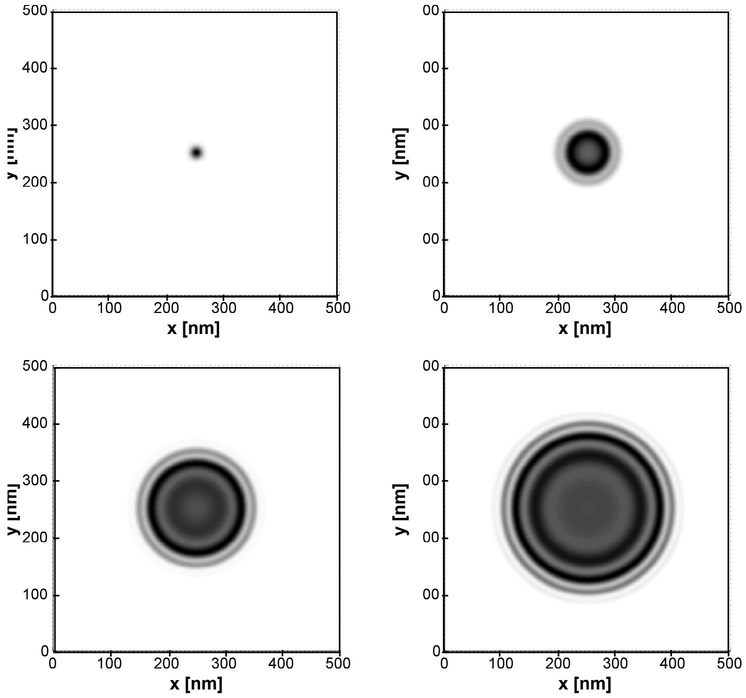

Figure 6.4: Wave packet propagation of an initial wave packet with a Gaussian upper component and a zero lower component of the spinor. In the four successive snapshots at $t_n = 0, 40, 80, 120$ the probability density is shown in gray-scale and $m = 0.04$ eV.

reflected, but propagates as electron state on one side of the step and as hole state at the other side (see Figs. 6.6 and 6.7). The phase velocity and also the group velocity for the hole state is opposite to the electron state. It leads to a negative angle of refraction. This behavior can be exploited to obtain a superlens effect, as can be seen in Fig. 6.8. A potential of $V = 0.1$ eV is applied in a region forming a middle barrier. The wave packet has a mean energy of $V = 0.05$ eV leading to a propagation as a hole state and negative refraction at the middle barrier.

6.2.3 Dynamics in external magnetization: Landau orbits and domain-wall fermions

The coupling of the Dirac fermion to an external magnetic field enters the effective Hamiltonian in two places. First it influences the orbital part of the equation, by adding to the momentum, in form of a vector potential $\mathbf{\Pi} = \mathbf{p} + \frac{e}{c}\mathbf{A}(x, y, t)$. Secondly, it couples to the spin $\boldsymbol{\sigma}\mathbf{B}$. More simulations with

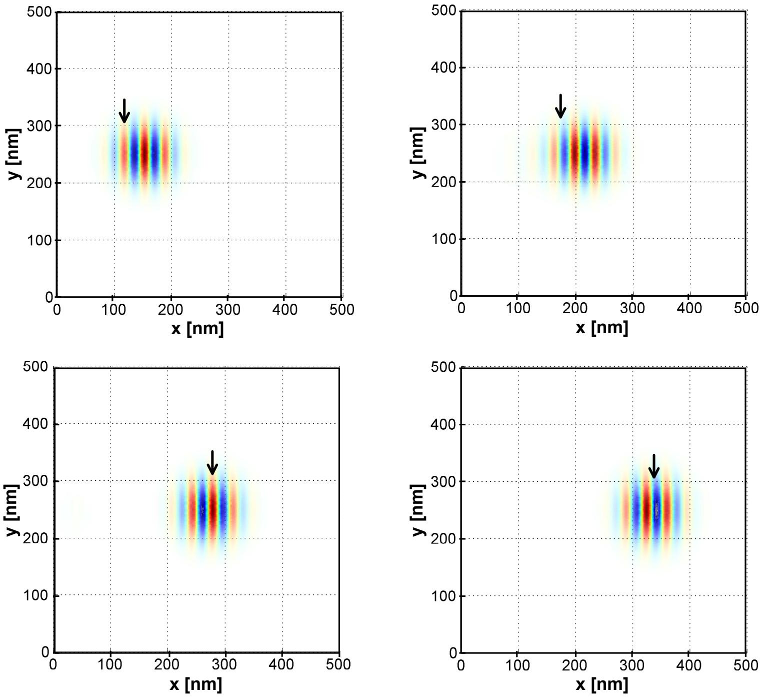

Figure 6.5: Propagation of an initial Gaussian wave packet. In the four successive snapshots at $t_n = 0, 50, 100, 150$ the probability density is shown as brightness saturation and the phase is encoded in the color/brightness variation. Here, the mean energy of the wave packet is chosen to be $E = 0.07$ eV and $m = 0.04$ eV. In this case the fine ripples move with phase-velocity and are slightly faster than the whole wave packet which moves with group-velocity. This is indicated by the black arrows.

inhomogeneous external potential, and in and out of plane magnetic field, can be found in the next SECTION 7.2 and in the paper reprints CHAPTER 9, 10 and 11.

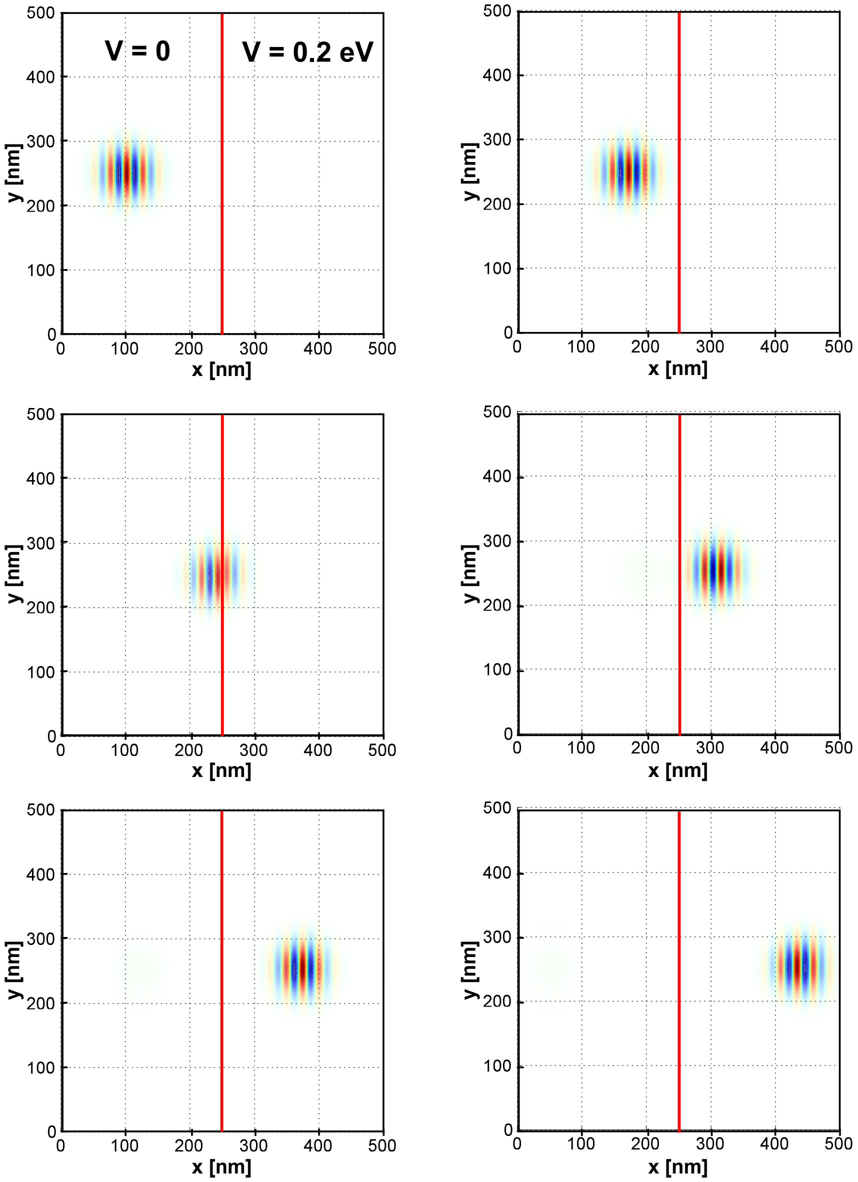

Figure 6.6: Initial Gaussian wave packet impinging a Klein step at 90^o. In the six successive snapshots at $t_n = 0, 50, 100, 150, 200, 250$ the probability density is shown as brightness saturation and the phase is encoded in the color/brightness variation. Here, the mean energy of the wave packet is chosen to be $E = 0.1$ eV, $m = 0$ eV and $V = 0.2$ eV at the left side of the step and $V = 0.2$ eV at the right side, respectively. The wave packet propagates as electron state on the left-hand and as hole state on the right-hand side.

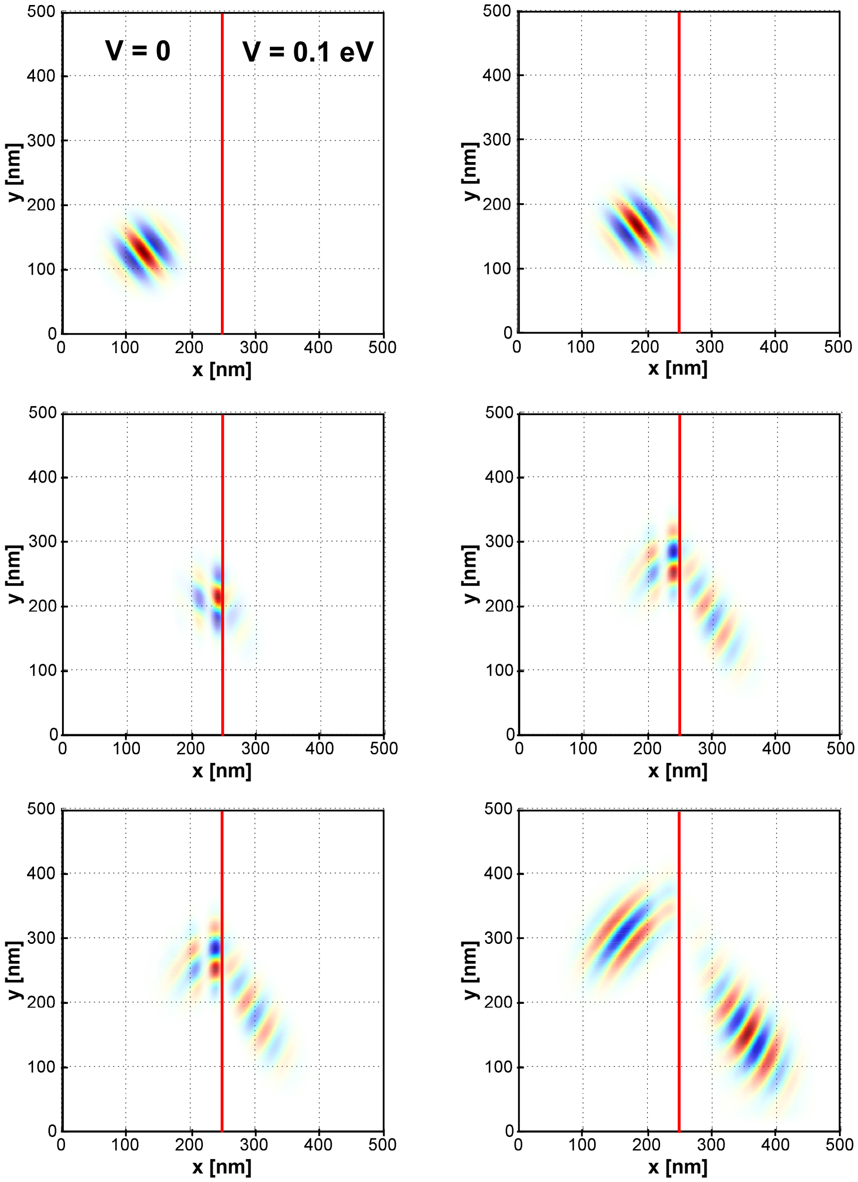

Figure 6.7: Initial Gaussian wave packet impinging a Klein step at 37^o to the lot. In the six successive snapshots at $t_n = 0, 50, 100, 150, 200, 250$ the probability density is shown as brightness saturation and the phase is encoded in the color/brightness variation. Here, the mean energy of the wave packet is chosen to be $E = 0.05$ eV, $m = 0$ eV and $V = 0.1$ eV at the left side of the step and $V = 0.2$ eV at the right side respectively. At the right side the phase velocity and the group velocity are opposite to one other, leading to a negative angle of refraction.

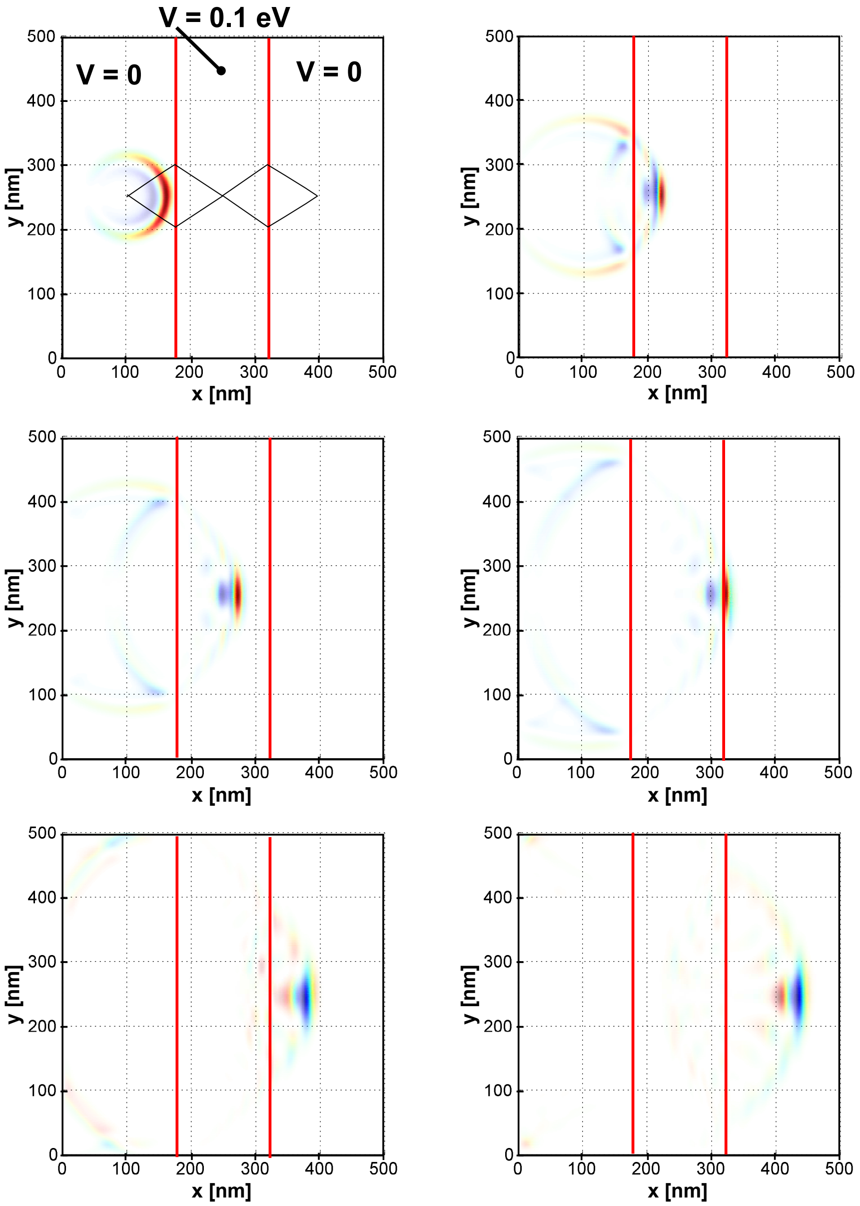

Figure 6.8: The negative angle of refraction in the metamaterial-like middle barrier $V = 0.1\text{eV}$ leads to superlens-focusing. This is shown for six successive snapshots at $t_n = 40, 80, 120, 160, 200, 240$. The probability density is shown as brightness saturation and the phase is encoded in the color/brightness variation.

REFERENCES

[1] E. Abrahams, P. W. Anderson, D. C. Licciardello, and T. V. Ramakrishnan, Scaling Theory of Localization: Absence of Quantum Diffusion in two Dimensions, Phys. Rev.Lett. 42 (1979) 673-676.

[2] H. Peng, K. Lai, D. Kong, S. Meister, Y. Chen, X. L. Qi, S. C. Zhang, Z. X. Shen, and Y. Cui, Aharonov-Bohm Interference in Topological Insulator Nanoribbons, Nature Materials 9, 225 (2010).

[3] X. L. Qi and S. C. Zhang, Topological Insulators and Superconductors, Reviews of Modern Physics 83 (2011) 1057-1110, and references therein.

[4] S. Y. Xu, M. Neupane, C. Liu, D. Zhang, A. Richardella, L. A. Wray, N. Alidoust, M. Leandersson, T. Balasubramanian, J. Sánchez-Barriga, O. Rader, G. Landolt, B. Slomski, J. H. Dil, J. Osterwalder, T. R. Chang, H. T. Jeng, H. Lin, A. Bansil, N. Samarth, and M. Z. Hasan, Hedgehog Spin Texture and Berry's Phase Tuning in a Magnetic Topological Insulator, Nat. Phys. 8 (2012) 616-622.

[5] Y. L. Chen, J. H. Chu, J. G. Analytis, Z. K. Liu, K. Igarashi, H. H. Kuo, X. L. Qi, S. K. Mo, R. G. Moore, D. H. Lu, et al., Massive Dirac Fermion on the Surface of a Magnetically Doped Topological Insulator, Science 329 (2010) 659-662.

[6] A. C. Neto, F. Guinea, N. M. R. Peres, K. S. Novoselov, and A. K. Geim, The Electronic Properties of Graphene, Rev. Mod. Phys. 81 (2009) 109-162, and references therein.

Chapter 7

TOPOLOGICAL DEFECTS: DOMAIN WALL FERMIONS AND VORTEX ZERO MODES

As already mentioned in the introduction CHAPTER 1, the development of topological band and field theory was a great success regarding the understanding and prediction of a completely new state of matter. The properties of this topological matter are fully determined by symmetry principles. These are the time-reversal, particle-hole, and chiral symmetry. They lead to 10 different Altland-Zirnbauer symmetry classes for the Bloch and Bloch Bogoliubov de Gennes Hamiltonians (BdG) [1]. The symmetry classes of the bulk material, together with its underlying dimension, fully determine the topological invariants [2]. These in turn, due to bulk boundary correspondence, are sufficient to determine the occurrence, or non-occurrence, of symmetry protected gap-less surface states [2, 4]. Within this classification one can also describe $\mathcal{D}$ dimensional defects within a d dimensional Hamiltonian. A $\mathcal{D}$ dimensional defect in real space can be enclosed by a $D = d - \mathcal{D} - 1$ dimensional surface. It is a general result that the topological invariant, and thus the properties of the defect, only depend on $\delta = d - D$ [3]. This can be arranged in a table given by the symmetry class and the dimension of the Hamiltonian. There are only four different entries: 0 for the trivial case showing no topological state at the defect, $\mathbb{Z}$ or $2\mathbb{Z}$ for odd or even Chern numbers respectively, and $\mathbb{Z}^2$. For systems having a Chern number there emerge chiral Dirac or Majorana defect states, whereas in the case of a $\mathbb{Z}^2$ number they are helical. Furthermore, for a Bloch Hamiltonian they are Dirac like states, whereas for the particle-hole symmetric BdG Hamiltonian they are Majorana states. In this classification, the surface ($\mathcal{D}$=2 defect) of the time-reversal invariant 3D bulk TI (being in the symmetry class AII) is classified by a $\mathbb{Z}_2$ topological invariant and therefore shows a helical surface state. The time-reversal breaking $d = 2$ bulk state of the integer QHE has a $\mathcal{D}$=1 defect with an odd Chern number showing chiral nature [3]. Here, we are interested in $\mathcal{D} = 0$ (skyrmions) and $\mathcal{D} = 1$ (domain-wall fermions) for the 3D bulk topological insulator $(d = 3)$.

7.1 Domain-wall fermions on topological insulators and some potential applications

Pedagogically, the domain-wall fermions can be described as a bound state on the line, where the mass parameter of the effective surface Dirac Hamiltonian Eq. (6.5) changes its sign. This is sketched in Fig. 7.1. The analytical solution of the quasi-1D chiral Dirac fermion state is described and used in the paper reprints CHAPTER 10 and 11. These one way channels can be exploited to build complex Dirac fermion networks, when combined with beam-splitters, forming at domain-wall crossings. Interference can be tuned by an external potential allowing a transistor-like setup, see CHAPTER 10. For the coating of the topological insulator with a thin magnetic film a free energy minimization gives a realistic mass texture (see CHAPTER 10 and 11).

In the experiment there are several possibilities for generating a current in the chiral channels. Besides electric contacts, tunneling from a STM tip and photo-excitation can be used. When the Fermi energy lies within the surface gap, permanent current in the 1D channels flows. This may be an unwanted property. An alternative is a lower (or higher) Fermi level and performing an excitation into the channels which is locally restricted in time and/or space. Then, as shown in Fig. 7.2, the lower (or alternatively upper) band-edge of the semiconductor contacts has to lie at the same energy as the 1D chiral states.

The lifetime of the 1D carriers are expected to be longer than the runtime in the chiral 1D paths, because of limited relaxation channels. The coherence length of the 2D surface states can be measured by Aharonov-Bohm oscillations to be in the μm range at low temperatures. The coherence length of the 1D channels may even be longer. When coherence is not required, and ballistic transport is sufficient, devices can have "macroscopic" size. This is the case for the beamsplitter (see CHAPTER 11) whose working principle, however, is local. Due to the close relation of the 1D chiral channels to the recently observed quantum anomalous Hall effect states, ballistic transport

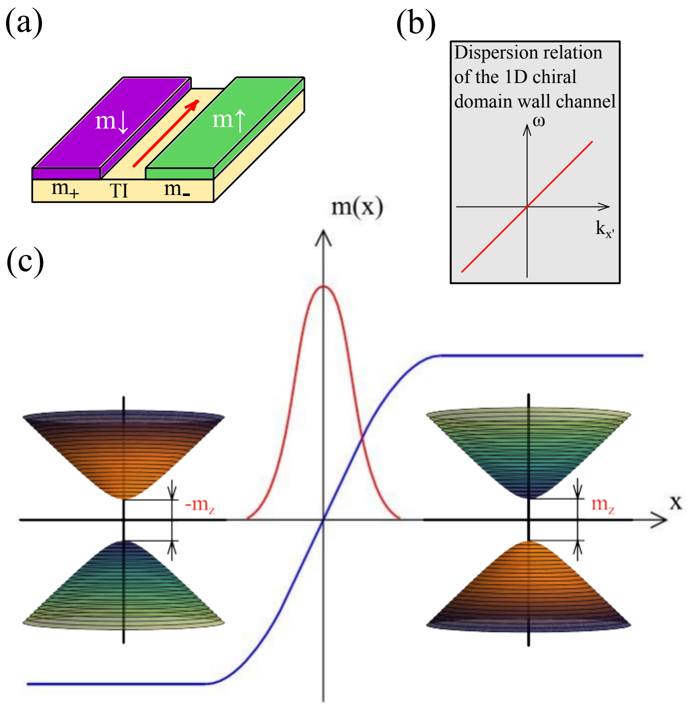

Figure 7.1: (a) 3D heterostructure consisting of a topological insulator and two ferromagnetic insulators with opposite perpendicular magnetization relative to the topological insulator surface. In this setup a quasi-1D, one-way, chiral Dirac fermion channel state emerges. (b) dispersion of the channel state. (c) mass of the 2D helical Dirac fermion on the topological insulator changing its sign perpendicular to the channel, leading to the quasi-1D channel state.

can be expected over several hundreds of μm [5].

7.2 Zero modes and bound states on topological insulators induced by magnetic vortex structures

Another defect on the TI surface which shows interesting physics, and could find application in TI devices is the mass vortex. Zero modes and bound states localized at in-plane magnetic vortices have been found analytically [6]. These solutions show spin polarized current around the vortex center. The standard representation for the Dirac equation was used, where the

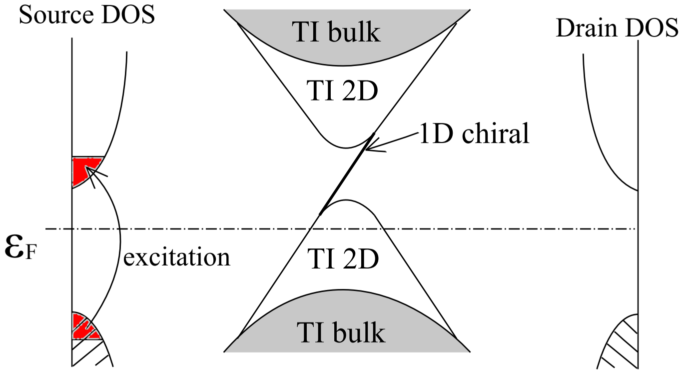

Figure 7.2: Possible alignment of source and drain bands relative to the TI bulk states, the 2D surface states and the 1D chiral states which allow e.g. optical excitation into the 1D chiral channels.

Pauli matrices represent the momentum direction Eq. 2.36.[1] In order to obtain the solution, the problem was written in polar coordinates. The in-plane vortex mass structure in polar coordinates can be written using the unit radial vector $\hat{r}$ and the unit angular vector $\hat{\phi}$.

$$\boldsymbol{M} = M_r\hat{r} + M_\phi\hat{\phi} \tag{7.1}$$

with

$$M_r = M\cos\phi_o\ , \qquad M_\phi = M\sin\phi_o\ . \tag{7.2}$$

For $\phi_o = \pm\pi/2$ one gets a curly type mass vortex, whereas $\phi_o = 0$ and $\phi_o = \pi$ corresponds to hedgehog configurations. The effective model Hamiltonian Eq. 2.36 for the TI surface Dirac fermions in polar coordinates becomes

$$H = -i\hbar v_F \begin{pmatrix} 0 & e^{-i\phi}\left(\frac{\partial}{\partial r} - \frac{i}{r}\frac{\partial}{\partial\phi} - \frac{M_\phi - iM_r}{\hbar v_F}\right) \\ e^{i\phi}\left(\frac{\partial}{\partial r} + \frac{i}{r}\frac{\partial}{\partial\phi} + \frac{M_\phi + iM_r}{\hbar v_F}\right) & 0 \end{pmatrix} \tag{7.3}$$

The product ansatz

$$\phi(r) = \begin{pmatrix} e^{im\phi}\chi_1(r) \\ e^{i(m+1)\phi}\chi_2(r) \end{pmatrix} \tag{7.4}$$

gives

$$\left(\frac{\mathrm{d}}{\mathrm{d}r} + \frac{m+1}{r} - \frac{M_\phi - iM_r}{\hbar v_F}\right)\chi_2(r) = i\frac{E}{\hbar v_F}\chi_1(r)\ , \tag{7.5}$$

---

[1] Another representation, where they directly correspond to the spin, is more frequently used in the literature [4] (see (3.22) the comment below it).

$$\left(\frac{\mathrm{d}}{\mathrm{d}r} - \frac{m}{r} + \frac{M_\phi + iM_r}{\hbar v_F}\right)\chi_1(r) = i\frac{E}{\hbar v_F}\chi_2(r)\,. \tag{7.6}$$

For $E = 0$ the differential equations decouple. For a mass vortex which is oriented clockwise $M_\phi = M$ one gets the zero-mode solution

$$\psi(t,\phi) = a_l \begin{pmatrix} 0 \\ 1 \end{pmatrix} \frac{1}{r^{l+1}} e^{-\frac{M}{\hbar v_F}} e^{i(l+1)\phi}\,, \qquad l = 0, \pm 1, \pm 2, \ \ldots\ . \tag{7.7}$$

For a counterclockwise oriented mass vortex $M_\phi = -M$ one gets

$$\psi(t,\phi) = b_l \begin{pmatrix} 1 \\ 0 \end{pmatrix} r^l e^{-\frac{M}{\hbar v_F}} e^{il\phi}\,, \qquad l = 0, \pm 1, \pm 2, \ \ldots\ . \tag{7.8}$$

a_l and b_l are normalizing constants and can be found in [6]. A radial component of the mass vortex enters the solution as an imaginary mass term in the solution [6].

Here, we use the time dependent scheme (CHAPTER 12 for the 2+1D case), to show the stationary solution (7.7) for different angular momentum quantum number $l = 0, 1, 2, 3, 4, 5$ Fig. 7.3. For all simulations with the mass vortex we use a magnitude of $M = 50$ meV. In Fig. 7.4 a quench from a purely radial vortex configuration to one where the magnetization is tilted slightly is shown. We choose a sudden tilt of 0.2π, which is enough to let a significant part of the probability density vanish to infinity, but let a remainder be bound to the vortex.

For the $E \neq 0$ case the problem is equivalent to that of a 2D hydrogen atom. The general solution, dependent on the energy quantum number n and the angular momentum number l is given by hypergeometric functions [6]. In Figs. 7.5 and 7.6 we show the scattering of a Gaussian wave packet having the mean energy $E = 2M$. In Fig. 7.5 the impact parameter is positive $b = 100$ nm corresponding to clockwise direction of the current, whereas the magnetization prefers anticlockwise current. This leads to a repulsing behavior (positive scattering angle). In Fig. 7.6 the same setup is shown with $b = -100$ nm, leading to attractive behavior.

Complex structures, consisting of vortices and domain-walls, are conceivable and will be an interesting subject to study for future studies.

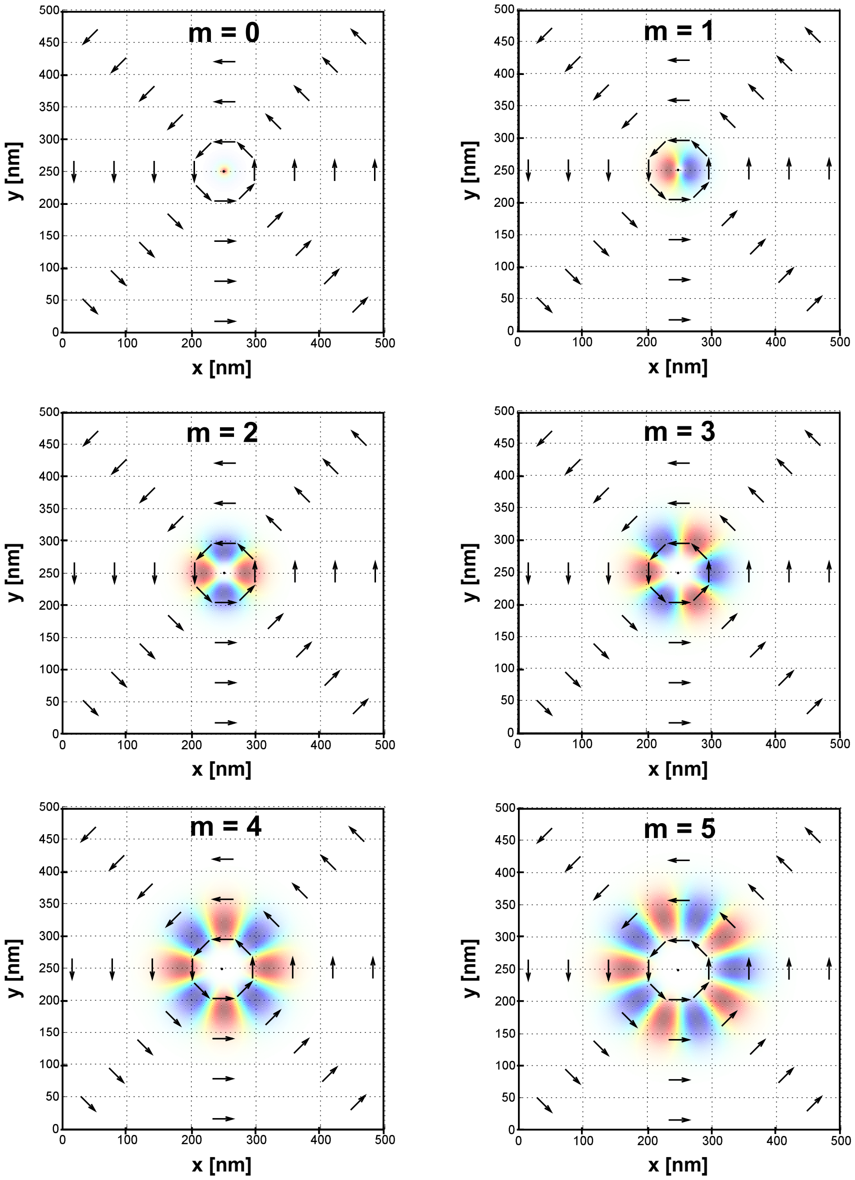

Figure 7.3: Spin polarized vortex zero modes on the topological insulator surface, shown for the angular momentum number $l = 0, 1, 2, 3, 4, 5$. The probability density is shown as brightness saturation and the phase is encoded in the color/brightness variation. The black arrows show the mass vortex.

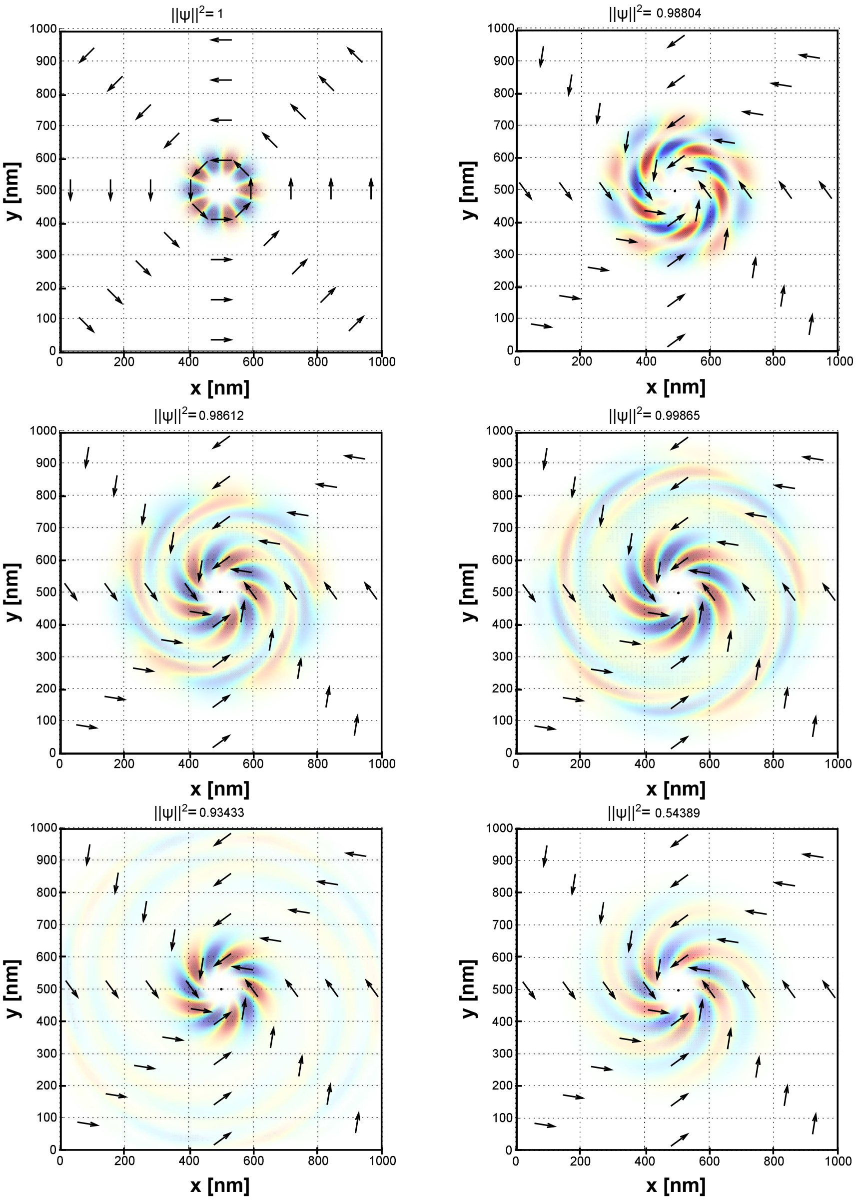

Figure 7.4: Spin polarized vortex zero mode $l = 5$ on the topological insulator surface after suddenly tilting the mass vortex $\phi_o = \pi/2 \rightarrow \phi_o = \pi/2 + 0.2\pi$ at $t = 0$, giving it a radial component. In the six successive snapshots at $t_n = 0, 100, 200, 300, 400, 10000$ the probability density is shown as brightness saturation and the phase is encoded in the color/brightness variation. The black arrows show the mass vortex. Part of the probability density vanishes to infinity, whereas the remainder is localized at the vortex.

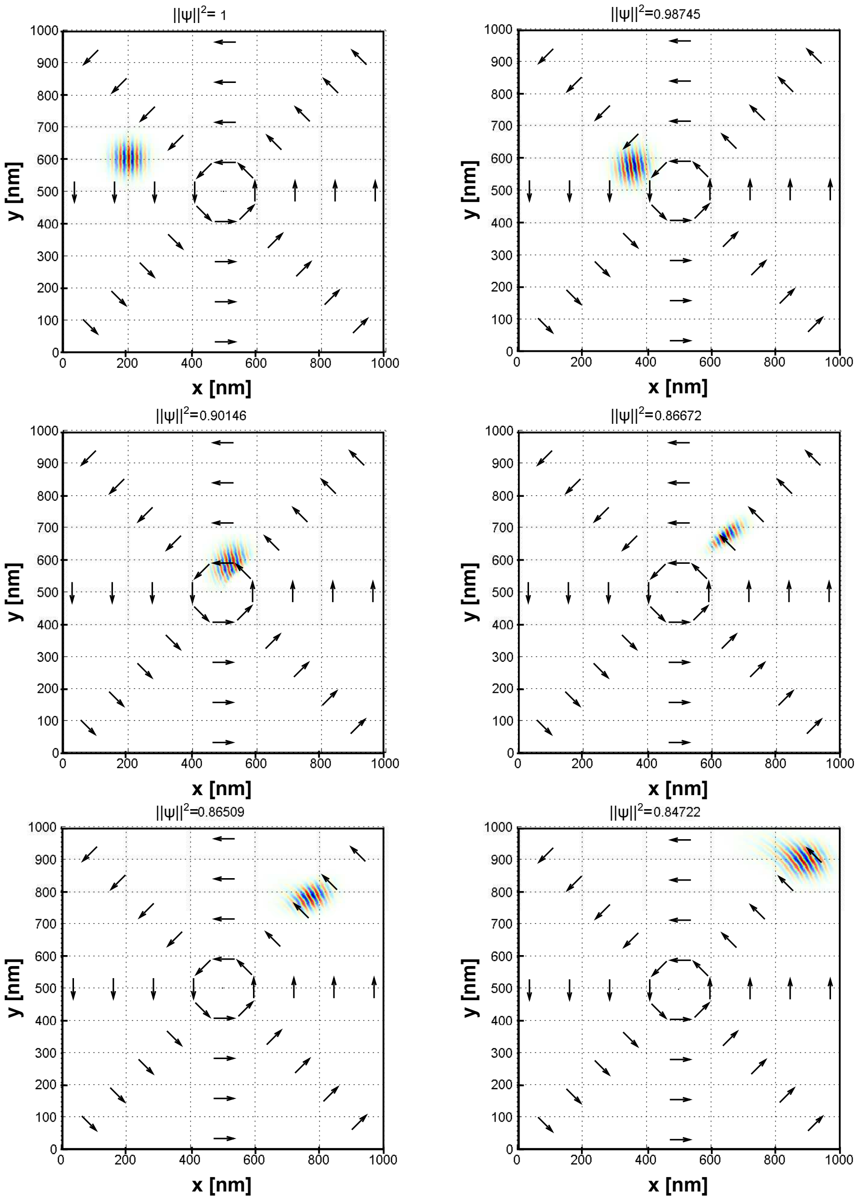

Figure 7.5: Dirac fermion scattered on a mass vortex with magnitude $m = 50$ meV, having the vortex core at $(500, 500)$ nm. The wave packet has the mean energy of $E = 100$ meV and an impact parameter of $b = 100$ nm. In the six successive snapshots at $t_n = 0, 120, 240, 360, 480, 600$ the probability density is shown as brightness saturation and the phase is encoded by the color/brightness variation. The black arrows show the mass vortex. The mass vortex acts repulsive, because it prefers an anticlockwise direction of the current.

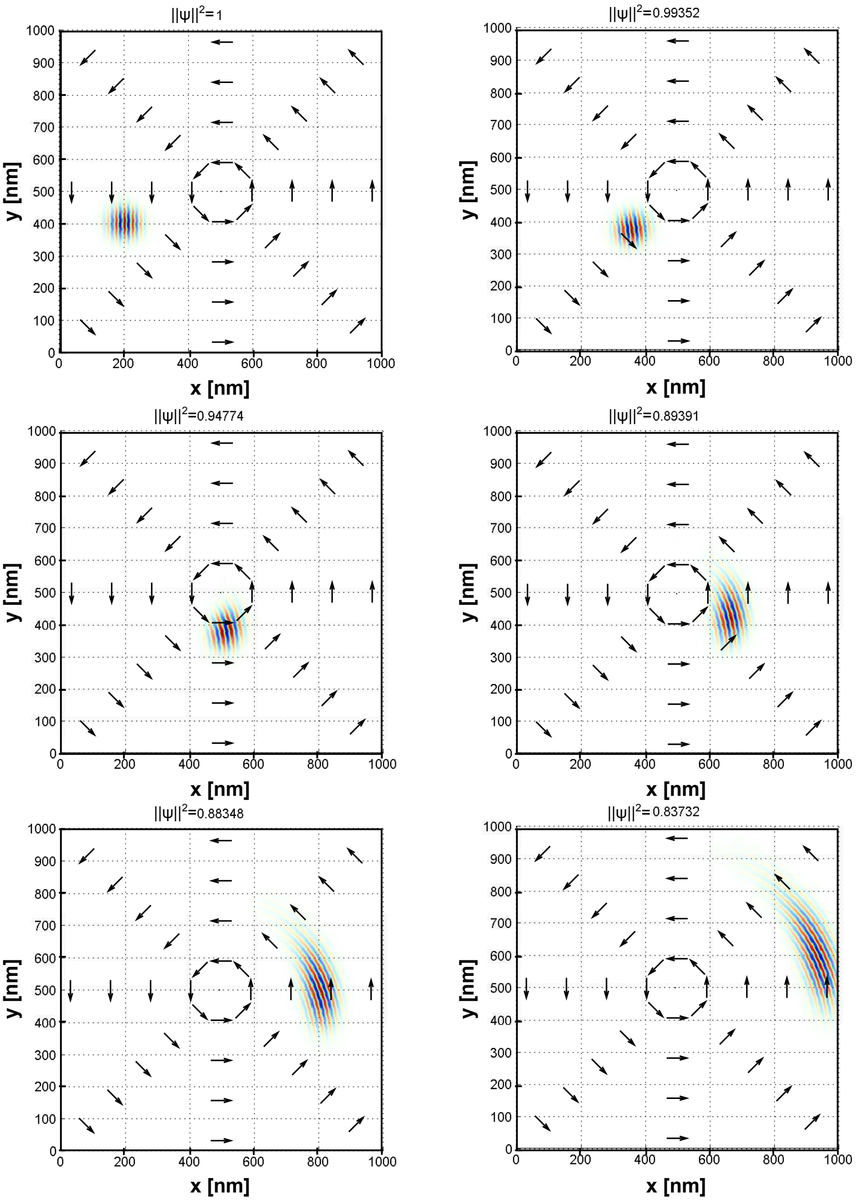

Figure 7.6: Dirac fermion scattered on a mass vortex with magnitude $m = 50$ meV, having the vortex core at $(500, 500)$ nm. The wave packet has the mean energy of $E = 100$ meV and a impact parameter of $b = -100$ nm. In the six successive snapshots at $t_n = 0, 120, 240, 360, 480, 600$ the probability density is shown as brightness saturation and the phase is encoded by the color/brightness variation. The black arrows show the mass vortex. The mass vortex acts attractive, because it prefers an anticlockwise direction of the current.

REFERENCES

[1] A. Altland and M. R. Zirnbauer, Nonstandard Symmetry Classes in Mesoscopic Normal-Superconducting Hybrid Structures, Phys. Rev. B 55 (1997) 1142-1161.

[2] A. P. Schnyder, S. Ryu, A. Furusaki, and W. W. Ludwig, Classification of Topological Insulators and Superconductors in Three Spatial Dimensions, Phys. Rev. B 78 (2008) 195125-1 - 195125-22.

[3] J. C. Y. Teo and C. L. Kane, Topological Defects and Gapless Modes in Insulators and Superconductors, Phys. Rev. B 82 (2010) 1151201-1 - 1151201-26.

[4] X. L. Qi and S. C. Zhang, Topological Insulators and Superconductors, Reviews of Modern Physics 83 (2011) 1057-1110, and references therein.

[5] C. Z. Chang, J. Zhang, X. Feng, J. Shen, Z. Zhang, M. Guo, K. Li, Y. Ou, P. Wei,L. L. Wang, Z. Q. Ji, Y. Feng, S. Ji, X. Chen, J. Jia, X. Dai, Z. Fang, S. C. Zhang, K. He, Yayu Wang, L. Lu, X. C. Ma, and Q. K. Xue, Experimental Observation of the Quantum Anomalous Hall Effect in a Magnetic Topological Insulator, Science 314 (2013) 167-170.

[6] J. M. Fonseca, W. A. Moura-Melo, and A. R. Pereira, Localized and Polarized Charged Zero Modes in Three-Dimensional Topological Insulators Induced by a Magnetic Vortex, arXiv:1210.3100 (2012).

Chapter 8

PAPER REPRINT: A DISPERSION AND NORM PRESERVING FINITE DIFFERENCE SCHEME WITH TRANSPARENT BOUNDARY CONDITIONS FOR THE DIRAC EQUATION IN (1+1)D

Journal of Computational Physics 256 (2014)
(in press)
http://dx.doi.org/10.1016/j.jcp.2013.09.022

R. Hammer, W. Pötz, and A. Arnold

A finite difference scheme is presented for the Dirac equation in (1+1)D. It can handle space- and time-dependent mass and potential terms and utilizes exact discrete transparent boundary conditions (DTBCs). Based on a space- and time-staggered leap-frog scheme it avoids fermion doubling and preserves the dispersion relation of the continuum problem for mass zero (Weyl equation) exactly. Considering boundary regions, each with a constant mass and potential term, the associated DTBCs are derived by first applying this finite difference scheme and then using the Z-transform in the discrete time variable. The resulting constant coefficient difference equation in space can be solved exactly on each of the two semi-infinite exterior domains. Admitting only solutions in l_2 which vanish at infinity is equivalent to im-

posing outgoing boundary conditions. An inverse Z-transformation leads to exact DTBCs in form of a convolution in discrete time which suppress spurious reflections at the boundaries and enforce stability of the whole space-time scheme. An exactly preserved functional for the norm of the Dirac spinor on the staggered grid is presented. Simulations of Gaussian wave packets, leaving the computational domain without reflection, demonstrate the quality of the DTBCs numerically, as well as the importance of a faithful representation of the energy-momentum dispersion relation on a grid.

8.1 Introduction

We start out with a brief summary regarding important properties of the Dirac equation, its role played in physics, existing numerical schemes for its solution, and the issue of open boundaries.

8.1.1 The Dirac equation

Next to its fundamental role in relativistic quantum mechanics and field theory, which provide the foundation of modern nuclear and high energy physics [1, 2], the Dirac equation has received a rapidly growing importance in condensed matter systems as well. Especially, in the context of the recent experimental realization of graphene [3], 2D and 3D topological insulators [4, 5], and optical lattices [6, 7, 8] the Dirac equation describes the underlying physics as an effective field theory. Historically it was proposed by Dirac with his ingenious idea of linearizing the square root of the relativistic energy momentum relation by the introduction of Dirac matrices and multi-component wave functions, nowadays known as Dirac spinors. Imposing the condition that the twofold application of this Dirac operator onto the spinor must yield the Klein-Gordon equation, leads to the Clifford algebra for the Dirac matrices. In (1+1)D and (2+1)D the minimum dimension for a representation of this group is two, whereas in (3+1)D the Dirac spinor must have a minimum of four components. However, one can work with two components if one accepts higher–order derivatives in space and time [1, 2]. The latter has lead to the prediction of anti-matter and the concept of the filled Fermi sea in many-particle physics. Alternatively, the Dirac equation emerges from an investigation of the transformation properties of spinors under the Lorentz group [9]. In condensed matter physics Dirac-like equations arise in context of low-energy two-band effective models, e.g. in $k \cdot p$ perturbation theory or the tight-binding approximations [5]. Indeed, the study of Dirac fermion realizations has developed into one of the most exciting current topics of condensed matter physics [5].

In this work we restrict ourselves to a study of the (1+1)D Dirac equation and present a numerically stable scheme for its solution under open boundary conditions. The latter are motivated by a particle transport situation, as well as the fact that, unlike for the Schrödinger particle, a deep one-particle potential does not ensure confinement for Dirac particles. In its Schrödinger form, also called the standard or Pauli-Dirac form, the (1+1)D Dirac equation may be written as (using $c = 1,\ e = 1,$ and $\hbar = 1$)

$$i\partial_t \boldsymbol{\psi}(x,t) = \hat{H}\boldsymbol{\psi}(x,t)\ , \quad \hat{H} = m(x,t)\sigma_z - i\partial_x\sigma_x - V(x,t)\mathbb{1}_2\ . \tag{8.1}$$

The σ_i's are the 2×2 Hermitian anti-commuting Pauli-matrices, and $\mathbb{1}_2$ is the identity matrix. $x \in \mathbb{R},\ t \in \mathbb{R}^+$, and $\boldsymbol{\psi} = \begin{pmatrix} u \\ v \end{pmatrix} \in \mathbb{C}^2$ is the complex 2-spinor. $m, V \in \mathbb{R}$ represent, respectively, a space- and time-dependent mass and scalar potential. For constant coefficients, Fourier-transformation in the space and time variable and solving the eigenvalue problem gives the energy spectrum $E_\pm = \pm\sqrt{m^2 + p^2}$. In the physical ground state all negative energy states are filled with fermions. Empty negative energy states are reinterpreted as filled hole states (anti-particles) with positive energy, in analogy to multi-band systems in (non-relativistic) condensed matter physics [1]. The norm of the spinor is defined as $|\boldsymbol{\psi}(x,t)|_2 = \sqrt{|u(x,t)|^2 + |v(x,t)|^2}$, and its square can be interpreted as the probability density in space for given time t. The norm is conserved because Eq. eqrefdirac-eq is of Schrödinger form and $\hat{H}$ is Hermitian [1]. Global gauge-invariance holds as for the case of the Schrödinger equation: the addition of a constant V simply adds a phase to the solution. The free Dirac equation has various other symmetries [1, 10]. First there are the continuous transformations of spatial rotation (only meaningful for more than one space dimension) which, with the Lorentz boost, form the Lorentz group. Together with space and time translations, they form the Poincaré group. The latter is the fundamental group in particle physics, but is of minor importance in solid state physics because the crystal lattice necessarily breaks these continuous symmetries. The discrete symmetries holding for arbitrary constants $m \in \mathbb{R}, V \in \mathbb{R}$ are space reflection (parity) and time reversal symmetry which will also be present in the finite difference scheme.

8.1.2 Numerical aspects

Several schemes have been proposed and used for particle transport simulations based on the time-dependent Dirac equation. For a numerical treatment one has to discretize the continuum problem either in real- or Fourier-space, or a combination thereof. Real-space schemes are, for example, the finite-difference [11, 12, 13] and finite-element methods [14], whereas the spectral methods [15] are examples for the momentum space approach. Split-operator methods separate the time-evolution operator into several parts, with each of them depending only on either momentum or position [16, 17]. There also exists a coordinate space split-operator method which transforms the Dirac equation into an advection equation and uses its characteristic solutions [18]. While having the advantage of a natural implementation of space- and time dependent potential and mass terms, the finite-difference and finite-element schemes have to deal with the issue of fermion doubling, which means that, for a given sign of the energy, there are two (or more) extrema in the $m \neq 0$ energy-momentum dispersion relation instead of the single one of the continuum problem [12]. In fact the 'Nielsen-Ninomiya no-go theorem' forbids the existence of a single fermion flavor for chirally invariant fermions on a regular grid without breaking either translational invariance, locality, or Hermiticity [19]. In (1+1)D one can get rid of the fermion doubling using a staggered grid for the two spinor components. This is equivalent to taking the left-sided first-order derivative operator for one component of the spinor and the right-sided for the other one [12]. One obtains a monotonic dispersion relation with only one minimum. Here we present a scheme which provides an even better result by applying staggering to both the space and the time coordinate. This yields a numerical scheme which preserves the exact dispersion relation of the continuum problem for the special choice of the ratio between time and space grid $r := \Delta t/\Delta x = 1$ and mass $m = 0$. For $m, V \neq 0$ and $r = 1$ the dispersion relation improves for all possible wave-numbers $k \in [-\pi/\Delta x, \pi/\Delta x]$ with the refinement of the grid. For $\Delta x \to 0$ the numerical dispersion relation becomes identical to the continuum one. This is not true for most finite difference schemes in general and, to our knowledge, no finite difference scheme with this property for the Dirac equation has been reported before.

Let us mention that numerical methods for the (1+1)D non-linear Dirac (NLD) equation also got some attention in the literature [20]. Besides being an interesting playground on its own, it might also have some physical relevance by incorporating electron self-interaction into the Dirac equation. Scalar self-interaction leads to the Soler model [21], whereas vector-like inclusion of the self-interaction leads to the Thirring model [22]. Interestingly, the latter is S-dual to the quantum sine-Gordon model [22]. In contrast to the linear Dirac equation it provides solitary wave solutions, standing wave solutions, and collapse after collision of two solitary waves [20]. As already for the Dirac equation, analytic solutions are rare, most of the behavior of the NLD equation can only be investigated numerically [20]. For this purpose plenty of algorithms can be found in the literature. Without claim to completeness, they are of Crank-Nicholson type [23, 24, 25], explicit finite difference schemes [26, 20], spectral schemes [27, 28], Runge-Kutta methods [29, 30], and moving mesh methods [31].

Remarkably, for the finite difference method no effort was made so far to eliminate the spurious solutions, e.g. by staggering the grid for the spinor components. Being well aware of the different behavior of the NLD equation, we think our scheme could also have some relevance there. At least it could serve to solve the linear part in the operator-splitting method, thus avoiding the transformation to Fourier space. From a physics perspective, however, the most natural way for the incorporation of self-consistency (e.g., self-interaction) is to solve the standard Dirac equation self-consistently and in parallel to the differential equations for the external potentials which appear in the former. A brief discussion will be given in the Conclusions in Sect. 8.5.

8.1.3 Boundary conditions

For a numerical treatment of a differential equation, such as the Dirac equation, the number of degrees of freedom must be finite. In addition to the discretization of the time and space variable in a real-space scheme one has to restrict the simulation domain to a finite region in time and space. Then, appropriate boundary conditions are needed to ensure that the solution obtained within the finite domain is (at least) a good approximation to the solution of the whole space problem. Generally, the time-dependent Dirac equation is solved as an initial-value problem in time. The standard approach for the derivation of spatial transparent boundary conditions (TBCs), e.g. for the Schrödinger equation, has been to solve the continuous exterior problem by using the Laplace-transformation in time and to discretize the continuous TBCs afterwards [32]. To avoid stability problems [33] and spurious reflections at the boundary from inconsistent discretization schemes, recently, a new improved approach in which the whole domain is discretized first and then solved exactly in the constant-coefficient exterior domains using a Z-transform in time has been developed for the Schrödinger equation [34, 37]. In this way one maintains the stability properties of the scheme on the whole space and avoids inconsistent discretization for the simulation region and the boundary conditions. The resulting discrete transparent boundary conditions (DTBCs) which are non-local in time are exact in the sense that they do not introduce a procedural error. An alternative approach which, in most cases is easier to handle because an inverse Z-transform can be avoided, is to discretize in space only, derive TBCs, and discretize in time thereafter. This has been done with good results for hyperbolic systems [38, 39, 40]. However for the proposed scheme, where the good properties regarding dispersion and conservation of norm arise from the *simultaneous* discretization of space and time in an interlaced manner, paying the extra price in form of an inverse Z-transformation is well justified. Therefore we follow the fully discrete approach of [34] to develop TBCs for the time- and space-staggered leap-frog scheme. Furthermore, in order to preserve the covariant symmetry of the Dirac equation on a space-time grid, time and space coordinates must be treated on an equal footing. This is particularly important in higher dimensions.

As a major difference to the Schrödinger equation one should mention that a massless relativistic particle cannot be trapped by a scalar one-particle potential [1]. The same holds for massive relativistic particles with energy E, when the potential depth V is such that $E+mc^2 > V > E-mc^2$. This phenomenon is related to the Klein paradox and is due to the two-band-nature of the dispersion relation, consisting of an electron and a positron band. One is necessarily dealing with a scattering problem whenever there are no bound states supported by the Hamiltonian. Then, for initial data which are compactly supported on the computational domain, the solution always reaches the boundary after a finite time. For simulation times beyond that threshold, open boundary conditions are required to close the finite difference scheme in a particle transport situation, similar to non-relativistic particle transport simulations in nano-devices [35, 36].

8.2 Continuous transparent boundary conditions for the Dirac equation in (1+1)D

In this section we derive continuous TBCs for the Dirac equation Eq. (8.1). We divide the entire space into the computational domain $(0, L)$, and the semi-infinite exterior domains $(-\infty, 0]$ and $[L, \infty)$. The mass is assumed to be constant $m(x,t) = m$ and the potential is constant in space $V(x,t) = V(t)$ in the exterior domains. This reduces to the case $V = 0$ with the following gauge change of the spinor:

$$\boldsymbol{\psi}(x,t) = e^{i\mathcal{V}(t)}\boldsymbol{\chi}(x,t) \quad \text{with} \quad \mathcal{V}(t) = \int_0^t V(s)ds \, . \tag{8.2}$$

With $\boldsymbol{\chi} = (u, v)$, in the exterior, we have

$$i \begin{pmatrix} u(x,t) \\ v(x,t) \end{pmatrix}_t = \begin{pmatrix} m & -i\partial_x \\ -i\partial_x & -m \end{pmatrix} \begin{pmatrix} u(x,t) \\ v(x,t) \end{pmatrix} . \tag{8.3}$$

The multiplication with σ_x and a Laplace transformation with respect to the time variable leads to

$$\begin{pmatrix} \tilde{u}(x,s) \\ \tilde{v}(x,s) \end{pmatrix}_x = \begin{pmatrix} 0 & -s+im \\ -s-im & 0 \end{pmatrix} \begin{pmatrix} \tilde{u}(x,s) \\ \tilde{v}(x,s) \end{pmatrix} . \tag{8.4}$$

Eq. (8.4) has the general solution

$$\begin{pmatrix} \tilde{u}(x,s) \\ \tilde{v}(x,s) \end{pmatrix} = c_1 \begin{pmatrix} -s+im \\ -\sqrt[+]{s^2+m^2} \end{pmatrix} e^{-\sqrt[+]{s^2+m^2}x} + c_2 \begin{pmatrix} -s+im \\ \sqrt[+]{s^2+m^2} \end{pmatrix} e^{\sqrt[+]{s^2+m^2}x} , \tag{8.5}$$

where $\sqrt[+]{}$ is written for the square root with positive real part. Because the solution must be in $L_2(\mathbb{R})$ the constant c_2 must vanish on the right exterior domain. For the same reason c_1 must be zero on the left exterior domain. Therefore, the boundary conditions on the right boundary are

$$\partial_x \tilde{u}(x,s)\big|_{x=L} = -\sqrt[+]{s^2+m^2}\, \tilde{u}(L,s)$$

and

$$\partial_x \tilde{v}(x,s)\big|_{x=L} = -\sqrt[+]{s^2+m^2}\, \tilde{v}(L,s) . \tag{8.6}$$

On the left boundary one gets

$$\begin{aligned} \partial_x \tilde{u}(x,s)\big|_{x=0} &= \sqrt[+]{s^2+m^2}\, \tilde{u}(0,s) \\ \partial_x \tilde{v}(x,s)\big|_{x=0} &= \sqrt[+]{s^2+m^2}\, \tilde{v}(0,s) . \end{aligned} \tag{8.7}$$

The structure for both spinor components and both boundaries is the same, so we proceed with $\tilde{u}$ on the right boundary. First we derive boundary conditions as a Neumann-to-Dirichlet map by writing

$$\tilde{u}(L,s) = -\frac{1}{\sqrt[+]{s^2+m^2}} \partial_x \tilde{u}(x,s)\big|_{x=L} . \tag{8.8}$$

Then the inverse Laplace transformation leads to the convolution at the right boundary:

$$u(L,t) = -J_0(mt) *_t \partial_x u(x,t)\big|_{x=L} = -\int_0^t J_0(m\tau) \partial_x u(L, t-\tau)\, d\tau , \tag{8.9}$$

with J_0 being the Bessel function of first kind. Analogously for the left boundary:

$$u(0,t) = J_0(mt) *_t \partial_x u(x,t)\big|_{x=0} \; . \tag{8.10}$$

Finally, this leads with the gauge Eq. (8.2) for $V \neq 0$ to the TBCs in the form of a Neumann-to-Dirichlet map:

$$\boldsymbol{\psi}(L,t) = -e^{i\mathcal{V}_r(t)}\Big\{ J_0(mt) *_t \Big[\partial_x \boldsymbol{\psi}(x,t)\big|_{x=L} e^{-i\mathcal{V}_r(t)}\Big]\Big\} \quad \text{...right TBC ,} \tag{8.11}$$

$$\boldsymbol{\psi}(0,t) = e^{i\mathcal{V}_l(t)}\Big\{ J_0(mt) *_t \Big[\partial_x \boldsymbol{\psi}(x,t)\big|_{x=0} e^{-i\mathcal{V}_r(t)}\Big]\Big\} \quad \text{...left TBC .} \tag{8.12}$$

For the derivation of TBCs in the form of a Dirichlet-to-Neumann map we write:

$$\partial_x \tilde{u}(x,s)\big|_{x=L} = -\tilde{g}(s)\tilde{u}(L,s) \; , \tag{8.13}$$

with:

$$\tilde{g}(s) := \sqrt[+]{s^2+m^2} = \left(\frac{s^2+m^2}{\sqrt[+]{s^2+m^2}} - s \right) + s \; . \tag{8.14}$$

We use

$$\tilde{f}(s) := \frac{1}{\sqrt[+]{s^2+m^2}} \quad \overset{\mathcal{L}^{-1}}{\to} \quad f(t) = J_0(mt) \tag{8.15}$$

and

$$s^2 \tilde{f}(s) - s f(0) \quad \overset{\mathcal{L}^{-1}}{\to} \quad m^2 J_0''(mt) \; . \tag{8.16}$$

This leads to the following inverse Laplace transform of $\tilde{g}(s)$:

$$\tilde{g}(s) \quad \overset{\mathcal{L}^{-1}}{\to} \quad g(t) = m^2\big[J_0''(mt) + J_0(mt)\big] + \delta' = \frac{m^2}{2}\big[J_2(mt) + J_0(mt)\big] + \delta' \; , \tag{8.17}$$

where δ' is the first derivative of the delta distribution. Then the TBC as a Dirichlet-to-Neumann map on the right boundary is

$$\partial_x \boldsymbol{\psi}(x,t)\big|_{x=L} = -e^{i\mathcal{V}_r(t)}\Big\{ \frac{m^2}{2}\big[J_2(mt) + J_0(mt)\big] *_t \boldsymbol{\psi}(L,t) e^{-i\mathcal{V}_r(t)} + \partial_t \boldsymbol{\psi}(L,t) e^{-i\mathcal{V}_r(t)} \Big\} \; . \tag{8.18}$$

On the left boundary one gets

$$\partial_x \boldsymbol{\psi}(x,t)\big|_{x=0} \tag{8.19}$$

$$= e^{i\mathcal{V}_r(t)}\left\{\frac{m^2}{2}\left[J_2(mt)+J_0(mt)\right] *_t \boldsymbol{\psi}(0,t)e^{-i\mathcal{V}_r(t)} + \partial_t\boldsymbol{\psi}(0,t)e^{-i\mathcal{V}_r(t)}\right\}.$$

Discretizations of Eqs. (8.11) and (8.12) or Eqs. (8.18) and (8.19) can serve as boundary conditions for arbitrary finite difference discretizations of the Dirac equation Eq. (8.1). But one has to be aware of the fact that inconsistent discretization of the differential equation and the associated boundary conditions usually leads to spurious reflections or even instability. As already mentioned in the introduction we will therefore first apply the discretization scheme to Eq. (8.1) for the the boundary regions also and derive the associated TBCs by Z-transformation. Eqs. (8.11), (8.12), (8.18), and (8.19) serve as a guide to gain intuition for the behavior of the convolution coefficients.

8.3 Time- and space-staggered leap-frog scheme

Leap-frog time-stepping, in combination with a staggered spatial grid, plays a special role among the finite difference methods because, in addition to the elimination of the fermion-doubling problem, it proves to be dispersion relation preserving in (1+1)D for the 'golden ratio' of $r = \Delta t/\Delta x = 1$, $m = 0$, and $V = 0$ (Weyl equation). Moreover, for $m \neq 0$ and/or $V \neq 0$ the dispersion relation is still monotone and improves with a refinement of the grid. It is identical to the exact analytic dispersion when $\Delta t, \Delta x \to 0$, for fixed $r = 1$. This is particularly important for simulations where the whole possible range of the wave numbers $k \in \left[-\frac{\pi}{\Delta x}, \frac{\pi}{\Delta x}\right]$ is used, for example, in strong external fields. An initial wave-packet which consists only of wave-components near $k = 0$ may acquire high wave number components due to strong spatial and/or temporal changes of potential and/or mass.

For schemes with non-monotonic dispersion a problem can also arise at the boundary. The modes of such a scheme consist of additional, spurious, numerically generated modes on the lattice which, nevertheless, must be accounted for in the DTBCs for consistency. This requires special attention at the boundary because improper realization of the boundary condition may lead to 'energy' transfer between the modes, spurious reflections, and eventually instability (see e.g. [40]). A correct dispersion relation means correct phase and group velocity on the grid and is essential for faithful long-time propagation studies. We now present such a scheme.

8.3.1 The discretization scheme

We shall consider the following leap-frog discretization of the Dirac equation in Pauli-Dirac form given in Eq.(8.1):

$$\frac{u_j^{n+1/2}-u_j^{n-1/2}}{\Delta t}+i(m_j^n-V_j^n)\frac{u_j^{n+1/2}+u_j^{n-1/2}}{2}+\frac{(Dv^n)_j}{\Delta x}=0\,, \tag{8.20}$$

$$\frac{v_{j-1/2}^{n+1}-v_{j-1/2}^{n}}{\Delta t}-i(m_{j-1/2}^{n+1/2}+V_{j-1/2}^{n+1/2})\frac{v_{j-1/2}^{n+1}+v_{j-1/2}^{n}}{2}+\frac{(Du^{n+1/2})_{j-1/2}}{\Delta x}=0\,, \tag{8.21}$$

with $j\in\mathbb{Z},\ n\in\mathbb{N}$. Here we used the notation $\boldsymbol{\psi}(x,t)=\big[u(x,t),v(x,t)\big]$ with $u(x_j,t^{n-1/2})\approx u_j^{n-1/2}$ and $v(x_{j-1/2},t^n)\approx v_{j-1/2}^n$. The symmetric spatial difference operator is defined as $(Dv^n)_j=v_{j+1/2}^n-v_{j-1/2}^n$ and $(Du^{n+1/2})_{j-1/2}=u_j^{n+1/2}-u_{j-1}^{n+1/2}$. For the mass and potential term we use the averages $g_j^n=\big(g_j^{n+1/2}+g_j^{n-1/2}\big)/2$ for the integer spacial grid-points and $g_{j-1/2}^{n+1/2}=\left(g_{j-1/2}^{n+1}+g_{j-1/2}^{n}\right)/2$ for the half-integer ones, where $g=m,V$. The space-time stencil is shown in Fig. 8.1 (a). As one can see, the components u and v are not defined on the same space-time grid points but on sub-grids shifted by a half time and space grid spacing. A Taylor expansion about the grid points (x_j,t_n) and $(x_{j-1/2},t_{n+1/2})$ shows that the staggered-grid leap-frog scheme is second order accurate in space and time.

The leap-frog time stepping is not self starting. Assume, for example, initial data $\boldsymbol{\psi}(x,t)$ given at the time-level t^0. Then the u component has to be propagated from t^0 to $t^{1/2}$. In principle this can be done by any time stepping method. We have chosen a symplectic Euler step [42] with half space-time grid spacing, which is algorithmically equivalent to the leap-frog scheme, with the exception that all the data (u and v) are stored at the same time and space level. Moreover it is only first order accurate (omitting indices for m and V):

$$\frac{u_j^{1/2}-u_j^0}{\Delta t/2}+i(m-V)\frac{u_j^{1/2}+u_j^0}{2}+\frac{v_j^0-v_{j-1/2}^0}{\Delta x/2}=0\,,\quad j\in\mathbb{Z}/2. \tag{8.22}$$

After this first initialization step the u-component is stored only at integer and the v-component at half integer spatial points. With a relabeling of the

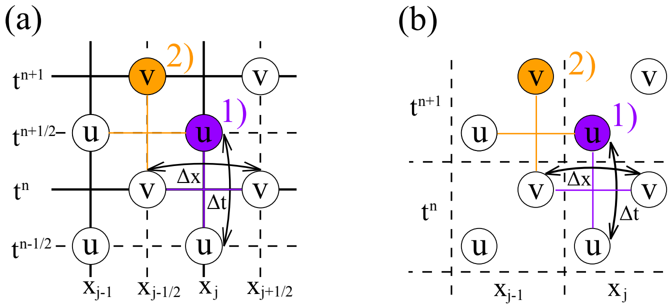

Figure 8.1: (a) Staggered-grid scheme for Dirac equation in Pauli-Dirac form with leap-frog time-stepping; (b) the algorithmically equivalent (except for starting procedure) symplectic Euler time-stepping.

indices, the algorithm Eq. (8.21) can be written as follows:

$$\begin{aligned} \frac{u_j^{n+1}-u_j^n}{\Delta t} + i(m-V)\frac{u_j^{n+1}+u_j^n}{2} + \frac{v_j^n - v_{j-1}^n}{\Delta x} &= 0\,, \\ \frac{v_j^{n+1}-v_j^n}{\Delta t} - i(m+V)\frac{v_j^{n+1}+v_j^n}{2} + \frac{u_{j+1}^{n+1} - u_j^{n+1}}{\Delta x} &= 0\,, \end{aligned} \tag{8.23}$$

with $j \in \mathbb{Z}$, $n \in \mathbb{N}_0$. Here we use the approximations $u_j^n \approx u(x_{j-1/4}, t^{n-1/4})$, $v_j^n \approx v(x_{j+1/4}, t^{n+1/4})$ (see Fig. 8.1 (b)). Rearranging of terms leads to the following equations for the explicit recursive update

$$u_j^{n+1} = \frac{2-i(m-V)\Delta t}{2+i(m-V)\Delta t}u_j^n - \frac{2\Delta t/\Delta x}{2+i(m-V)\Delta t}\left(v_j^n - v_{j-1}^n\right)\,, \tag{8.24}$$

$$v_j^{n+1} = \frac{2+i(m+V)\Delta t}{2-i(m+V)\Delta t}v_j^n - \frac{2\Delta t/\Delta x}{2-i(m+V)\Delta t}\left(u_{j+1}^{n+1} - u_j^{n+1}\right)\,. \tag{8.25}$$

The starting procedure for the leap-frog scheme with a symplectic Euler step of half grid-size is especially suitable since symplectic Euler is algorithmically equivalent to the leap-frog staggered-grid scheme and has the same dispersion relation for equal ratio r.

8.3.2 Von Neumann stability analysis

For constant coefficients in Eq. (8.23), Fourier analysis can be used to perform a von Neumann stability analysis and to derive the dispersion relation for the whole space problem. A Fourier transform in space of Eq. (8.23) leads to

$$\underbrace{\begin{pmatrix} \frac{1}{\Delta t} + \frac{i(m-V)}{2} & 0 \\ \frac{e^{-ik\Delta x}-1}{\Delta x} & \frac{1}{\Delta t} - \frac{i(m+V)}{2} \end{pmatrix}}_{=:\mathbf{A}} \begin{pmatrix} \tilde{u}^{n+1} \\ \tilde{v}^{n+1} \end{pmatrix} \tag{8.26}$$
$$+ \underbrace{\begin{pmatrix} -\frac{1}{\Delta t} + \frac{i(m-V)}{2} & \frac{1-e^{ik\Delta x}}{\Delta x} \\ 0 & -\frac{1}{\Delta t} - \frac{i(m+V)}{2} \end{pmatrix}}_{=:\mathbf{B}=-\mathbf{A}^*} \begin{pmatrix} \tilde{u}^{n} \\ \tilde{v}^{n} \end{pmatrix} = 0 \; .$$

Using the definitions $\xi = k\Delta x$, $\mu = m\Delta t$, $\nu = V\Delta t$, and $r = \Delta t/\Delta x$ the eigenvalues of the amplification matrix

$$\mathbf{G} = -\mathbf{A}^{-1}\mathbf{B} = \mathbf{A}^{-1}\mathbf{A}^* = \begin{pmatrix} \frac{2i-\nu+\mu}{2i+\nu-\mu} & \frac{2ir(e^{i\xi}-1)}{2i+\nu-\mu} \\ \frac{2r(1-e^{-i\xi})(2+i\nu-i\mu)}{4-\nu^2-4\nu i+\mu^2} & \frac{4+\nu^2-\mu^2+4\mu i+8r^2[\cos\xi-1]}{4-\nu^2-4\nu i+\mu^2} \end{pmatrix} \tag{8.27}$$

are computed by means of

$$\lambda_\pm = P/2 \pm \sqrt{\left(P/2\right)^2 - Q} \; , \tag{8.28}$$

where $P = \mathrm{tr}[\mathbf{G}]$ and $Q = \det[\mathbf{G}]$, with

$$P = \left[2(\nu^2-\mu^2) + 8(1 - r^2 + r^2\cos\xi)\right]/N \tag{8.29}$$

and

$$Q = \left[\mu^2 - (\nu - 2i)^2\right]/N \; , \tag{8.30}$$

where $N = \mu^2 - (\nu + 2i)^2$. A lengthy but straightforward computation yields $|\lambda_\pm| = 1$ for $r \leq 1$. The eigenvalues are non-degenerate except for the case $k = \mu = 0$ and $r = 1$ (with geometric multiplicity 2), as well as the case $k = \pi/\Delta x$, $\nu = 0$, and $r = 1$ (with geometric multiplicity 1). Except for the latter case, the scheme is stable under the constraint $r \leq 1$, which constitutes its Courant-Friedrichs-Lewy (CFL) condition. Below we use a different technique to prove stability which allows one also to identify a functional (related to the l_2-norm defined on the staggered grid) which is exactly conserved.

8.3.3 The energy-momentum dispersion relation

The Fourier transform of Eq. (8.26) with respect to the time variable with $\tilde{\omega} = \omega\Delta t$ leads to the homogeneous system

$$(e^{i\tilde{\omega}}\mathbf{A} + \mathbf{B})\tilde{\boldsymbol{\psi}} = 0 \; , \tag{8.31}$$

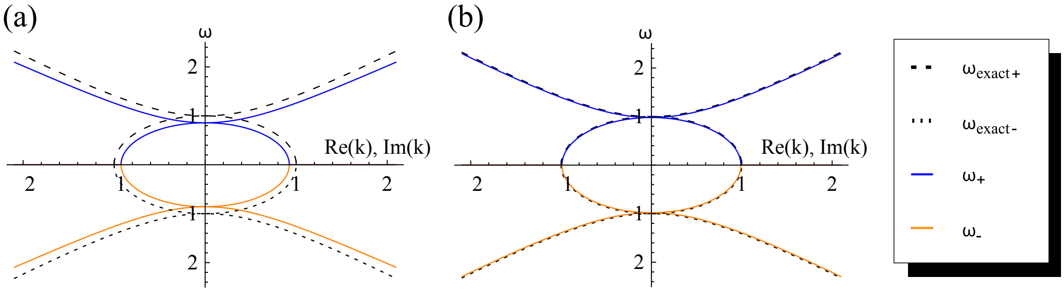

Figure 8.2: Numerical dispersion relation $\omega(k)$ for the staggered-grid leapfrog scheme with $m = 1$ and $r = 1$ for real k (hyperbolically shaped curves) and for imaginary k inside the energy gap (elliptically shaped curve) shown as solid lines. The dispersion relation for the continuum problem is shown for comparison using dotted lines: (a) very coarse grid $\Delta x = 1.5$ and $k \in [\pi/\Delta x, \pi/\Delta x]$; (b) finer grid $\Delta x = 0.5$ where merely an excerpt of the wave number range $k \in [\pi/(3\Delta x), \pi/(3\Delta x)]$ is shown.

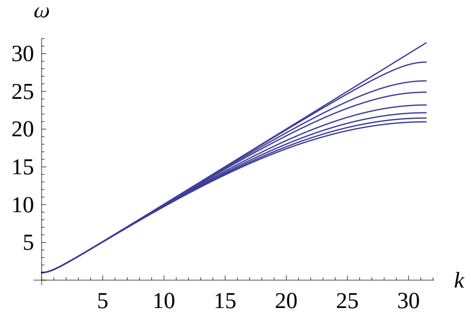

Figure 8.3: Dispersion relation $\omega(k)$ for $V = 0$, $m = 1$, and $\Delta x = 0.1$, and $k \in [0, \pi/\Delta x]$ with $r = 1, 0.99, 0.95, 0.9, 0.8, 0.7, 0.6, 0.5$ (from top to bottom).

with the solutions for $r \leq 1$:

$$\tilde{\omega}_{\pm} = -\frac{i}{r} \ln[\lambda_{\pm}] \, , \tag{8.32}$$

where $\lambda_{\pm}$ is given in Eq. (8.28). By setting $\mu, \nu = 0$ they reduce to

$$\tilde{\omega}_{\pm} = -\frac{i}{r} \ln \left\{ 1 + r^2 \big(\cos\xi - 1 \big) \pm \sqrt{\Big[r^2 \big(\cos\xi - 1 \big) + 1 \Big]^2 - 1} \right\}, \tag{8.33}$$

and with the choice $r = 1$ they read

$$\tilde{\omega}_{\pm} = -i \ln \Big(\cos\xi \pm \sqrt{\cos^2\xi - 1} \Big) = -i \ln \Big(\cos\xi \pm i \sin\xi \Big) = \pm\xi \, . \tag{8.34}$$

Thus for $\mu, \nu = 0$, and $r = 1$ the linear dispersion of the continuum problem (Weyl equation) is exactly preserved.

The connection to the phase of the growth factor (i.e. eigenvalues of $\mathbf{G}$) can be established via

$$\tilde{\omega}_{\pm} = -\frac{i}{r}\ln[\lambda_{\pm}] = -\frac{i}{r}[\ln|\lambda_{\pm}| + i\arg(\lambda_{\pm}) + 2\pi i n] = \frac{1}{r}[\arg(\lambda_{\pm}) + 2\pi n] \ . \quad (8.35)$$

In Fig. 8.2 the dispersion relation for a rather coarse grid with $\Delta x = 1.5$ is compared to that of a finer one using $\Delta x = 0.5$, for $m = 1$, $V = 0$, and $r = 1$. Clearly, the quality of the numerical dispersion relation improves for a finer grid and, for all wave-numbers $k \in [-\pi/\Delta x, \pi/\Delta x]$, it approaches the continuum form in the limit $\Delta x \to 0$ and $r = 1$. In Fig. 8.3 the dispersion relation for fixed values of m and V is shown for several values of r and $\Delta x = 0.1$.

In Fig. 8.4, the scheme is compared to a scheme using a centered approximation for the space derivative and Crank-Nicolson time averaging, showing the fermion-doubling problem. The comparison is made for $m = 0 = V$, $r = 1$, and initial Gaussian wave packets with different mean energies. The Crank-Nicolson scheme shows large dispersive errors and for high mean energy (large wavenumbers) and even propagation in the wrong direction (fermion-doubling) occurs, whereas the leap-frog staggered-grid scheme yields (almost) the exact solution.

8.3.4 Phase error and gauge invariance

One can define the phase error for one time-step as

$$\epsilon_{\text{phase}}(k, r, \Delta t) = \big[\omega_{\text{analytical}}(k) - \omega_{\text{numerical}}(k, r, \Delta t)\big]\Delta t \ , \quad (8.36)$$

where the analytic dispersion relation is $\omega_{\text{analytical}} = \pm\sqrt{m^2 + k^2}$ and the numerical one is given in Eq. (8.32). Together with Eq. (8.34) it follows that ϵ_{phase} vanishes in the case of $m = V = 0$ and $r = 1$ where the scheme indeed propagates the solution without error. In Fig. 8.5, ϵ_{phase} is shown for different values of m and V on a coarse grid $\Delta t = \Delta x = 0.01$ (a) and (b), and on a finer grid $\Delta t = \Delta x = 10^{-4}$ (c) and (d).

Due to gauge invariance, when adding a diagonal term V (constant scalar

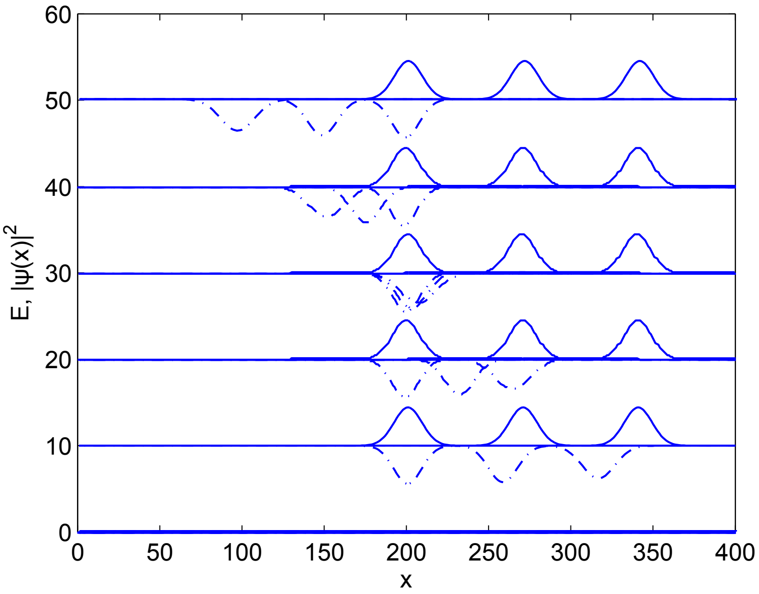

Figure 8.4: Comparison of the leap-frog staggered-grid scheme with a scheme that is centered in space and Crank-Nicolson in time. We have choosen $\Delta t = \Delta x = 0.05$ and $m = V = 0$. The Gaussian wave packet is initially placed at the center ($x = 200$) and should then move to the right. We give the results for 5 different energy mean values ($E = 10, ..., 50$). For each prescribed energy we merge the simulation results at three times ($t = 0, 70, 140$) into one graphics. The figures show the probability density $|\psi(x)|^2$ (solid lines for the leap-frog staggered-grid scheme) and the negative probability density (dash-dotted lines) for the Crank-Nicolson scheme. The latter shows large dispersive errors, whereas the leap-frog staggered-grid scheme shows the correct propagation.

potential) to the Hamitionan Eq. (8.1) one can introduce a new spinor

$$\breve{\psi}(t) = \psi(t) \exp\big(-iVt\big) , \tag{8.37}$$

which fulfills the original equation. Therefore the gauge error per time-step is equivalent to ϵ_{phase} due to a finite V (see Fig. 8.5 (b) and (d)). The gauge invariant introduction of the electromagnetic vector potential is shown in 8.7.

8.3.5 Stability analysis within a multiplication technique

The von Neumann analysis above and the fact that the dispersion relation $\omega(k)$ is real for $r \neq 1$ revealed the stability conditions of the scheme for con-

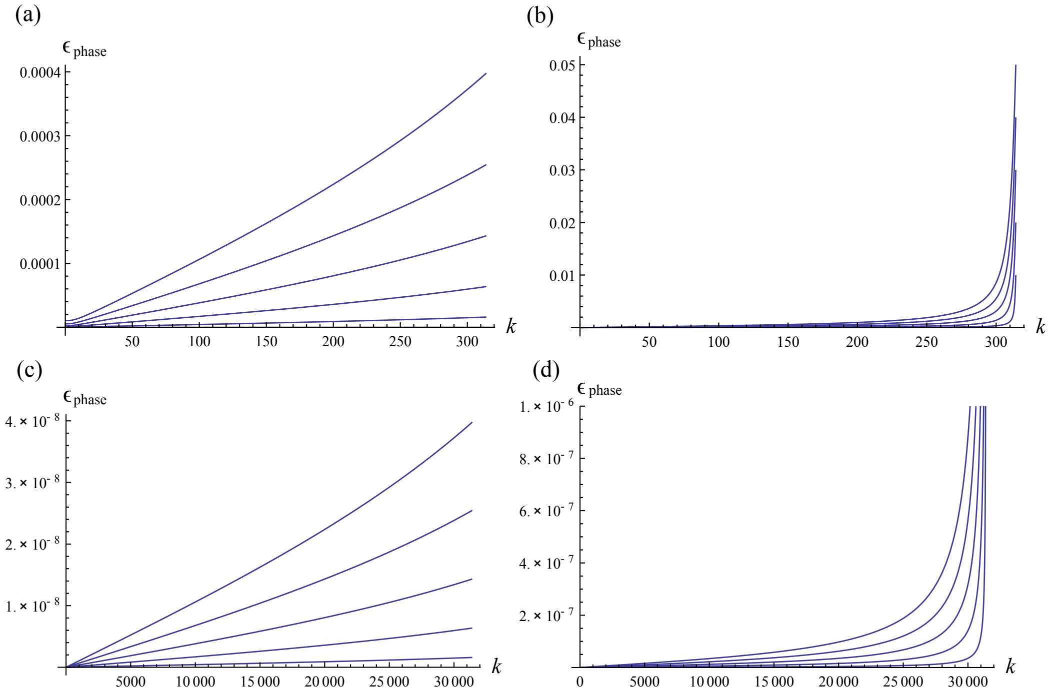

Figure 8.5: The dependence of the phase error ϵ_{phase} on the wave vector $k \in [0, \pi/\Delta x]$ for $V = 0$, $m = 1, 2, 3, 4, 5$ (from bottom to top): (a) coarse grid $\Delta t = \Delta x = 0.01$, (c) fine grid $\Delta t = \Delta x = 10^{-4}$; for $V = 1, 2, 3, 4, 5$ (from bottom to top), $m = 0$: (b) coarse grid $\Delta t = \Delta x = 0.01$, (d) fine grid $\Delta t = \Delta x = 10^{-4}$. In (d) the functions exceed the plot-range, where the maxima for $V = (1, 2, 3, 4, 5)$ are $\epsilon_{\text{phase}} = (1, 2, 3, 4, 5) * 10^{-4}$ at $k = 10^4\pi$.

stant mass and potential terms. However, there is another technique available which is not based on the Fourier transform and leads to the identification of an “energy" functional which is exactly conserved by the scheme, even in the presence of non-constant mass and potential terms. The use of this multiplication technique has been inspired by a stability analysis of a leap-frog pseudo-spectral scheme for the Schrödinger equation [43].

We define the inner product $(u, v) := \sum_j u_j \bar{v}_j$ on $l^2(\mathbb{Z}; \mathbb{C})$ and we will use the notation $\|u\|^2 := (u, u)$. Taking the inner product of Eq. (8.20) with $(u^{n+1/2} + u^{n-1/2})$ and taking the real part gives

$$\left\|u^{n+1/2}\right\|^2 - \left\|u^{n-1/2}\right\|^2 + r\Re\Big[(Dv^n, u^{n+1/2} + u^{n-1/2})\Big] = 0\,. \tag{8.38}$$

Eq. (8.21) is multiplied by $(\bar{v}^{n+1} + \bar{v}^n)$ and again the real part is taken to give

$$\left\|v^{n+1}\right\|^2 - \|v^n\|^2 + r\Re\Big[(Du^{n+1/2}, v^{n+1} + v^n)\Big] = 0\,. \tag{8.39}$$

Performing a summation by parts with vanishing boundary terms at infinity gives

$$\Re\Big[(Dv^n, u^{n+1/2} + u^{n-1/2})\Big] = -\Re\Big[(Du^{n+1/2} + Du^{n-1/2}, v^n)\Big]\,. \tag{8.40}$$

Then adding Eq. (8.38) and Eq. (8.39) leads to

$$\left\|u^{n+1/2}\right\|^2 + \left\|v^{n+1}\right\|^2 + r\Re\Big[(Du^{n+1/2}, v^{n+1})\Big] = \left\|u^{n-1/2}\right\|^2 + \|v^n\|^2 + r\Re\Big[(Du^{n-1/2}, v^n)\Big] \tag{8.41}$$

and one immediately identifies the conserved functional

$$E_r^n := \left\|u^{n+1/2}\right\|^2 + \left\|v^{n+1}\right\|^2 + r\Re\Big[(Du^{n+1/2}, v^{n+1})\Big] = \text{const} = E_r^0\,. \tag{8.42}$$

With this result one obtains the stability condition for the scheme by using

$$\left|\Re\Big[(Du^{n+1/2}, v^{n+1})\Big]\right| \le \left\|u^{n+1/2}\right\|^2 + \left\|v^{n+1}\right\|^2\,. \tag{8.43}$$

This gives the estimate

$$\left\|u^{n+1/2}\right\|^2 + \left\|v^{n+1}\right\|^2 \le \frac{E_r^0}{1-r} \quad \forall\, n\,, \tag{8.44}$$

for $r < 1$. The case $r = 1$ must be treated separately and one rewrites E_1^n as

$$E_1^n = \sum_j |u_j^{n+1/2}|^2 + |v_{j+1/2}^{n+1}|^2 + \Re\sum_j \big(u_{j+1}^{n+1/2} - u_j^{n+1/2}\big)\bar{v}_{j+1/2}^{n+1} \tag{8.45}$$

$$= \frac{1}{2}\sum_j |u_j^{n+1/2} - v_{j+1/2}^{n+1}|^2 + \frac{1}{2}\sum_j |u_{j+1}^{n+1/2} + v_{j+1/2}^{n+1}|^2\,. \tag{8.46}$$

Alternatively, when shifting indices, one obtains

$$E_1^n = \frac{1}{2}\sum_j |u_j^{n+1/2} + v_{j-1/2}^{n+1}|^2 + \frac{1}{2}\sum_j |u_j^{n+1/2} - v_{j+1/2}^{n+1}|^2\,. \tag{8.47}$$

Using $\frac{1}{4}\left\|a_1+a_2\right\|^2 \leq \frac{1}{4}\big(\left\|a_1+b\right\|+\left\|a_2-b\right\|\big)^2 \leq \frac{1}{2}\left\|a_1+b\right\|^2+\frac{1}{2}\left\|a_2-b\right\|^2$ gives

$$\text{from Eq. (8.46):} \qquad \left\|\tilde{u}^{n+1/2}\right\|^2 := \sum_j \left|\frac{u_j^{n+1/2}+u_{j+1}^{n+1/2}}{2}\right|^2 \leq E_1^n = E_1^0 \quad \forall n \tag{8.48}$$

$$\text{from Eq. (8.47):} \qquad \left\|\tilde{v}^{n+1}\right\|^2 := \sum_j \left|\frac{v_{j-1/2}^{n+1}+v_{j+1/2}^{n+1}}{2}\right|^2 \leq E_1^n = E_1^0 \quad \forall n$$

$$\Rightarrow \qquad \left\|\tilde{u}^{n+1/2}\right\|^2 + \left\|\tilde{v}^{n+1}\right\|^2 \leq 2E_1^0\,. \tag{8.49}$$

One easily verifies that $\|\tilde{u}\|$ is a norm on $l^2(\mathbb{Z})$. Indeed, $\tilde{u}=0$ implies $u_j = (-1)^j\lambda$ for some $\lambda \in \mathbb{C}$. And $u \in l^2$ then yields $u = 0$.

This allows us to conclude that the scheme is stable for all $r = \Delta t/\Delta x \leq 1$. Moreover we have identified the functional which is conserved by the scheme (see Eq. (8.42)). In fact, it is conserved for arbitrary time and space dependent $m, V \in \mathbb{R}$.

8.3.6 Time-reversal invariance

The time reversal invariance of the scheme can easily be seen in Eqs. (20) and (8.21). One has to set $\Delta t \to -\Delta t$ and replace the role of the old and new time-levels $n-1/2 \leftrightarrow n+1/2$ and $n \leftrightarrow n+1$. Then one observes that the scheme for the backward propagation has exactly the same form as for the forward propagation and concludes the scheme is time-reversal invariant.

8.4 Discrete transparent boundary conditions for the staggered-grid leap-frog scheme

Having discussed the properties of the leap-frog scheme we now turn to the derivation of the associated TBCs. Again, we divide the entire space into the computational domain $(0, L)$, a left semi-infinite exterior domain $(-\infty, 0]$, and a right semi-infinite exterior domain $[L, \infty)$. This corresponds to a typical device simulation geometry (scattering scenario) in which the nano-device is placed in the computational domain and the (macroscopic) contacts are represented by the exterior domains. We make the following simplifying assumptions:

- The initial data $\psi_0(x) = \psi(0,x)$ is compactly supported inside the computational domain.
- In each exterior domain the mass $m(x,t) = m$ and potential $V(x,t) = V$ are constant in t and x.

Both assumption are made for simplicity but can be loosened when needed, as will be discussed below.

We first Z-transform Eq. (8.23) in t-direction on each of the exterior domains, $j \in \{\dots,-2,-1,0\}$ and $j \in \{J, J+1, J+2, \dots\}$, and solve the resulting finite difference equations explicitly. Using the definition of the Z-transform $b(z) := Z(b_n) = \sum\limits_{n=0}^{\infty} b_n z^{-n}$, its shifting property $Z(b_{n+1}) = \sum\limits_{n=0}^{\infty} b_{n+1} z^{-n} = \sum\limits_{n\acute{}=1}^{\infty} b_{n\acute{}} z^{-n\acute{}+1} = zb(z) - zb_0$, and setting $b_0 = 0$ (since the initial spinor is compactly supported on $(0,L)$) we obtain

$$\begin{pmatrix} \frac{1}{\Delta t}(z-1) + \frac{i(m-V)}{2}(z+1) & \frac{1}{\Delta x} \\ \frac{z}{\Delta x} & 0 \end{pmatrix} \begin{pmatrix} u_j(z) \\ v_j(z) \end{pmatrix} + \begin{pmatrix} 0 & -\frac{1}{\Delta x} \\ -\frac{z}{\Delta x} & \frac{1}{\Delta t}(z-1) - \frac{i(m+V)}{2}(z+1) \end{pmatrix} \begin{pmatrix} u_{j-1}(z) \\ v_{j-1}(z) \end{pmatrix} = 0 \,. \tag{8.50}$$

Translation from grid point j to $j+1$ therefore is given by

$$\begin{pmatrix} u_j \\ v_j \end{pmatrix} = \begin{pmatrix} n_{11} & n_{12} \\ n_{21} & n_{22} \end{pmatrix} \begin{pmatrix} u_{j-1} \\ v_{j-1} \end{pmatrix} , \tag{8.51}$$

where

$$n_{11} = 1 \,,$$

$$n_{21} = \frac{\Delta x}{\Delta t}(1-z) - \frac{i(m-V)\Delta x}{2}(1+z) \,,$$

$$n_{12} = \frac{\Delta x}{\Delta t}\frac{1-z}{z} + \frac{i(m+V)\Delta x}{2}\frac{1+z}{z} \,,$$

and

$$n_{22} = 1 + \frac{\Delta x^2}{z}\Big[\frac{(1-z)^2}{\Delta t^2} + iV\frac{1-z^2}{\Delta t} + \frac{(m^2-V^2)(z+1)^2}{4}\Big] \,.$$

This can also be written as

$$\begin{pmatrix} u_j - u_{j-1} \\ v_j - v_{j-1} \end{pmatrix} = \underbrace{\begin{pmatrix} 0 & a \\ b & c \end{pmatrix}}_{=:\mathbf{M}} \begin{pmatrix} u_{j-1} \\ v_{j-1} \end{pmatrix} , \tag{8.52}$$

with

$$a = \frac{\Delta x}{\Delta t}\frac{1-z}{z} + \frac{i(m+V)\Delta x}{2}\frac{1+z}{z} ,$$
$$b = \frac{\Delta x}{\Delta t}(1-z) - \frac{i(m-V)\Delta x}{2}(1+z) ,$$

and $c = ab$. Solving the system Eq. (8.52) leads to

$$u_{j+1} - (2+c)u_j + u_{j-1} = 0 , \tag{8.53}$$

whose characteristic equation has the roots:

$$\tau_{1,2} = 1 + \frac{c}{2} \pm \sqrt{c + \frac{c^2}{4}}. \tag{8.54}$$

The same result is obtained for the component v. Since $\tau_1\tau_2 = 1$, there is one decaying mode (as $j \to \infty$) with $|\tau_1| \le 1$ and one increasing mode with $|\tau_2| \ge 1$. In order to have a solution in $l_2(\mathbb{Z})$ one has to choose the mode with $|\tau_1| \le 1$. At each boundary only one spinor component couples to the contact region. The spinor components u and v, respectively, only need a right and a left TBC (see Eq. (8.23) and Fig. 8.1)

$$\begin{aligned} v_0(z) &= \tau_1(z)v_1(z) \\ u_J(z) &= \tau_1(z)u_{J-1}(z) \end{aligned} \tag{8.55}$$

Then, the inverse Z-transformed boundary conditions are in the form of a convolution in the discrete time variable:

$$v_0^n = \sum_{k=0}^{n} \tau_1^{(n-k)} v_1^k . \tag{8.56}$$

$$u_J^n = \sum_{k=0}^{n} \tau_1^{(n-k)} u_{J-1}^k . \tag{8.57}$$

$\tau_1(z)$ is a non-rational function of z, hence there is no easy way of finding an analytic expression for its inverse Z-transformed in general. However,

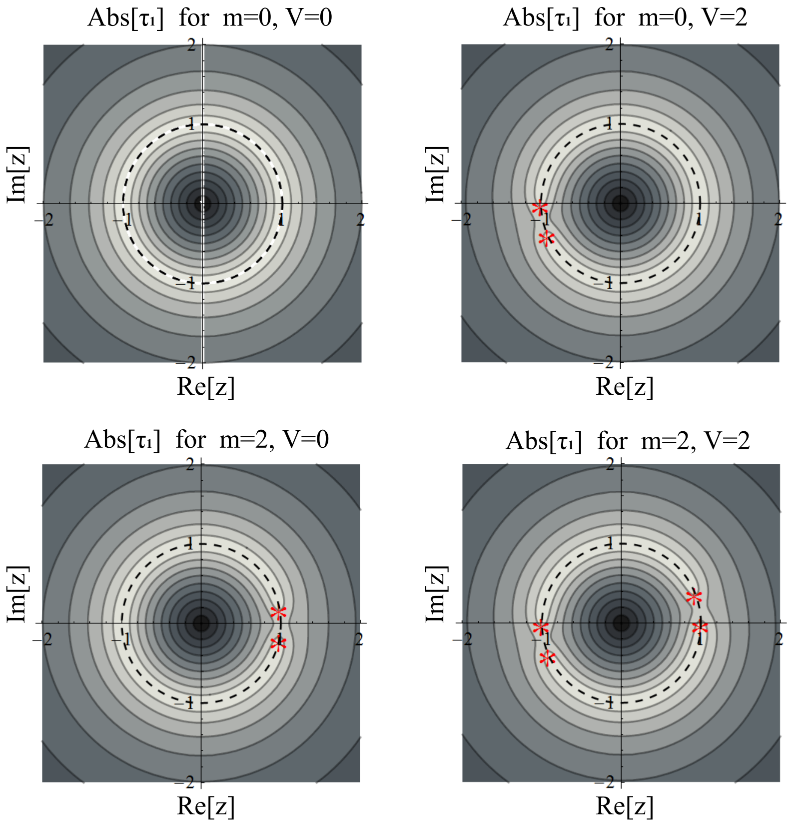

Figure 8.6: Absolute value of $\tau_1 = 1/\tau_2$ which is zero at $|z| = 0$ and $|z| = \infty$, shown for $\Delta t = \Delta x = 0.1$. The contour lines are at 0.1, 0.2, 0.3 $\ldots$ etc. The branch-point locations are marked by (red) stars.

the poles and branch-points in the z-plane, which determine the general behavior of their inverse Z-transformed in (discrete) real time n, can be identified. We give a brief discussion of these special points for $\Delta := \Delta t = \Delta x$. First, one observes that τ_1 has no poles. For the branch cuts we examine the branch points of the square root function – due to zeros of its argument. This leads to the four branch points of τ_1 (Fig. 8.6):

$$z_1 = -1\,, \quad z_2 = -\frac{4(1+iV\Delta)+(m^2-V^2)\Delta^2}{4(1-iV\Delta)+(m^2-V^2)\Delta^2} \quad \text{and} \quad z_{3,4} = \frac{2i-(V\pm m)\Delta}{2i+(V\pm m)\Delta}\,. \tag{8.58}$$

It can easily be seen that they all lie on the unit circle. These branch points induce damped oscillations in time for the convolution coefficients $\tau_1^{(n)}$. The high frequency part $(-1)^n$ of these oscillations, which arises from $z_1 = -1$, can introduce numerical problems because of subtractive cancellation. It may be advantageous to eliminate this behavior: A multiplication of τ_1(z) by $(z+1)/z$ allows one to construct new coefficients as a linear combination of the original coefficients involving the two time steps $\tilde{\tau}^{(k)} = \tau^{(k)} + \tau^{(k-1)}$ (see [34, 41]). Then (8.56) becomes

$$v_0^n = \sum_{k=0}^{n-1} \tilde{\tau}_1^{(n-k)} v_1^k - v_0^{n-1} \, ,$$

where we used $\tau_1^0 = \lim_{z\to\infty} \tau_1(z) = 0$.

For our numerical simulations, the inverse Z-transformation was carried out by performing a power series expansion about $z = 0$ using Mathematica. In Fig. 8.7 we show the convolution coefficients $\tau_1^{(n)}$ for $\Delta t = \Delta x = 0.1$ and various values of m and V. For the special case $m = V = 0$ and $r = 1$ the inverse Z-transform can be computed analytically. One gets

$$\tau_1 = \frac{1}{2}\Big(z + \frac{1}{z}\Big) - \frac{1}{2}\sqrt{\Big(z - \frac{1}{z}\Big)^2} = \ldots = \frac{1}{z} \, . \tag{8.59}$$

The convolution coefficient then simply is $\tau_1^{(n)} = \delta_1^n$, where δ_k^n is the Kronecker symbol. In the 8.6 we shall give an explicit, analytic derivation of the convolution coefficients $\tau_1^{(n)}$ in the general case.

8.4.1 Numerical examples

With the general properties of the scheme established and the associated TBCs identified, we now put it to test in challenging numerical applications.

In Fig. 8.8 we show the results of a simulation run for a Gaussian wave packet starting out with a mean value of $k = 15.92\%$ of k_{max} and a standard deviation of $\sigma_k = 1.59\%$ of k_{max}. A coarse grid $\Delta t = \Delta x = 0.05$ is used. The individual figures show the probability density $|\psi(x,t)|^2$ computed with

$$|\psi_j^n|^2 := |u_j^{n+1/2}|^2 + |v_{j+1/2}^{n+1}|^2 + \Re\Big[\big(u_{j+1}^{n+1/2} - u_j^{n+1/2}\big)\bar{v}_{j+1/2}^{n+1}\Big] \, , \tag{8.60}$$

which gives the conserved functional Eq. (12.53) when summed over j on an infinite grid. Additionally, the real part of the upper component u, and the mass-gap (= energy region between the minimum of the electron band and the maximum of the positron/hole band) is shown. One can observe that the wave packet leaves the simulation domain without reflections (the numerical error is less than machine precision = 2.2204e-16).

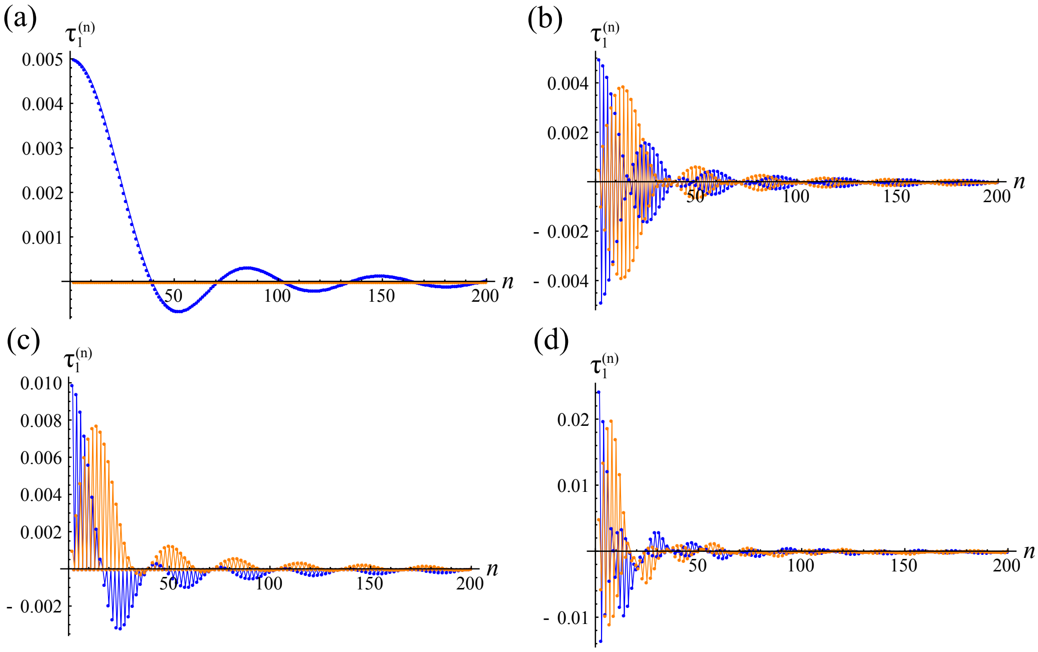

Figure 8.7: Decay of the convolution coefficients $\tau_1^{(n)}$ for different values of m and V for $\Delta t = \Delta x = 0.1$: (a) $m = 1$ and $V = 0$, (b) $m = 0$ and $V = 1$, (c) $m = 1$ and $V = 1$, (d) $m = 1$ and $V = 2$. The darker (blue) color shows the real part of the coefficients, the brighter (orange) color shows the imaginary part. The zeroth coefficient $\tau_1^{(0)}$ is always zero and is not shown in the plots. The first coefficient exceeds the plot-range and has the values: (a) $\tau_1^{(1)} = 0.9975$, (b) $\tau_1^{(1)} = 0.9925 + 0.0995i$, (c) $\tau_1^{(1)} = 0.9901 + 0.0990i$, (d) $\tau_1^{(1)} = 0.9682 + 0.1951i$.

In Fig. 8.9 the time dependence of the probability for finding the Dirac particle inside the computational interval $\|\psi(t)\|^2$ (:= Eq. (8.60) summed over j on the computational domain) is shown for this simulation.

In Fig. 8.10 we show the reflection at a mass barrier (= spatial region where the energy of the wave packet lies inside the mass-gap) with $m = 7$ and a width of 25 grid-points placed near the center of the simulation region. A variation of the mass term can be achieved for Dirac fermions on topological insulators by magnetic texturing [47, 48]. The wave packet initially has a mean value of $k = 1.59\%$ of k_{max} and a standard deviation of $\sigma_k = 1.99\%$ of k_{max}, where $\Delta t = \Delta x = 0.01$. In this tunneling problem it is of profound importance that the dispersion relation is correct also for imaginary k, which is the case for the proposed scheme already for relatively coarse grids, as illustrated in Fig. 8.2.

Fig. 8.11 shows a simulation for an initial wave packet with a mean value of $k = 27.06\%$ of k_{max} and a standard deviation of $\sigma_k = 1.99\%$ of k_{max} moving across a linear potential drop. In this process, the wave number grows beyond the maximum wave number provided by the grid k_{max}, where the wave packet is under-sampled. The propagation is still correctly described because the dispersion and therefore the group velocity is well approximated for all possible wave numbers resolved by the grid.

8.4.2 Non-compactly supported initial condition for the spinor and time-dependent exterior potential

The constraints stated at the beginning of SECTION 8.4 can be loosened:

- The DTBCs can readily be generalized to the case where the initial wave packet is not compactly supported inside the computational domain $x \in (0, L)$. The inhomogeneous boundary conditions can be derived by substituting $\boldsymbol{\psi}(x_{r,l}, t)$ with $\boldsymbol{\psi}(x_{r,l}, t) - \boldsymbol{\psi}_{in}(x_{r,l}, t)$ and carrying out the procedure as detailed in SECTION 8.4. Here, $\boldsymbol{\psi} - \boldsymbol{\psi}_{in}$ should initially have compact support in $(0, L)$. And $\boldsymbol{\psi}_{in}$ should be a solution to the discrete exterior domain problem, e.g. a *discrete* plain wave (see [44] for details in the analogous Schrödinger case). Re-substitution afterwards leads to the result

$$u_J^n = \sum_{k=0}^{n} \left(\tau_1^{(n-k)} u_{J-1}^k \right) + u_{J,in}^n \,, \tag{8.61}$$

$$v_0^n = \sum_{k=0}^{n} \left(\tau_1^{(n-k)} v_1^k \right) + v_{0,in}^n \,. \tag{8.62}$$

  The rationale is that the Dirac equation is a linear differential equation which here is approximated by a linear finite difference scheme. Therefore one may simply add inhomogeneous boundary terms via the superposition principle.

- The scalar potential $V(t)$ on the exterior domain may depend on time. This is useful when considering a time-dependent net potential drop across the system. As for the case of the Schrödinger equation a time-dependent exterior potential, e.g. at the right boundary, can be incorporated by treating it in the interaction picture which removes $V(t)$ from the Hamiltonian and leads to a gauge (phase change) for the spinor Eq. (8.2) [41].

8.5 Conclusions and future work

In this paper we have presented a finite difference scheme for the numerical solution of the time-dependent Dirac equation in (1+1)D, allowing fully time- and space-dependent mass and potential terms. Owing to a combined staggering of the grid both in space and time, unphysical additional Dirac cones are avoided and, for the special case of the Weyl equation, the linear dispersion is preserved exactly for all wave numbers supported by the grid. In the case of finite mass and/or potential terms the dispersion relation improves for all wave numbers, approaching the continuum dispersion relation exactly, when the grid is refined. This is a relevant feature when modeling Dirac fermions on a lattice, such as Dirac fermions propagating on topological insulator surfaces, graphen, or in quantum spin Hall states. The electromagnetic potentials accounting for an external electromagnetic field are included in gauge invariant fashion. A stability analysis of the scheme was performed and a functional, exactly conserved by the scheme, was identified. It provides a valid norm for the spinor on the proposed staggered grid.

Furthermore, we have derived exact DTBCs to close the finite difference scheme for constant mass and potential in the boundary regions. With these BCs one is in the position to deal with particle transport scenarios and to account for the multi-band nature of the Dirac equation which may cause inter-band transfer rather than quantum confinement. For completeness, DTBCs were also derived for the (1+1) Dirac (differential) equation in Schrödinger form.

Using the norm for a measure, numerical simulations of Gaussian wave packets show them leaving the computational domain without reflections (with an error below computer precision), thus verifying the quality of the DTBCs numerically. The importance of a faithful representation of the energy-momentum dispersion relation, in particular, avoiding fermion doubling, is exemplified in numerical simulations.

The assumptions of constant mass and potential on the exterior domain can be loosened. It is however desirable that an analytic solution on the discrete exterior domain can be found. The case of purely time-dependent exterior potential can be treated by using a proper phase change of the spinor. Initial conditions for which the initial wave packet is not compactly supported on the computational domain can be handled as well, leading to inhomogeneous terms in the boundary conditions. There are various ways to extend the proposed leap-frog scheme to the (2+1)D Dirac equation where it retains many of its attractive features [45, 46, 49]. The formulation of DT-

BCs for the (2+1)D Dirac equation in the spirit of this paper is the subject of future work [49].

In view of existing work on non-linear versions of the Dirac equation accounting, for example, for self-interaction corrections in a single equation, we wish to point out that a self-consistent treatment of such effects can be treated readily (and in more generality) within the present approach based on the standard Dirac equation and a parallel self-consistent update of the effective electromagnetic potentials. In a semi-classical picture, for example, the latter may be accomplished within Maxwell's theory for the electromagnetic potentials [53]. In this fashion, a self-consistent open-boundary treatment of the Schrödinger equation was performed whereby, instead of the nonlinear Hartree term, equivalently the Poisson equation was solved in parallel [35]. Any nonlinearity arising from the (classical) electromagnetic interaction can readily be treated within this approach and its advantages be exploited, as long as the conditions on the asymptotic regions made for the linear Dirac equation can be met. This is the case, for example, when nonlinear effects are confined to the simulation region and/or nonlinear effects in the outer regions can be accounted for by constant electromagnetic potential and mass terms. Clearly, the direct use of non-linear versions of the Dirac equation requires the use of individually matched transparent boundary conditions, as for the case of the Schrödinger equation [41].

Acknowledgments

We thank B. A. Stickler and C. Ertler for stimulating discussions.
We also gratefully acknowledge funding by the Austrian Science Foundation under project I395-N16.

8.6 APPENDIX A: Analytic derivation of the convolution coefficients $\tau_1^{(n)}$ for the general case

We shall first consider the case $m = V = 0$ where (8.54) reads

$$\tau_1(z) = 1 + \frac{1}{2r^2 z}(z-1)^2 - \frac{z-1}{2r^2 z}\sqrt{z^2 - 2\mu z + 1}\,,$$

with $\mu := 1 - 2r^2$. Here, the branch of the square root is chosen such that $\tau_1(z) = \mathcal{O}(|z|^{-1})$ as $z \to \infty$. Using

$$Z^{-1}\left\{\frac{\sqrt{z^2-2\mu z+1}}{z}\right\} = P_{n-2}(\mu)-2\mu P_{n-1}(\mu)+P_n(\mu) = \frac{1}{n}[P_{n-2}(\mu)-\mu P_{n-1}(\mu)]\,, \tag{8.63}$$

where P_n denotes the Legendre polynomials (with the convention $P_{-1} = P_{-2} := 0$), we obtain

$$\tau_1^{(n)} = (1-\frac{1}{r^2})\delta_0^n+\frac{1}{2r^2}\delta_1^n-\frac{1}{2r^2}\Big[P_{n+1}(\mu)-(2\mu+1)(P_n(\mu)-P_{n-1}(\mu))-P_{n-2}(\mu)\Big],$$

and

$$n \geq 0\,.$$

And this simplifies to $\tau_1^{(n)} = \delta_1^n$ for $r = 1$.

Next we shall discuss the general case with $m,\, V \in \mathbb{R}$. Here we have

$$\tau_1(z) = 1 + \frac{\tilde{c}}{2z} - \frac{1}{2z}\sqrt{\tilde{c}}\sqrt{\tilde{c}+4z}\,,$$

where $\tilde{c}(z) := z\,c(z) = \alpha z^2+\beta z+\gamma$ is a quadratic polynomial given by (8.52). Using again (8.63), both square root factors can be inverse Z-transformed. And the explicit formula for the coefficients $\tau_1^{(n)}$ would then involve a discrete convolution.

But we shall proceed differently here and rather derive a recursion relation for $\tau_1^{(n)}$ (similar as in §3 of [50]). A lengthy, but straightforward computation shows that $\hat{\tau}_1(z) := z\,\tau_1(z)$ satisfies the inhomogeneous differential equation

$$\tilde{c}(\tilde{c}+4z)\,\hat{\tau}_1'-[2\alpha^2z^3+3\alpha(\beta+2)z^2+(\beta^2+4\beta+2\alpha\gamma)z+(\beta+2)\gamma]\,\hat{\tau}_1 = 2z(\gamma-\alpha z^2)\,. \tag{8.64}$$

Since all coefficients in (8.64) are polynomials we shall use the Laurent series of $\hat{\tau}_1$, i.e. $\hat{\tau}_1 = \sum_{n=0}^{\infty} s^{(n)}z^{-n}$, with $\tau_1^{(n)} = s^{(n-1)}$. A comparison of the coefficients then yields:

$$s^{(0)} = \frac{1}{\alpha}, \quad s^{(1)} = -\frac{\beta+2}{\alpha^2}, \quad s^{(2)} = \frac{\beta^2+4\beta+5-\alpha\gamma}{\alpha^3}\,,$$

and the exact recursion

$$(n+5)\alpha^2 s^{(n+3)} + (2n+7)\alpha(\beta+2)s^{(n+2)} + (n+2)(\beta^2+4\beta+2\alpha\gamma)s^{(n+1)}$$
$$+(2n+1)(\beta+2)\gamma s^{(n)} + (n-1)\gamma^2 s^{(n-1)} = 0\,,$$

for $n \geq 0$ with the convention $s^{(-1)} := 0$.

8.7 APPENDIX B: Gauge-invariant introduction of the electromagnetic vector potential

Dirac equation Eq. (8.1) sofar has been written for a charged massive particle in a scalar potential. For a general account of external electromagnetic fields and/or self-interaction both scalar and vector potential are needed. A gauge invariant introduction of the electromagnetic vector potential $A(x,t)$ is executed by replacing the complex 2-spinor $\boldsymbol{\psi} = \begin{pmatrix} u(x,t) \\ v(x,t) \end{pmatrix}$ in Eq. (8.1) by $\boldsymbol{\psi}(x,t)\exp\{-ia(x,t)\} = \begin{pmatrix} u(x,t)\exp\{-ia(x,t)\} \\ v(x,t)\exp\{-ia(x,t)\} \end{pmatrix}$, with[51, 52]

$$a(x,t) := \frac{q}{\hbar c}\int_{x_o}^{x} dy A(y,t)\ .$$

Position x_o is arbitrary but constant. Under this Peierls substitution the canonical momentum $p := \frac{\hbar}{i}\frac{\partial}{\partial x}$ in Eq. (8.1) is replaced by the kinetic momentum $p - \frac{q}{c}A(x,t) = \frac{\hbar}{i}\frac{\partial}{\partial x} - \frac{q}{c}A(x,t)$. Under local gauge transformation $A(x,t) \to A(x,t) + \frac{\partial}{\partial x}\Lambda(x,t)$, $\Phi(x,t) \to \Phi(x,t) - \frac{\partial}{c\partial t}\Lambda(x,t)$, the spinor acquires the phase factor $\exp\{-i\frac{q}{\hbar c}\left(\Lambda(x,t) - \Lambda(x_o,t)\right)\}$, and the electromagnetic fields E and B remain invariant.

Here it should be pointed out that in a (1+1)D model, orbital forces are confined to one spatial direction (i.e., x), while non-vanishing torque on the spin degree of freedom (in a Larmor term) arising from $A_x(x,t) = A(x,t)$ requires a non-vanishing B field component in the plane orthogonal to x. Note, however, that the two-component nature of an effective Dirac model may not arise from the spin degree of freedom. Most notable example in 2+1D is graphene [3]. This shows that the physical interpretation of the effective Dirac equation and the way an electromagnetic field couples to the system is determined by the underlying basic theory.

We now discuss the consequences of the Peierls substitution on the leap-frog scheme Eqs. (8.20) and (8.21). Again, we have $V(x,t) = -\Phi(x,t)$, and for any grid point x_j, t_n we define $a_j^n := a(x_j,t_n)$. The leap-frog scheme for non-zero vector potential is obtained by the substitution

$$\begin{aligned} u_j^{n-1/2} &\to \hat{u}_j^{n-1/2} := u_j^{n-1/2}\exp\{-ia_j^{n-1/2}\}\ , \\ v_{j-1/2}^{n} &\to \hat{v}_{j-1/2}^{n} := v_{j-1/2}^{n}\exp\{-ia_{j-1/2}^{n}\}\ . \end{aligned} \tag{8.65}$$

Likewise, the stability analysis for zero vector potential detailed above can immediately be extended to the case of a non-vanishing vector potential by the substitution Eq. (8.65) and noting that the vector potential $A(x,t)$ is real valued. Hence, a strictly conserved functional $\hat{E}_r^n$ is identified by this substitution applied to the expression for E_r^n in Eq. (8.42) for arbitrary time t and space x dependent $m, V, A \in \mathbb{R}$. It follows that the scheme remains stable for all $r = \Delta t/\Delta x \leq 1$.

Expressed in terms of spinor components u and v the scheme in presence of an external electromagnetic potential takes the form

$$\begin{align}
& f^+(a_j^{n+1/2}, a_j^{n-1/2})\Bigg[\frac{u_j^{n+1/2} - u_j^{n-1/2}}{\Delta t} \tag{8.66}\\
& + i\left(m_j^n - V_j^n - \frac{a_j^{n+1/2} - a_j^{n-1/2}}{\Delta t}\right)\frac{u_j^{n+1/2} + u_j^{n-1/2}}{2}\Bigg] \nonumber\\
& + i f^-(a_j^{n+1/2}, a_j^{n-1/2})(m_j^n - V_j^n)\frac{u_j^{n+1/2} - u_j^{n-1/2}}{2} \nonumber\\
& + f^+(a_{j+1/2}^n, a_{j-1/2}^n)\left[\frac{(Dv^n)_j}{\Delta x} - i\frac{a_{j+1/2}^n - a_{j-1/2}^n}{\Delta x}\frac{v_{j+1/2}^n + v_{j-1/2}^n}{2}\right] = 0\ , \tag{8.67}
\end{align}$$

$$\begin{align}
& f^+(a_{j-1/2}^{n+1}, a_{j-1/2}^n)\Bigg[\frac{v_{j-1/2}^{n+1} - v_{j-1/2}^n}{\Delta t} \tag{8.68}\\
& - i(m_{j-1/2}^{n+1/2} + V_{j-1/2}^{n+1/2} + \frac{a_{j-1/2}^{n+1} - a_{j-1/2}^n}{\Delta t})\frac{v_{j-1/2}^{n+1} + v_{j-1/2}^n}{2}\Bigg] \nonumber\\
& - i f^-(a_{j-1/2}^{n+1}, a_{j-1/2}^n)(m_{j-1/2}^{n+1/2} + V_{j-1/2}^{n+1/2})\frac{v_{j-1/2}^{n+1} - v_{j-1/2}^n}{2} \nonumber\\
& + f^+(a_j^{n+1/2}, a_{j-1}^{n+1/2})\left[\frac{(Du^{n+1/2})_{j-1/2}}{\Delta x} - i\frac{a_j^{n+1/2} - a_{j-1}^{n+1/2}}{\Delta x}\frac{u_j^{n+1/2} + u_{j-1}^{n+1/2}}{2}\right] = 0\ . \tag{8.69}
\end{align}$$

Here we have used the definition $f^{\pm}(a_1, a_2) := (e^{-ia_1} \pm e^{-ia_2})/2$. As in the main text, we set $c = \hbar = 1 = -q$. For slowly varying vector potential (or within first order in Δt) one may approximate these equations by

$$\frac{u_j^{n+1/2} - u_j^{n-1/2}}{\Delta t} + i(m_j^n - \hat{V}_j^n)\frac{u_j^{n+1/2} + u_j^{n-1/2}}{2} \\ + \left[\frac{(Dv^n)_j}{\Delta x} + iA_j^n \frac{v_{j+1/2}^n + v_{j-1/2}^n}{2}\right] = 0\ , \tag{8.70}$$

$$\frac{v_{j-1/2}^{n+1} - v_{j-1/2}^n}{\Delta t} - i(m_{j-1/2}^{n+1/2} + \hat{V}_{j-1/2}^{n+1/2})\frac{v_{j-1/2}^{n+1} + v_{j-1/2}^n}{2} \\ + \left[\frac{(Du^{n+1/2})_{j-1/2}}{\Delta x} + iA_{j-1/2}^{n+1/2} \frac{u_j^{n+1/2} + u_{j-1}^{n+1/2}}{2}\right] = 0\ . \tag{8.71}$$

Here we have used the following abbreviations on the two sub-lattices: $\hat{V}_j^n := V_j^n + \frac{a_j^{n+1/2} - a_j^{n-1/2}}{\Delta t}$ and $\hat{V}_{j-1/2}^{n+1/2} = V_{j-1/2}^{n+1/2} + \frac{a_{j-1/2}^{n+1} - a_{j-1/2}^n}{\Delta t}$ denote the net scalar potential associated with the E field after introduction of the vector potential, and $A_j^n = \frac{a_{j-1/2}^n - a_{j+1/2}^n}{\Delta x}$ and $A_{j-1/2}^{n+1/2} = \frac{a_{j-1}^{n+1/2} - a_j^{n+1/2}}{\Delta x}$ are the vector potential, as defined by symmetric spatial derivatives of $a(x,t)$. Note that we use $q = -1$.

The approximate scheme (8.70) and (8.71) may have been guessed directly by inspection of Eqs. (8.20) and (8.21). Going the present way, however, not only has given the way for precise implementation of the vector potential into the latter but also has taken care of the stability analysis for this general case. Finding an exactly conserved functional for the approximate scheme is complicated by the fact that the vector potential leads to additional coupling between the spinor components u and v.

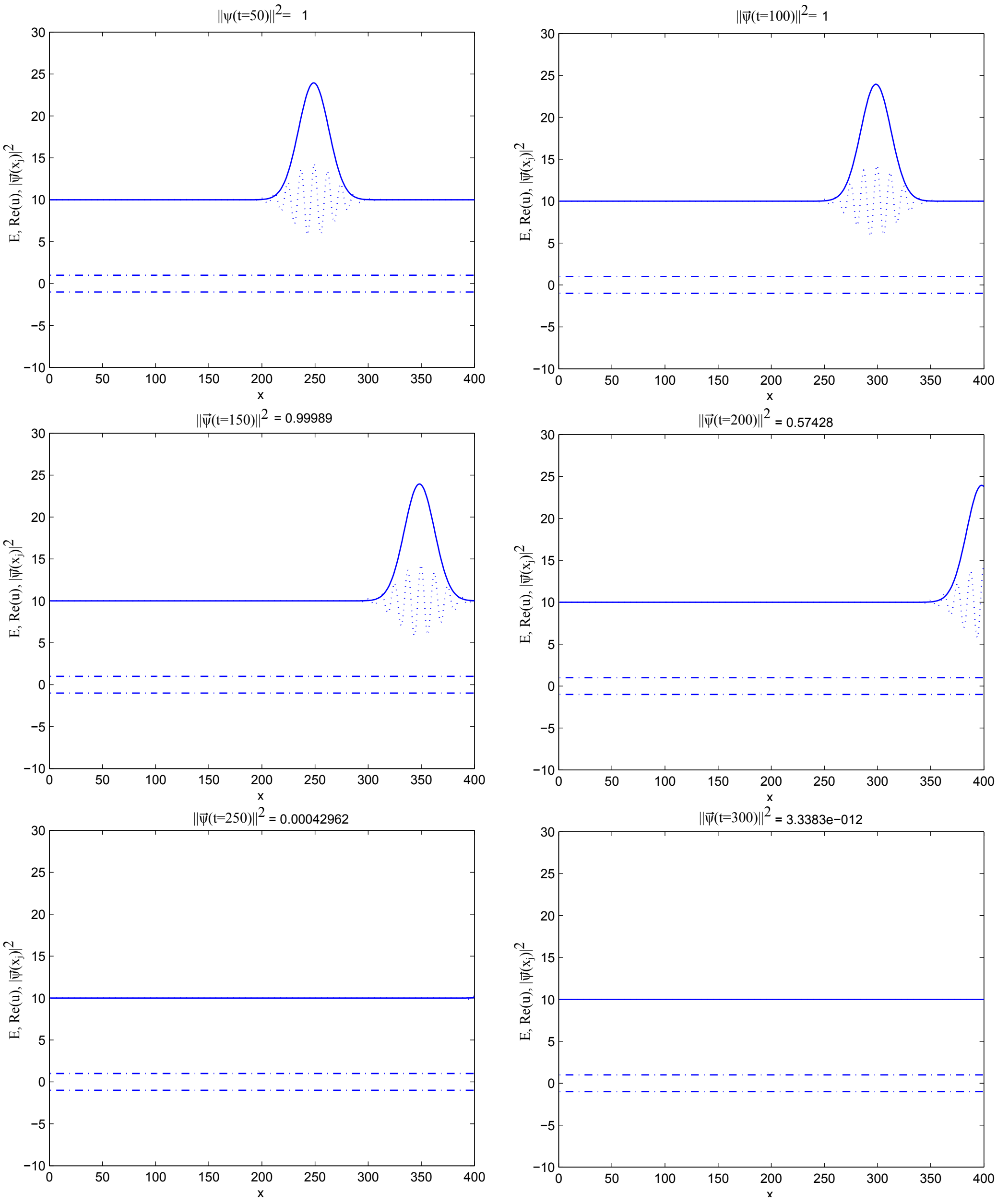

Figure 8.8: Simulation run for a coarse grid $\Delta t = \Delta x = 0.05$ and an initial Gaussian wave packet with a mean value of $k = 15.92\%$ of k_{max} and a standard deviation of $\sigma_k = 1.59\%$ of k_{max}. The figures show the probability density $|\psi(x)|^2$ (solid lines), the real part of the upper component u (dotted lines), and the mass-gap (point-dotted lines). The zero line on the vertical axis is shifted by 10, which is the mean energy of the wave packet. With time evolving, the probability $\|\psi\|^2$ for finding the particle in the computational domain approaches zero because the wave packet leaves the domain without reflection.

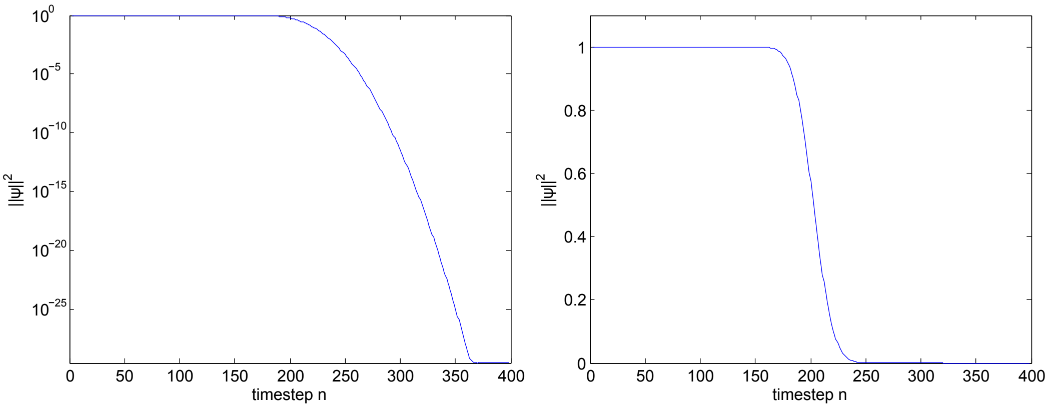

Figure 8.9: Time dependence of the spinor norm $\|\boldsymbol{\psi}(t)\|$ of the simulation run shown in Fig. 8.8: logarithmic scale (left) and linear scale (right).

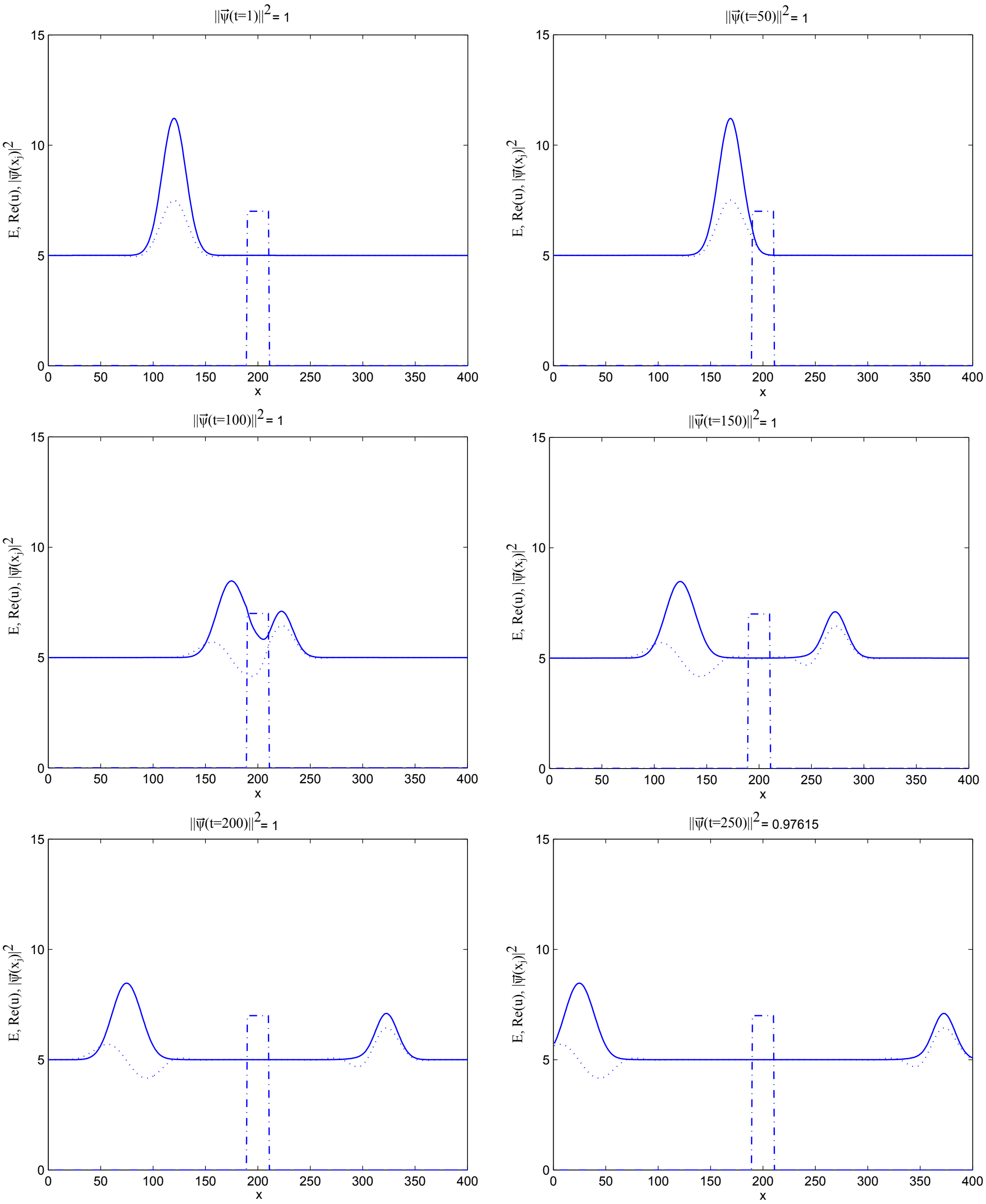

Figure 8.10: Reflection at a mass barrier with a width of 25 grid-points and a height of $m = 7$. $\Delta t = \Delta x = 0.01$, the initial Gaussian wave packet has a mean value of $k = 1.59\%$ of k_{max} and a standard deviation of $\sigma_k = 1.99\%$ of k_{max}. The individual figures show the probability density $|\psi(x)|^2$ (solid lines), the real part of the upper component u (dotted lines), and the mass (dash-dotted lines). The zero for the vertical axis is shifted by 5, which corresponds to the mean energy of the initial wave packet.

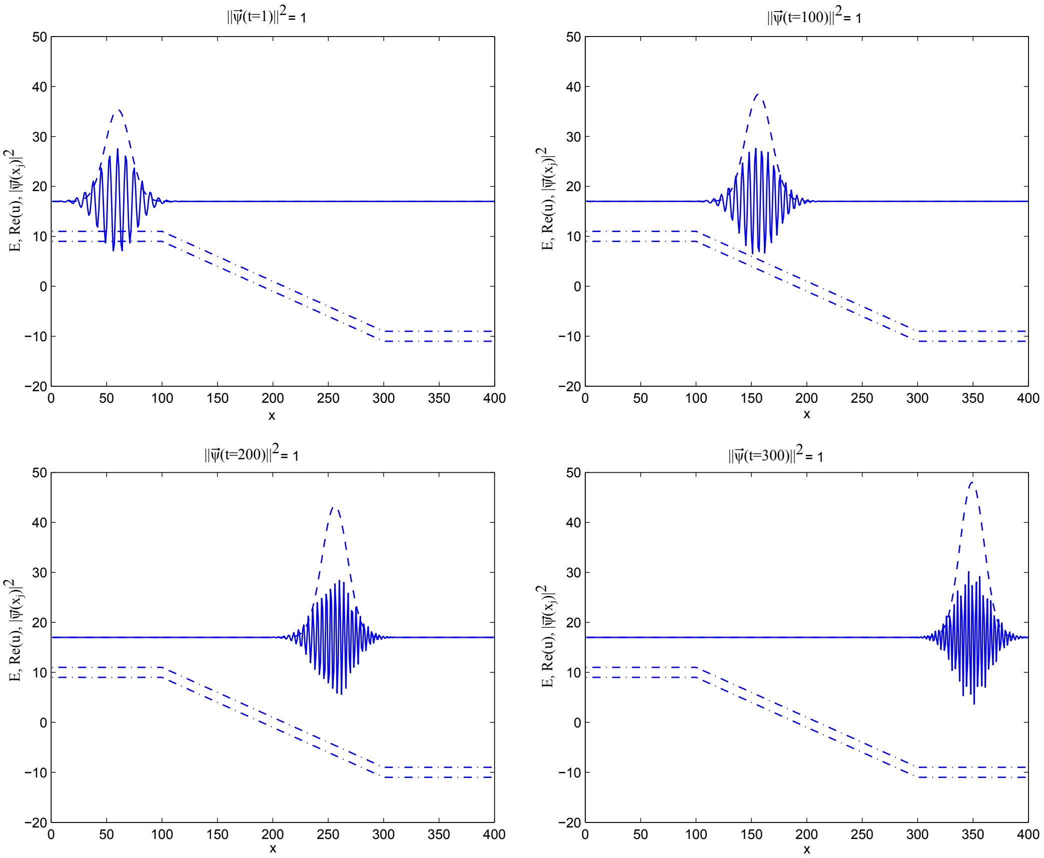

Figure 8.11: Initial Gaussian wave packet with a mean value of $k = 27.06\%$ of k_{max} and a standart deviation of $\sigma_k = 1.99\%$ of k_{max} meeting a linear potential. A rather coarse grid $\Delta t = \Delta x = 0.05$ is used. The figures show the probability density $|\psi(x)|^2$ as dashed line, the real part of the upper component u as solid line, and the mass-gap as dash-dotted lines. The zero line is shifted by 17 which is the value for the mean energy of the wave packet.

REFERENCES

[1] W. Greiner, Relativistic quantum mechanics: wave equations, 3rd ed., Springer Berlin (2000).

[2] B. Thaller, The Dirac Equation, Springer Berlin (1992).

[3] A. H. Castro-Neto, F. Guinea, N. M. R. Peres, K. S. Novoselov and A. K. Geim, The electronic properties of graphene, Reviews of Modern Physics 81 (2009) 109-162.

[4] B. A. Bernevig, T. L. Hughes, and S. C. Zhang, Quantum Spin Hall Effect and Topological Phase Transition in HgTe Quantum Wells, Science 314 (2006) 1757-1761.

[5] X. L. Qi and S. C. Zhang, Topological insulators and superconductors, Reviews of Modern Physics 83 (2011) 1057-1110.

[6] L. Lamata, J. Casanova, R. Gerritsma, C. F. Roos, J. J. García-Ripoll and E. Solano, Relativistic quantum mechanics with trapped ions, New Journal of Physics 13 (2011) 1367-2630.

[7] D. Witthaut, T. Salger, S. Kling, C. Crossert and M. Weitz, Effective Dirac dynamics of ultracold atoms in bichromatic optical lattices, Physical Review A 84 (2011) 033601.

[8] N. Szpak and R. Schützhold, Optical lattice quantum simulator for quantum electrodynamics in strong external fields: spontaneous pair creation and the Sauter-Schwinger effect, New Journal of Physics 14 (2012) 035001.

[9] L. H. Ryder, Quantum field theory, 2nd ed., University Press Cambridge (1996).

[10] B. Thaller, Advanced Visual Quantum Mechanics, Springer New York (2005).

[11] O. Busic, N. Grün, and W. Scheid, A new treatment of the fermion doubling problem, Physics Letters A 254 (1999) 337-340.

[12] R. Stacey, Eliminating lattice fermion doubling, Physical Review D 26, (1982) 468-472.

[13] J. Tworzydlo, C. W. Groth, and C. W. J. Beenakker, Finite difference method for transport properties of massless Dirac fermions, Physical Review B 78 (2008) 235438.

[14] C. Müller, N. Grün, and W. Scheid, Finite element formulation of the Dirac equation and the problem of fermion doubling, Physics Letters A 242 (1998) 245-250.

[15] K. Momberger and A. Belkacem, Numerical treatment of the time-dependent Dirac equation in momentum space for atomic processes in relativistic heavy-ion collisions, Physical Review A 53 (1996) 1605-1622.

[16] J. W. Braun, Q. Su, and R. Grobe, Numerical approach to solve the time-dependent Dirac equation, Physical Review A 59 (1999) 604-612.

[17] G. R. Mocken and C. H. Keitel, Quantum dynamics of relativistic electrons, Journal of Computational Physics 199 (2004) 558-588.

[18] F. Fillion-Gourdeau, E. Lorin, and A. D. Bandrauk, Numerical Solution of the Time-Dependent Dirac Equation in Coordinate Space without Fermion-Doubling, Comp. Phys. Comm. 183 (2012) 1403-1415.

[19] H. B. Nielsen and M. Ninomiya, A no-go theorem for regularizing chiral fermions, Physics Letters B 105 (1981) 219-223.

[20] J. Xu, S. Shao, and H. Tang, Numerical methods for non-linear Dirac equation, J. Comp. Phys. 245 (2013) 131-149.

[21] M. Soler, Classical, stable, nonlinear spinor field with positive rest energy, Phys. Rev. D (1970) 2766-2769.

[22] S. Coleman, Quantum sine-Gordon equation as the massive Thirring model, Phys. Rev. D 11 (1975) 2088-2097.

[23] A. Alvarez and B. Carreras, Interaction dynamics for the solitary waves of a nonlinear Diracmode, Physics Letters 86A (1981) 327-332.

[24] A. Alvarez, P.Y. Kuo, L. Vázquez, The numerical study of a nonlinear one-dimensional Dirac equation, Appl. Math. Comput. 13 (1983) 1-15.

[25] A. Alvarez, Linearized Crank-Nicholson scheme for nonlinear Dirac equations, J. Comp. Phys. 99 (1992) 348-350.

[26] P. Gordon, Nonsymmetric difference equations, SIAM J. Appl. Math. 13 (1965) 667-673.

[27] J. De Frutos, J. M. Sanz-Serna, Split-step spectral schemes for nonlinear Dirac systems, J. Comput. Phys. 83 (1983) 407-423.

[28] Z. q: Wang, B. Y. Guo, Modified Legendre rational spectral method for the whole line, J. Comput. Math. 22 (2004) 457-474.

[29] J. L. Hong, C. Li, Multi-symplectic Runge-Kutta methods for nonlinear Dirac equations, J. Comput. Phys. 211 (2006) 448-472.

[30] S. H. Shao, H. Z. Tang, Higher-order accurate Runge-Kutta discontinuous Galerkin methods for a nonlinear Dirac model, Discrete Cont. Dyn. Syst. B 6, (2006) 623-640.

[31] H. Wang, H. Tang, An efficient adaptive mesh redistribution method for a nonlinear Dirac equation, Journal of Computational Physics 222 (2007) 176-193.

[32] V. A. Baskakov and A.V. Popov, Implementation of transparent boundaries for numerical solution of the Schrödinger equation, Wave Motion 14 (1991) 123-128.

[33] B. Mayfield, University of Rhode Island, Providence, Ph.D. thesis (1989).

[34] A. Arnold, M. Ehrhardt, and I. Sofronov, Discrete transparent boundary conditions for the Schrödinger equation: fast calculation, approximation, and stability, Communications in Mathematical Sciences 1 (2003) 501-556.

[35] M. A. Talebian and W. Pötz, Open boundary conditions for a time-dependent analysis of the resonant tunneling structure, Applied Physics Letters 69 (1996) 1148-1150.

[36] W. Pötz, Scattering theory for mesoscopic quantum systems with non-trivial spatial asymptotics in one dimension, Journal of Mathematical Physics 36 (1995) 1707.

[37] A. Zisowsky, A. Arnold, M. Ehrhardt, and T. Koprucki, Discrete transparent boundary conditions for transient kp-Schrödinger equations with application to quantum heterostructures, Journal of Applied Mathematics and Mechanics 11 (2005) 793-805.

[38] I. Alonso-Mallo and N. Reguera, Weak Ill-Posedness of Spatial Discretizations of Absorbing Boundary Conditions for Schrödinger-Type Equations, SIAM Journal on Numerical Analysis 40 (2002) 134-158.

[39] C. Lubich and A. Schädle, Fast Convolution for Nonreflecting Boundary Conditions, SIAM Journal on Scientific Computing 24 (2002) 161-182.

[40] C. W. Rowley and T. Colonius, Discretely Nonreflecting Boundary Conditions for Linear Hyperbolic Systems, Journal of Computational Physics 157 (2000) 500-538.

[41] X. Antoine, A. Arnold, C. Besse, M. Ehrhardt, and A. Schädle, A Review of Transparent and Artificial Boundary Conditions Techniques for Linear and Nonlinear Schröodinger Equations, Communications in Computational Physics 4 (2008) 729-796.

[42] E. Hairer, C. Lubich, and G. Wanner, Geometric numerical integration illustrated by the Störmer/Verlet method, Acta Numerica 12 (2003) 399-450.

[43] A. Borzì and E. Decker, Analysis of a leap-frog pseudospectral scheme for the Schrödinger equation, Journal of Computational and Applied Mathematics 193 (2006) 65-88.

[44] A. Arnold, Mathematical concepts of open quantum boundary conditions, Transp. Theory Stat. Phys. 30/4-6 (2001) 561-584.

[45] R. Hammer and W. Pötz, Staggered-grid leap-frog scheme for the (2+1)D Dirac equation, accepted in Computer Physics Communications, http://dx.doi.org/10.1016/j.cpc.2013.08.013

[46] R. Hammer, C. Ertler, and W. Pötz, Dirac fermion wave guide networks on topological insulator surfaces, arXiv:1205.6941 (2012).

[47] R. Hammer, C. Ertler, and W. Pötz, Solitonic Dirac fermion wave guide networks on topological insulator surfaces, Appl. Phys. Lett. 102, (2013) 193514-1 - 193514-4.

[48] R. Hammer and W. Pötz, Dynamics of domain-wall Dirac fermions on a topological insulator: a chiral fermion beam splitter, arXiv:1306.6139

[49] A manuscript showing the extension of the (1+1)D scheme to a (2+1)D scheme which conserves the monotone dispersion relation (= having a single Dirac cone) is in preparation.

[50] M. Ehrhardt and A. Arnold, Discrete Transparent Boundary Conditions for the Schrödinger Equation, Revista di Matematica della Universita di Parma 6/4 (2001) 57-108.

[51] R. Peierls, Zur theorie des diamagnetismus von leitungselektronen, Z. Phys. 80 (1933) 763-791.

[52] M. Graf and P. Vogl, Electromagnetic fields and dielectric response in empirical tight-binding theory, Phys. Rev. B 51 (1995) 4940-4949, and references therein.

[53] J.D. Jackson, Classical Electrodynamics, 2nd edition (Wiley, New York, 1975).

Chapter 9

PAPER REPRINT: STAGGERED GRID LEAP-FROG SCHEME FOR THE (2+1)D DIRAC EQUATION

Computer Physics Communications
(in press)
http://dx.doi.org/10.1016/j.cpc.2013.08.013

R. Hammer and W. Pötz

A numerical scheme utilizing a grid which is staggered in both space and time is proposed for the numerical solution of the (2+1)D Dirac equation in presence of an external electromagnetic potential. It preserves the linear dispersion relation of the free Weyl equation for wave vectors aligned with the grid and facilitates the implementation of open (absorbing) boundary conditions via an imaginary potential term. This explicit scheme has second order accuracy in space and time. A functional for the norm is derived and shown to be conserved. Stability conditions are derived. Several numerical examples, ranging from generic to specific to textured topological insulator surfaces, demonstrate the properties of the scheme which can handle general electromagnetic potential landscapes.

9.1 Introduction

Ever since its presentation by P.A.M. Dirac in 1928, the Dirac equation has played a central role in the development of modern physics [1]. It has lead not only to the prediction and observation of antimatter but has also been instrumental to the development of modern many-body physics [1, 2, 3, 37]. Known as the Weyl equation for zero mass, it has been of relevance to early neutrino physics [35]. While its initial applications naturally were devoted mainly to high-energy elementary particle physics, it has been known for quite a while that touching energy bands in crystalline solids also can lead to a Dirac-fermion-like energy dispersion [4, 5]. This can readily be seen for a Schrödinger particle in a one-dimensional (1D) periodic potential: Since the spectrum for Bloch solutions has degeneracy two at most, energy bands cannot overlap. If they touch, they must have linear dispersion near the point of contact [6]. A prominent example for such a situation is graphene, which has regained great publicity due to its recent experimental realization [7, 8]. For this 2D system, the Brillouin zone features 4 (counting spin) Dirac cones with a small gap due to the spin-orbit interaction. Odd numbers of Dirac cones have been predicted and experimentally verified on individual surfaces of topological insulators (TIs) [9, 10, 11, 12, 13, 14]. In the simplest case, a single Dirac cone of topologically protected metallic surface states can occur on one side of a TI.

In a condensed matter environment, effective 2D model systems for our 3D world frequently emerge in the low energy limit. The synthesization of nano-structured materials has led to a number of systems in which electron motion in one spatial dimension is confined to within a few atomic layers but essentially free (quasi-particle) motion over macroscopic length scales occurs in the other two dimensions. Celebrated examples for such genuine (2+1)D systems are the 2DEG and graphene [8]. Layered high-T_c systems may be seen as an example in the wider sense [15]. Optical lattices also constitute a rich play ground for the engineering of 2D physics with the possibility of tuning various parameters and therewith controlling atom localization and effective many-body interactions [17, 18, 19]. Surfaces of solids in general provide a natural environment for the study of (quasi-) 2D phenomena, with a remarkable recent example provided by the topologically protected 2D metallic surface states of TIs. Their intrinsically gap-less energy spectrum can be manipulated by perturbations which break time-reversal symmetry to introduce an energy gap (mass term). Electromagnetic texturing can provide a landscape of electric potential and effective mass, taking positive and negative values, potentially leading to protected

1D chiral channel states [16, 9, 20, 21].

A theoretical analysis of the rich dynamics of Dirac fermion quasiparticles in (2+1)D requires reliable numerical methods which can handle position- and time- dependent potential and mass landscapes. Existing methods are the real-space schemes, such as the finite-difference and finite-element methods [22, 23, 27]. Momentum-space spectral methods and split-operator methods have been developed also [28, 29, 30, 31]. While finite-difference and finite-element schemes allow for an easy implementation of non-constant coefficients they have to deal with the fermion doubling problem. This is expressed in the Nielsen-Ninomiya no-go theorem which forbids a single minimum in the energy dispersion of a Dirac-type equation on a regular grid without breaking either Hermiticity, translational invariance, or locality [32]. Elimination of fermion doubling by means of a nonlocal approximation for the spatial derivative operator has been introduced by Stacey [23] and implemented numerically for a stationary problem [33]. Fermion doubling can also be avoided by split-operator methods [30]. A scheme with a non-monotonic dispersion relation does not have to be ruled out for numerical studies, but, the latter can severely constrain its useful domain of wave numbers in momentum space and may require a very fine grid in real space. Here we will present an easy-to-implement, explicit, finite-difference method which preserves the zero-mass free Dirac-dispersion of the continuum problem along the main axes of the grid and provides only one extra Dirac cone at the corners of the first Brillouin zone. This scheme is especially well-suited for long-time propagation studies where the occurring wave vectors mostly are aligned parallel to the grid as envisioned, for example, in Dirac fermion wave guides [21]. Details of the numerical approach and the properties of this scheme are discussed in Sec. 9.2. Numerical examples for the free particle propagation, the Klein step, and basic domain wall structures are given in Sect. 9.3. Summary and conclusions can be found in Sects. 9.4 and 9.5. Further details are given in the appendix.

9.2 The numerical approach

The generic (2+1)D Dirac equation in normalized units (velocity $c = 1$, Planck's constant $\hbar = 1$, elementary charge $e = 1$) in Schrödinger form may be written as

$$i\partial_t \boldsymbol{\psi}(x,y,t) = \hat{H}\boldsymbol{\psi}(x,y,t) \,, \tag{9.1}$$

where $\boldsymbol{\psi}(x,y,t) \in \mathbb{C}^2$ is a 2-component spinor and the Hamiltonian is of the form

$$\hat{H} = \sigma_x p_x + \sigma_y p_y + \boldsymbol{\sigma} \cdot \mathbf{m}(x,y,t) + V(x,y,t) \,, \tag{9.2}$$

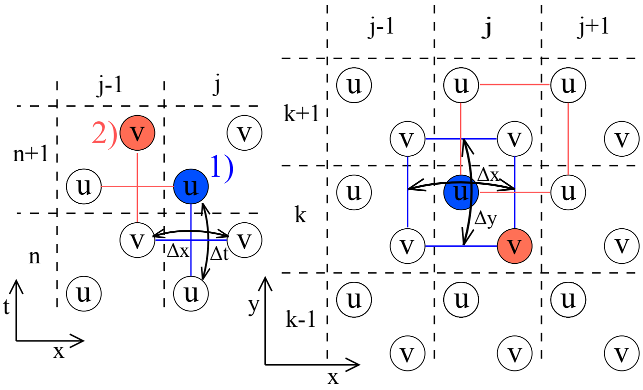

Figure 9.1: Leap-frog staggered-grid scheme: The left part shows the time-stepping sequence where 1) the new u components (blue/dark gray) are computed by the previous u and the spatial differences of old v-values. 2) Then (knowing u at t_{n+1}) the new v components (red/light gray) are computed at t_{n+1} . The right part of this figure shows the pattern for the spatial derivatives in x and y.

p_i represents the component $i = x, y$ of the momentum operator and $\boldsymbol{\sigma} = (\sigma_x, \sigma_y, \sigma_z)$ is the vector of Pauli matrices. The scalar potential in Eq. (9.2) is represented by V. The "magnetization vector" $\mathbf{m}(x, y, t) = [m_x(x, y, t), m_y(x, y, t), m_z(x, y, t)]$ may have its origin in a vector potential or an exchange coupling to a ferromagnetic medium. Note that $m_z \neq 0$ provides the mass term to the equation.

This generic two-component Dirac equation provides an effective model for a number of physical systems. For topological insulators, this model describes the low energy surface excitations. The spin is locked to the momentum, whereby the physical spin quantization axis is $\mathbf{S} \propto \hat{\mathbf{z}} \times \boldsymbol{\sigma}$, corresponding to a fermion with 2 degrees of freedom [9]. For given momentum, the presence of two components may be interpreted as accounting either for the existence of positive and negative energy solutions or the presence of two spin directions. Note, that flipping the spin for given momentum is equivalent to switching between the positive to negative energy branch. Indeed, by a simple unitary transformation applied to Eq. (9.2) one can arrive at a "physical" representation such that $\mathbf{S} \propto \boldsymbol{\sigma}$ which is useful in the presence of external electromagnetic fields. Note that, in accordance with the Nielsen-Ninomiya no-go theorem, a second Dirac cone is located on the opposite side of the TI surface. For graphene, the two components arise from the $|p_z\rangle$ bonding and anti-bonding band (without spin) [8]. In contrast, the standard four-component Dirac equation describes a spin-1/2 particle (Dirac fermion) with positive and negative energy solutions amounting to $2 \times 2 = 4$ degrees of freedom (“two energy bands and two spin directions"). The Majorana fermion solution is a special case. It is its own antiparticle, making it “half a Dirac fermion" with two degrees of freedom [34, 36, 35, 37, 38].

9.2.1 Numerical scheme

We propose a staggering of the grid both in time and space with second-order approximation for the time and space derivative, as shown in Fig. 9.1,

$$
\begin{aligned}
\frac{u^{n+1}_{j,k} - u^{n}_{j,k}}{\Delta t} &= -i\left((m_z)^{n}_{j,k} + V^{n}_{j,k}\right)\frac{u^{n+1}_{j,k} + u^{n}_{j,k}}{2} \\
&- \frac{(v^{n}_{j,k-1} - v^{n}_{j-1,k-1}) + (v^{n}_{j,k} - v^{n}_{j-1,k})}{2\Delta x} \\
&+ i\,\frac{(v^{n}_{j-1,k} - v^{n}_{j-1,k-1}) + (v^{n}_{j,k} - v^{n}_{j,k-1})}{2\Delta y}\,, \\
\frac{v^{n+1}_{j,k} - v^{n}_{j,k}}{\Delta t} &= i\left((m_z)^{n+1}_{j,k} - V^{n+1}_{j,k}\right)\frac{v^{n+1}_{j,k} + v^{n}_{j,k}}{2} \\
&- \frac{(u^{n+1}_{j+1,k} - u^{n+1}_{j,k}) + (u^{n+1}_{j+1,k+1} - u^{n+1}_{j,k+1})}{2\Delta x} \\
&- i\,\frac{(u^{n+1}_{j,k+1} - u^{n+1}_{j,k}) + (u^{n+1}_{j+1,k+1} - u^{n+1}_{j+1,k})}{2\Delta y}
\end{aligned}
\tag{9.3}
$$

with the notation $\boldsymbol{\psi}(x_j, y_k, t_n) \approx \boldsymbol{\psi}^{n}_{j,k} = (u^{n}_{j,k}, v^{n}_{j,k})$ where n and j, k, respectively, are the discrete time and space indices.

Here the mass term m_z and the potential V enter the scheme in a Crank-Nicolson time-averaged manner. A consistent incorporation of a "vector potential" m_x and m_y will be detailed below. Since the time averaged functions for the former only depend on one spatial grid-point a rearranging of terms leads to an explicit scheme. We call it a leap-frog scheme because u and v are computed in an alternating manner where first $u^{n+1}_{j,k}$ is computed from $u^{n}_{j,k}$ and $v^{n}_{j,k}$. Then using the updated components $u^{n+1}_{j,k}$, as shown in Fig. 9.1, the new $v^{n+1}_{j,k}$ are computed. This spatial staggering allows for a centered approximation of the first spatial partial derivatives without omitting the central grid point, as is the case for a centered symmetric first derivative operator on a regular grid. This eliminates one source of fermion-doubling. Here it should be recalled that by using one-sided difference operators with alternating direction for for u and v, fermion doubling can be avoided for the (1+1)D Dirac equation. For the (1+1)D case the latter is equivalent to the present spatial staggering of the grid [23, 24]. We use staggering in time to further improve the dispersion relation, which will be shown below.

m_x and m_y terms in the Hamiltonian Eq. (9.2) are incorporated consistently into the scheme above, for $m_x = m_y = 0$, using a Peierls substitution[25, 26],

$$\begin{aligned} u^n_{j,k} &\to \hat{u}^n_{j,k} \equiv u^n_{j,k} \exp\{i a^n_{j,k}\} \\ v^n_{j,k} &\to \hat{v}^n_{j,k} \equiv v^n_{j,k} \exp\{i a^n_{j,k}\} \ , \end{aligned} \tag{9.4}$$

where the real phase $a^n_{j,k}$ is defined as the line integral over the two-dimensional magnetization vector $\mathbf{m}$, starting at arbitrary, but fixed position (x_o, y_o) and ending on the lattice point $(x, y) = (j\Delta x, k\Delta y)$,

$$a^n_{j,k} = \int_{(x_o,y_o)}^{(x,y)} d\mathbf{s} \cdot \mathbf{m}(\mathbf{s}, t) \ |_{x=j\Delta x, y=k\Delta y, t=n\Delta t} \ .$$

This substitution introduces m_x and m_y in covariant fashion when interpreted as components of the electromagnetic vector potential, leading to $p_x \to p_x + m_x$ and $p_y \to p_y + m_y$ in the Dirac Hamiltonian Eq. (9.2). Details of the resulting scheme are discussed in 9.6. In the limit of smooth variation of m_x and m_y in space and time the scheme takes the form

$$\begin{aligned} &\frac{u^{n+1}_{j,k} - u^n_{j,k}}{\Delta t} = -i\left((m_z)^n_{j,k} + \hat{V}^n_{j,k}\right) \frac{u^{n+1}_{j,k} + u^n_{j,k}}{2} \\ &- \frac{v^n_{j,k-1} - v^n_{j-1,k-1} + v^n_{j,k} - v^n_{j-1,k}}{2\Delta x} \\ &+ i\frac{v^n_{j-1,k} - v^n_{j-1,k-1} + v^n_{j,k} - v^n_{j,k-1}}{2\Delta y} \\ &- i(m_x)^n_{j,k}\frac{v^n_{j,k} + v^n_{j-1,k} + v^n_{j,k-1} + v^n_{j-1,k-1}}{4} \\ &- (m_y)^n_{j,k}\frac{v^n_{j-1,k} + v^n_{j-1,k-1} + v^n_{j,k} + v^n_{j,k-1}}{4} \ , \end{aligned} \tag{9.5}$$

and

$$\begin{aligned}
\frac{v_{j,k}^{n+1}-v_{j,k}^{n}}{\Delta t} &= i\left((m_z)_{j,k}^{n+1}-\hat{V}_{j,k}^{n+1}\right)\frac{v_{j,k}^{n+1}+v_{j,k}^{n}}{2}\\
&-\frac{u_{j+1,k}^{n+1}-u_{j,k}^{n+1}+u_{j+1,k+1}^{n+1}-u_{j,k+1}^{n+1}}{2\Delta x}\\
&-i\frac{u_{j,k+1}^{n+1}-u_{j,k}^{n+1}+u_{j+1,k+1}^{n+1}-u_{j+1,k}^{n+1}}{2\Delta y}\\
&-i(m_x)_{j,k}^{n+1}\frac{u_{j+1,k}^{n+1}+u_{j,k}^{n+1}+u_{j+1,k+1}^{n+1}+u_{j,k+1}^{n+1}}{4}\\
&+(m_y)_{j,k}^{n+1}\frac{u_{j,k+1}^{n+1}+u_{j,k}^{n+1}+u_{j+1,k+1}^{n+1}+u_{j+1,k}^{n+1}}{4}\,. \qquad (9.6)
\end{aligned}$$

Here $\hat{V}_{j,k}^{n+1}$ is the net scalar potential. Its relation to $V_{j,k}^{n+1}$ is is given in A.1.

9.2.2 Von Neumann stability analysis

For this linear system and constant coefficients, Fourier analysis is used to determine the dispersion introduced by the grid. Furthermore, we use periodic boundary conditions (absorbing layers as introduced later do not violate periodicity). Thus, von Neumann stability analysis is sufficient to explore the stability of the finite difference scheme [39]. The Fourier transform of Eq. (3) from real space to momentum space leads to:

$$\underbrace{\begin{pmatrix} a_{11} & a_{12}\\ a_{21} & a_{22}\end{pmatrix}}_{=:A}\begin{pmatrix}\tilde{u}^{n+1}\\ \tilde{v}^{n+1}\end{pmatrix}+\underbrace{\begin{pmatrix} b_{11} & b_{12}\\ b_{21} & b_{22}\end{pmatrix}}_{=:B}\begin{pmatrix}\tilde{u}^{n}\\ \tilde{v}^{n}\end{pmatrix}=0\,, \qquad (9.7)$$

where we define

$$\begin{aligned}
a_{11} =& \frac{1}{\Delta t}+\frac{i(m_z+V)}{2}\,, \qquad (9.8)\\
a_{12} =& 0\,,\\
a_{21} =& +\frac{\left(1-e^{ik_x\Delta_x}\right)\left(1+e^{ik_y\Delta_y}\right)}{2\Delta x}\\
&-i\frac{\left(1+e^{ik_x\Delta_x}\right)\left(1-e^{ik_y\Delta_y}\right)}{2\Delta y}\\
&+i\frac{(m_x-im_y)\left(2+e^{ik_x\Delta_x}+e^{ik_y\Delta_y}\right)}{4}\,,\\
a_{22} =& \frac{1}{\Delta t}-\frac{i(m_z-V)}{2}\,,
\end{aligned}$$

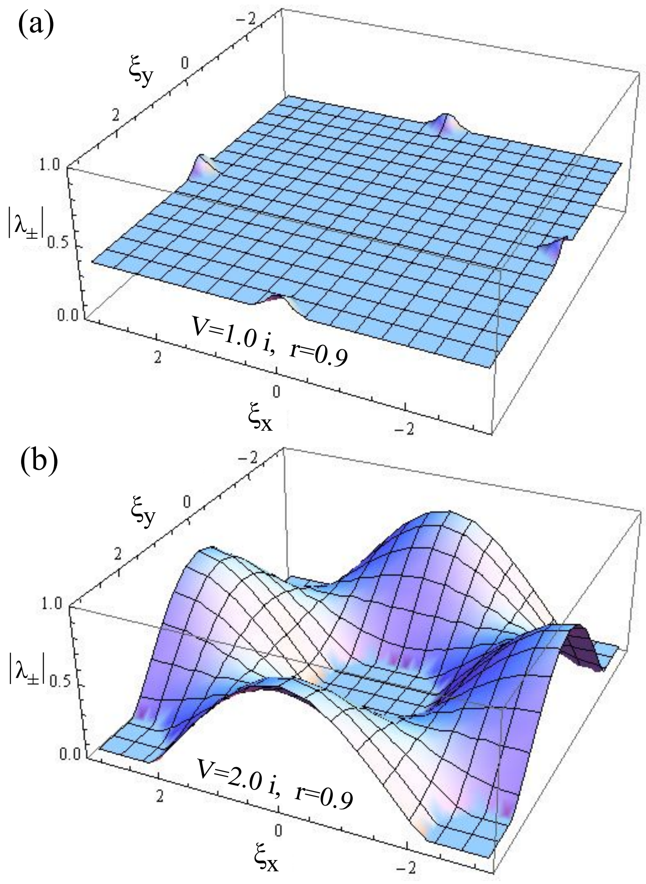

Figure 9.2: The largest eigenvalue of the growth matrix G max($|\lambda_\pm|$) shown over the entire scaled k-space for $m = 0$ and two different values of imaginary V, for ratio $r = \Delta t/\Delta = 0.9$.

$$
\begin{aligned}
b_{11} =& -\frac{1}{\Delta t} + \frac{i(m_z + V)}{2} \,, \\
b_{12} =& -\frac{\left(1 - e^{-ik_x\Delta_x}\right)\left(1 + e^{-ik_y\Delta_y}\right)}{2\Delta x} \\
& - i\frac{\left(1 + e^{-ik_x\Delta_x}\right)\left(1 - e^{-ik_y\Delta_y}\right)}{2\Delta y} \\
& + i\frac{(m_x + im_y)\left(2 + e^{-ik_x\Delta_x} + e^{-ik_y\Delta_y}\right)}{4} \,, \\
b_{21} =& 0 \,, \\
b_{22} =& -\frac{1}{\Delta t} - \frac{i(m_z - V)}{2} \,.
\end{aligned}
\tag{9.9}
$$

It is convenient to define the amplification matrix $G = -A^{-1}B$ and to use $\xi_x = k_x\Delta_x$, $\xi_y = k_y\Delta_y$ Eq. (9.7) becomes

$$\tilde{\psi}^{n+1}(\xi_x, \xi_y) = G(\xi_x, \xi_y)\tilde{\psi}^{n}(\xi_x, \xi_y)\ . \tag{9.10}$$

We now consider $\Delta x = \Delta y = \Delta$ and define the ratio $r = \Delta t/\Delta$. Introducing rescaled variables $\mu_i = m_i\Delta t$ and $\nu = V\Delta t$, we write the eigenvalues of G using the root formula

$$\lambda_\pm = P/2 \pm \sqrt{\left(P/2\right)^2 - Q}\ , \tag{9.11}$$

where $P = \mathrm{tr}[G]$ and $Q = \det[G]$. The resulting lengthy expressions write as:

$$\begin{aligned} P =& \Big[16(1-r^2) + 4(\nu^2 - \mu_z^2) - 3(\mu_x^2 + \mu_y^2) \\ &+ 4r(\mu_x - \mu_y) - 2(\mu_x^2 + \mu_y^2)(\cos\xi_x + \cos\xi_y) \\ &+ 4r(\mu_x + \mu_y)(\cos\xi_x - \cos\xi_y) \\ &- (\mu_x^2 + \mu_y^2)(\cos\xi_x\cos\xi_y + \sin\xi_x\sin\xi_y) \\ &- 4r(\mu_x - \mu_y)(\cos\xi_x\cos\xi_y - \sin\xi_x\sin\xi_y) \\ &+ 8r\big(\mu_x\sin\xi_x + \mu_y\sin\xi_y + \mu_x\sin\xi_x\cos\xi_y \\ &+ \mu_y\cos\xi_x\sin\xi_y + 2r\cos\xi_x\cos\xi_y\big)\Big]/(2N)\ , \\ Q =& [\mu_z^2 - (\nu - 2i)^2]/N\ , \end{aligned} \tag{9.12}$$

where $N = 4 + \mu_z^2 - 4i\nu - \nu^2$. For $\mu_x = \mu_y = 0$ it reduces to: $P = [2(\nu^2 - \mu_z^2) + 8r^2(1/r^2 - 1 + \cos\xi_x\cos\xi_y)]/N$. Now one can show that for $r < 1$ and $\mu_z, \nu \in \mathbb{R}$: $|\lambda_\pm| = 1$ for all allowed wave numbers on the grid, $\xi_x, \xi_y \in [-\pi, \pi]$. Since under this constraints the eigenvalues are simple the the scheme is stable for the ratio $r < 1$, which constitutes the CFL condition for the scheme. For $\mu_i \neq 0$ the scheme is stable for $r < \min\big[\sqrt{1 - (\mu_x/4)^2} - \mu_y/4, \sqrt{1 - (\mu_y/4)^2} + \mu_x/4\big]$. Let's, for now and in momentum space, define the square of the l_2 norm of the spinor as:
$\|\tilde{\boldsymbol{\psi}}\|^2 = \int_{-\pi}^{\pi} \mathrm{d}\xi_x \int_{-\pi}^{\pi} \mathrm{d}\xi_y (|\tilde{u}(\xi_x, \xi_y)|^2 + |\tilde{v}(\xi_x, \xi_y)|^2)$. It is preserved because $\|G\tilde{\boldsymbol{\psi}}\| = \|\tilde{\boldsymbol{\psi}}\|$. If m_z has an imaginary part, it turns out that the scheme is unstable because the absolute value of one of the λ's becomes larger than one in the vicinity of the points $(\xi_x, \xi_y) = (0, 0)$ and $(\xi_x, \xi_y) = (\pm\pi, \pm\pi)$. If, on the other hand, the potential V has an imaginary part its sign determines the stability of the scheme: for $\Im\{V\} < 0$ it is unstable. For $\Im\{V\} > 0$ it is stable,

however, max($|\lambda_\pm|$) < 1 and the norm is not conserved. One can utilize this property to create absorbing layers which act as absorbing (open) boundary conditions within this scheme. Furthermore, internal absorbing layers can be used to simulate particle source and drain. In Fig. 9.2 we show, for illustration, max($|\lambda_\pm|$) and its behavior for different values of r and $\Im\{V\} > 0$.

9.2.3 Dispersion relation

Let us now turn our attention to the dispersion relation of the proposed scheme. It is obtained by a Fourier transformation of Eq. (9.10) in time or, again by looking at the eigenmodes of the scheme. The ansatz: $\tilde{u}^{n+1} = e^{i\tilde{\omega}}\tilde{u}^n$ where $\tilde{\omega} = \omega\Delta t$, gives us, in the notation from above, the homogeneous system

$$(e^{i\tilde{\omega}}A + B)\tilde{\boldsymbol{\psi}} = 0 \,, \tag{9.13}$$

from which the non-trivial solutions are determined for $\tilde{\omega}$ and expressed in terms of the growth factor $\lambda_\pm$ (see Eq. (9.11))

$$\tilde{\omega} = -\frac{i}{r}\ln[\lambda_\pm] \,. \tag{9.14}$$

Here again the necessary and sufficient condition for the conservation of the norm, using $\lambda_\pm^n = e^{i\omega r n}$, shows up as $\Im(\omega) = 0$ which, for $\mu_x, \mu_y = 0$, gives $|\lambda_\pm| = 1$. Setting $\mu_z = 0$ and $\nu = 0$ it simplifies to

$$\begin{aligned}\tilde{\omega} = -\frac{i}{r}\ln\Bigg\{1 + r^2\big(\cos\xi_x\cos\xi_y - 1\big) \qquad\qquad & \qquad (9.15)\\ \pm\sqrt{\Big[r^2\big(\cos\xi_x\cos\xi_y - 1\big) + 1\Big]^2 - 1}\Bigg\},&\end{aligned}$$

where choosing $r = 1$ leads to:

$$\tilde{\omega} = -i\ln\Big(\cos\xi_x\cos\xi_y \pm \sqrt{\cos^2\xi_x\cos^2\xi_y - 1}\Big) \,, \tag{9.16}$$

which is plotted in Fig. 9.3. It can be seen that the dispersion relation is linear along the x- and y-axis. For example, at the x axis where $\xi_y = 0$, we get

$$\tilde{\omega} = -i\ln\Big(\cos\xi_x \pm i\sin\xi_x\Big) = \pm\xi_x \,.$$

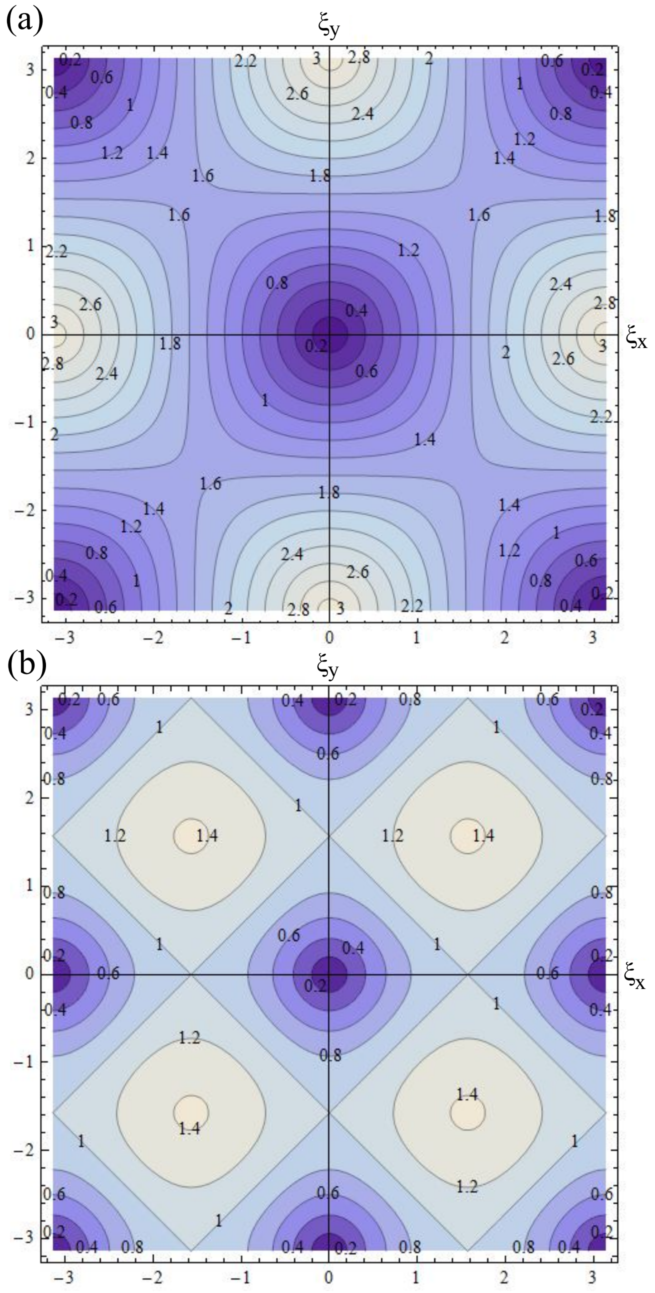

Figure 9.3: Dispersion relation for $\Delta x = \Delta y = \Delta$, $\mu_i = 0$, $\nu = 0$ and $r = 1$. (a) Leap-frog staggered-in-space-and-time scheme. For comparison: (b) centered differences in space and Crank-Nicolson in time, without grid staggering.

This means that the dispersion relation of the continuum model (Weyl equation) is preserved along the x- and y- axis. For comparison we also show the dispersion relation for a scheme using a centered second-order approximation without spatial staggering of the spatial differences and without time staggering but using Crank-Nicolson in time instead (Fig. 9.3 (b)). With the staggered scheme one gets two Dirac cones, at $(\xi_x, \xi_y) = (0, 0)$ and $(\xi_x, \xi_y) = (\pm\pi, \pm\pi)$ respectively, in contrast to the four Dirac cones obtained by the scheme without staggering. The dispersion relation for $\mu_y \neq 0$ is computed numerically and shown in Fig. 9.4.

Putting a genuine continuum model on a lattice inevitably leads to changes in the spectral properties. The spatial grid destroys momentum conservation of the free-particle Dirac equation and introduces an invariance under discrete (primitive) translations in real space. As a consequence, k-vectors are defined up to reciprocal lattice vectors only. Similarly, a time grid with spacing Δt makes frequency well defined only within the interval $(-\pi/\Delta t, +\pi/\Delta t]$. One remarkable feature of the present model is that for the special case of $r = 1$ the linear energy dispersion of the free-particle Weyl equation is preserved exactly along k_x and k_y. This is shown in Fig. 9.5 (a). No phase errors occur in this case, which, has recently been used to study the dynamics of Dirac fermions in a 2D interferometer setup [21]. As expected, however, errors (deviation from continuum behavior - dashed lines in Fig. 9.5) occurs in all other cases: Adding a (constant) potential V, Fig. 9.5 (b), introduces an artificial “energy gap" at the BZ boundary while the correct dispersion should remain linear, merely shifted vertically by V. In this case, periodic motion (Bloch oscillation) occurs when the k-vector crosses the BZ boundary. Similarly for finite mass, Fig. 9.5 (c), a wave packet will disperse while undergoing Bloch oscillations. Errors in the dispersion also occur for $r < 1$, Fig. 9.5 (e). The effect of $m_x \neq 0$ is shown in Fig. Fig. 9.5 (d). While it changes the kinetic momentum leading to a horizontal shift of the dispersion in the continuum model, additional band curvature arises on the lattice.

9.2.4 The norm

The definition of a discrete L_2 norm on a staggered grid requires some care due to ambiguities when taking the continuum limit. In particular, the sim-

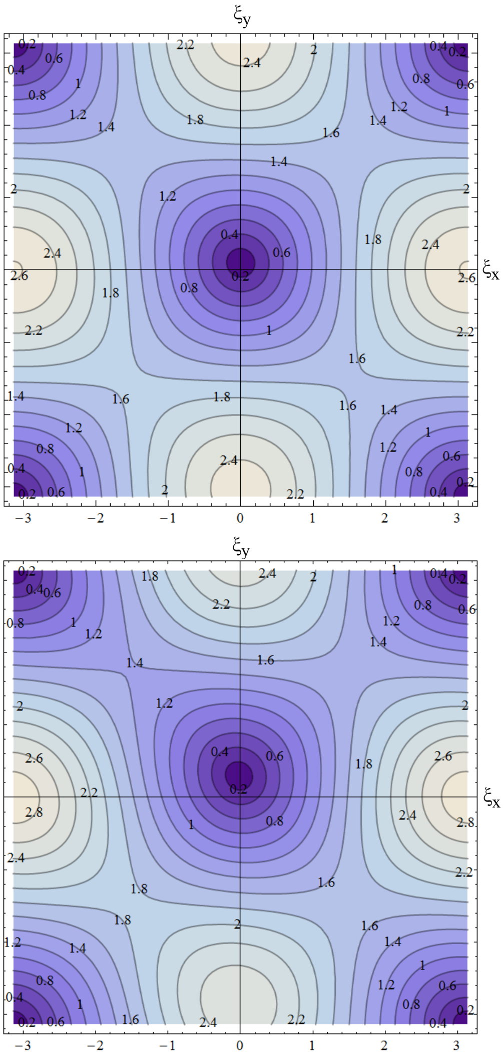

Figure 9.4: Dispersion relation of the present leap-frog scheme with $r = 0.9$, $\Delta x = \Delta y = \Delta$, $m_x = m_z = V = 0$ and $m_y = 0.1, 0.2, 0.3, 0.4$ from the upper left to the lower right figure. One observes a shift of the Dirac cone away from the center of the momentum space by m_y consistent with the continuum solution.

ple local form

$$||\psi||_2^n := \sqrt{\sum_{j,k} \left(|u_{j,k}^n|^2 + |v_{j,k}^n|^2\right)} \tag{9.17}$$

proves to be a poor choice since numerical tests show that, while conserved on time average, it can show strong oscillations around its mean value.

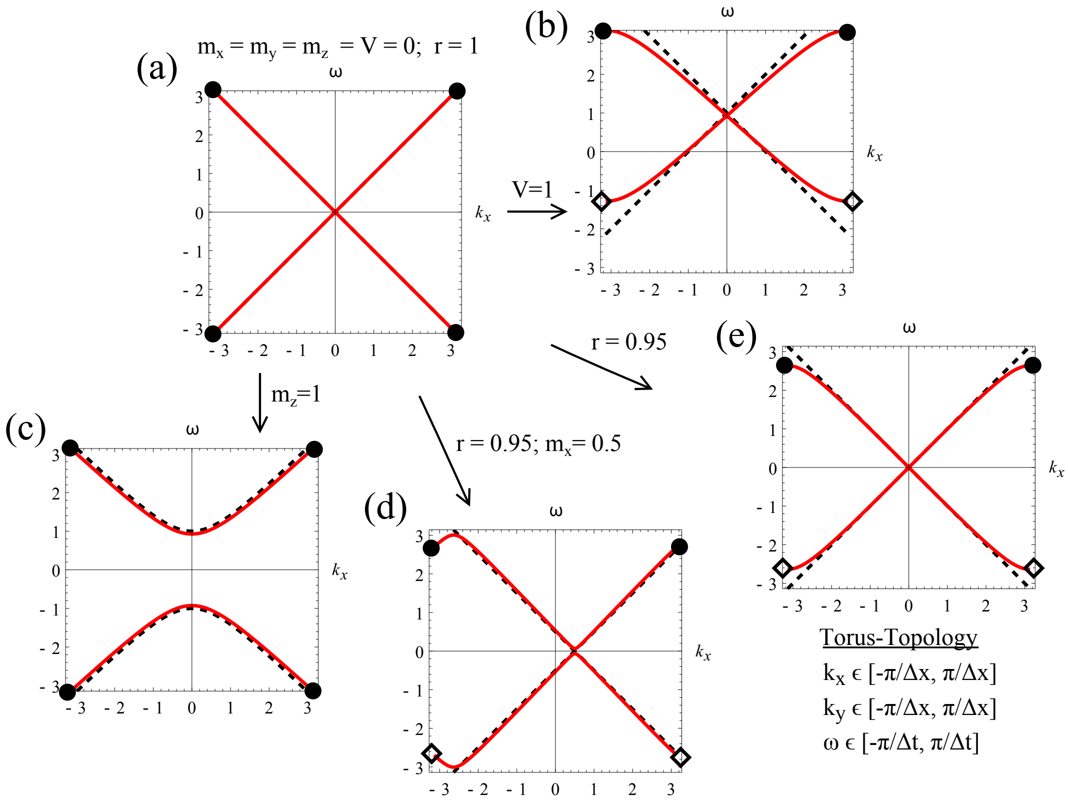

Figure 9.5: Dispersion relation for wave vectors aligned with the k_x axis ($k_y = 0$), $\Delta x = 1$ for various parameters. The topology of the dispersion relation is that of a torus, periodic in k_x, k_y, and ω. In each figure, equivalent points in the dispersion are marked by pairs of black filled circles and empty diamonds, respectively. For comparison, the dispersion relation for the continuum equation is shown by dashed lines.

In order to define a norm which is invariant under this scheme we first define a scalar product between spinor components on the lattice as follows

$$(u^n; v^{n'})_{0,0} = (u^n; v^{n'}) = \sum_{j,k} (u^n_{j,k})^* v^{n'}_{j,k} \ , \tag{9.18}$$

and

$$||u^n||^2 = (u^n; u^n) \ . \tag{9.19}$$

Furthermore we define scalar products with shifted spinor components as

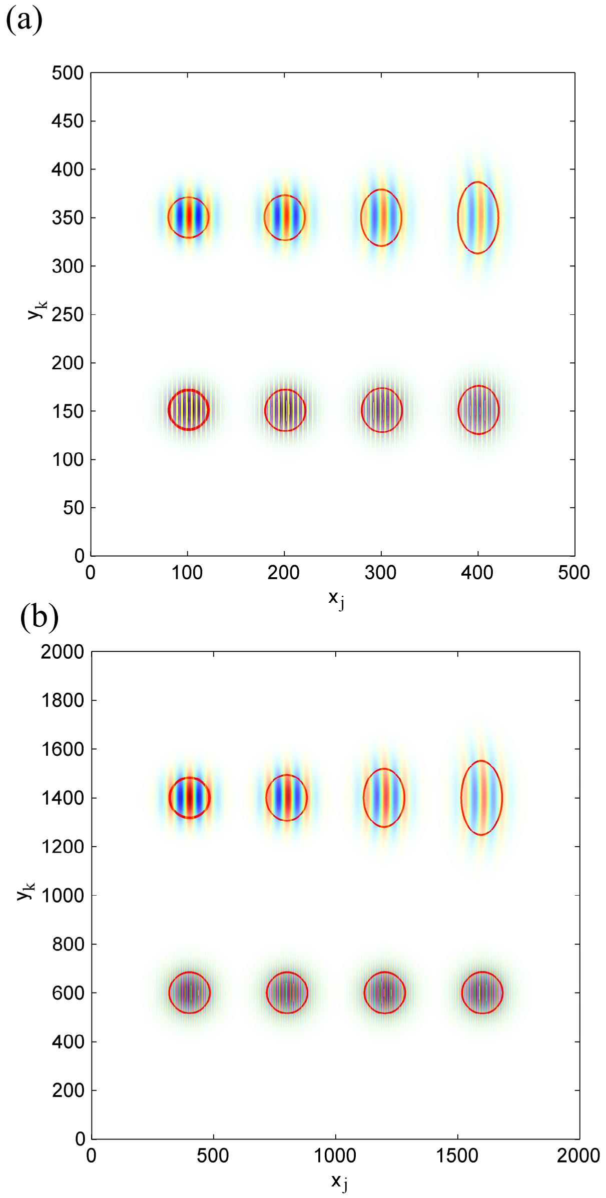

Figure 9.6: (a) Comparison of the propagation of a packet for $m = V = 0$ with a low wave numbers $(k_x, k_y) = (10.0 \pm 1.3, 0.0 \pm 1.3)\%$ to one prepared with a mean wave number near the maximum for the grid $(k_x, k_y) = (80.0 \pm 1.3, 0.0 \pm 1.3)\%$. (b) The same initial data using a finer grid having $(k_x, k_y) = (2.50 \pm 0.32, 0.0 \pm 0.32)\%$ and $(k_x, k_y) = (20.0 \pm 0.32, 0.0 \pm 0.32)\%$. The closed lines represent the FWHM the brightness saturation the probability density and the color/brightness variation encodes the phase.

follows

$$(u^n; v^{n'})_{\pm,0} = (u^n; v^{n'}_{\pm,0}) = \sum_{j,k} (u^n_{j,k})^* v^{n'}_{j\pm1,k} \; ,$$
$$(u^n; v^{n'})_{0,\pm} = (u^n; v^{n'}_{0,\pm}) = \sum_{j,k} (u^n_{j,k})^* v^{n'}_{j,k\pm1} \; ,$$

and

$$(u^n; v^{n'})_{\pm,\pm} = (u^n; v^{n'}_{\pm,\pm}) = \sum_{j,k} (u^n_{j,k})^* v^{n'}_{j\pm1,k\pm1} \; , \tag{9.20}$$

Here the sum j, k runs over all lattice sites. n, n' denote two time sheets, and u and v denote any combination of two upper and/or lower spinor components.

For any physical situation, we may consider either zero boundary conditions or periodic boundary conditions. In both cases, a norm which is conserved by the scheme Eqs. (9.3) for real-valued and finite $m_z(x, y, t)$ and $V(x, y, t)$, and $m_x = m_y = 0$ is given by

$$\begin{aligned} E_{n+1} = E_n =& ||u^n||^2 + ||v^n||^2 \\ & - r_x \Re\big\{ (u^n; v^n)_{0,-} - (u^n; v^n)_{-,-} \\ & + (u^n; v^n)_{0,0} - (u^n; v^n)_{-,0} \big\} \\ & - r_y \Im\big\{ (u^n; v^n)_{-,0} - (u^n; v^n)_{-,-} \\ & + (u^n; v^n)_{0,0} - (u^n; v^n)_{0,-} \big\} \; . \end{aligned} \tag{9.21}$$

with $r_x = \Delta t/(2\Delta x)$ and $r_y = \Delta t/(2\Delta y)$.

Furthermore, for the general case of non-vanishing m_x and m_y, the conserved norm $\hat{E}_n$ under the exact scheme (see A.1 and 9.7) is obtained by subjecting u and v in E_n to the Peierls transformation Eq. (9.4), noting that $\exp\{ia^n_{j,k}\}$ is a local gauge field. Note also that the scheme Eq. (9.5) and Eq. (9.6) is valid only in the limit of slowly-varying m_x and m_y and hence will conserve $\hat{E}_n$ only in this limit. The proof for the conservation of E_n and, respectively, $\hat{E}_n$ is given in 9.7.

This definition of a norm also allows a stability analysis of the scheme. In particular, it is valid for time- and position-dependent magnetization, mass, and electromagnetic potential.

One finds

$$||u^n||^2 + ||v^n||^2 \leq \frac{E_o}{1-\tilde{r}}, \text{for } \tilde{r} = 2\sqrt{r_x^2 + r_y^2} < 1 \; , \tag{9.22}$$

for scheme Eq. (9.3), as well as

$$||\hat{u}^n||^2 + ||\hat{v}^n||^2 \leq \frac{\hat{E}_o}{1-\tilde{r}}, \text{for } \tilde{r} = 2\sqrt{r_x^2 + r_y^2} < 1\,, \tag{9.23}$$

for scheme Eqs. (9.30) and (9.32), which is approximated by the scheme Eqs. (9.5) and (9.6) above. Stability can also be shown for $\tilde{r} = 1$. The proof is given in 9.8.

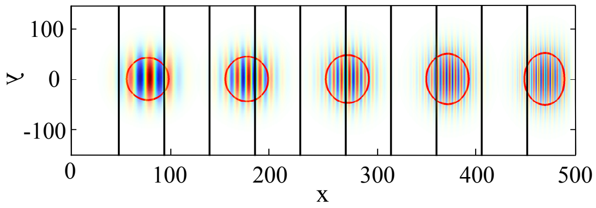

Figure 9.7: Wave packet with $(k_x, k_y) = (10.0 \pm 1.3, 0.0 \pm 1.3)\%$ for $m = 0$ in a potential, shown by contour lines, rising linearly in x-direction from 0 to 0.2. The closed lines represent the FWHM, the brightness saturation the probability density, and the color/brightness variation encodes the phase.

9.3 Numerical examples

With the numerical approach presented above, one is in a perfect position to simulate ballistic Dirac fermion dynamics in (2+1)D in complex potential landscapes under open boundary conditions. The numerical examples below have been selected mainly to demonstrate the properties of the scheme and provide some intuition for (2+1)D ballistic Dirac fermion dynamics in simple effective TI mass and potential textures. For the examples given below, we have chosen a spatial region of 500×500 units and use a rather coarse discretization $\Delta x = \Delta y = 1$, and $r = 0.9$. We give k in percents $(\%)$ of $k_{max} = \pi/\Delta$. While movies are ideally suited to visualize our numerical results of Dirac fermion dynamics, here the figures show snapshots taken every 100 time steps which are combined in a single plot. The closed lines in these figures mark the FWHM of the wave packet for a given time step and the brightness saturation shows the probability density $||\psi||^2$. Color/brightness indicates the phase of the wave packet which is associated with the real part of the upper spinor component u.

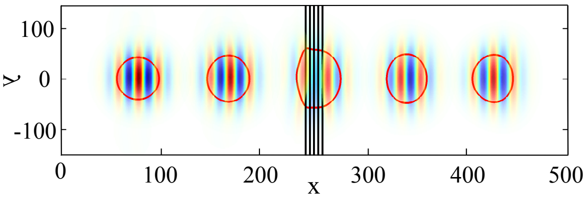

Figure 9.8: Wave packet with $(k_x, k_y) = (10.0 \pm 1.3, 0.0 \pm 1.3)\%$ for $m = 0$ at a Klein step: on the left side the potential $V = 0$ and rises linearly to $V = 0.1$ at the right side of the figure, as shown by contour lines. The closed lines represent the FWHM, the brightness saturation gives the probability density, and the color/brightness variation encodes the phase.

9.3.1 Dispersive properties of the scheme

Due to the chosen staggered-grid discretization a rather faithful representation of the exact continuum Dirac cone dispersion and constant "magnetization" $\mathbf{m}$,

$$\Omega(k_x, k_y) = \sqrt{\left(k_x - m_x\right)^2 + \left(k_y - m_y\right)^2 + m_z^2} + V \,, \tag{9.24}$$

is possible over a wide region of k-space. Eq. (9.24) is to be compared with the dispersion provided by the staggered grid discretization given in Eq. (9.14).

First we demonstrate the quality of the dispersion on the lattice and investigate a "race" between two massless Dirac fermions on the grid. One is described by a wave packet with small wave numbers, prepared with a mean wave number of $(k_x, k_y) = (10.0, 0.0)\%$ of k_{max}, the other by a wave packet with a high central wave number of k_{max}: $(k_x, k_y) = (80.0, 0.0)\%$. Both wave packets have a Gaussian half width in k_x and k_y of $(1.3, 1.3)\%$ of k_{max}. Remember k_{max} is the maximum wave number provided by the grid $k_{max} = \pi/\Delta$. Below we use the abbreviated notation $(k_x, k_y) = (80.0 \pm 1.3, 0.0 \pm 1.3)\%$. Results are shown in Fig. 9.6 (a). Since the systematic errors in group velocity associated with the present scheme are small the two wave packets propagate essentially with equal speed. For this particular simulation we chose $r = 1$ because it provides the best approximation to the exact linear dispersion. The stronger distortion of the wave packet with the smaller wave number compared to the one with higher wave number is due to a different slope in the y-direction of the dispersion for the wave packet lying closer/farther to the center of the Dirac cone. This effect is also present for the continuum problem. To demonstrate this fact we show this "race" using the a very fine grid Fig. 9.6 (b).

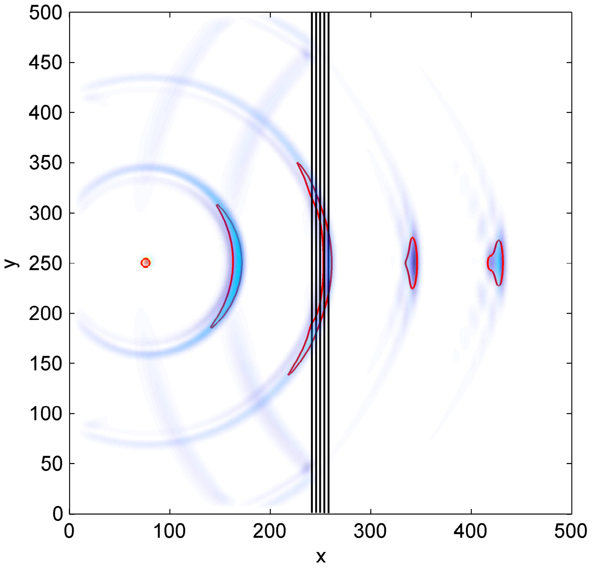

Figure 9.9: Wave packet with $(k_x, k_y) = (5.0 \pm 6.4, 0.0 \pm 6.4)\%$ for $m = 0$ at a Klein step where on the left side $V = 0$ and rising linearly to $V = 0.1$ at the right side of the figure as shown by contour lines. The closed lines represent the FWHM, the brightness saturation gives the probability density, and the color/brightness variation encodes the phase.

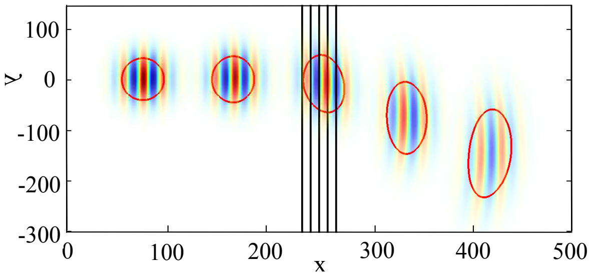

Figure 9.10: (color online). Wave packet with $(k_x, k_y) = (10.0\pm1.3, 0.0\pm1.3)\%$ for $V = 0$ at a step where on the left side $m_y = 0$ and is rising linearly to $m_y = -0.2$ to the right side of the figure as shown by contour lines. The closed lines represent the FWHM, the brightness saturation gives the probability density, and the color/brightness variation encodes the phase.

In Fig. 9.7 we show a wave packet of mass zero in a region of constant electric field represented by a linear potential V growing from 0 to 0.1. The

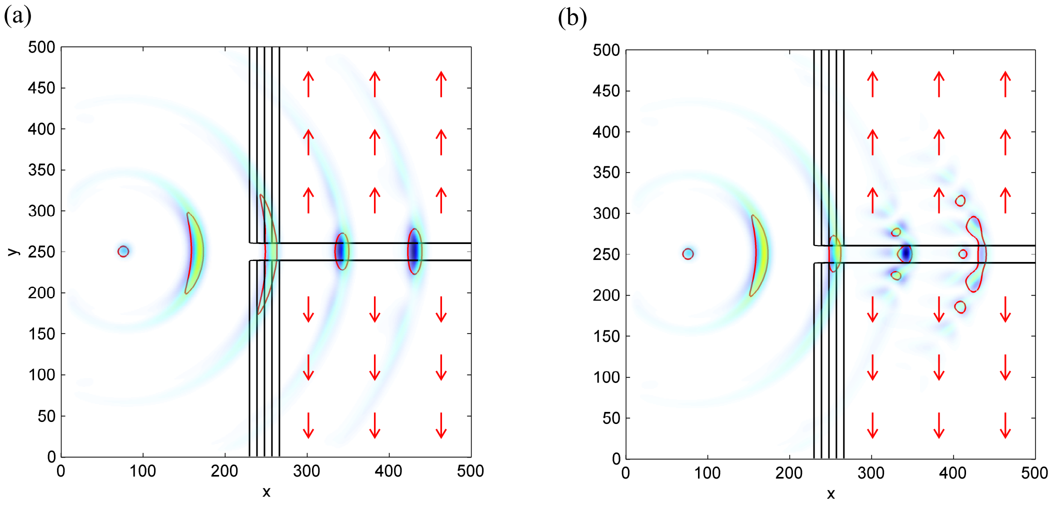

Figure 9.11: (a) Wave packet with $(k_x, k_y) = (5.0 \pm 6.4, 0.0 \pm 6.4)\%$ for $m = 0$ at a step where on the left side $m_y = 0$ and rising linearly to $m_y \pm 0.01$ (magnitude shown by contour lines and direction by arrows) where at the upper right-hand quarter of the figure $m_y = 0.01$ and at the lower right-hand quarter of the figure $m_y = -0.01$. (b) the same as in (a) but with $m_y = 0.03$. The closed lines represent the FWHM, the brightness saturation gives the probability density, and the color/brightness variation encodes the phase.

initial Gaussian wave packet is prepared with $(k_x, k_y) = (10.0, 0.0)\%\ k_{max}$ and a half width of $(1.3, 1.3)\%$. The speed of propagation does not change because the massless fermion on the grid always moves at maximum wave velocity ($c = 1$). The change in kinetic energy shows up in the growth of the wave number. Here it is remarkable that the wave number grows close to the maximum wave number provided by the grid and yet the simulated propagation is still a good approximation to the exact result for the continuum problem. This is due to the ecellent dispersion properties of the scheme for wave numbers aligned with the grid.

9.3.2 Dynamics at Klein steps

Next we consider a Klein potential step at which the wave packet $(k_x, k_y) = (10.0 \pm 1.3, 0.0 \pm 1.3)\%$ propagates in positive energy states on the left-hand side, where $V = 0$, and in negative energy states on the right-hand side of the step, where $V = 0.1$. For this simulation shown in Fig. 9.8 we choose $\mathbf{m} = 0$. This situation leads to a high transmission of ≈ 1 of the wave packet under normal incidence since the potential step resonantly connects particle states on one side to hole (anti-particle) states on the other. For the case $m_z \neq 0$, as is well known, the transmission probability grows with the height of the potential step [37].

Figure Fig. 9.9 shows the same Klein potential step but for an initial wave packet $(k_x, k_y) = (5.0 \pm 6.4, 0.0 \pm 6.4)\%$. The observed focusing behavior is a consequence of phase and group velocity changing their sign across the step. Also demonstrated in this figure is the successful implementation of absorbing boundary conditions. Note that wave contributions impinging upon the simulation boundaries disappear without artificial reflection.

9.3.3 Dynamics under finite $\mathbf{m}$

In this second part we explore simple cases for which $\mathbf{m} \neq 0$ emulating, for example, TI surfaces with ferromagnetic texture. First we consider a situation where $m_y(x)$ changes from zero to a finite constant value. As seen in Eq. (9.24) a constant m_y shifts the dispersion relation in y-direction of momentum space. Thus, when a wave packet impinges upon such a "magnetic Klein step" a wave packet starting with group velocity component $v_y = 0$ ends up with a finite group velocity component, as demonstrated numerically in Fig. 9.10. This effect can be exploited for the focusing of an incoming fermion beam, as shown in Fig. 9.11. We set, for the right upper quarter of the simulated domain, $m_y = const$ and $m_y = -const$ in the lower right quarter. Therefore, for sufficiently small k_y, the group velocity component v_y changes sign at the interface between these two regions. As a result, one observes the emergence of interference fringes where the distance of the maxima depends on m_y, see Fig. 9.11 (a) and (b).
Fig. 9.12 shows a mass-zero wave packet traveling on a relativistic Landau orbit enforced by a magnetization in z-direction represented by a vector potential m_y with linear x-dependence. Positions of constant m_y are indicated in the figure by vertical lines. The Gaussian wave packet sets out in the 12 o'clock position and propagates in the direction indicated by the arrows. In this case a strongly dispersive behavior is observed: inner portions of the wave packet move ahead of the outer portion leading to a significantly elongated wave packet after one completed orbit. This dispersive effect is not a numerical error but a represents a peculiarity of a mass zero particle in a magnetic field, for which the period T for completion of one orbit fulfills $T \propto k/B$, where k is the magnitude of the k-vector and B the z-component

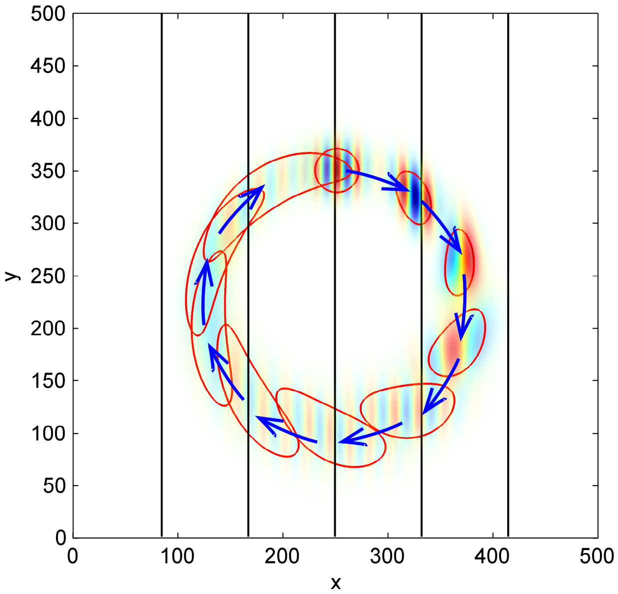

Figure 9.12: Wave packet starting with $(k_x, k_y) = (10.0 \pm 0.8, 0.0 \pm 0.8)\%$ for $V = 0$ moving in a constant magnetic field in z-direction, represented by a vector potential m_y rising linearly with x. The closed lines mark the FWHM, the brightness saturation gives the probability density, and the color/brightness variation encodes the phase.

of the magnetic field. Since the particle moves at constant group velocity, also the classical cyclotron radius R_c scales linearly with k. Thus portions of the wave packet closer to the center of the orbit move ahead of those further away from it, as is clearly revealed in the numerical simulation shown in Fig. 9.12. This effect is of course closely related to the $\sqrt{n}$ dependence of the cyclotron mass of graphene, with n denoting the particle density, which has lead to the measurement of the Fermi velocity in graphene, as discussed in a recent review article [8]. This effect can also be seen in a publication where a FFT-split-operator code was used [40].

This numerical approach has also served as the basis for a theoretical study of Dirac fermion propagation on magnetically textured surfaces of topological insulators, in the vicinity of domain walls, domain wall intersections, and Dirac fermion wave guides [20, 21].

9.4 Discussion

The main advantages from this compact scheme are the preservation of the free Weyl-Dirac fermion dispersion relation for wave vectors aligned along both the x- and the y-axis, as well as a large, nearly isotropic monotonic region near the center of k-space. In particular for long-time simulations of magnetic textures which are aligned along the main axes, like rectangular waveguide structures which we have modeled [21], the advantages of the present scheme pay off. As demonstrated above, for such setups errors in phase and group velocity relative to the continuum model are small (see, for example, the dispersion relation along the axes in Fig. 9.3 (a)). The results show high accuracy for wave-components up to the grid maximum of two grid-points per wavelength, known as the Nyquist wave number. It should also be remembered that the effective model captured by the Hamiltonian in Eq. (9.2) is valid only in the vicinity of the degeneracy point of the surface states of a TI or the graphene band structure and for weak contributions from the "magnetization" term. Therefore, the presence of a second cone at $(k_x, k_y) = (\pm\frac{\pi}{\Delta x}, \pm\frac{\pi}{\Delta y})$ does not provide a serious drawback for most applications.

Furthermore, this scheme leaves open the option to choose, within its explicitly derived convergence limits, any desirable ratios in the grid spacings. For simulations with arbitrary propagation directions one has to estimate the occurring wave numbers and choose the grid size such that the dispersion relation on the grid is a good approximation to the one for the continuum equation. Again, the present scheme has a significant advantage (in addition of being explicit) over the standard scheme using a symmetric form of the spatial derivatives, see Fig. 9.3 (b), since the region of k-space where a good approximation of the continuum energy dispersion is provided is significantly enlarged. Typical simulations shown here take a few minutes of CPU time on an average PC. For this second order accurate scheme the numerical cost increases linearly with the number of (space+time) grid-points, offering a profound advantage compared to implicit schemes of the same order, whenever simulations of high accuracy are required. If necessary, the second Dirac cone can be removed within this scheme by adding mass to the doublers using a Wilson term [41]. When properly implemented into the present staggered grid scheme it leads to an implicit scheme which will be shown elsewhere.

9.5 Summary, conclusions, and outlook

In summary, we have presented a staggered-grid leap-frog scheme for the numerical solution of the (2+1)D Dirac equation which has the following favorable properties: it is an explicit scheme, it has the minimum number "two" of Dirac cones on the lattice whereby the second cone sits at the corners of the “1st Brillouin zone", for the case of mass zero it provides the correct linear dispersion along x- and y-direction, and it allows for the implementation of absorbing boundary conditions for simulations on a finite grid without spurious reflections from its boundaries, as well as the simulation of particle sources and sinks. Here, generic numerical examples have been given to demonstrate and explore these properties. As a consequence, this approach is well suited for the study of Dirac fermion dynamics in potential landscapes provided by external electromagnetic potentials, typical to TI surface states. Applications to TI surface state dynamics based on this algorithm have and will be presented elsewhere [20, 21]. A related numerical treatment of the (1+1)D two-spinor-component Dirac equation including *exact* absorbing boundary conditions, displaying a single Dirac cone, has been presented by us recently [24]. Furthermore, we have been able to develop a scheme, respectively, for the to the (2+1)D two-spinor-component Dirac equation and the (3+1)D four-spinor-component Dirac equation with a single cone only [42].

Acknowledgments

We acknowledge support from the Austrian Science Foundation under project I395-N16.
Furthermore, we thank B. A. Stickler, A. Arnold and C. Ertler for helpful comments.

REFERENCES

[1] P. A. M. Dirac, Proceedings of the Royal Society of London Series A 117 (1928) 610.

[2] C. D. Anderson, Physical Review 43 (1933) 491.

[3] R. P. Feynman, Physical Review 76 (1949) 769.

[4] P. R. Wallace, Physical Review 71 (1946) 622.

[5] E. O. Kane, J. Phys. Chem. Solids 1 (1957) 249.

[6] W. Pötz, J. Math. Phys. 36 (1995) 1707.

[7] K. S. Novoselov, A. K. Geim, S. V. Morozov, D. Jiang, M. I. Katsnelson, I. V. Grigorieva, S. V. Dubonos, and A. A. Firsov, Nature 438 (2005) 197.

[8] A. H. Castro-Neto, F. Guinea, N. M. R. Peres, K. S. Novoselov, and A. K . Geim, Rev. Mod. Phys. 81 (2009) 109. G. W. Semenoff, Phys. Rev. Lett. 53, (1984) 2449.

[9] X. L. Qi and S. C. Zhang, Rev. Mod. Phys. 83 (2011) 1057.

[10] J. E. Moore and L. Balents, Phys. Rev. B 75 (2007) 121306.

[11] L. Fu and C. L. Kane, Phys. Rev. B 76 (2007) 045302.

[12] X. L. Qi, T. L. Hughes, and S. C. Zhang, Phys. Rev. B 78 (2008) 195424.

[13] Y. Xia, D. Qian, D. Hsieh, L. Wray, A. Pal, H. Lin, A. Bansil, D. Grauer, Y. S. Hor, R. J. Cava, and M. Z. Hasan, Nature Physics 5 (2009) 398.

[14] D. Hsieh, Y. Xia, D. Qian, L. Wray, F. Meier, J. H. Dil, J. Osterwalder, L. Patthey, A. V. Fedorov, H. Lin, et al., Phys. Rev. Lett. 103 (2009) 146401.

[15] P. W. Anderson, The Theory of Superconductivity in the High-Tc Cuprate Superconductors, Princeton University Press Princeton (1997).

[16] R. Jackiw and C. Rebbi, Phys. Rev. D 13 (1976) 3398.

[17] L. Lamata, J. Casanova, R. Gerritsma, C. F. Roos, J. J. Garcia-Ripoll, and E. Solano, New J. of Phys. 13 (2011) 095003.

[18] D. Witthaut, T.Salger, S. Kling, C. Grossert, and M. Weitz, Phys. Rev. A 84 (2011) 033601.

[19] N. Szpak and R. Schützhold, New J. of Phys. 14 (2012) 035001.

[20] R. Hammer, C. Ertler, and W. Pötz, arXiv:1205.6941 (2012).

[21] R. Hammer, C. Ertler, and W. Pötz, Appl. Phys. Lett. 102 (2013) 193514.

[22] U. Becker, N. Grün, and W. Scheid, J. Phys. B 16 (1983) 1967.

[23] R. Stacey, Phys. Rev. D 26 (1982) 468.

[24] R. Hammer, W. Pötz, and A. Arnold arXiv:1302.5587 (2013).

[25] R. Peierls, Z. Phys. 80 (1933) 763.

[26] M. Graf and P. Vogl, Phys. Rev. B 51 (1995) 4940.

[27] C. Müller, N. Grün, and W. Scheid, Physics Letters A 242 (1998) 245.

[28] K. Momberger, A. Belkacem, and A. H. Sorensen, Phys. Rev. A 53 (1996) 1605.

[29] J. W. Braun, Q. Su, and R. Grobe, Phys. Rev. A 59 (1999) 604.

[30] G. R. Mocken and C. H. Keitel, J. of Comp. Phys. 199 (2004) 558.

[31] F. F. Gourdeau, E. Lorin, and A. D. Bandrauk, Comp. Phys. Comm. 183 (2012) 1403.

[32] H. B. Nielsen and M. Ninomiya, Phys. Lett. B 105 (1981) 219.

[33] J. Tworzydlo, C. W. Groth, and C. W. J. Beenakker, Phys. Rev. B 78 (2008) 235438.

[34] J. J. Sakurai, Advanced Quantum Mechanics, Pearson Education India (2006).

[35] L. H. Ryder, Quantum Field Theory, Cambridge University Press (1996).

[36] W. Greiner, Relativistic quantum mechanics: Wave equations, Springer Berlin (2000).

[37] C. Itzykson and J. B. Zuber, Quantum Field Theory, Dover Publications Inc. New York (2005).

[38] M. Srednicki, Quantum Field Theory, Cambridge University Press (2007).

[39] J. C. Strikwerda, Finite Difference Schemes and Partial Differential Equations, SIAM Philadelphia (2004).

[40] G. R. Mocken and C. H. Keitel, Comp. Phys. Comm. 178 (2008) 868.

[41] P. H. Ginsparg and K. G. Wilson, Phys. Rev. D 25 (1982) 2649.

[42] R. Hammer, W. Pötz, unpublished.

9.6 APPENDIX A: Scheme with Peierls substitution for the introduction of non-vanishing in-plane "magnetization" m_x and m_y

Here we show the consequence of the Peierls substitution Eq. (9.4) into the scheme Eq. (9.3) to introduce non-vanishing "magnetization" m_x and m_y terms into the numerical scheme.

We first explore the effect of the substitution on difference quotients (derivative terms)

$$\frac{u_1 - u_2}{\Delta} \to \frac{e^{ia_1}u_1 - e^{ia_2}u_2}{\Delta} \, . \tag{9.25}$$

Simple regrouping gives the exact "product rule for differentiation on the lattice"

$$\frac{e^{ia_1}u_1 - e^{ia_2}u_2}{\Delta} = f_+(a_1, a_2)\frac{u_1 - u_2}{\Delta} + \frac{e^{ia_1} - e^{ia_2}}{\Delta}\frac{u_1 + u_2}{2} \, , \tag{9.26}$$

using the definition $f_\pm(a_1, a_2) = (e^{ia_1} \pm e^{ia_2})/2$. The last term on the rhs contains a difference quotient representing the derivative of an exponential. It may be approximated by the "chain rule" for the derivative of exponentials on the grid

$$\frac{e^{ia_1} - e^{ia_2}}{\Delta} = f_+(a_1, a_2)\frac{i(a_1 - a_2)}{\Delta} + \frac{1}{\Delta}O((a_1 - a_2)^3) \, . \tag{9.27}$$

The second type of terms to be dealt with are spatial averages of the structure

$$\frac{u_1 + u_2}{2} \to \frac{e^{ia_1}u_1 + e^{ia_2}u_2}{2} \, . \tag{9.28}$$

Here one arrives at

$$\frac{e^{ia_1}u_1 + e^{ia_2}u_2}{2} = f_+(a_1, a_2)\frac{u_1 + u_2}{2} + f_-(a_1, a_2)\frac{u_1 - u_2}{2} \, . \tag{9.29}$$

The scheme which then arises from the Peierls substitution (9.4) into Eq. (9.3) is

$$\begin{aligned}
& f_+(a_{j,k}^{n+1}, a_{j,k}^{n}) \left[\frac{u_{j,k}^{n+1} - u_{j,k}^{n}}{\Delta t} + i \left((m_z)_{j,k}^{n} + V_{j,k}^{n} \right) \frac{u_{j,k}^{n+1} + u_{j,k}^{n}}{2} \right] \\
& + \frac{e^{ia_{j,k}^{n+1}} - e^{ia_{j,k}^{n}}}{\Delta t} \frac{u_{j,k}^{n+1} + u_{j,k}^{n}}{2} + i f_-(a_{j,k}^{n+1}, a_{j,k}^{n}) \left((m_z)_{j,k}^{n} - V_{j,k}^{n} \right) \frac{u_{j,k}^{n+1} - u_{j,k}^{n}}{2} \\
& + \frac{1}{2} f_+(a_{j,k-1}^{n}, a_{j-1,k-1}^{n}) \frac{v_{j,k-1}^{n} - v_{j-1,k-1}^{n}}{\Delta x} + \frac{e^{ia_{j,k-1}^{n}} - e^{ia_{j-1,k-1}^{n}}}{\Delta x} \frac{v_{j,k-1}^{n} + v_{j-1,k-1}^{n}}{4} \\
& + \frac{1}{2} f_+(a_{j,k}^{n}, a_{j-1,k}^{n}) \frac{v_{j,k}^{n} - v_{j-1,k}^{n}}{\Delta x} + \frac{e^{ia_{j,k}^{n}} - e^{ia_{j-1,k}^{n}}}{\Delta x} \frac{v_{j,k}^{n} + v_{j-1,k}^{n}}{4} \\
& - \frac{i}{2} f_+(a_{j-1,k}^{n}, a_{j-1,k-1}^{n}) \frac{v_{j-1,k}^{n} - v_{j-1,k-1}^{n}}{\Delta y} - i \frac{e^{ia_{j-1,k}^{n}} - e^{ia_{j-1,k-1}^{n}}}{\Delta y} \frac{v_{j-1,k}^{n} + v_{j-1,k-1}^{n}}{4} \\
& - \frac{i}{2} f_+(a_{j,k}^{n}, a_{j,k-1}^{n}) \frac{v_{j,k}^{n} - v_{j,k-1}^{n}}{\Delta y} - i \frac{e^{ia_{j,k}^{n}} - e^{ia_{j,k-1}^{n}}}{\Delta y} \frac{v_{j,k}^{n} + v_{j,k-1}^{n}}{4} = 0 \,,
\end{aligned} \tag{9.30}$$

and

$$\begin{aligned}
& f_+(a_{j,k}^{n+1}, a_{j,k}^{n}) \left[\frac{v_{j,k}^{n+1} - v_{j,k}^{n}}{\Delta t} - i \left((m_z)_{j,k}^{n+1} - V_{j,k}^{n+1} \right) \frac{v_{j,k}^{n+1} + v_{j,k}^{n}}{2} \right] \\
& + \frac{e^{ia_{j,k}^{n+1}} - e^{ia_{j,k}^{n}}}{\Delta t} \frac{v_{j,k}^{n+1} + v_{j,k}^{n}}{2} - i f_-(a_{j,k}^{n+1}, a_{j,k}^{n}) \left((m_z)_{j,k}^{n+1} + V_{j,k}^{n+1} \right) \frac{v_{j,k}^{n+1} - v_{j,k}^{n}}{2} \\
& + \frac{1}{2} f_+(a_{j+1j,k}^{n+1}, a_{j,k}^{n+1}) \frac{u_{j+1,k}^{n+1} - u_{j,k}^{n+1}}{\Delta x} + \frac{e^{ia_{j+1,k}^{n+1}} - e^{ia_{j,k}^{n+1}}}{\Delta x} \frac{u_{j+1,k}^{n+1} + u_{j,k}^{n+1}}{4} \\
& + \frac{1}{2} f_+(a_{j+1,k+1}^{n+1}, a_{j,k+1}^{n+1}) \frac{u_{j+1,k+1}^{n+1} - u_{j,k+1}^{n+1}}{\Delta x} + \frac{e^{ia_{j+1,k+1}^{n+1}} - e^{ia_{j,k+1}^{n+1}}}{\Delta x} \frac{u_{j+1,k+1}^{n+1} + u_{j,k+1}^{n+1}}{4} \\
& + \frac{i}{2} f_+(a_{j,k+1}^{n+1}, a_{j,k}^{n+1}) \frac{u_{j,k+1}^{n+1} - u_{j,k}^{n+1}}{\Delta y} + i \frac{e^{ia_{j,k+1}^{n+1}} - e^{ia_{j,k}^{n+1}}}{\Delta y} \frac{u_{j,k+1}^{n+1} + u_{j,k}^{n+1}}{4} \\
& + \frac{i}{2} f_+(a_{j+1,k+1}^{n+1}, a_{j+1,k}^{n+1}) \frac{u_{j+1,k+1}^{n+1} - u_{j+1,k}^{n+1}}{\Delta y} + i \frac{e^{ia_{j+1,k+1}^{n+1}} - e^{ia_{j+1,k}^{n+1}}}{\Delta y} \frac{u_{j+1,k+1}^{n+1} + u_{j+1,k}^{n+1}}{4} \\
& = 0 \,.
\end{aligned} \tag{9.31}$$

It immediately becomes more transparent when the chain rule approximation Eq. (9.27) is used

$$
\begin{aligned}
&f_+(a^{n+1}_{j,k}, a^n_{j,k}) \left[\frac{u^{n+1}_{j,k} - u^n_{j,k}}{\Delta t} + i \left((m_z)^n_{j,k} + V^n_{j,k} + \frac{a^{n+1}_{j,k} - a^n_{j,k}}{\Delta t} \right) \frac{u^{n+1}_{j,k} + u^n_{j,k}}{2} \right] \\
&+ i f_-(a^{n+1}_{j,k}, a^n_{j,k}) \left((m_z)^n_{j,k} - V^n_{j,k} \right) \frac{u^{n+1}_{j,k} - u^n_{j,k}}{2} \\
&+ \frac{1}{2} f_+(a^n_{j,k-1}, a^n_{j-1,k-1}) \left[\frac{v^n_{j,k-1} - v^n_{j-1,k-1}}{\Delta x} + \frac{v^n_{j,k-1} + v^n_{j-1,k-1}}{2} \frac{i(a^n_{j,k-1} - a^n_{j-1,k-1})}{\Delta x} \right] \\
&+ \frac{1}{2} f_+(a^n_{j,k}, a^n_{j-1,k}) \left[\frac{v^n_{j,k} - v^n_{j-1,k}}{\Delta x} + \frac{v^n_{j,k} + v^n_{j-1,k}}{2} \frac{i(a^n_{j,k} - a^n_{j-1,k})}{\Delta x} \right] \\
&- \frac{i}{2} f_+(a^n_{j-1,k}, a^n_{j-1,k-1}) \left[\frac{v^n_{j-1,k} - v^n_{j-1,k-1}}{\Delta y} + \frac{v^n_{j-1,k} + v^n_{j-1,k-1}}{2} \frac{i(a^n_{j-1,k} - a^n_{j-1,k-1})}{\Delta y} \right] \\
&- \frac{i}{2} f_+(a^n_{j,k}, a^n_{j,k-1}) \left[\frac{v^n_{j,k} - v^n_{j,k-1}}{\Delta y} + \frac{v^n_{j,k} + v^n_{j,k-1}}{2} \frac{i(a^n_{j,k} - a^n_{j,k-1})}{\Delta y} \right] = 0\,,
\end{aligned}
\tag{9.32}
$$

and

$$
\begin{aligned}
&f_+(a^{n+1}_{j,k}, a^n_{j,k}) \left[\frac{v^{n+1}_{j,k} - v^n_{j,k}}{\Delta t} - i \left((m_z)^{n+1}_{j,k} - V^{n+1}_{j,k} - \frac{a^{n+1}_{j,k} - a^n_{j,k}}{\Delta t} \right) \frac{v^{n+1}_{j,k} + v^n_{j,k}}{2} \right] \\
&- i f_-(a^{n+1}_{j,k}, a^n_{j,k}) \left((m_z)^{n+1}_{j,k} + V^{n+1}_{j,k} \right) \frac{v^{n+1}_{j,k} - v^n_{j,k}}{2} \\
&+ \frac{1}{2} f_+(a^{n+1}_{j+1j,k}, a^{n+1}_{j,k}) \left[\frac{u^{n+1}_{j+1,k} - u^{n+1}_{j,k}}{\Delta x} + \frac{u^{n+1}_{j+1,k} + u^{n+1}_{j,k}}{2} \frac{i(a^{n+1}_{j+1,k} - a^{n+1}_{j,k})}{\Delta x} \right] \\
&+ \frac{1}{2} f_+(a^{n+1}_{j+1,k+1}, a^{n+1}_{j,k+1}) \left[\frac{u^{n+1}_{j+1,k+1} - u^{n+1}_{j,k+1}}{\Delta x} + \frac{u^{n+1}_{j+1,k+1} + u^{n+1}_{j,k+1}}{2} \frac{i(a^{n+1}_{j+1,k+1} - a^{n+1}_{j,k+1})}{\Delta x} \right] \\
&+ \frac{i}{2} f_+(a^{n+1}_{j,k+1}, a^{n+1}_{j,k}) \left[\frac{u^{n+1}_{j,k+1} - u^{n+1}_{j,k}}{\Delta y} + \frac{u^{n+1}_{j,k+1} + u^{n+1}_{j,k}}{2} \frac{i(a^{n+1}_{j,k+1} - a^{n+1}_{j,k})}{\Delta y} \right] \\
&+ \frac{i}{2} f_+(a^{n+1}_{j+1,k+1}, a^{n+1}_{j+1,k}) \left[\frac{u^{n+1}_{j+1,k+1} - u^{n+1}_{j+1,k}}{\Delta y} + \frac{u^{n+1}_{j+1,k+1} + u^{n+1}_{j+1,k}}{2} \frac{i(a^{n+1}_{j+1,k+1} - a^{n+1}_{j+1,k})}{\Delta y} \right]
\end{aligned}
\tag{9.33}
$$

$$
= 0\,.
$$

Consistent with the “chain rule", under weak spatial and temporal variation of the magnetization (vector potential) $\mathbf{m}(x, y, t)$, the f_- terms may be dropped and the f_+ factors may be eliminated, leading to a simplified version of the form

$$
\begin{aligned}
&\frac{u^{n+1}_{j,k} - u^{n}_{j,k}}{\Delta t} + i\left((m_z)^n_{j,k} + V^n_{j,k} + \frac{a^{n+1}_{j,k} - a^n_{j,k}}{\Delta t} \right) \frac{u^{n+1}_{j,k} + u^n_{j,k}}{2} \\
&+ \frac{1}{2}\left[\frac{v^n_{j,k-1} - v^n_{j-1,k-1}}{\Delta x} + \frac{v^n_{j,k-1} + v^n_{j-1,k-1}}{2} \frac{i(a^n_{j,k-1} - a^n_{j-1,k-1})}{\Delta x} \right] \\
&+ \frac{1}{2}\left[\frac{v^n_{j,k} - v^n_{j-1,k}}{\Delta x} + \frac{v^n_{j,k} + v^n_{j-1,k}}{2} \frac{i(a^n_{j,k} - a^n_{j-1,k})}{\Delta x} \right] \\
&- \frac{i}{2}\left[\frac{v^n_{j-1,k} - v^n_{j-1,k-1}}{\Delta y} + \frac{v^n_{j-1,k} + v^n_{j-1,k-1}}{2} \frac{i(a^n_{j-1,k} - a^n_{j-1,k-1})}{\Delta y} \right] \\
&- \frac{i}{2}\left[\frac{v^n_{j,k} - v^n_{j,k-1}}{\Delta y} + \frac{v^n_{j,k} + v^n_{j,k-1}}{2} \frac{i(a^n_{j,k} - a^n_{j,k-1})}{\Delta y} \right] = 0\,,
\end{aligned}
\tag{9.34}
$$

$$
\begin{aligned}
&\frac{v^{n+1}_{j,k} - v^{n}_{j,k}}{\Delta t} - i\left((m_z)^{n+1}_{j,k} - V^{n+1}_{j,k} - \frac{a^{n+1}_{j,k} - a^n_{j,k}}{\Delta t} \right) \frac{v^{n+1}_{j,k} + v^n_{j,k}}{2} \\
&+ \frac{1}{2}\left[\frac{u^{n+1}_{j+1,k} - u^{n+1}_{j,k}}{\Delta x} + \frac{u^{n+1}_{j+1,k} + u^{n+1}_{j,k}}{2} \frac{i(a^{n+1}_{j+1,k} - a^{n+1}_{j,k})}{\Delta x} \right] \\
&+ \frac{1}{2}\left[\frac{u^{n+1}_{j+1,k+1} - u^{n+1}_{j,k+1}}{\Delta x} + \frac{u^{n+1}_{j+1,k+1} + u^{n+1}_{j,k+1}}{2} \frac{i(a^{n+1}_{j+1,k+1} - a^{n+1}_{j,k+1})}{\Delta x} \right] \\
&+ \frac{i}{2}\left[\frac{u^{n+1}_{j,k+1} - u^{n+1}_{j,k}}{\Delta y} + \frac{u^{n+1}_{j,k+1} + u^{n+1}_{j,k}}{2} \frac{i(a^{n+1}_{j,k+1} - a^{n+1}_{j,k})}{\Delta y} \right] \\
&+ \frac{i}{2}\left[\frac{u^{n+1}_{j+1,k+1} - u^{n+1}_{j+1,k}}{\Delta y} + \frac{u^{n+1}_{j+1,k+1} + u^{n+1}_{j+1,k}}{2} \frac{i(a^{n+1}_{j+1,k+1} - a^{n+1}_{j+1,k})}{\Delta y} \right] = 0\,,
\end{aligned}
\tag{9.35}
$$

Here $\hat{V}^{n(+1)}_{j,k} = V^{n(+1)}_{j,k} + \frac{a^{n+1}_{j,k} - a^n_{j,k}}{\Delta t}$ denotes the net scalar potential in presence of a vector potential. The x and y components of the magnetization (vector potential) on the grid, respectively, are given by

$$
\begin{aligned}
(m_x)^n_{j,k} &\approx \frac{a^n_{j,k} - a^n_{j-1,k}}{\Delta x} \approx \frac{a^n_{j,k-1} - a^n_{j-1,k-1}}{\Delta x}\,, \\
(m_y)^n_{j,k} &\approx \frac{a^n_{j-1,k} - a^n_{j-1,k-1}}{\Delta y} \approx \frac{a^n_{j,k} - a^n_{j-1,k-1}}{\Delta y}\,, \\
(m_x)^{n+1}_{j,k} &\approx \frac{a^{n+1}_{j+1,k} - a^{n+1}_{j,k}}{\Delta x} \approx \frac{a^{n+1}_{j+1,k+1} - a^{n+1}_{j,k+1}}{\Delta x}\,,
\end{aligned}
$$

and

$$(m_y)^{n+1}_{j,k} \approx \frac{a^{n+1}_{j,k+1} - a^{n+1}_{j,k}}{\Delta y} \approx \frac{a^{n+1}_{j+1,k+1} - a^{n+1}_{j+1,k}}{\Delta y} \,. \tag{9.36}$$

Using these simplifications we finally arrive at the scheme Eqs. (9.5) and (9.6)

$$\begin{aligned}\frac{u^{n+1}_{j,k} - u^{n}_{j,k}}{\Delta t} = &- i\left((m_z)^n_{j,k} + \hat{V}^n_{j,k}\right)\frac{u^{n+1}_{j,k} + u^{n}_{j,k}}{2}\\ &- \frac{v^n_{j,k-1} - v^n_{j-1,k-1} + v^n_{j,k} - v^n_{j-1,k}}{2\Delta x}\\ &+ i\frac{v^n_{j-1,k} - v^n_{j-1,k-1} + v^n_{j,k} - v^n_{j,k-1}}{2\Delta y}\\ &- i(m_x)^n_{j,k}\frac{v^n_{j,k} + v^n_{j-1,k} + v^n_{j,k-1} + v^n_{j-1,k-1}}{4}\\ &- (m_y)^n_{j,k}\frac{v^n_{j-1,k} + v^n_{j-1,k-1} + v^n_{j,k} + v^n_{j,k-1}}{4} \,,\end{aligned} \tag{9.37}$$

and

$$\begin{aligned}\frac{v^{n+1}_{j,k} - v^{n}_{j,k}}{\Delta t} = &+ i\left(m_z - \hat{V}^{n+1}_{j,k}\right)\frac{v^{n+1}_{j,k} + v^{n}_{j,k}}{2}\\ &- \frac{u^{n+1}_{j+1,k} - u^{n+1}_{j,k} + u^{n+1}_{j+1,k+1} - u^{n+1}_{j,k+1}}{2\Delta x}\\ &- \frac{u^{n+1}_{j,k+1} - u^{n+1}_{j,k} + u^{n+1}_{j+1,k+1} - u^{n+1}_{j+1,k}}{2\Delta y}\\ &- i(m_x)^{n+1}_{j,k}\frac{u^{n+1}_{j+1,k} + u^{n+1}_{j,k} + u^{n+1}_{j+1,k+1} + u^{n+1}_{j,k+1}}{4}\\ &+ (m_y)^{n+1}_{j,k}\frac{u^{n+1}_{j,k+1} + u^{n+1}_{j,k} + u^{n+1}_{j+1,k+1} + u^{n+1}_{j+1,k}}{4} \,.\end{aligned} \tag{9.38}$$

9.7 APPENDIX B: Derivation of a functional for the norm which is exactly conserved by the scheme

The proof of Eq. (9.21) can be given as follows [24]. Form the scalar product of the first of equation Eqs. (9.3) with $(u^{n+1} + u^n)$, with the latter applied from the left, and retain the real part of the resulting equation. This gives, using the scalar products introduced above Eqs. (9.18) to (9.20),

$$\begin{aligned}\frac{||u^{n+1}||^2 - ||u^n||^2}{\Delta t} = &- \Re\left\{ \frac{(u^{n+1}+u^n; v^n)_{0,-} - (u^{n+1}+u^n; v^n)_{-,-}}{2\Delta x} \right. \\ &\left. \qquad + \frac{(u^{n+1}+u^n; v^n)_{0,0} - (u^{n+1}+u^n; v^n)_{-,0}}{2\Delta x} \right\} \\ &- \Im\left\{ \frac{(u^{n+1}+u^n; v^n)_{-,0} - (u^{n+1}+u^n; v^n)_{-,-}}{2\Delta y} \right. \\ &\left. \qquad + \frac{(u^{n+1}+u^n; v^n)_{0,0} - (u^{n+1}+u^n; v^n)_{0,-}}{2\Delta y} \right\} .\end{aligned} \tag{9.39}$$

Form the scalar product between the second equation of Eqs. (9.3) with $(v^{n+1} + v^n)$, with the latter applied from the right, and take the real part of this equation. This gives

$$\begin{aligned}\frac{||v^{n+1}||^2 - ||v^n||^2}{\Delta t} = &- \Re\left\{ \frac{(u^{n+1}; v^{n+1}+v^n)_{-,0} - (u^{n+1}; v^{n+1}+v^n)_{0,0}}{2\Delta x} \right. \\ &\left. \qquad + \frac{(u^{n+1}; v^{n+1}+v^n)_{-,-} - (u^{n+1}; v^{n+1}+v^n)_{0,-}}{2\Delta x} \right\} \\ &- \Im\left\{ \frac{(u^{n+1}; v^{n+1}+v^n)_{0,-} - (u^{n+1}; v^{n+1}+v^n)_{0,0}}{2\Delta y} \right. \\ &\left. \qquad + \frac{(u^{n+1}; v^{n+1}+v^n)_{-,-} - (u^{n+1}; v^{n+1}+v^n)_{-,0}}{2\Delta y} \right\} .\end{aligned} \tag{9.40}$$

Adding these two equations yields, on the lhs, $||u^{n+1}||^2 + ||v^{n+1}||^2 - ||u^n||^2 + ||v^n||^2$. On the rhs one finds three types of terms: scalar products between equal-time components (respectively n with n and $n{+}1$ with $n{+}1$) and those mixing n with $n+1$. The latter cancel in pairs using a shift of indices, such as $(u^n; v^{n'})_{-,0} - (u^n; v^{n'}) = \sum_{jk}(u^n_{j,k}; v^{n'}_{j-1,k} - v^{n'}_{j,k}) = \sum_{jk}(u^n_{j+1,k} - u^n_{j,k}; v^{n'}_{j,k})$. The m_z and scalar potential terms vanish when taking the real part. One obtains,

$$
\begin{aligned}
&||u^{n+1}||^2 - ||u^n||^2 + ||v^{n+1}||^2 - ||v^n||^2 = \\
&- r_x \Re\left\{(u^n; v^n)_{0,-} - (u^n; v^n)_{-,-} + (u^n; v^n)_{0,0} - (u^n; v^n)_{-,0}\right\} \\
&- r_y \Im\left\{(u^n; v^n)_{-,0} - (u^n; v^n)_{-,-} + (u^n; v^n)_{0,0} - (u^n; v^n)_{0,-}\right\} \\
&+ r_x \Re\left\{(u^{n+1}; v^{n+1})_{-,0} - (u^{n+1}; v^{n+1})_{0,0} + (u^{n+1}; v^{n+1})_{-,-} - (u^{n+1}; v^{n+1})_{0,-}\right\} \\
&+ r_y \Im\left\{(u^{n+1}; v^{n+1})_{0,-} - (u^{n+1}; v^{n+1})_{0,0} + (u^{n+1}; v^{n+1})_{-,-} - (u^{n+1}; v^{n+1})_{-,0}\right\} .
\end{aligned}
\tag{9.41}
$$

This is the identity $E_{n+1}{=}E_n$.

In case of space and/or time dependent m_x or m_y, an exactly conserved quantity is not obtained in this fashion from the Eqs. (9.5) and (9.6). However, it is readily constructed for the “exact" equations obtained within the Peierls substitution, Eqs. (9.30) and (9.32), by simply applying it to E_n to give $\hat{E}_n$ which has the exact structure of E_n, just with u, v replaced by $\hat{u}, \hat{v}$.

9.8 APPENDIX C: Stability

In this appendix we prove the stability conditions for arbitrary space- and time-dependent magnetization vector and potential terms, Eq. 9.22 and Eq. 9.23. We use norm conservation Eq. (9.21) and proceed as follows

$$\begin{aligned} E_0 = E_n =& ||u^n||^2 + ||v^n||^2 \\ & - r_x \Re\left\{(u^n;v^n)_{0,-} - (u^n;v^n)_{-,-} + (u^n;v^n)_{0,0} - (u^n;v^n)_{-,0}\right\} \\ & - r_y \Im\left\{(u^n;v^n)_{-,0} - (u^n;v^n)_{-,-} + (u^n;v^n)_{0,0} - (u^n;v^n)_{0,-}\right\} \end{aligned}$$

$$\begin{aligned} &= ||u^n||^2 + ||v^n||^2 - \Re\Big\{(r_x + ir_y)\big[(u^n;v^n)_{0,-} - (u^n;v^n)_{-,0}\big] \\ &\qquad\qquad - (r_x - ir_y)\big[(u^n;v^n)_{-,-} - (u^n;v^n)_{0,0}\big]\Big\} \\ &\geq ||u^n||^2 + ||v^n||^2 - \Bigg|\Re\Big\{(r_x + ir_y)\big[(u^n;v^n)_{0,-} - (u^n;v^n)_{-,0}\big] \\ &\qquad\qquad - (r_x - ir_y)\big[(u^n;v^n)_{-,-} - (u^n;v^n)_{0,0}\big]\Bigg|\Big\} \end{aligned}$$

$$\begin{aligned} &\geq ||u^n||^2 + ||v^n||^2 - \mid \Re\left\{(r_x + ir_y)(u^n;v^n)_{0,-}\right\} \mid - \mid \Re\left\{(r_x + ir_y)(u^n;v^n)_{-,0}]\right\} \mid \\ &\qquad - \mid \Re\left\{(r_x - ir_y)u^n;v^n)_{-,-}\right\} \mid - \mid \Re\left\{(r_x - ir_y)(u^n;v^n)_{0,0}\right\} \mid \end{aligned}$$

$$\begin{aligned} &\geq ||u^n||^2 + ||v^n||^2 - \sqrt{r_x^2 + r_y^2}\Big[\mid \Re\left\{(u^n_-;v^n)_{0,-}\right\} \mid + \mid \Re\left\{(u^n_-;v^n)_{-,0}\right\} \mid \\ &\qquad + \mid \Re\left\{(u^n_+;v^n)_{-,-}\right\} \mid + \mid \Re\left\{(u^n_+;v^n)_{0,0}\right\} \mid \Big] \end{aligned}$$

$$\geq ||u^n||^2 + ||v^n||^2 - 2\sqrt{r_x^2 + r_y^2}\left(||u^n||^2 + ||v^n||^2\right) = (1 - \tilde{r})\left(||u^n||^2 + ||v^n||^2\right).$$

Here we have used the inequality $2 \mid \Re\{(a,b)\} \mid \leq ||a||^2 + ||b||^2$, as well as the abbreviation $u^n_\pm = e^{\pm i\phi}u_n$, where $\phi = \arctan\left(r_y/r_x\right)$. Note also that the norm of a spinor component shifted by $\pm\Delta x, \pm\Delta y$ is equal to the norm of the unshifted component under zero or periodic boundary conditions.

The case $\tilde{r} = 1$ can be dealt with as follows (omitting the superscript n for brevity). Starting from the last identity in the previous proof, for this case one may write

$$E_0 = E_n = ||u||^2 + ||v||^2 + \frac{1}{2}\Re\left\{(u_-;v)_{-,0} - (u_-;v)_{0,-} + (u_+;v)_{-,-} - (u_+;v)_{0,0}\right\}$$
$$= \frac{1}{4}\left[||\ u_+ + v_{-,-}\ ||^2 + ||\ u_+ - v\ ||^2 + ||\ u_- + v_{-,0}\ ||^2 + ||\ u_- - v_{0,-}\ ||^2\right] \tag{9.42}$$

Note once more, that the single subscript on the spinor component (u) indicates a phase shift, while a double subscript indicates a shift on the spatial grid (here applied to component v). Here we use identities of the form

$$\frac{1}{4}\left[||u_\pm + v||^2 + ||u_\pm - v'||^2\right] = \frac{1}{2}\left[||u||^2 + ||v||^2 + \Re\left\{(u_\pm, v) - (u_\pm, v')\right\}\right]$$

when $||v|| = ||v'||$. Note that this identity can be applied no more than twice, since $||u||^2 + ||v||^2$ is available in $E_n = E_0$. This limits the magnitude of $\tilde{r}$. In the second step we apply the inequality $2\left[||a_1 + b||^2 + ||a_2 - b||^2\right] \geq ||a_1 + a_2||^2$, whereby $u_\pm$ plays the role of b, to obtain

$$E_0 \geq \frac{1}{8}\left[||v_{-,-} + v||^2 + ||v_{0,-} + v_{-,0}||^2\right] \equiv ||\tilde{v}||^2 \; .$$

Attaching the phase factor of $r_\pm$ to the components v and the grid shifts to the components u, one obtains

$$E_0 \geq \frac{1}{8}\left[||u_{+,+} + u|^2 + ||u_{0,+} + u_{+,0}||^2\right] \equiv ||\tilde{u}||^2 .$$

Hence

$$||\tilde{u}||^2 + ||\tilde{v}||^2 \leq 2E_0 \; .$$

This discussion also shows that $E_n = E_0 \geq 0$ for $\tilde{r} \leq 1$ and thus provides a meaningful definition for a spinor norm within the scheme.

With E_0, u^n, and v^n, respectively, replaced by $\hat{E}_0$, $\hat{u}^n$, and $\hat{v}^n$ the stability condition for Eqs. (9.30) and (9.32) is shown under arbitrary space-time dependence of the external fields.

Chapter 10

PAPER REPRINT: SOLITONIC DIRAC FERMION WAVE GUIDE NETWORKS ON TOPOLOGICAL INSULATOR SURFACES

Applied Physics Letters 102 (2013)

R. Hammer, C. Ertler, and W. Pötz

Magnetic texturing on the surface of a topological insulator allows the design of wave guide networks and beam splitters for domain-wall Dirac fermions. Guided by simple analytic arguments we model a Dirac domain-wall fermion interferometer consisting of two parallel pathways imprinted by solitonic ferromagnetic texturing. A specially developed staggered-grid leap-frog discretization scheme in 2+1 dimensions with absorbing boundary conditions is employed to study the interferometer in an open device geometry. Its net transmission can be tuned from constructive to destructive interference, either by variation of the magnetization texture (effective path length) or an applied gate bias (wave length). Possible ways to observe and utilize this effect are discussed.

In this Letter we study the dynamics of domain-wall (DW) Dirac fermions, as may be found at the surface of a magnetically textured topological insulator. Beam splitters for chiral fermions based on magnetic texturing are used to model quantum interference effects, in analogy to interference in optical wave guides. We numerically investigate a two-armed quantum interferometer which can be controlled by magnetic structuring and an electric gate bias. It provides the operation principle for a Dirac fermion transistor. A recently developed numerical algorithm is used to demonstrate the 2+1 dimensional fermion wave packet dynamics within the interferometer under variation of gate bias and other structural properties.[1] Generalization to more complex networks is discussed.

Rapid progress has been made in the understanding, realization, and control of metallic surface states on three-dimensional (3D) topological insulators (TI).[2] Both the theoretical foundation for the existence and topological protection of Dirac fermion surface states within Chern-Simons theory, as well as subsequent experimental verification of Dirac-cone helical surface states with and without mass-gap have been presented.[2, 3, 4, 5] For a single cone, the essential dynamics near the TR degeneracy point is described by an effective 2D field theory and a single-particle Hamiltonian[2]

$$H = v\,(\boldsymbol{\sigma} \times \boldsymbol{\Pi}) \cdot \hat{\mathbf{z}} + \mathbf{M}(x, y) \cdot \boldsymbol{\sigma} + V(x, y, t)\mathbb{1} \tag{10.1}$$

leading to a 2D (2+1) Dirac equation for the surface states.[4, 6] Here, $v(\approx 5 \times 10^5 m/s)$, $\boldsymbol{\Pi} = \mathbf{p} + \frac{e}{c}\mathbf{A}$, and $\boldsymbol{\sigma}$ denote, respectively, the effective velocity, the kinetic momentum, and the Pauli vector. The first term on the r.h.s. describes the Dirac fermion spin-orbit interaction for vector potential $\mathbf{A}$, while second and third contribution, respectively, account for the Zeeman term in presence of a (quasi-static) effective magnetic field and an external scalar potential from a gate bias. The net effective magnetic field in general arises from an external B field and, more importantly, from an exchange interaction with magnetic impurities deposited at the surface. Physical origin may be ferromagnetic STM-like tips near the surface, magnetic texturing introduced by the proximity of insulating ferromagnetic layers, and/or magnetic doping.[4, 7, 8] It breaks TR symmetry of H and provides a space-dependent "mass term" $M_z(x, y)$. The order-of-magnitude for the mass-gap is expected to be several 10's of meV.[9] In contrast to graphene, the Pauli vector in Eq. (11.2) is proportional the physical fermion spin whereby the spin direction is locked perpendicular to the particle current density and the normal vector to the surface $\hat{\mathbf{z}}$.[2]

Electric currents measured near the surface of a TI have bulk and surface state contributions. With the positioning of the Fermi energy inside of

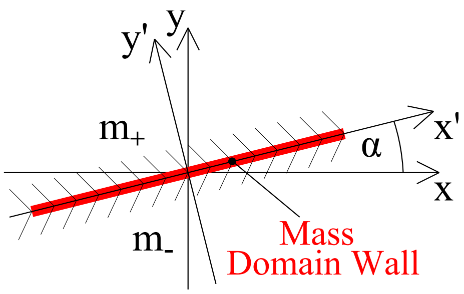

Figure 10.1: Mass DW on the 2D surface of a 3D TI: For $\lim_{y'\to\pm\infty} M(x',y') = m_\pm$ and $m_- m_+ < 0$ a CDWS localized in y'-direction forms.

the bulk gap of the insulator the bulk current contribution can be strongly suppressed.[10, 11] The surface contributions arise from the helical surface states and, under suitable magnetic texturing, from chiral domain-wall states (CDWS). Both are captured by H in Eq. (11.2). Realization of chiral surface states opens the door for new types of transport phenomena and prospects for device designs which utilize their coherence properties. Here we investigate theoretically ballistic Dirac fermion dynamics along helical edge channels.

Quasi-1D one-way edge channel form along the domain boundary between two 2D TI surface areas when the effective mass changes its sign, as sketched in Fig.10.1.[2, 4, 12] X-shaped crossings between pairs of DWs, as sketched in Fig.10.2, produce a "beam splitter" for chiral fermions, as shown below. To illustrate its principle we recall the low energy eigenstate localized near an effective-mass DW. For example let, as in Fig.10.1, the mass $M_z(x,y) = M_z(y')$ be allowed to vary in y'-direction only, with $y' = -x\sin\alpha + y\cos\alpha$, and let us thus assume translational invariance in x'-direction ($x' = x\cos\alpha + y\sin\alpha$), such that $\lim_{y'\to\pm\infty} M_z(y') = m_\pm$ and $m_- m_+ < 0$. Then, considering a Bloch DWCS, i. e., $M_{y'} = V = 0$, for the sake of discussion, a low energy channel state

$$\langle x, y\,|X', \pm\rangle \propto \phi_{\mathbf{o}}(\alpha) e^{\pm\frac{1}{\hbar v}\int_{y'_o}^{y'}(M_z(y'')\mp iM_{x'}(y''))dy'' + ik'_x x'},$$

$$\phi_{\mathbf{o}}(\alpha) = \frac{1}{\sqrt{2}}\begin{pmatrix} \pm i e^{-i\alpha/2} \\ e^{i\alpha/2} \end{pmatrix}, \tag{10.2}$$

exists for Eq. (11.2), with $E = \pm v\hbar\, k'_x$, with the upper sign for $m_+ < 0$ and $m_- > 0$, and the lower sign for $m_- < 0$ and $m_+ > 0$.

Now consider the symmetric junction A in Fig.10.2(a) arising from a rectangular crossing of two DWs, where the DW channel in $+x$-direction splits into the two channels along the $\pm y$-direction ($\alpha = \pm\pi/2$). At this junction we can express the incoming wave function $|X,+\rangle$ as a superposition of the Y-out-channel states $|X,+\rangle = 1/\sqrt{2}\,(|Y,+\rangle + i\,|-Y,+\rangle)$. The two components $|Y,+\rangle$ and $|-Y,+\rangle$, respectively, channeled along path 1 and 2, necessarily recombine at junction B in Fig.10.2(a) to $|X,+\rangle$ as long as the the phase difference between the upper and the lower channel is zero. However, the relative phase γ between path 1 and 2 can be set to a desired value by adjusting the gate bias V as shown in Fig.10.2(b) and/or by changing the relative path length by selectively changing the size of individual magnetic domains. Using the decomposition $|\pm Y,+\rangle = 1/\sqrt{2}\,(|\pm X,+\rangle - i\,|\mp X,+\rangle)$ one has at junction B, up to an overall phase,

$$|\psi(\gamma)\rangle = \cos(\gamma/2)\,|X,+\rangle + \sin(\gamma/2)\,|-X,+\rangle \ .$$

This gives $|X,+\rangle$ for $\gamma = 0$ and $|-X,+\rangle$ for $\gamma = \pi$ which corresponds to fermions propagating, respectively, from junction B out to the right (towards drain 2) and fermions going to the left (towards junction A). The phase difference determines selection of the out-channel. A phase shift can be introduced by an electric potential V, which locally shifts the dispersion by V. For a constant potential V applied over a path length L, a phase shift $\gamma = -V \cdot L/(v\hbar)$ is obtained. The transmission probability into drain 2 in Fig.10.2(b) may be written

$$T_2 = |\langle X,+|\,\psi\rangle|^2 = \cos^2\left(\frac{VL}{2v}\right) \ ,$$

and the transmission probability to drain 1 in Fig.10.2(b) is $T_1 = 1 - T_2$. Switching gate potentials, rather than the relative size and shape of magnetic domains, most likely is the more convenient way to control the device. Gate potentials can also be used to compensate imperfect magnetic texturing to calibrate the interferometer in experimental realizations.

We now proceed to study more realistic structures numerically. The interferometer is based on static solitonic 2D ferromagnetic DW structures, justified for hard, firmly pinned, and/or thick ferromagnetic domains, and sufficiently low currents.[14, 15] The DW dynamics in general is known to be slow compared to the fermion dynamics allowing for adiabatic solution procedures.[16] We construct a model for the magnetic texture with anisotropy in z-direction from local-minimum solutions to the generic free energy functional in unit magnetization $|\,\mathbf{m}\,| = 1$ and $a, b > 0$

$$\mathcal{F}(\mathbf{m}) = \frac{1}{2}\int dV\,\left[a\big((\nabla m_x)^2 + (\nabla m_y)^2 + (\nabla m_z)^2\big) - b m_z^2\right] \ .$$

In spherical coordinate parametrization $\theta(x,y)$ and $\phi(x,y)$ the functional in

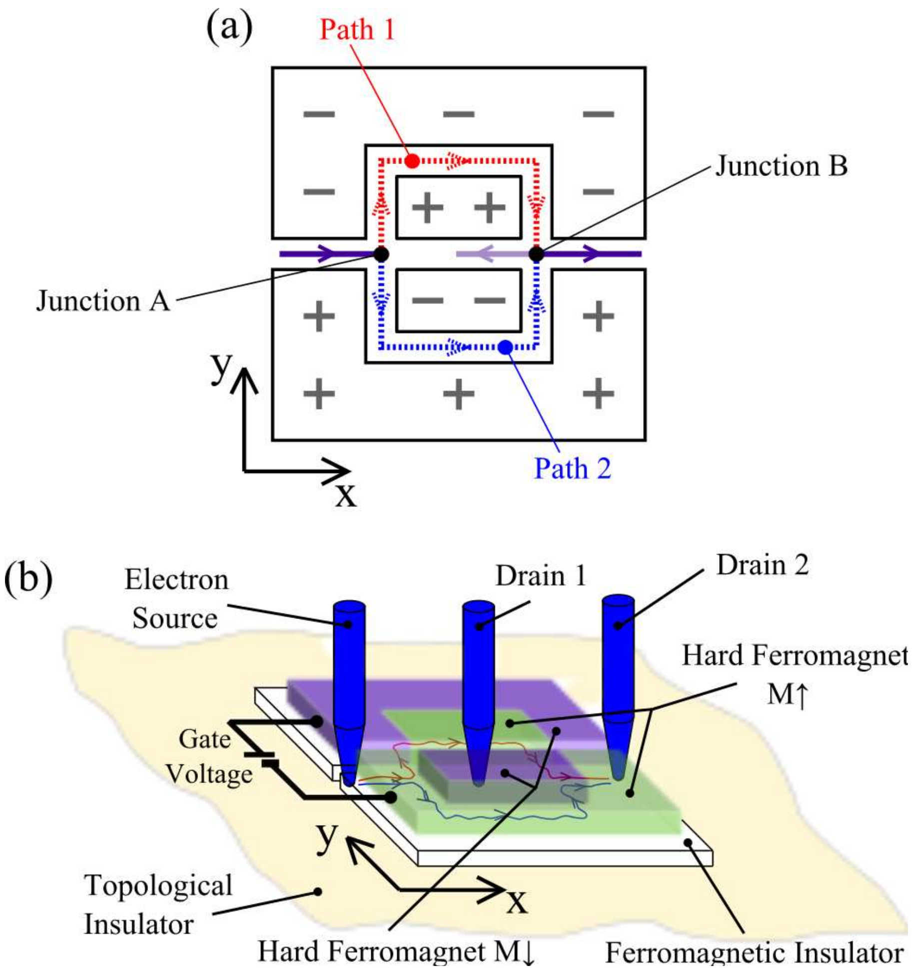

Figure 10.2: Coherent Dirac fermion interferometer on a TI surface: Chiral channel states form at the domain boundaries between magnetization regions of opposite direction ($M\uparrow\ /M\downarrow$). There are two allowed paths trough the structure (wavy lines). When a gate voltage is applied the paths pick up an additional phase leading to destructive or constructive interference depending on its magnitude and the device can be switched from transmission to the left (drain 1) to transmission to the right (drain 2).

$\mathbf{m} = (\sin\theta\cos\phi, \sin\theta\sin\phi, \cos\theta)$ is degenerate with respect to ϕ

$$\mathcal{F}(\mathbf{m}) = \frac{1}{2}\int dxdy\,\left[a(\partial x\theta)^2 - b\cos(\theta)^2\right]\ .$$

For a DW in y-direction the magnetization varies in x-direction only and variational calculus leads to the (static) sine-Gordon equation $\theta_{xx} = \sin\theta$

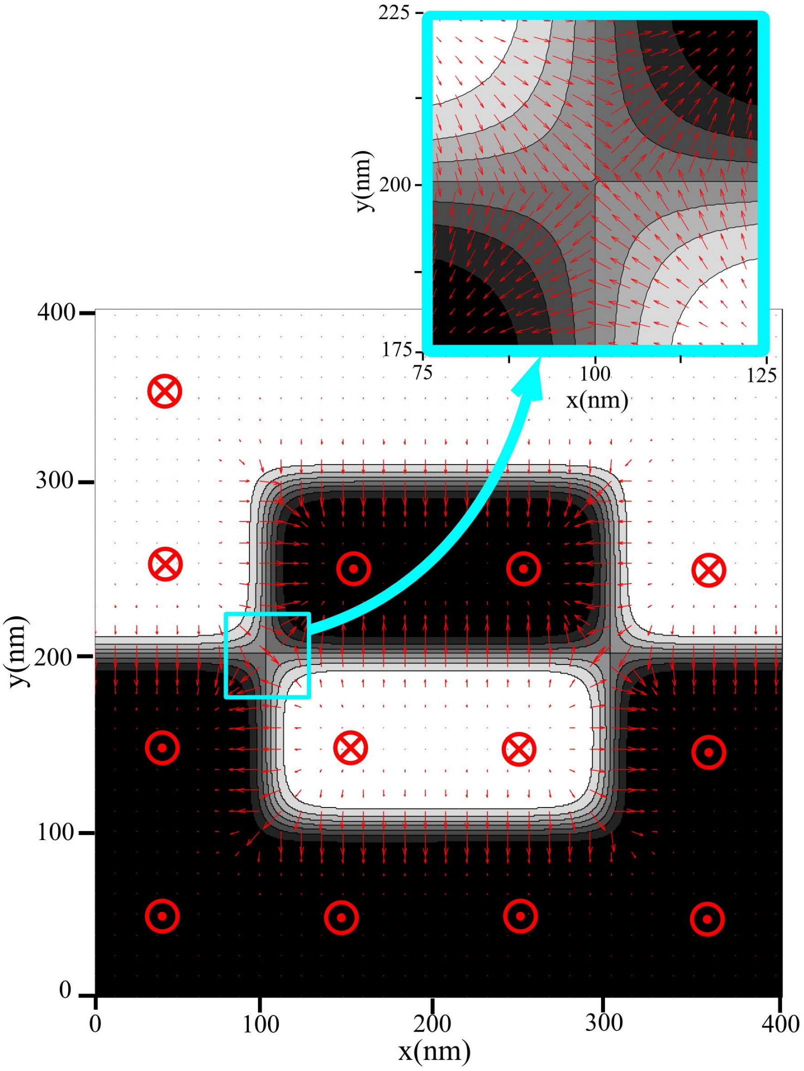

Figure 10.3: Magnetic Néel wall texture of the insulating ferromagnet on the surface of the topological insulator. The contour plot shows the z-component of the magnetization m_z. The asymptotic values $m_z = -1$ are represented by black and $m_z = +1$ by white color. The vector plot shows (m_x, m_y). The dotted and crossed circles represent the magnetization direction of the thick hard ferromagnets pinning the thin insulating ferromagnetic layer.

giving, for present boundary conditions, the well-known kink-soliton solution, degenerate in DW position x_{dw}, $\theta(x) = 2\tan^{-1} e^{-(x-x_{dw})/\lambda_{dw}}$, with $\lambda_{dw} = \sqrt{a/b}$. [13] The azimuthal angle can e.g. be chosen to be $\phi = \pm\pi/2$

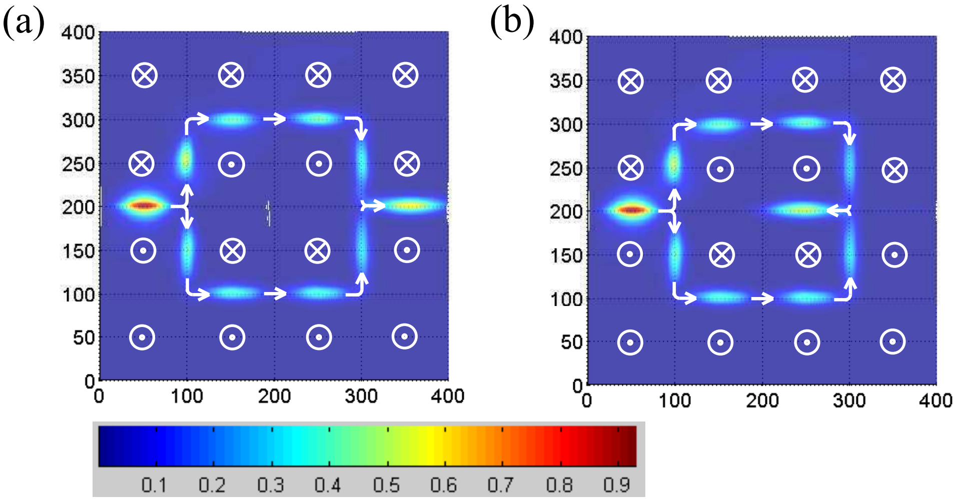

Figure 10.4: Wave packet propagation in the interferometer with Bloch walls for (a) phase difference $\gamma = 0$ and (b) phase difference $\gamma = \pi$. The wave packet is shown for increasing time as it propagates along the DW channels. The color (or brightness variation) encodes the probability density $|\psi|^2$.

for a Bloch or $\phi = 0$ or π for a Néel DW. The superposition of such soliton solutions at given angle gives a new stationary soliton solution.[17, 18] For an individual rectangular intersection of two DWs we use the two soliton solution[18]

$$\theta(x) = 2\tan^{-1}\frac{e^{-(x-x_{dw})/\lambda_{dw}} + e^{(y-y_{dw})/\lambda_{dw}}}{1 + e^{-(x-x_{dw})/\lambda_{dw}-(y-y_{dw})/\lambda_{dw}}}\ .$$

The width of the DWs is chosen to be small compared to the distance between parallel DW solitons. Thus, in good approximation, these two-soliton solutions can be superposed to construct the magnetic texture for a Dirac fermion interferometer, as shown in Fig.10.3 for a magnetic Néel wall realization. For the simulations below individual magnetic domains are chosen to have a length scale which is large compared to the transverse localization length of the channel state which is determined by the asymptotic values of the mass-profile, see Eq.(10.2). Physically such ferromagnetic DW structures may be produced below T_c by ferromagnetic impurities at the surface with the magnetization direction controlled and stabilized by nanomagnets above the surface.

According to Eq. (11.2) the presence of magnetic impurities and a stabilizing external B-field has several implications for the Dirac fermion dynamics. The net B-field consisting of external B-field and the magnetization of impurity spins enters the spin-orbit term via $\mathbf{A}$. Both contributions

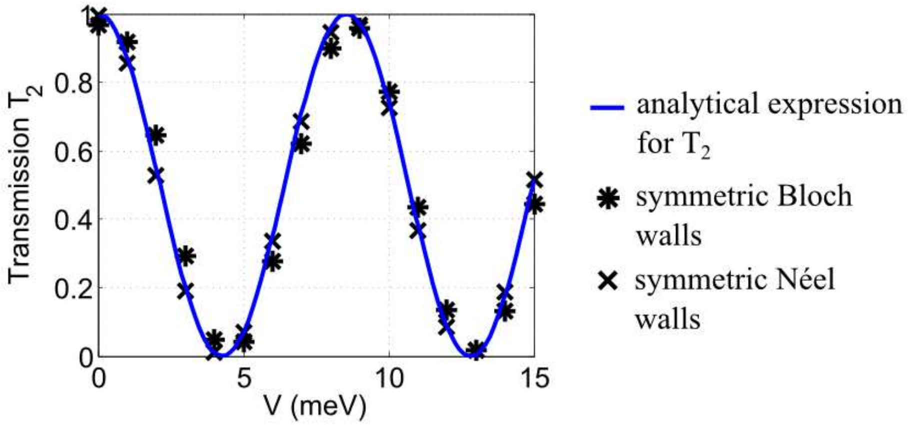

Figure 10.5: Transmission of the coherent fermion interferometer (to drain 2) as a function of the gate voltage. The solid line represents the analytic expression, and the markers are results of the simulation.

also enter the Zeeman term ("mass term"): the external B-field produces a Zeeman splitting and the impurity magnetization leads to an exchange interaction with the Dirac fermion. Here the latter, estimated to be of the order of several tens of meV represents the dominant contribution.[9] With a coupling strength $J \approx 130$ meV nm^2, fermion g-factor 20 the effective magnetic exchange field associated with a mass gap of 25 meV is of the order of 10T, making the influence of a realistic additional external B-field arising from nanomagnets of the order of 0.1T (or less) negligible in the Zeeman term.[8, 19, 20] The impurity magnetization contribution to the total B-field can be estimated to be less than 10^{-2} T, e.g. for Mn impurities.[21] Finally, the contribution of the external B-field to the spin-orbit term has a negligible effect on the dynamics of DW Dirac fermions compared to the in plane component of the exchange term, as we have verified numerically. Their formation and dynamics is dictated by the DW structure and the external bias. In principle there is an additional topological field, due to the magnetoelectric effect, but it is extremely small in magnitude ($\leq 10^{-6}T$).[2, 15]

Numerical treatment of the Dirac fermion wave packet dynamics in the soliton interferometer texture is treated within a staggered-grid leap frog scheme which preserves the free-particle linear energy dispersion along the main simulation axes exactly. By putting a layer with imaginary potential around the simulation region it allows an easy implementation of absorbing boundary conditions. Similarly, particle source and drain can be modeled.[1, 22] For the present numerical analysis of the wave packet dynamics the magnetic texture shown in Fig.10.3 is fed into Eq.(11.2) using $\mathbf{M}(x,y) = J\mathbf{m}(\mathbf{x},\mathbf{y})$. In general, J may differ for in-plane and perpendicular (z) direction of magnetization $\mathbf{m}$. In addition a gate bias is applied on the upper half-plane (path 1) over a channel length of ≈ 300 nm to adjust the relative phase in the two arms. We use $v = 6.2 \times 10^5 m/s$. The initial wave packet is prepared with mean energy of 30 meV and half Gaussian width ≈ 15 meV. The maximum mass gap due to the magnetization is chosen to be 50 meV. This leads to a transverse localization length of about 50 nm for an isolated CDWS. Note, however, that the numerical simulation accounts for the magnetic texture of the entire structure and does not assume isolated channel states. The network of chiral channels in fact is a property of the entire structure and robust against moderate (magnetic) disorder. In particular, any cross talk between channels, essential near DW crossings, is accounted for and, in fact, utilized in the interferometer. Results for the interferometer, laid out in Fig.10.2 and imprinted upon the surface by using magnetic textures shown in Fig.10.3, are given in Figs.10.4 and 10.5. Fig.10.4 shows snapshots of the wave packet during its propagation across the structure. Incident from the left, at junction A it splits into two parts to propagate, respectively, along path 1 and 2, to recombine at junction B. For a phase difference $\gamma = 0$, shown in part (a) of Fig.10.4, the wave packet leaves the interferometer to the right, whereas for $\gamma = \pi$ in part (b) the wave packet is forced to the left back into the interferometer. Thus, Dirac fermions can exit the device either at drain 2 or 1 in Fig. 10.2, thus forming the foundation for a transistor based on DW fermions. Over the range of ≈ 4 meV the out-channel to drain 2 can be tuned from open to closed. The computed interference fringes versus gate bias for transmission probability T_2, plotted in Fig.10.5, confirm the analytic predictions above for both Bloch and Néel wall configuration.

In summary, we propose electronic networks of CDWS arising from magnetic domains built into the surface of topological insulators. The CDWS can be understood as arising from the interface between two half quantized Hall states with opposite Hall conductivity, leading to a net integer quantum Hall state.[2] The intersection of two DWs provides a Dirac fermion beam splitter. The combination of two such splitters leads to an interferometer which can be controlled by an electric gate and be extended to produce a “Dirac fermion transistor". The device is robust against (magnetic) perturbations as long as the overall domain structure is preserved, domain sizes are large compared to the transverse localization length of the CDWS and DWs can be stabilized on a time scale characteristic for the fermion transmission. Structural imperfections and disorder can readily be modeled within our approach. The extension to more complex Dirac fermion networks is straight-forward in principle, with DWs serving as one-way wave guides and intersections of DW boundaries providing beam splitters. Phase differences can be calibrated and controlled by electric gates, and charge can be provided by electric contacts. More complex time-dependent phenomena, including Dirac-fermion-induced DW motion, can be treated within our numerical approach when adding to it the dynamics of the solitonic magnetic DWs, e.g within a Landau-Lifshits-Gilbert-type equation.[14, 16] Experimental challenges for realization include the avoidance of unwanted current contributions, a problem related to the positioning of the Fermi level, as well as successful magnetic texturing of TI surfaces. A preliminary summary of the numerical scheme and a study of Dirac fermion propagation near non-rectangular DW intersections is available online.[22]

We acknowledge support from the Austrian Science Foundation project I395-N16.

REFERENCES

[1] R. Hammer and W. Pötz, Staggered-grid leap-frog scheme for the (2+1)D Dirac equation, submitted.

[2] X. L. Qi and S. C. Zhang, Rev. Mod. Phys. 83, 1057 (2011).

[3] J. E. Moore and L. Balents, Phys. Rev. B 75, 121306 (2007).

[4] X. L. Qi, T. L. Hughes, and S. C. Zhang, Phys. Rev. B 78, 195424 (2008).

[5] Y. Xia, D. Qian, D. Hsieh, L. Wray, A. Pal, H. Lin, A. Bansil, D. Grauer, Y. S. Hor, R. J. Cava, and M. Z. Hasan, Nature Physics 5, 398 (2009).

[6] W. Y. Shan, H. Z. Lu, and S. Q. Shen, New J. Phys. 12, 043048 (2010).

[7] Y. L. Chen, J. H. Chu, J. G. Analyits, Z. K. Liu, K. Igarashi, H. H. Kuo, X. L. Qi, S. K. Mo, R. G. Moore, D. H. Lu, et al., Science 329, 659 (2010).

[8] Q. Liu, C. X. Liu, C. Xu, X. L. Qi, and S. C. Zhang, Phys. Rev. Lett. 102, 156603 (2009).

[9] W. Luo and X. L. Qi, Phys. Rev. B 87, 085431 (2013).

[10] J. G. Analytis, J. H. Chu, Y. Chen, F. Corredor, R. D. McDonald, Z. X. Shen, and Ian R. Fisher, Phys. Rev. B 81, 204507 (2010).

[11] H. Peng, K. Lai, D. Kong, S. Meister, Y. Chen, X. L. Qi, S. C. Zhang, Z. X. Shen, and Y. Cui, Nature Materials 9, 225 (2010).

[12] C. Wickles and W. Belzig, Phys. Rev. B 86, 035151 (2012).

[13] L. D. Landau, E. Lifshitz, Phys. Z. Sowjetunion 8 (1935).

[14] H. How, R. C. O'Handley, and F. R. Morgenthaler, Phys. Rev. B 40, 4808 (1989).

[15] I. Garate and M. Franz, Phys. Rev. Lett. 104, 146802 (2010).

[16] See, for example, M. Wenin, A. Windisch, and W. Pötz, J. Appl. Phys. 108, 103717 (2010).

[17] Graham Bowtell and Allan. E. G. Stuart, Phys. Rev. D 15, 3580 (1977).

[18] S. Novikov, S. V. Manakov, L. P. Pitaevskii, and V. E. Zarkharov, Theory of Solitons, Consultants Bureau, New York (1984).

[19] Zhenhua Wu, F. M. Peeters, and Kai Chang, Appl. Phys. Lett. 98, 162101 (2011).

[20] T. Hanaguri, K. Igarashi, M. Kawamura, H. Takagi, and T. Sasagawa, Phys. Rev. B 82, 081305 (2010).

[21] A. Van Esch, L. Van Bockstal, J. De Boeck, G. Verbanck, A. S. van Steenbergen, P. J. Wellmann, B. Grietens, R. Bogaerts, F. Herlach and G. Borghs, Phys. Rev. B 56, 13103 (1997).

[22] R. Hammer, C. Ertler, and W. Pötz, arXiv:1205.6941

Chapter 11

PAPER REPRINT: DYNAMICS OF DOMAIN-WALL DIRAC FERMIONS ON A TOPOLOGICAL INSULATOR: A CHIRAL FERMION BEAM SPLITTER

submitted to Physical Review B
preprint available at arXiv:1306.6139

R. Hammer and W. Pötz

The intersection of two ferromagnetic domain walls placed on the surface of topological insulators provides a one-way beam splitter for domain-wall Dirac fermions. Based on an analytic expression for a static two-soliton magnetic texture we perform a systematic numerical study of the propagation of Dirac wave packets along such intersections. A single-cone staggered-grid finite difference lattice scheme is employed in the numerical analysis. It is shown that the angle of intersection plays a decisive role in determining the splitting ratio of the fermion beam. For a non-rectangular intersection, the width and, to a lesser extent, the type of domain walls, e.g. Bloch or Néel, determine the properties of the splitter. As the ratio between domain-wall width and transverse localization length of the Dirac fermion is increased its propagation behavior changes from quantum-mechanical (wave-like) to classical ballistic (particle-like). An electric gate placed near the intersection offers a dynamic external control knob for adjusting the splitting ratio.

11.1 Introduction

There has been considerable progress in the investigation of Dirac fermions on (textured) TI surfaces in external electromagnetic fields. Experimentally, the Dirac cone spectrum with and without external magnetic field has been verified in recent experiments.[1, 2, 3] Position control of the Fermi energy within the bulk gap of the insulator has become feasible.[4, 5, 6, 7, 8, 9] Magnetic texturing of TI surfaces has been explored experimentally.[2, 10, 11] In one study using iron as the dopant, however, the easy axis has been reported to be in plane.[10] In thin films of MBE grown Cr doped ternary $(\mathrm{Bi}_x\mathrm{Sb}_{1-x})_2\mathrm{Te}_3$ ferromagnetic order has been reported.[12] With the theoretically predicted existence of topologically protected surface states confirmed in experiment, one of the next steps is to learn to manipulate them by structural design and to utilize their properties in chiral fermion devices. On the theoretical side, numerous papers have been published on related topics, such as magneto-transport on TI surfaces in presence of ferromagnetic layers, [13, 14, 15, 16, 17, 18] spin-polarized magnetic impurities on TI surfaces and Landau levels,[19, 20, 21, 22, 23] the interaction of magnetic domain walls with Dirac fermions,[24, 25, 26] lensing effects and transport perpendicular to domain walls,[27, 28] crossover from weak anti-localization to weak localization,[29] and gate control of TI channel states.[30] An interferometer for chiral fermions has been proposed recently.[31]

Surfaces of 3D topological insulators can be interpreted as a 2D domain wall between a spin-orbit driven band inversion within the insulator and normal band ordering in vacuum.[32, 34, 33, 35] The topologically protected gapless surface states in form of helical-state Dirac cones can be manipulated further by time-reversal-symmetry-breaking (TRB) perturbations applied to the surface.[32, 36, 37] Indeed, it has been known for quite a while that an effective-mass inversion domain wall can produce a 1D chiral edge eigenstate for a 2D Dirac fermion Hamiltonian.[38] Such edge states are required to observe a quantized Hall effect. TRB can be induced by exposure to an (effective) external magnetic field. For example, a ferromagnetic tip or permanent magnetic texture arising from the proximity of ferromagnets, in conjunction with magnetic doping of the surface, may be used to induce sign changes in the mass term of the effective Dirac equation.[35, 10, 11, 37, 2] The expected order-of-magnitude for the mass-gap in materials, such as $\mathrm{Bi}_2\mathrm{Se}_3$, is up to several tens of meV.[2, 39]

Nanostructuring of TIs enhances the surface over the bulk contributions to fermion charge transport and provides another promising means to produce edge states, following strategies previously applied to graphene. It should be recalled that the properties of the surface states are a consequence of the TI bulk properties. Bulk doping can be used to manipulate surface state behavior.[40, 41, 42, 43] Compositional tuning of Dirac fermion electronic structure has been demonstrated for BiTl($S_{1x}Se_d$)$_2$, $Bi_2(Te_{3-x}Se_x)$. [44, 45] Placed on a substrate, electric contacts have been made to the TI.[41, 46] Metal-TI junctions have been studied theoretically.[47] Such structuring can be expected to lead to the realization of interesting quantum interference effects due to the helical nature of surface states, implying spin-polarized electric currents, the absence of back scattering, and robustness to moderate disorder. This strategy has lead to the experimental observation of the quantum anomalous Hall effect in a magnetic topological insulator.[46] Quantum oscillations in TI nanoribbons in conjunction with high surface conductance (e.g., for Bi_2Te_3) have been investigated theoretically and in experiment.[48, 49, 41]

In this paper the dynamic properties of chiral fermions in channel states introduced by magnetic texturing of the surface of a TI insulator are explored. We perform a theoretical study of the propagation of chiral domain-wall fermions along the intersection of two ferro-magnetic domain walls imprinted upon the surface of a TI. In a systematic numerical analysis, we extract the one-way beam splitting properties regarding magnetic texturing, such as the angle of intersection, domain-wall thickness, and details of in-plane magnetization. Our time-dependent analysis is based on a newly developed scheme for a numerical treatment of the (2+1)D Dirac equation in presence of electromagnetic fields, whose numerical mathematical properties will be presented in a forthcoming publication. Here, the analysis is performed using static solitonic domain-wall crossings, valid in the adiabatic regime. The paper is organized as follows. In Sect. 11.2 we give a brief summary of chiral (domain wall) fermions in external electromagnetic fields, as relevant for TI surfaces and introduce 2-soliton magnetic textures. In Sect. 11.2.3 we give the model Hamiltonian for our numerical analysis. Sect. 11.3 gives a summary of our single-cone numerical lattice model for (2+1) Dirac fermions. Sect. 11.4 features some of our numerical results for chiral fermion beam splitters. Finally, a general summary and our conclusions are given in Sect. 11.5.

11.2 Chiral domain-wall fermions

11.2.1 Basic considerations

An effective (2+1)D model for the dynamics of Dirac fermions on a magnetically textured TI surface may be founded upon a Hamiltonian

$$H = H_F + H_I + H_{FI} \, , \tag{11.1}$$

consisting of the fermion Hamiltonian H_F, the impurity Hamiltonian H_I, and the interaction H_{FI}. For, the Dirac fermions in an external electromagnetic field one may write

$$H_F = v\,(\boldsymbol{\sigma} \times \mathbf{\Pi}) \cdot \hat{\mathbf{z}} + \mu_B g_F \boldsymbol{\sigma} \mathbf{B}(x,y,t) + V(x,y,t) \tag{11.2}$$

Here, $\mathbf{\Pi} = \mathbf{p} + \frac{e}{c}\mathbf{A}(x,y,t)$ in the spin-orbit term denotes the kinetic momentum in presence of a vector potential $\mathbf{A}$ associated with the external magnetic field $\mathbf{B}(x,y,t)$, $V(x,y,t) = -e\Phi(x,y,t)$ is the scalar potential energy, and $\mu_B = \frac{e\hbar}{2mc}$ and g_F in the Pauli term are, respectively, the electron Bohr magneton and the Landé factor. The Pauli vector is proportional to the physical fermion spin with its direction-locked perpendicular to the particle current density and the normal vector to the surface $\hat{\mathbf{z}}$.[32] Note, that the simple form of the spin-orbit term can be extended to more precisely represent the energy dispersion away from the Dirac point, such as an account of hexagonal warping.[32, 50]

The impurity spins may be modeled by a generic Heisenberg-type Hamiltonian of the form

$$H_I = -\sum_{i,j} J_{ij} \mathbf{S}_i \mathbf{S}_j - \sum_i g_I \mu_B \mathbf{S}_i \mathbf{B}_i^o \, , \tag{11.3}$$

and the Dirac fermion-impurity interaction by

$$H_{FI} = -\sum_i J_i' \mathbf{S}_i \boldsymbol{\sigma} \, . \tag{11.4}$$

Here $\mathbf{S}_i$ and $\mathbf{B}_i^o$ denote, respectively, the impurity spin and external magnetic field, for impurity site i. Note that one must differentiate between the "external" magnetic field experienced by fermions and impurities.

The physical situation envisioned and captured by the Hamiltonian H is that of a TI surface which is densely covered by magnetic impurities which interact with one another, as well as with the Dirac fermions under an exchange interaction. Several possible origins for an exchange interaction J_{ij}

have been discussed in the literature.[51, 39] An external magnetic field may be applied to imprint and stabilize domain-wall formation between ferromagnetic ordered domains.

Subjecting $H_I + H_{FI}$ to a mean-field approximation one obtains $H_I + H_{FI} \rightarrow (H_I + H_{FI})^{MF} = -\sum_i g_I \mu_B \mathbf{B}^{(\mathbf{I})}{}_i$, where the effective magnetic field at impurity site i is given as

$$\mathbf{B}_i^{(I)} = \mathbf{B}_i^o + \frac{1}{g_I \mu_B}\left[\sum_j J_{ij}\langle \mathbf{S}_j \rangle + \langle J_i' \boldsymbol{\sigma} \rangle\right] . \tag{11.5}$$

The three contributions arise from the external magnetic field (including contributions from the orbital motion of Dirac fermions), impurity magnetization, and fermion spin polarization. The latter gives rise to a spin-transfer torque.

Similarly for the fermions,

$$\begin{aligned} H_F \quad &+ \quad H_{FI} \rightarrow (H_F + H_{FI})^{MF} \\ &= \quad v\,(\boldsymbol{\sigma} \times \boldsymbol{\Pi}') \cdot \hat{\mathbf{z}} + \mu_B g_F \boldsymbol{\sigma} \mathbf{B}^{(\mathbf{F})}(x,y,t) + V(x,y,t) \ , \end{aligned} \tag{11.6}$$

where the effective magnetic field in the Pauli term is given by

$$\mathbf{B}^F(x,y,t) = \mathbf{B}'(x,y,t) - \frac{1}{g_F \mu_B}\sum_i \langle J_i' \mathbf{S}_i \rangle \boldsymbol{\sigma} \ , \tag{11.7}$$

and the vector potential $\mathbf{A}'$ entering the canonical momentum $\boldsymbol{\Pi}'$ in the spin-orbit term contains the contribution from the external magnetic field and the magnetization of the impurities, as will be discussed below, such that $\mathbf{B}'(x,y,t) = \boldsymbol{\nabla} \times \mathbf{A}'(x,y,z,t)\ |_{z=0}$.

In what follows we concentrate on the Dirac fermion dynamics. The impurity dynamics, in principle, can be treated self-consistently in parallel. However, it is generally accepted that the latter occurs on a time-scale which is long compared to the fermion dynamics and adiabatic schemes have been used successfully to model the interplay between the two subsystems.[52]

According to Eq. (11.6) the presence of magnetic impurities and a stabilizing external B-field has two consequences for the dynamics of Dirac fermions: an impurity spin polarization (magnetization) $\mathbf{M}$ modifies the net external magnetic field from $\mathbf{B}$ to $\mathbf{B}'$ and, for $M_z \neq 0$, introduces an exchange term ("mass term"), in addition to the Zeeman term, in Eqs. (11.6) and (11.2) below. Such a mass term has been estimated to be of the order of up to several tens of meV and represents the dominant magnetic-field contribution.[39] For a fermion g-factor 20 the effective magnetic exchange field required for a mass gap of 25 meV is about 10 T.[37, 53] Such a magnetic exchange field will, as usual for ferromagnets, dominate any typical static external field $\mathbf{B} \leq 0.5$ T in Eq. (11.7) in the Pauli term of Eq. (11.6).

In order to estimate the magnetization $\mathbf{M}$ associated with an exchange field of 10 T, we use parameters typical for Mn impurities.[54] Within the simple form $J_i' = J'\delta(x - x_i)\delta(y - y_i)$ and $J' \approx 130$ meV nm^2 one needs an impurity density of about 0.1 nm^{-2} to achieve a mass gap of 25 meV. Using $g_I \approx 2$, the magnetization per area is of the order of 1.2×10^{-6} meV/(Gauss nm^2). Based on this estimate and a layer thickness of 1 nm, the order of magnitude of the magnetization contribution to B', $|B' - B| = 4\pi M$, is about 2.5×10^{-3} T, making this effect negligible in both the spin-orbit and Pauli term of Eq. (11.6). In principle there also is a topological field contribution due to the magneto-electric effect, but it is extremely small in magnitude ($\leq 10^{-6}T$).[32, 55] In summary, the dominant magnetic-field effect onto the Dirac fermions arises from the exchange field, followed in importance by the external magnetic field in the spin-orbit term. The effect of an external magnetic field on the spectrum of TI Dirac fermions has been investigated both theoretically and experimentally (see Introduction 11.1). It has a negligible effect on the dynamics of domain-wall Dirac fermions when compared to the in-plane component of the exchange term, as we have verified numerically in our studies detailed below. We conclude that the formation of domain-wall states and the dynamics of domain-wall Dirac fermions is dictated predominantly by the magnetic domain-wall structure (exchange field) and the external electric bias. However, the presence of an external magnetic field may be essential to pin domain walls and to imprint and stabilize a specific ferromagnetic domain-wall structure.

11.2.2 Solitonic magnetic textures

The rich physics of ferromagnetic domain wall dynamics has been well documented in the literature.[56, 57, 24, 25, 26] Here we consider well-pinned hard ferromagnetic textures and explore domain-wall fermion dynamics on a time-scale which allows for a quasi-static treatment of the domain wall structure, neglecting spin-transfer torque effects.[52] The latter implies the regime of low current density. Our numerical approach can handle time-dependent magnetic domains, however, such an analysis will be the topic of future investigations.

An analytic model for stable, local-minima, 2D magnetic textures can be derived from solutions to a simple free energy functional which consists of an isotropic exchange term and an anisotropy term with z as the easy axis. In terms of the unit magnetization $\mathbf{m} = (m_x, m_y, m_z) = (\sin\theta\cos\phi, \sin\theta\sin\phi, \cos\theta)$

and with $a, b > 0$ it is

$$\mathcal{F}(\mathbf{m}) = \frac{1}{2} \int dxdy \left[a(\mathbf{grad\ m})^2 - b m_z^2 \right] . \tag{11.8}$$

In spherical coordinates $\theta(x, y)$ and $\phi(x, y)$ $\mathcal{F}$ takes the simple form

$$\begin{aligned} \mathcal{F}(\mathbf{m}) &= \frac{1}{2} \int dxdy[a \sum_{i=x,y} \left((\partial_{x_i}\theta)^2 + (\partial_{x_i}\phi \sin\theta)^2 \right) \\ & \quad -b\cos(\theta)^2] . \end{aligned} \tag{11.9}$$

Optimality conditions lead to $\partial_{x_i}\phi = 0$ and

$$\theta_{xx} + \theta_{yy} = \frac{b}{2a} \sin 2\theta. \tag{11.10}$$

Setting $u = 2\theta$ and rescaling $x_i \rightarrow \sqrt{b/a} x_i$ one obtains the sine-Gordon equation (in "imaginary time" iy)

$$u_{xx} + u_{yy} = \sin 2u.$$

Multi-soliton solutions are most directly found using Hirota's bilinear expansion in ϵ.[58, 59, 60] The single-soliton solution takes the form

$$\begin{aligned} \theta^{(1)}(x, y) &= 2 \arctan \left\{ e^{\eta(x,y)} \right\}, \\ \eta(x, y) &= \sqrt{b/a}(x' - x'_o),\ x'_o = -\sqrt{a/b} \ln \epsilon \\ x' &= x\cos\beta + y \sin\beta,\ \beta \in [0, 2\pi] \\ \phi(x, y) &= \phi_o,\ \phi_o \in [0, 2\pi]. \end{aligned} \tag{11.11}$$

This solution represents a magnetization domain wall along $y' = -x \sin\beta + y\cos\beta$ at x_o.

A magnetic domain-wall intersection which represents a local minimum to the free energy functional Eq. (11.8) can be constructed from the two-soliton solution

$$\begin{aligned} \theta^{(2)}(x, y) &= 2 \arctan \left\{ \frac{e^{\eta_1(x,y)} + e^{\eta_2(x,y)}}{1 + \kappa_{12} e^{\eta_1(x,y)+\eta_2(x,y)}} \right\}, \\ \eta_i(x, y) &= \sqrt{b/a}(x_i - x_o^i), \\ x_i &= x \cos\alpha_i + y \sin\alpha_i,\ \alpha_i \in [0, 2\pi], i = 1, 2 \\ \kappa_{12} &= \frac{(\cos\alpha_1 - \cos\alpha_2)^2 + (\sin\alpha_1 - \sin\alpha_2)^2}{(\cos\alpha_1 + \cos\alpha_2)^2 + (\sin\alpha_1 + \sin\alpha_2)^2} \\ \phi(x, y) &= \phi_o,\ \phi_o \in [0, 2\pi] . \end{aligned} \tag{11.12}$$

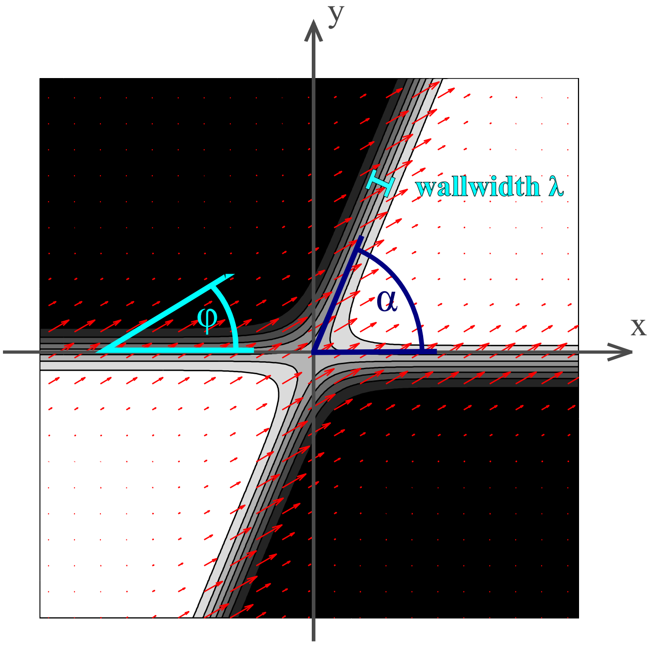

Figure 11.1: Magnetic texture of a domain wall intersection. The contour plot encodes the M_z component of the magnetization, asymptotically taking the values ± | M | (black and white regions). The arrows show the in-plane components (M_x, M_y). α is the angle of intersection and ϕ is the angle of the in-plane magnetization direction relative to the x-axis. The wall width is given by $\lambda = \sqrt{a/b}$, where a is the exchange constant and b the anisotropy parameter (see main text).

We place the point of intersection at the coordinate origin, setting $x_o^1 = x_o^2 = 0$, retaining $\alpha_1 - \alpha_2 (\neq 0, \pi)$ and ϕ_o to characterize the type of intersection. With suitable magnetic impurities present at or near the surface of the TI, such a ferromagnetic domain wall intersection may be induced by an array of magnetic poles of the form $\begin{bmatrix} + & - \\ - & + \end{bmatrix}$ facing the TI surface.

11.2.3 The model Hamiltonian and domain-wall states

According to Sect. 11.2 the effective Hamiltonian for a single Dirac cone on the surface of the TI interacting with magnetic texture $\mathbf{M}(x, y)$ may be written[32, 35, 61]

$$H = v\,[\boldsymbol{\sigma} \times \boldsymbol{\Pi}(x, y, t)] \cdot \hat{\mathbf{z}} + \mathbf{M}(x, y) \cdot \boldsymbol{\sigma} + V(x, y)\;. \tag{11.13}$$

According to Eq. (11.7) second and third term on the r.h.s., respectively, account for the presence of the magnetic texturing $\mathbf{M}(x, y) = \hat{\mathbf{J}}\mathbf{m}(x, y)$, with $\hat{\mathbf{J}}$ denoting the effective exchange coupling tensor, and an external scalar electric potential arising, for example, from a gate bias.

This effective Hamiltonian describes the 2D excitation spectrum near the Dirac point, including 1D edge states in presence of domain walls. Domain-wall edge states are responsible for an integer quantum Hall effect on the TI surface, as discussed in the literature.[32, 35] For H Eq. (11.13) and a single-soliton domain wall Eq. (11.11), with $\lim_{x'\to\pm\infty} M_z(x') = M_\pm$ and $M_- M_+ < 0$, a domain-wall eigenstate exists which takes the simple form[36]

$$\langle x, y\,|Y', \pm\rangle \propto \frac{1}{\sqrt{2}} \begin{pmatrix} \pm e^{-i\alpha/2} \\ e^{i\alpha/2} \end{pmatrix} e^{\mp\frac{1}{\hbar v}\int_{x'_o}^{x'} M_z(x'')dx'' + ik'_y y'} \,, \tag{11.14}$$

when neglecting in-plane contributions to the magnetization (valid when sufficiently far away from the domain wall).[31] It features a linear dispersion $E = \pm v\hbar\, k'_y$, with the upper sign for $M_- < 0$ and $M_+ > 0$, and the lower sign for $M_+ < 0$ and $M_- > 0$. Note that a constant potential V in Eq.(11.2) simply adds to the eigenvalue E. Parallel and curved zero-mass lines have also been studied in the literature.[62] For a general form of an in-plane magnetization $M_x(x'), M_y(x') \neq 0$ or other more complicated domain-wall structures eigenfunctions are best found numerically.

More complex magnetic texturing, where islands of positive mass neighbor islands of negative mass, produces a network of one-way chiral channel states.[31] Here we study an elementary building block of such a network in form of an intersection of two linear domain walls. With the realization of such a texture a reflection-less beam splitter for chiral fermions is established. This is demonstrated numerically below for the two-soliton texture Eq. (11.12).

11.3 Numerical method: a single-cone lattice model

The time-dependent Dirac equation is solved numerically for H in Eq. (11.2). Putting the (single cone) Dirac equation onto a grid for numerical solution traditionally has been hampered by fermion doubling, that is, the lattice model has more eigenmodes than the original continuum model. Two different numerical finite difference schemes have been employed and compared in the course of this analysis. Both use a staggering of the spinor components in space and time. The first one has the following advantageous features:[63] (i) it provides the exact (linear) dispersion relation for mass-less free Dirac fermions along the main axes k_x and k_y, (ii) it allows an implementation of absorbing boundary conditions via an imaginary potential term, and (iii) it allows for a removal of the second Dirac cone, located at the corners of the Brillouin zone, by a Wilson term.[64] The second one, briefly outlined below, avoids the fermion doubling problem altogether at the cost of loosing the perfect (i.e., linear) dispersion property along the main coordinate axes for mass zero.[65] It features a single Dirac cone dispersion without the need for using a Wilson mass term to get rid of the doublers. For simple rectangular magnetic structures aligned with the grid's x and y axis the first scheme has higher accuracy, for general setups, however, the second scheme performs better. The figures shown below are obtained with the second scheme. Results from various simulations within the first scheme have and will be presented elsewhere.[31, 66, 63] Global grid refinement experiments where done and then the simulations where executed with a grid for which a further halving of the grid-spacings gave an improvement no more than 1%. For comparison some simulations were done with scheme one showing a difference in the result for the transmission of less than 1%.

The finite difference scheme for the Dirac equation $i\partial_t \boldsymbol{\psi}(x,y,t) = \hat{H}\boldsymbol{\psi}(x,y,t)$ with the Hamiltonian Eq. (11.2), where $\boldsymbol{\psi}(x,y,t) \in \mathbb{C}^2$ is a 2-component spinor, may be summarized as follows. Introducing the space-time staggered according to in Fig. 11.2 for the components of the spinor $\boldsymbol{\psi} = (u,v)$ and using symmetric second order accurate approximations for the derivatives we propose the following discretization of the (2+1)D Dirac equation

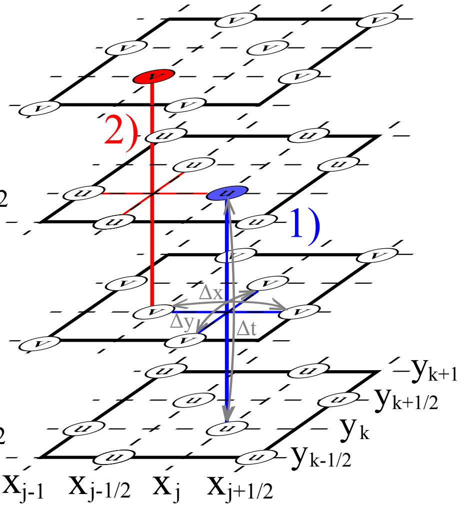

Figure 11.2: Leap-frog time stepping on a time and space staggered grid for the (2+1)D Dirac equation.

$$
\begin{aligned}
&\frac{u^{n+1/2}_{j,k} - u^{n-1/2}_{j,k}}{\Delta t} = \\
&- i\big[(M_z)^n_{j,k} - V^n_{j,k}\big]\,\frac{u^{n+1/2}_{j,k} + u^{n-1/2}_{j,k}}{2} \\
&- \frac{(v^n_{j+1/2,k} - v^n_{j-1/2,k})}{\Delta x} + i\,\frac{(v^n_{j,k+1/2} - v^n_{j,k-1/2})}{\Delta y}\ , \\
&- (M_x)^n_{j,k}\,\frac{(v^n_{j+1/2,k} + v^n_{j-1/2,k})}{2} \\
&- i(M_y)^n_{j,k}\,\frac{(v^n_{j,k+1/2} + v^n_{j,k-1/2})}{2}\ , \\
\\
&\frac{v^{n+1}_{j-1/2,k} - v^n_{j-1/2,k}}{\Delta t} = \\
&+ i\big[(M_z)^{n+1}_{j-1/2,k} + V^{n+1}_{j-1/2,k}\big]\,\frac{v^{n+1}_{j-1/2,k} + v^n_{j-1/2,k}}{2} \\
&- \frac{(u^{n+1/2}_{j,k} - u^{n+1/2}_{j-1,k})}{\Delta x} - i\,\frac{(u^{n+1/2}_{j-1/2,k+1/2} - u^{n+1/2}_{j-1/2,k-1/2})}{\Delta y} \\
&- (M_x)^{n+1}_{j-1/2,k}\,\frac{(u^{n+1/2}_{j,k} + u^{n+1/2}_{j-1,k})}{\Delta x} \\
&+ i(M_y)^{n+1}_{j-1/2,k}\,\frac{(u^{n+1/2}_{j-1/2,k+1/2} + u^{n+1/2}_{j-1/2,k-1/2})}{\Delta y}\ .
\end{aligned}
\tag{11.15}
$$

The u-component defined for the discrete time indices $n - 1/2 \in \mathbb{Z}$ 'lives' on the discrete space grid points $(j,k) \in \mathbb{Z}^2$ and $(j-1/2, k-1/2) \in \mathbb{Z}^2$, while the v-component defined for $n \in \mathbb{Z}$ is defined for space indices $(j - 1/2, k) \in \mathbb{Z}^2$ and $(j, k - 1/2) \in \mathbb{Z}^2$.

The dispersion relation for constant coefficients is revealed using a plane-wave ansatz $u^{n+1}_{j+1,k+1} = e^{i(\omega\Delta t - k_x\Delta x - k_y\Delta y)} u^n_{j,k}$ (and analogously for v). The centered approximation for the time and space derivatives, respectively, translates into a multiplication by $\frac{2i}{\Delta t} \sin \frac{\omega\Delta t}{2}$ and $\frac{2i}{\Delta x,y} \sin \frac{k_{x,y}\Delta x,y}{2}$. Time averaging leads to the factor $\cos \frac{\omega\Delta t}{2}$. Solving for ω gives the dispersion relation for $M_x = M_y = V = 0$

$$\omega = \pm \frac{2}{\Delta t} \arcsin \left[\frac{\Delta t}{2 + (M_z)^2 \Delta t} \right. \\ \left. \sqrt{(M_z)^2 + \left(\frac{2}{\Delta x} \sin \frac{k_x \Delta x}{2} \right)^2 + \left(\frac{2}{\Delta y} \sin \frac{k_y \Delta y}{2} \right)^2} \right] . \tag{11.16}$$

The dispersion relation for $M_x = M_y = V = 0$ is monotonic and has its single minimum at $k_x = k_y = 0$. On the grid the k vectors are defined up to reciprocal lattice vectors, only, leading to $k \in (-\pi/a, \pi/a]$, where $a = \Delta x, \Delta y$. Accordingly the domain for the frequency is $\omega \in (-\pi/\Delta t, \pi/\Delta t]$. Fig. 11.3 compares the dispersion within the (2+1)D lattice model for the lattice parameters $\Delta_x = \Delta_y = 1$ and $\Delta_t = 1/\sqrt{2}$ and a mass gap $2m = 1$ to the exact cone of the continuum model (in green). A more detailed analysis of the scheme including a rigorous stability analysis (as performed recently for the (1+1)D case)[67] for general time- and space-dependent mass vector M and electro-magnetic potentials will be given elsewhere.[68]

11.4 A Dirac fermion beam splitter: numerical results

The asymptotic value for the z-component of the magnetization in Eq. (11.2) is chosen to be $| m_z |= 7.5$ meV. This value is realistic in view of the expected exchange coupling.[39] Note that the results obtained for this value can be scaled to other values due to the scale invariant nature of the problem at hand. Indeed, the relevant parameters characterizing a physical situation can be separated into ratios and scale-free (absolute) parameters. The relevant ratios are: the ratio of the confinement length of the wave packet to the

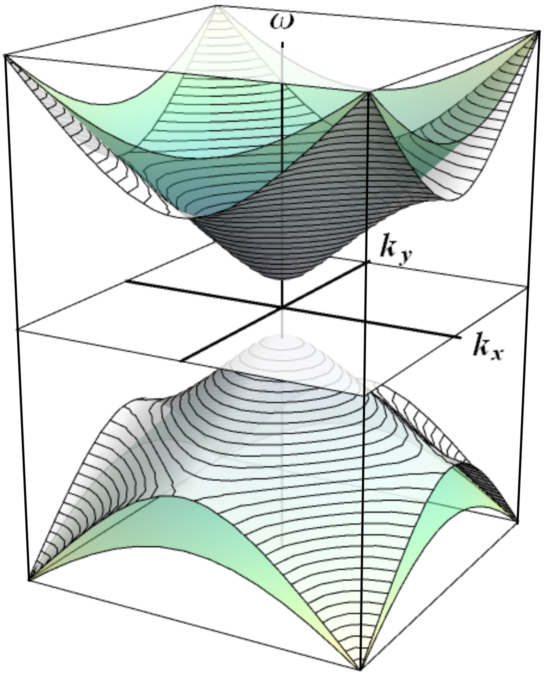

Figure 11.3: The dispersion within the numerical approach for a mass gap $2M_z = 1$ compared to the exact cone of the continuum approach (in green). The grid spacings are chosen to be $\Delta_x = \Delta_y = 1$ and $\Delta_t = 1/\sqrt{2}$.

domain wall width, the ratio of the wave packet energy to the gap (established by the asymptotic value of the z-component of the magnetization), and the ratio of the in-plane to the out-of-plane exchange coupling constant (in principle, the in plane component can also have an anisotropy). The scale free parameters are the angle of intersection and the angle ϕ for the in plane magnetization direction (see Fig. 11.1). For real structures in experiment sample-specific imperfections, such as unwanted irregularities in the magnetic structure, may play a role.

A typical simulation region of 1000×1000 nm is used and, for the simulations to follow, we place an initial Gaussian wave packet in the in-channel (see also Fig. 11.1). It is characterized by its energy mean value E and standard deviation, see Fig. 11.5. Its initial shape perpendicular to the channel is given by Eq. (11.12). Following the time-evolution of the wave packet along the structure we determine the splitting ratio from the transmission into the outgoing upward-running channel, *i.e.* in positive y-direction, for rectangular intersections (see also Fig. 11.1).

11.4.1 Rectangular intersections

Fig. 11.4 (a) gives a series of snapshots showing the wave packet as it propagates horizontally along the in-channel and splits more or less symmetrically into two outgoing wave packets traveling along the vertical channels. For rectangular two-soliton magnetic textures of the form Eq. (11.12) there are the domain width λ and the angle ϕ characterizing the in-plane magnetization across the domain wall which can be varied. For the first simulations of these dependencies for rectangular intersections shown in Figs. 11.5 and 11.6, the domain wall width is chosen to be a relatively large $\lambda = 25$ nm compared to the perpendicular confinement of the wave packet ≈ 100 nm to bring out more clearly the influence of the details of the in-plane components of the magnetization on the wave packet propagation.

In Fig. 11.6 we show the effects on the transmission into the upper channel when the domain wall width λ and the magnetization angle ϕ are varied. Here, the wave packet is prepared with an energy mean value $E = 0$. The color-coded figures show grid lines (in gray), altitude lines (black) as well as the altitude (as interpolated color map) which should allow the reader to assign a transmission value to every parameter combination shown in the plot. One observes that even for relatively large domain wall widths the influence of the in plane magnetization to the splitting behavior is moderate and, to a very high accuracy, a rectangular intersection provides a 50-50 beam splitter for domain wall states over a wide energy range. This is important for robustness of the splitting ratio under local imperfections.

This situation can be changed, when an electrode is placed asymmetrically onto the junction, as sketched in Fig. 11.4 (b). The chosen bias value is 15 mV. Note that a static potential cannot close the channel or revert the propagation direction. However, if sufficiently large it provides a mixing of 2D surface states with the channel state and, when spatially confined perpendicular to the out channel, provides a wave guide-like channel, as is shown in the simulation in Fig. 11.4 (b). This confinement effect, arising from wave number mismatch, has been discussed in the literature.[13] Here it is used, to control the splitting ratio which is shown for varying V and E and $\lambda = 25$ nm and $\phi = 0$ in Fig. 11.8. Dynamically, the confining effect by the (rectangular) gate resembles total internal reflection which arises under glancing incidence onto the potential wall. Tailoring the shape of the electrode helps in effective “funneling" of fermions back into the domain-wall state. This is demonstrated in Fig. 11.7 (a) and (b) in which we compare the effect of a rectangular versus a triangular bias region.

Note that asymmetric biasing of one out channel shows influence on the splitting ratio only when the applied voltage is sufficiently high to energetically move the Dirac fermion out of the magnetization gap (see Figs. 11.7 and 11.8). Otherwise it cannot influence significantly the propagation because the addition of a scalar potential does not change the group velocity due to the linear dispersion relation of the channel states.

11.4.2 45-degree intersections

We now turn to 45-degree intersections and study them as a function of ϕ (domain-wall type), λ (channel width), and E (mean energy of the wave packet). Fig. 11.9 shows snapshots of the wave packet as it propagates along the in-channel and splits up at the intersection. It is observed that the preferred out-channel depends on the channel width. For wide channels the upper out-channel is preferred, while for narrow channel width, the lower channel is the preferred exit. This trend arises from an increased overlap of the in-channel wave-packet with the lower out-channel as the channel width decreases, whereas for wide channels, the path of lower momentum transfer wins out. This effect therefore also displays an energy dependence, in contrast to the rectangular case.

Results from a more systematic analysis are summarized in the following figures. In Fig. 11.10 we show the transmission as a function of the in plane magnetization angle ϕ and the energy mean value E for $\lambda = 25$ nm. In Fig. 11.11 we vary the wall width λ and the in-plane magnetization angle ϕ using $E = 0$. Fig. 11.12 shows the same setup but for $E = 5$ meV. Compared to the rectangular intersections (Figs. 11.6 and 11.10) the influence of the in-plane magnetization direction is more pronounced. For a fixed interaction angle the most relevant parameter still is the wall width since it determines the degree of asymmetry in the “channel cross-talk" near the junction, as shown in quantitative detail in these figures. As the fermion approaches the intersection it probes the surroundings and begins to leak into the lower out-channel before it detects the upper one.

11.4.3 General angles of intersection

Referring to Fig. 11.1, general angles of intersection α are investigated. In conjunction with the domain-wall thickness the angle of intersection plays the dominant role for establishing the splitting ratio of such an intersection. Results are summarized in the following figures. In Fig. 11.13 we vary α and λ for $E = \phi = 0$. For Fig. 11.14 we change E to $E = 5$ meV. Fig. 11.15 shows the variation of E and α where $\phi = \pi/2$ and $\lambda = 25$ nm. For $\lambda = 10$ nm this setup shows a quite different behavior Fig 11.16. It is remarkable that for small domain-wall widths, relative to the spatial extent of the Dirac fermion wave packet, the transmission into the upper channel decreases for a more acute angle α. For large widths, on the other hand, the transmission into this out channel is favored, as one would suspect "intuitively" (see Fig. 12 and 13). This effect is most dominant for wave packets with a center energy of $E = 0$. The two competing effects responsible for this behavior are the difference in spatial (time-dependent) overlap of the incident wavepacket with the two outgoing channels and the "wave-vector" mismatch at the intersection. As already pointed out for the $\alpha = 45^o$, the behavior of narrow channels is dominated by the former, while wide channels act ballistic, favoring low momentum transfer. In other words, when going from narrow to wide channels, the Dirac fermion scattering behavior changes from quantum-mechanical wave-like to "classical" particle-like. Note that, as per Eq. (11.14), the (stationary) transverse extent of the wave packet is determined by the asymptotic values of the magnetic texture, while the width of the domain wall independently is determined by the relative importance between anisotropy and exchange contribution in the free energy functional of the magnetization, Eq. (11.8). Hence, in principle, structural design allows for both situations to occur.

11.5 Summary and conclusions

In summary, we have investigated numerically the dynamics of domain-wall Dirac fermions at the intersections of two linear ferromagnetic domain walls. To model a realistic stable magnetic intersection texture we have used a two-soliton solution of the sine-Gordon equation which establishes the optimality condition for a minimum of a free energy functional accounting for exchange and anisotropy. The time-dependent analysis of chiral fermion propagation is based on a staggered grid numerical scheme to solve the effective (2+1)D Dirac equation. Developed for this particular purpose, it is constructed such that fermion doubling is avoided and absorbing boundary conditions in form of regions of imaginary scalar potential can be incorporated. Details of this model and an extension to (3+1)D can be found elsewhere.[68]

The properties of such magnetic intersections as a one-way beam splitters for chiral fermions have been investigated. Based on this study, we can conclude that the splitting ratio for domain-wall fermions at the intersection depends strongly on the angle of intersection and, in case of non-rectangular intersections, on the width of the domain-wall. The latter determines the importance of the wave nature of the fermion onto the transmission behavior: quantum-tunneling dominates the behavior at the intersection when the (transverse) localization length of the domain-wall fermion is large compared to the channel width. For wide domain walls the Dirac fermion behavior at the intersection becomes particle-like. The type of domain wall, as well as the mean energy of the Dirac fermion wave packet, have a weaker influence on the splitting ratio. The former is characterized by the angle of the in-plane magnetization when its z-component goes through zero and allows one to compare Bloch- to Néel-type intersections. Although experimental setups will have imperfections regarding the magnetic structure our results should give a qualitative guide for the splitting behavior in such structures, as long as defects do not destroy the channel states.

External control of of the splitting ratio may become feasible in experiment via asymmetrically biased electric gates placed near the junction. Using specially tapered electrodes, “funneling" of laterally confined fermions back into domain-wall states is shown in our simulation.

Here we have confined our analysis to the intersection of two linear domain walls. If more complex magnetic textures on topological insulators can be realized in experiment, domain-walls can be used as chiral Dirac fermion waveguides, with their mutual intersections acting as beam-splitters as, for example, in a proposal for a domain-wall electric-gate controlled fermion interferometer. [31]

The work is supported by the Austrian Science Foundation under Project No. I395-N16.

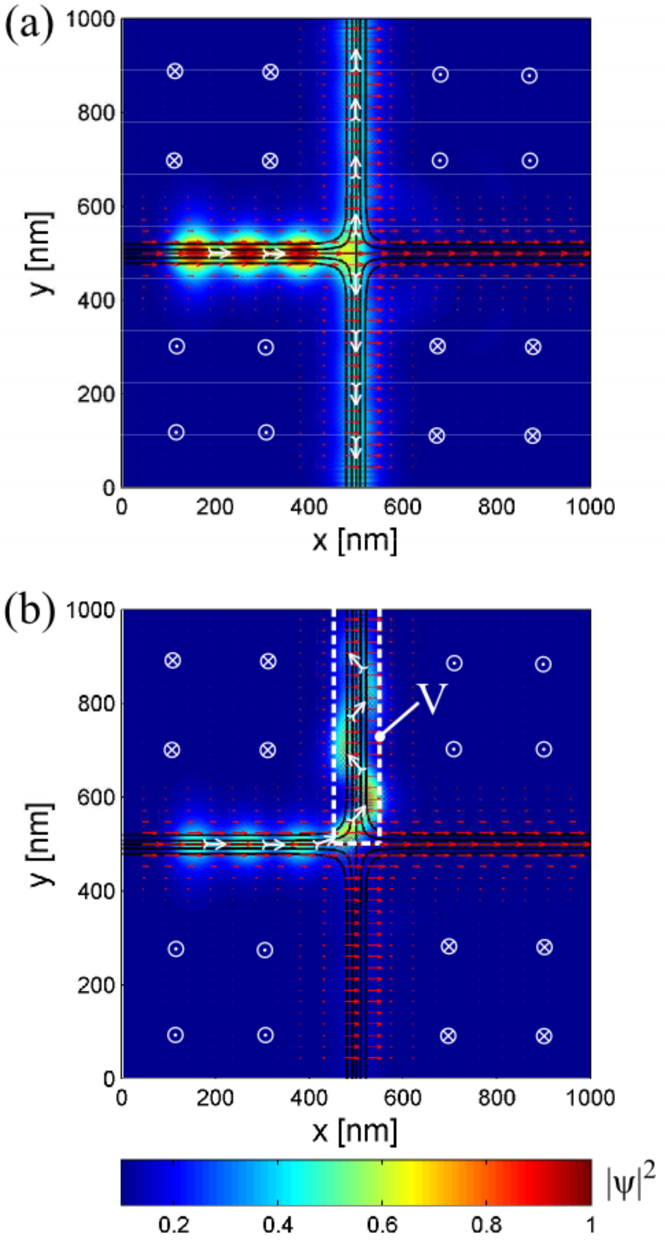

Figure 11.4: Snapshots of the wave packet propagation in a 90-degree domain wall intersection: (a) unbiased, (b) biased (15 mV). The color (or brightness variation) shows the probability density $|\psi|^2$ (see color-bar). The black contour lines and the white crossed and dotted circles show the M_z-component of the magnetization. The vector plot shows the direction and magnitude of the in-plane magnetization (M_x, M_y).

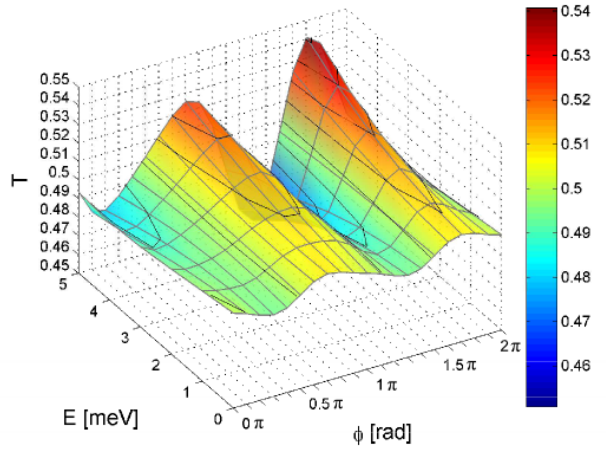

Figure 11.5: Relative transmission to the upper channel in a rectangular domain wall intersection with wall width $\lambda = 25$ nm as a function of the in-plane magnetization angle ϕ and the energy mean value E of the wave packet.

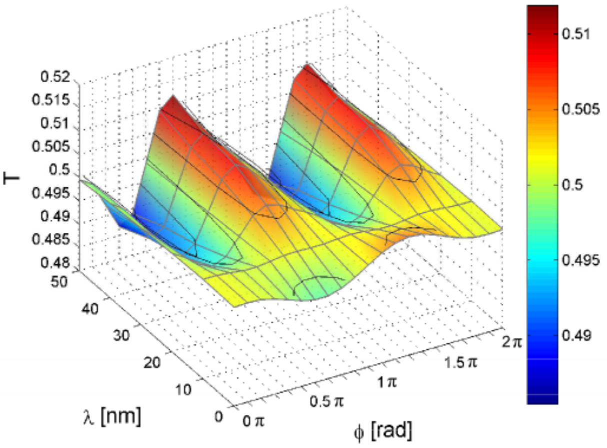

Figure 11.6: Relative transmission to the upper channel in a rectangular domain wall intersection as a function of the in-plane magnetization angle ϕ and wall width λ. The in propagation-direction Gaussian initial wave packet is prepared with an energy mean value of $E = 0$.

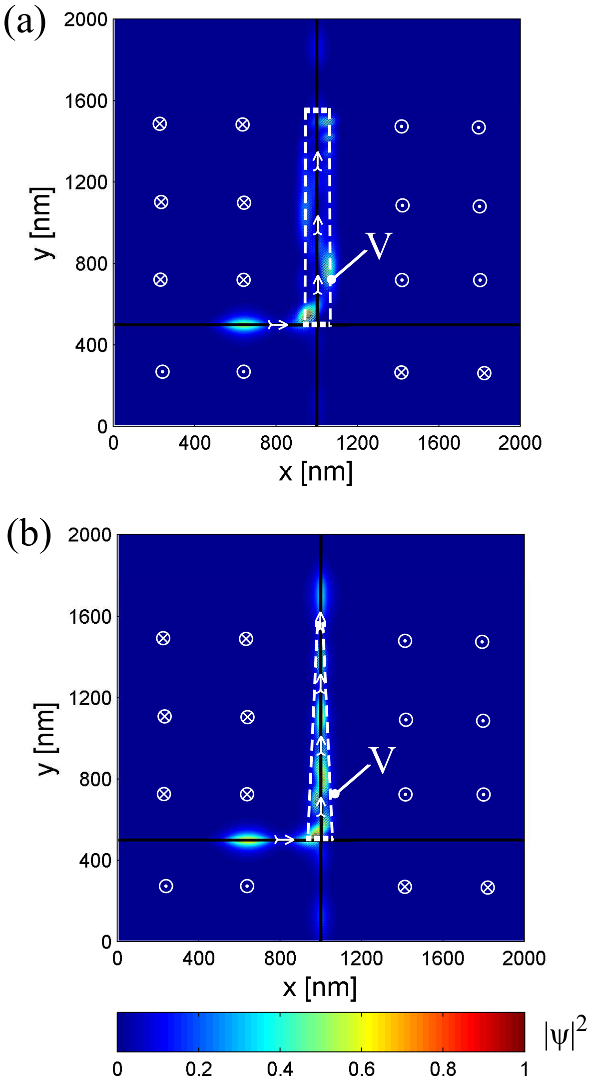

Figure 11.7: Snapshots of the wave packet propagation in a 90-degree domain wall intersection: (a) with rectangular electrode, (b) with tailored electrode and a bias of 15 mV. The color (or brightness variation) shows the probability density $|\psi|^2$ (see color-bar). The black contour lines and the white crossed and dotted circles show the M_z-component of the magnetization.

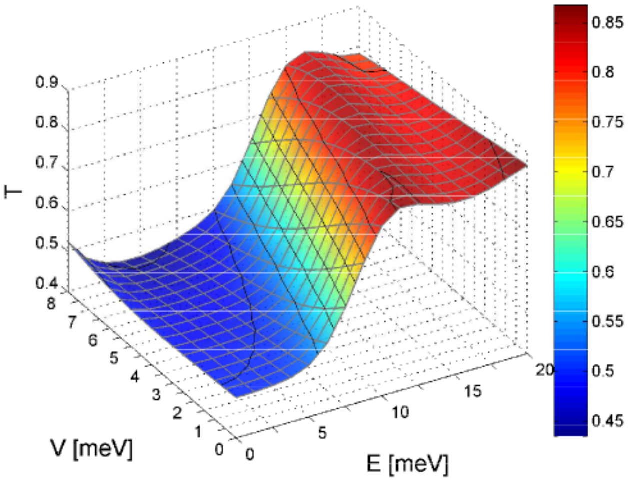

Figure 11.8: Relative transmission to the upper channel in a rectangular domain wall intersection as a function of the mean energy of the wave packet E and the gating potential V as shown in Fig. 11.4 (b). The wall width is chosen to be $\lambda = 25$ nm and $\phi = 0$.

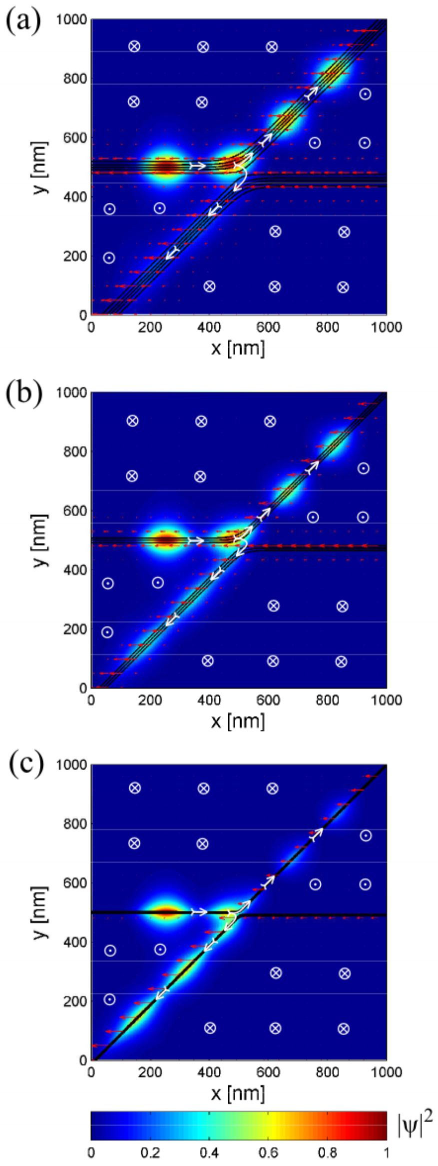

Figure 11.9: Snapshots of the wave packet propagation in a 45-degree domain wall with a wall width of (a) $\lambda = 25$ nm, (b) $\lambda = 15$ nm and (c) $\lambda = 5$ nm. $E = \phi = \pi$. The color (or brightness variation) shows the probability density $|\psi|^2$ (see color-bar). The black contour lines and the white crossed and dotted circles show the M_z-component of the magnetization. The vector plot shows the direction and magnitude of the in-plane magnetization (M_x, M_y).

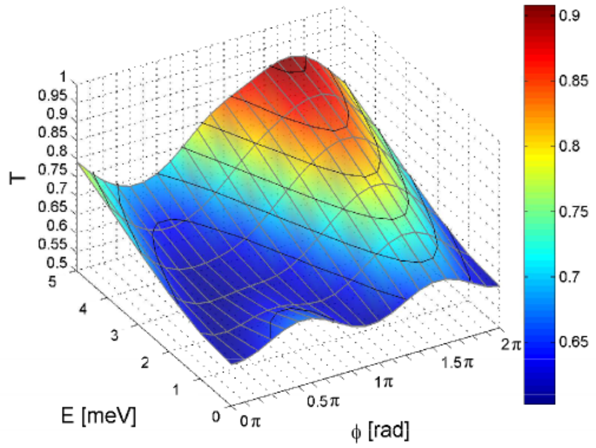

Figure 11.10: Relative transmission to the upper channel in a 45-degree domain wall intersection with wall width $\lambda = 25$ nm as a function of the in-plane magnetization angle ϕ and the energy mean value E of the wave packet.

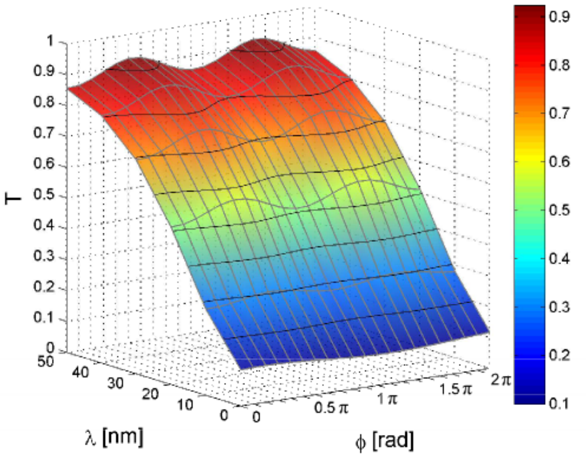

Figure 11.11: Relative transmission to the upper channel in a 45-degree domain wall intersection as a function of the in-plane magnetization angle ϕ and wall width λ. The in propagation-direction Gaussian shaped initial wave packet is prepared with an energy mean value of $E = 0$.

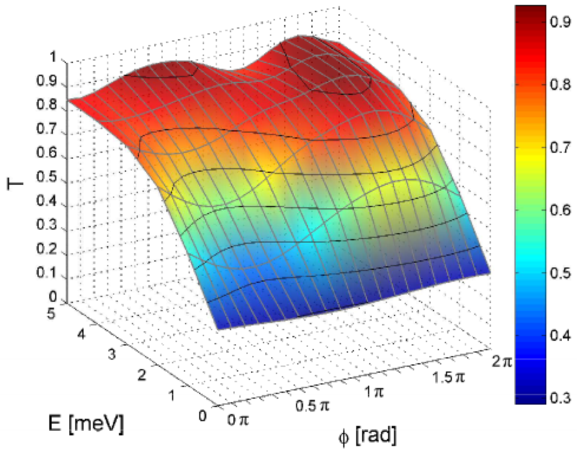

Figure 11.12: Relative transmission to the upper channel in a 45-degree domain wall intersection as a function of the in-plane magnetization angle ϕ and wall width λ. The in propagation-direction Gaussian shaped initial wave packet is prepared with an energy mean value of $E = 5$ meV.

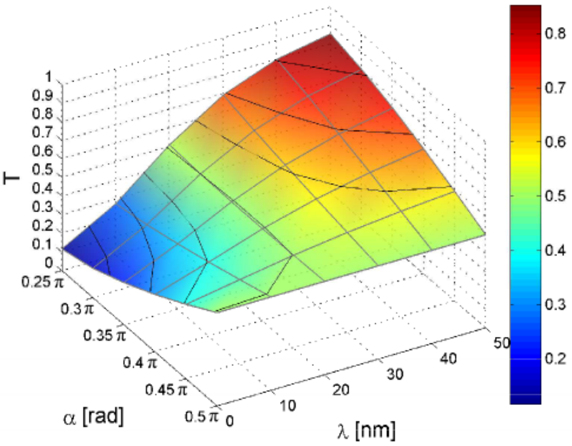

Figure 11.13: Relative transmission to the upper channel in a domain wall intersection where the intersection angle α and the wall width λ are varied. $E = 0$ meV and $\phi = 0$.

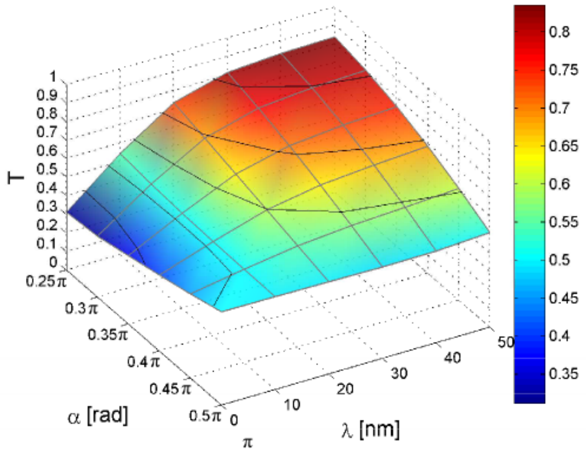

Figure 11.14: Relative transmission to the upper channel in a domain wall intersection where the intersection angle α and the wall width λ are varied. $E = 5$ meV and $\phi = 0$.

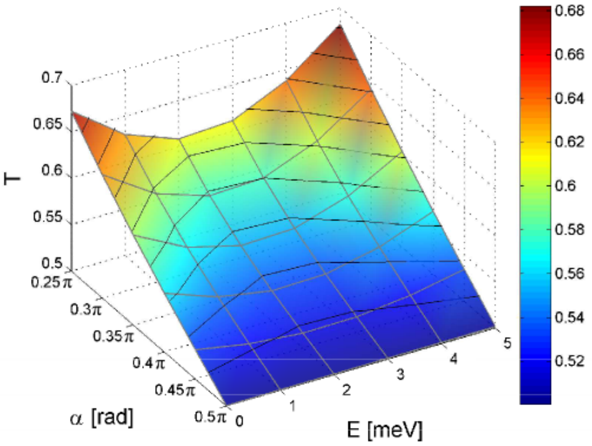

Figure 11.15: Relative transmission to the upper channel in a domain wall intersection where the intersection angle α and the mean energy E are varied. $\phi = \pi/2$ and $\lambda = 25$ nm.

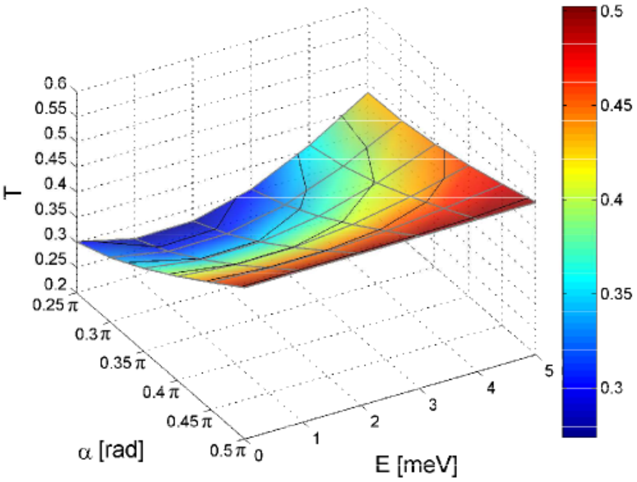

Figure 11.16: Relative transmission to the upper channel in a domain wall intersection where the intersection angle α and the mean energy E are varied. $\phi = \pi/2$ and $\lambda = 10$ nm.

REFERENCES

[1] J. G. Analytis, J. H. Chu, Y. Chen, F. Corredor, R. D. McDonald, Z. X. Shen, and Ian R. Fisher, Phys. Rev. B 81, 205407 (2010).

[2] Y. L. Chen, J. H. Chu, J. G. Analyits, Z. K. Liu, K. Igarashi, H. H. Kuo, X. L. Qi, S. K. Mo, R. G. Moore, D. H. Lu, et al., Science 329, 659 (2010).

[3] Y. Xia, D. Qian, D. Hsieh, L. Wray, A. Pal, H. Lin, A. Bansil, D. Grauer, Y. S. Hor, R. J. Cava, and M. Z. Hasan, Nature Physics 5, 398 (2009).

[4] J. Chen, H. J. Qin, F. Yang, J. Liu, T. Guan, F. M. Qu, G. H. Zhang, J. R. Shi, X. C. Xie, C. L. Yang, K. H. Wu, Y. Q. Li, and L. Lu, Phys. Rev. Lett. 105, 176602 (2010).

[5] J. G. Checkelsky, Y. S. Hor, R. J. R. J. Cava, and N. P. Ong, Phys. Rev. Lett. 106, 196801 (2011).

[6] F. Xiu, L. He, Y. Wang, L. Cheng, L. T. Chang, M. Lang, G. Huang, X. Kou, Y. Zhou, X. Jiang, Z. Chen, J. Zou, A. Shailos, and K. L. Wang, Nat. Nanotech. 6, 216 (2011).

[7] D. Kim, S. Cho, N. P. Butch, P. Syers, K. Kirshenbaum, S. Adam, J. Paglione, and M. S. Fuhrer, Nat. Phys. 8, 459 (2012).

[8] Y. Wang, F. Xiu, L. Cheng, L. He, M. Lang, J. Tang, X. Kou, X. Yu, X. Jiang, Z. Chen, J. Zou, and, K. L. Wang, Nano Lett. 12, 1170 (2012).

[9] Z. Ren, A. A. Taskin, S. Sasaki, K. Segawa, and Y. Ando, Phys. Rev. B 85, 155301 (2012).

[10] J. Honolka, A. A. Khajetoorians, V. Sessi, T. O. Wehling, S. Stepanow, J. L. Mi, B. B. Iversen, T. Schlenk, J. Wiebe, N. B. Brookes, A. I. Lichtenstein, P. Hofmann, K. Kern, and R. Wiesendanger, Phys. Rev. Lett. 108, 256811 (2012).

[11] P. Wei, F. Katmis, B. A. Assaf, H. Steinberg, P. Jarillo-Herrero, D. Heiman, and J. S. Moodera, Phys. Rev. Lett. 110, 186807 (2013).

[12] C. Z. Chang et al., Adv. Mat. 25, 1065 (2013).

[13] T. Yokoyama, Y. Tanaka, and N. Nagaosa, Phys. Rev. B 81, 121401(R) (2010).

[14] B. Soodchomshom, Phys. Lett. A 374, 2894 (2010).

[15] J. Yuan, Y. Zhang, J. Zhang, and Z. Cheng, Eur. Phys. J. B, 86 (2013).

[16] B. D. Kong, Y. G. Semenov, C. M. Krowne, and K. W. Kim, Appl. Phys. Lett. 98, 243112 (2011).

[17] A. Suwanvarangkoon, I. M. Tang, R. Hoonsawat, B. Soodchomshom, Physica E 43, 1867 (2011).

[18] Z. Wu, F. M. Peeters, and K. Chang, Phys. Rev. B 82, 115211 (2010).

[19] T. Misawa, T. Yokoyama, and S. Murakami, Phys. Rev. B 84, 165407 (2011).

[20] M. M. Vazifeh and M. Franz, Phys. Rev. B 86, 045451 (2012).

[21] P. Schwab and M. Dzierzawa, Phys. Rev. B 85, 155403 (2012).

[22] K. Nomura and N. Nagaosa, Phys. Rev. Lett. 106, 166802 (2011).

[23] A. A. Burkov, D. G. Hawthorn, Phys. Rev. Lett. 105, 066802 (2010).

[24] Y. Tserkovnyak and D. Loss, Phys. Rev. Lett. 108, 187201 (2012).

[25] S. T. Chui and V. N. Ryzhov, Phys. Rev. Lett. 78, 2224 (1997).

[26] J. Castro, S. T. Chui and V. N. Ryzhov, Phys. Rev. B 60, 10271 (1999).

[27] F. Hassler, A. R. Akhmerov, and C. W. J. Beenakker, Phys. Rev. B 82, 125423 (2010).

[28] C. Wickles and W. Belzig, Phys. Rev. B 86, 035151 (2012).

[29] M. Liu, J. Zhang, C. Z. Chang, Z. Zhang, X. Feng, K. Li, K. He, L. L. Wang, X. Chen, X. Dai, Z. Fang, Q. K. Xue, X. Ma, and Y. Wang, Phys. Rev. Lett. 108, 036805 (2012).

[30] T. Yokoyama, A. V. Balatsky, and N. Nagaosa, Phys. Rev. Lett. 104, 246806 (2010).

[31] R. Hammer, C. Ertler, and W. Pötz, Appl. Phys. Lett. 102, 193514 (2013).

[32] X. L. Qi and S. C. Zhang, Rev. Mod. Phys. 83, 1057 (2011).

[33] J. E. Moore and L. Balents, Phys. Rev. B 75, 121306 (2007).

[34] L. Fu, C. L. Kane, Phys. Rev. B 76, 045302 (2007).

[35] X. L. Qi, T. L. Hughes, and S. C. Zhang, Phys. Rev. B 78, 195424 (2008).

[36] M. Z. Hasan and C. L. Kane, Rev. Mod. Phys. 82, 3045 (2010).

[37] Q. Liu, C. X. Liu, C. Xu, X. L. Qi, and S. C. Zhang, Phys. Rev. Lett. 102, 156603 (2009).

[38] R. Jackiw and C. Rebbi, Phys. Rev. D 13, 3398 (1976).

[39] W. Luo and X. L. Qi, Phys. Rev. B 87, 085431 (2013).

[40] L. Andrew Wray, Su-Yang Xu, Yuqi Xia, David Hsieh, Alexei V. Fedorov, Yew San Hor, Robert J. Cava, Arun Bansil, Hsin Lin, and M. Zahid Hasan, Nature Physics 7, 32Ð37 (2011).

[41] Faxian Xiu, Liang He, Yong Wang, Lina Cheng, Li-Te Chang, Murong Lang, Guan Huang, Xufeng Kou, Yi Zhou, Xiaowei Jiang, Zhigang Chen, Jin Zou, Alexandros Shailos, and Kang L. Wang, Nature Nanotechnology 6, 216Ð221 (2011).

[42] Haim Beidenkopf, Pedram Roushan, Jungpil Seo, Lindsay Gorman, Ilya Drozdov, Yew San Hor, R. J. Cava, and Ali Yazdani, Nature Physics 7, 939Ð943 (2011).

[43] Duming Zhang, Anthony Richardella, David W. Rench, Su-Yang Xu, Abhinav Kandala, Thomas C. Flanagan, Haim Beidenkopf, Andrew L. Yeats, Bob B. Buckley, Paul V. Klimov, David D. Awschalom, Ali Yazdani, Peter Schiffer, M. Zahid Hasan, and Nitin Samarth, Phys. Ref. B 86, 205127 (2012).

[44] Su-Yang Xu, Y. Xia, L. A. Wray, S. Jia, F. Meier, J. H. Dil, J. Osterwalder, B. Slomski, A. Bansil, H. Lin, R. J. Cava, M. Z. Hasan, Science 332, p560-564 (2011).

[45] Chaoyu Chen, Zhuojin Xie, Ya Feng, Hemian Yi, Aiji Liang, Shaolong He, Daixiang Mou, Junfeng He, Yingying Peng, Xu Liu, Yan Liu, Lin Zhao, Guodong Liu, Xiaoli Dong, Jun Zhang, Li Yu, Xiaoyang Wang, Qinjun Peng, Zhimin Wang, Shenjin Zhang, Feng Yang, Chuangtian Chen, Zuyan Xu, and X. J. Zhou, Scient. Reports 3 : 2411, DOI: 10.1038/srep02411, pp 1-6 (2013).

[46] Cui-Zu Chang, Jinsong Zhang, Xiao Feng, Jie Shen, Zuocheng Zhang, Minghua Guo, Kang Li, Yunbo Ou, Pang Wei, Li-Li Wang, Zhong-Qing Ji, Yang Feng, Shuaihua Ji, Xi Chen, Jinfeng Jia, Xi Dai, Zhong Fang, Shou-Cheng Zhang, Ke He2, Yayu Wang, Li Lu, Xu-Cun Ma, Qi-Kun Xue, Science Vol. 340 no. 6129, pp. 167-170 (2013).

[47] S. Modak, K. Sengupta, and Diptiman Sen, Phys. Rev. B 86, 205114 (2012).

[48] Hailin Peng, Keji Lai, Desheng Kong, Stefan Meister, Yulin Chen, Xiao-Liang Qi, Shou-Cheng Zhang, Zhi-Xun Shen, and Yi Cui, Nature Materials 9, 225Ð229 (2010).

[49] Thomas Ihn, Nature Materials 9, 187Ð188 (2010).

[50] Z. Alpichshev, J. G. Analytis, J. H. Chu, I. R. Fisher, Y. L. Chen, Z. X. Shen, A. Fang, and A Kapitulnik, Phys. Rev. Lett. 104, 016401 (2010).

[51] G. Rosenberg, M. Franz, Phys. Rev. B 85, 195119 (2012).

[52] M. Wenin, A. Windisch, and W. Pötz, J. Appl. Phys. 108, 103717 (2010), and references therein.

[53] Zhenhua Wu, F. M. Peeters, and Kai Chang, Appl. Phys. Lett. 98, 162101 (2011).

[54] A. Van Esch, L. Van Bockstal, J. De Boeck, G. Verbanck, A. S. van Steenbergen, P. J. Wellmann, B. Grietens, R. Bogaerts, F. Herlach and G. Borghs, Phys. Rev. B 56, 13103 (1997).

[55] I. Garate and M. Franz, Phys. Rev. Lett. 104, 146802 (2010).

[56] H. How, R. C. O'Handley, and F. R. Morgenthaler, Phys. Rev. B 40, 4808 (1989).

[57] Takehito Yokoyama, Jiadong Zang, and Naoto Nagaosa, Phys. Rev. B 81, 241410(R) (2010).

[58] R. Hirota, J. Phys. Soc. Jpn. 33, 1459 (1972).

[59] Graham Bowtell and A. E. G. Stuart, Phys. Rev. D 15, 3580 (1977).

[60] S. Novikov, S. V. Manakov, L. P. Pitaevskii, and V. E. Zarkharov, Theory of Solitons, Consultants Bureau, New York (1984).

[61] W. Y. Shan, H. Z. Lu, and S. Q. Shen, New J. Phys. 12, 043048 (2010).

[62] Timur Tudorovskiy and Mikhail I. Katsnelson, Phys. Rev. B 86, 045419 (2012).

[63] R. Hammer and W. Pötz, Comp. Phys. Comm., in press, http://dx.doi.org/10.1016/j.cpc.2013.08.013

[64] P. H. Ginsparg and K. G. Wilson, Physical Review D 25, 2649 (1982).

[65] H. B. Nielsen and M. Ninomiya, Physics Letters B 105, 219 (1981).

[66] R. Hammer, C. Ertler, and W. Pötz, arXiv:1205.6941

[67] R. Hammer, W. Pötz, and A. Arnold, J. Comp. Phys. 256, 728 (2014), in press, http://dx.doi.org/10.1016/j.jcp.2013.09.022

[68] R. Hammer, W. Pötz, and A. Arnold, submitted to Journal of Computational Physics (2013), preprint available at arXiv:1309.3452.

Chapter 12

PAPER REPRINT: SINGLE-CONE REAL-SPACE FINITE DIFFERENCE SCHEME FOR THE TIME-DEPENDENT DIRAC EQUATION

---

submitted to Journal of Computational Physics
preprint available at arXiv:1309.3452

R. Hammer, W. Pötz, and A. Arnold

A finite difference scheme for the numerical treatment of the (3+1)D Dirac equation is presented. Its staggered-grid intertwined discretization treats space and time coordinates on equal footing, thereby avoiding the notorious fermion doubling problem. This explicit scheme operates entirely in real space and leads to optimal linear scaling behavior for the computational effort per space-time grid-point. It allows for an easy and efficient parallelization. A functional for a norm on the grid is identified. It can be interpreted as probability density and is proved to be conserved by the scheme. The single-cone dispersion relation is shown and exact stability conditions are derived. Finally, a single-cone scheme and its properties are presented for the two-component (2+1)D Dirac equation.

12.1 Introduction

12.1.1 The Dirac Equation and Numerical Schemes

Even more than 80 years after its presentation by P. A. M. Dirac in 1928, the Dirac equation has not lost its fascination and significance in physics [1]. The Dirac equation (in quantized form) has been of fundamental importance to the development of modern field theories and many-particle physics [2, 3, 4, 5]. Interestingly, even today analytic solutions are very rare[1] [6, 7, 8, 9]. In general, solutions have to be obtained numerically. They have gained in relevance by rapidly increasing computational resources, as well as the development of efficient numerical schemes. In a single particle picture, the (3+1)D Dirac equation is applicable whenever the external electromagnetic fields are strong enough to accelerate a spin-$1/2$ particle to relativistic speeds, but many-particle effects and electron-positron pair production can be neglected [10, 11]. This regime is reached in the study of light-matter interaction with the availability of short-pulse laser light in the (sub-)femtosecond range and intensities in excess of 10^{18}W/cm^2, which corresponds to the relativistic threshold[2] [10, 11]. Much of the physics in strong laser fields has been understood within a classical treatment of the relativistic electron. More recently, a numerical treatment of the quantum wave packet dynamics has become feasible [12, 13]. For an electron in a plane wave field, a wave-packet description of an electron reveals a drift of the wave packet in the direction of light propagation along with its spreading and shearing [12]. For this investigation a (2+1)D FFT-split-operator code was used. In such an approach, the propagation induced by the momentum part of the Hamiltonian is computed in momentum space, and the remainder in real-space, using fast Fourier transformation between the two representations [12]. The computational effort scales like $\mathcal{O}(N \ln N)$ where N is the number of grid-points. An efficient code using operator splitting in real space, in combination with the exact characteristic solutions in each space direction, was introduced for the (3+1)D case of the Dirac equation recently [13]. It leads to the highly efficient operations count of $\mathcal{O}(N)$.

In condensed matter physics, relativistic effects frequently are well accounted for by corrections to the Pauli equation derived from the Dirac equation [2]. Recently, however, (topological) condensed matter systems supporting effective Dirac and Majorana fermions have become a vivid play-

---

[1] E.g., spin-$1/2$ particle in a homogeneous magnetic field [6], the Dirac oscillator [7], an electromagnetic plane wave [8], or the Coulomb potential [9].

[2] The electron is accelerated to relativistic speeds during one laser cycle.

ground for this community [14, 15, 17]. In particular, metallic surface states on topological insulator surfaces display 2D Dirac cone dispersion [16, 17, 18, 19]. A dynamic analysis of such Dirac fermions, e.g., in presence of effective electromagnetic fields calls for numerical schemes which faithfully represent the low-energy excitation spectrum. We have recently developed and applied such schemes for the (1+1)D and (2+1)D effective 2-component Dirac equation. In the (1+1)D case, we have presented a single-cone lattice scheme for which exactly absorbing open boundaries were derived [25]. In (2+1)D, we have first developed a staggered grid scheme with one additional artificial cone which, however, is able to preserve the linear dispersion of the free $m = 0$ Dirac spin-$1/2$ particle along x- and y-axis [26]. More recently, a staggered grid single-cone scheme was developed for the two-component (2+1)D Dirac equation and used in studies of Dirac fermion dynamics on textured TI surfaces [27, 28]. This scheme, its properties, and its generalization to the four-spinor-component (3+1)D Dirac equation are topic of this paper. It operates entirely in real space and, due to symmeric staggering, treats space and time on equal terms. This scheme avoids the notorious fermion doubling characteristic of direct discretization of the Dirac derivative operators on a real space lattice [20]. To our knowledge, this is the first multi-D finite difference scheme with this property. This is achieved by redistributing the spinor components on a grid, staggered in space *and* time, such that individual spinor components sit on different (adjacent) time sheets. The proposed scheme, as will be shown below, shows an $\mathcal{O}(N)$ scaling behavior.

12.1.2 The Fermion Doubling Problem

Real-space finite-difference schemes for the Dirac equation have been plagued by the fermion doubling problem[3]. It was shown rigorously by Nielsen and Ninomiya that the discretization of the Dirac equation on a regular space grid forbids a single chirally invariant fermion flavor without breaking one or more of the following assumptions: translational invariance, locality, and Hermiticity [20]. Obtaining additional spurious solutions due to discretization is not a problem specific to the Dirac equation, but can occur in all the cases where one discretizes a first derivative operator on a grid. Standard symmetric finite-difference approximations for the first derivatives are applied to preserve Hermiticity. They leave out the central grid point which, in turn, can take on arbitrary values without changing

---

[3] It manifests itself in a non-monotonic dispersion relation leading to additional Dirac cones, in addition to the one at $k = 0$ of the underlying continuum Hamiltonian. For d discretized spatial dimensions one ends up with up to 2^d cones (“fermion flavors").

the specific value which the finite difference expression yields. For example, both a constant function and a function oscillating with the maximum frequency which can be resolved on the grid lead to zero for the central finite difference expression. Already the simplest model, the advection equation in 1D shows a non-monotonic behavior with a second minimum in the dispersion when a central approximation for the first spatial derivative is used (e.g., the forward-time central-space (FTCS) method). In other words, a symmetric first derivative in space utilizes twice the lattice spacing of the underlying grid thereby, in the language of solid state physics, shrinking the effective Brillouin zone in this direction by a factor of two.

Fermion doubling on a grid can be avoided by following basically two main strategies: (i) the incorporation or (ii) the complete avoidance of the central grid point in the scheme. As to the former, the use of a one-sided finite difference operator leads to so-called upwind schemes. For the Dirac equation this seems to work only in 1D, when a unitary time-evolution (conserving the norm) is to be maintained [29]. In this particular case it is equivalent to distributing the spinor components over a staggered grid [29, 25]. Unfortunately in higher dimensions this strategy either leads to non-Hermiticity and a non-unitary scheme or again to the introduction of fermion doubling. We note that the claim for a recently presented coordinate space operator splitting scheme was not troubled by fermion doubling could not be verified by us [13]. In contrast, we find that monotonic dispersion behavior is limited to $K = c\Delta_t/\Delta_x \leq 1/2$ for the (2+1)D and (3+1)D case within this scheme. However, in its present form it can only be executed for $K \in \mathbb{N}$, because characteristic solutions for advection equations, e.g. $f(x, t + \Delta_t) = f(x + K\Delta_x, t)$, are used. It might be possible to repair the scheme by using the reservoir technique, where the main idea is to wait n time steps before updating the solution, which then allows one to use a smaller $\tilde{\Delta}_t = \Delta_t/n$ [30].

The presence of the central grid point in the scheme can also be enforced by adding artificial terms to the scheme, such as the momentum-dependent mass term suggested by Wilson, which lifts (splits) the spurious cones at high momentum, but retains a $k = 0$ cone in good approximation of the continuum dispersion [32]. This strategy comes with its price. In case of the Dirac equation, it spoils chiral invariance for the physical mass $m = 0$ case[4] [32]. Alternatively, one can violate one of the other premises of the Nielsen-Ninomiya no-go theorem, for example, by breaking translational invariance in an extra dimension. This leads to domain-wall fermions [33, 20]. Interestingly, nature uses this trick in topological insulators [15].

---

[4] For $m \neq 0$ chiral symmetry already is broken in the continuum problem.

The other option is to retain the centered approximation and to ensure that the disturbing central grid point cannot cause a problem: get rid of the point - get rid of the problem. This is achieved by the use of a staggered ("checkerboard") grid whereby the grid is subdivided into subsets, with a particular spinor component defined on one of them, but not on the other(s). For the Dirac equation the idea of a staggered grid may be tracked back to Kogut and Susskind in the context of lattice QCD [31]. Here we utilize a staggered grid in space and time which treats time and space on equal footing, in accordance with the covariance of the underlying continuum model. Given initial conditions on a time slice, time propagation is executed in a leap-frog manner where the upper spinor components are computed from the lower ones and vice versa in an explicit recursive scheme.

The paper is organized as follows. In Section 12.2 we present the (3+1)D scheme and proceed with a discussion of its properties, such as norm conservation, stability, and the scaling behavior. In Section 12.3 we present this analysis for the corresponding scheme applied to (2+1)D. Finally the gauge-invariant inclusion of an external electromagnetic potential and its consequences are outlined in Section 12.4. Summary and conclusions are given in Section 12.5.

12.2 Numerical Scheme for the (3+1)D Dirac Equation

The single particle Dirac equation offers a relativistic description of spin $1/2$ particles capturing their particle-antiparticle and spin degree of freedom. A common representation is the (3+1)D Schrödinger form [34, 2]

$$i\hbar c \frac{\partial}{\partial x_o} \vec{\psi}(x_\mu) = \left[-i\hbar c \sum_{j=1,2,3} \alpha_j \frac{\partial}{\partial x_j} + mc^2 \beta + V(x_\mu) \mathbb{1}_4 \right] \vec{\psi}(x_\mu) \,. \tag{12.1}$$

Here we use the 4×4 Dirac matrices in Pauli-Dirac (“standard") form [34]

$$\alpha_j = \sigma_x \otimes \sigma_j = \begin{pmatrix} 0 & \sigma_j \\ \sigma_j & 0 \end{pmatrix} \tag{12.2}$$

and

$$\beta = \sigma_z \otimes \mathbb{1}_2 = \begin{pmatrix} \mathbb{1}_2 & 0 \\ 0 & -\mathbb{1}_2 \end{pmatrix} \,, \tag{12.3}$$

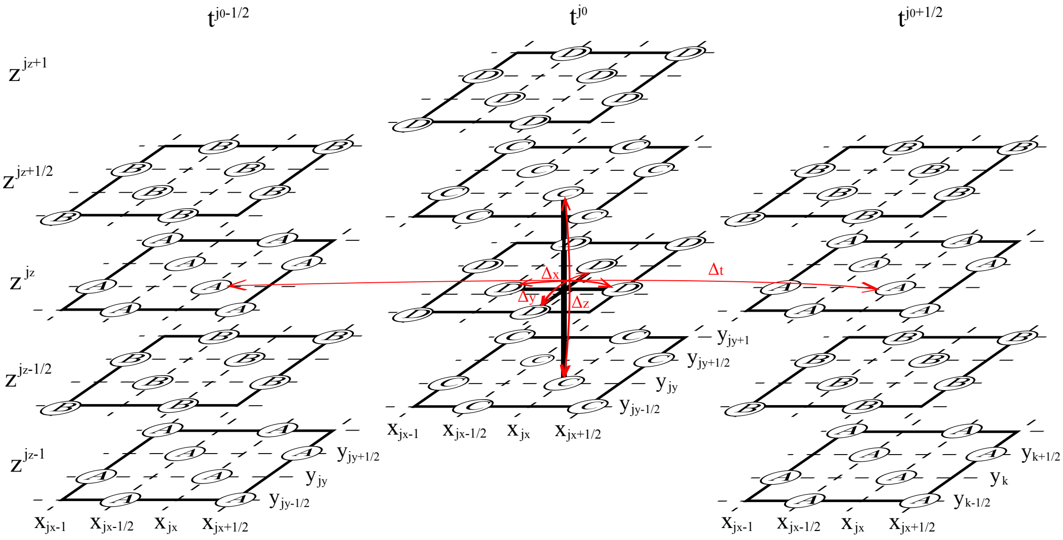

Figure 12.1: Space-time stencil for the first sub-step with explicit leap-frog time stepping for the space-time staggered finite difference scheme of the (3+1)D Dirac equation. The components A, B, C and D are defined on special positions of the space-time grid in order to allow a centered approximation of the first derivative without inducing fermion doubling.

expressed by the Pauli matrices σ_j and the 2×2 unit matrices $\mathbb{1}_2$. The first element in the direct product form accounts for the particle-antiparticle subspace and the second one represents the spin degree of freedom. As usual, $(x_\mu) = (x_o = ct, x_1 = x, x_2 = y, x_3 = z)$ is the space-time four vector.
Writing the Dirac spinor as

$$\vec{\psi}(x_\mu) = \begin{pmatrix} A(x_\mu) \\ B(x_\mu) \\ C(x_\mu) \\ D(x_\mu) \end{pmatrix} \tag{12.4}$$

one observes that, in the standard representation, components A and B, as well as C and D, decouple. The remaining couplings are of two types: the mass and potential terms couple the time derivative of a particular component with itself, secondly, the time derivative of each of the upper two components couples to spatial derivatives of the lower two components. With j_o, j_x, j_y, and $j_z \in \mathbb{Z}$, we define the time step progression in units Δ_t, with $\Delta_o = c\Delta_t$, for the spinor in two steps as shown in Fig. 12.1. First A and B are propagated from time-sheet $t-\Delta_t/2$ (i.e. index $j_o-1/2$) to $t+\Delta_t/2$ (i.e. index $j_o + 1/2$), followed by the propagation of C and D from time-sheet t (j_o) to

$t + \Delta_t\ (j_o + 1)$. One needs x-, y-, and z-derivatives of C and D on time sheet j_0, for the former, and of A and B on time sheet $j_o{+}1/2$, for the latter update. Each spinor component is placed onto every other time sheet: A and B are put on half-integer time sheets $j_o \pm 1/2$ and C and D are put on integer time sheets, such as j_o and $j_o + 1$. This allows one to compute symmetric time derivatives with step width Δ_t. If one then puts A on a rectangular spatial grid, j_x, j_y, j_z the implementation of symmetric x- and y-derivatives of D requires the latter to be put on a face-centered rectangular (fcr) sublattice with grid points $(j_x, j_y + 1/2)$, $(j_x + 1/2, j_y)$ in the x-y planes. In order to be able, in turn, to provide symmetric x-and y-derivatives of A when D is updated, the sublattice of A has to be extended from simple rectangular to fcr (adding lattice points $j_x + 1/2, j_y + 1/2$). Since it is necessary to compute the z-derivative of C to obtain A at the new time sheet, C has to be given at the $j_z + 1/2$ sites, sharing its x- and y-positions with A. A and D may share the same j_z grid points. Similarly, B and D share grid points on the x- and y- axis, while B and C share their grid points along the z-axis. This determines all lattice sites on which individual spinor components need to be defined as follows (again with j_o, j_x, j_y and $j_z \in \mathbb{Z}$)

$$\begin{aligned}
A(x_\mu) &\to A^{j_o-1/2,j_z}_{j_x,j_y}, \quad A^{j_o-1/2,j_z}_{j_x+1/2,j_y+1/2}, \\
B(x_\mu) &\to B^{j_o-1/2,j_z+1/2}_{j_x+1/2,j_y}, \quad B^{j_o-1/2,j_z+1/2}_{j_x,j_y+1/2}, \\
C(x_\mu) &\to C^{j_o,j_z+1/2}_{j_x,j_y}, \quad C^{j_o,j_z+1/2}_{j_x+1/2,j_y+1/2}, \\
D(x_\mu) &\to D^{j_o,j_z}_{j_x+1/2,j_y}, \quad D^{j_o,j_z}_{j_x,j_y+1/2}.
\end{aligned} \tag{12.5}$$

As the attentive reader probably has already recognized, the construction of the grid above was influenced by the use of the standard representation and the requirement of symmetric derivatives using single-lattice constant discretization with a fully symmetric structure in time and space. One can summarize: A and B (C and D) live on the same time sheets, A and D (B and C) on the same z-sheets, and A and C (B and D) are defined on the same $x - y$ positions respectively. Let us discuss the number of grid-points available (occupied and unoccupied) vs. the number of grid-points where a spinor component is actually defined. The number of grid-points altogether (occupied and unoccupied) is $2^4 = 16$ times the number of grid-points available on a space-time-grid without the half-integer positions. Each component is defined on two times the number of integer positions. Thus we can conclude that $1/8$ of all available grid-points are occupied by one concrete spinor component (e.g. A). Remember that for an non-staggered grid, in three spatial dimensions, one obtains $2^3 = 8$ Dirac cones. Here, as we will see below 12.2.1, one has only one Dirac cone. Due to the staggering of the lattice (here also in time!), all partial derivatives can be performed in centered fashion about the grid points without modification of the "lattice constants".

With j_o, j_x, j_y, and $j_z \in \mathbb{Z}$ the scheme looks as follows. For the update of the first spinor component A on the (j_x, j_y) integer grid-points one has

$$\begin{aligned}
&\frac{A^{j_o+1/2,j_z}_{j_x,j_y} - A^{j_o-1/2,j_z}_{j_x,j_y}}{\Delta_o} + \frac{C^{j_o,j_z+1/2}_{j_x,j_y} - C^{j_o,j_z-1/2}_{j_x,j_y}}{\Delta_z} \\
&+ \frac{D^{j_o,j_z}_{j_x+1/2,j_y} - D^{j_o,j_z}_{j_x-1/2,j_y}}{\Delta_x} - i\frac{D^{j_o,j_z}_{j_x,j_y+1/2} - D^{j_o,j_z}_{j_x,j_y-1/2}}{\Delta_y} \\
&= \frac{1}{i\hbar c}(mc^2+V)^{j_o,j_z}_{j_x,j_y}\frac{A^{j_o+1/2,j_z}_{j_x,j_y} + A^{j_o-1/2,j_z}_{j_x,j_y}}{2} \; .
\end{aligned} \tag{12.6}$$

For the half-integer $(j_x + 1/2, j_y + 1/2)$ grid-points the update is

$$\begin{aligned}
&\frac{A^{j_o+1/2,j_z}_{j_x+1/2,j_y+1/2} - A^{j_o-1/2,j_z}_{j_x+1/2,j_y+1/2}}{\Delta_o} + \frac{C^{j_o,j_z+1/2}_{j_x+1/2,j_y+1/2} - C^{j_o,j_z-1/2}_{j_x+1/2,j_y+1/2}}{\Delta_z} \\
&+ \frac{D^{j_o,j_z}_{j_x+1,j_y+1/2} - D^{j_o,j_z}_{j_x,j_y+1/2}}{\Delta_x} - i\frac{D^{j_o,j_z}_{j_x+1/2,j_y+1} - D^{j_o,j_z}_{j_x+1/2,j_y}}{\Delta_y} \\
&= \frac{1}{i\hbar c}(mc^2+V)^{j_o,j_z}_{j_x+1/2,j_y+1/2}\frac{A^{j_o+1/2,j_z}_{j_x+1/2,j_y+1/2} + A^{j_o-1/2,j_z}_{j_x+1/2,j_y+1/2}}{2} \; .
\end{aligned} \tag{12.7}$$

For B one has on the $(j_x + 1/2, j_y)$ sub-grid

$$\begin{aligned}
&\frac{B^{j_o+1/2,j_z}_{j_x+1/2,j_y} - B^{j_o-1/2,j_z}_{j_x+1/2,j_y}}{\Delta_o} - \frac{D^{j_o,j_z+1/2}_{j_x+1/2,j_y} - D^{j_o,j_z-1/2}_{j_x+1/2,j_y}}{\Delta_z} \\
&+ \frac{C^{j_o,j_z}_{j_x+1,j_y} - C^{j_o,j_z}_{j_x,j_y}}{\Delta_x} + i\frac{C^{j_o,j_z}_{j_x+1/2,j_y+1/2} - C^{j_o,j_z}_{j_x+1/2,j_y-1/2}}{\Delta_y} \\
&= \frac{1}{i\hbar c}(mc^2+V)^{j_o,j_z}_{j_x+1/2,j_y}\frac{B^{j_o+1/2,j_z}_{j_x+1/2,j_y} + B^{j_o-1/2,j_z}_{j_x+1/2,j_y}}{2} \; ,
\end{aligned} \tag{12.8}$$

and on the $(j_x, j_y + 1/2)$ sub-grid one uses

$$\begin{aligned}
&\frac{B^{j_o+1/2,j_z}_{j_x,j_y+1/2} - B^{j_o-1/2,j_z}_{j_x,j_y+1/2}}{\Delta_o} - \frac{D^{j_o,j_z+1/2}_{j_x,j_y+1/2} - D^{j_o,j_z-1/2}_{j_x,j_y+1/2}}{\Delta_z} \\
&+ \frac{C^{j_o,j_z}_{j_x+1/2,j_y+1/2} - C^{j_o,j_z}_{j_x-1/2,j_y+1/2}}{\Delta_x} + i\frac{C^{j_o,j_z}_{j_x,j_y+1} - C^{j_o,j_z}_{j_x,j_y}}{\Delta_y} \\
&= \frac{1}{i\hbar c}(mc^2+V)^{j_o,j_z}_{j_x,j_y+1/2}\frac{B^{j_o+1/2,j_z}_{j_x,j_y+1/2} + B^{j_o-1/2,j_z}_{j_x,j_y+1/2}}{2} \; .
\end{aligned} \tag{12.9}$$

The update for the C-components living on (j_x, j_y) writes

$$\begin{aligned}
&\frac{C^{j_o+1,j_z}_{j_x,j_y} - C^{j_o,j_z}_{j_x,j_y}}{\Delta_o} + \frac{A^{j_o+1/2,j_z+1/2}_{j_x,j_y} - A^{j_o+1/2,j_z-1/2}_{j_x,j_y}}{\Delta_z} \\
&+ \frac{B^{j_o+1/2,j_z}_{j_x+1/2,j_y} - B^{j_o+1/2,j_z}_{j_x-1/2,j_y}}{\Delta_x} - i\frac{B^{j_o+1/2,j_z}_{j_x,j_y+1/2} - B^{j_o+1/2,j_z}_{j_x,j_y-1/2}}{\Delta_y} \\
&= \frac{1}{i\hbar c}(-mc^2 + V)^{j_o+1/2,j_z}_{j_x,j_y} \frac{C^{j_o+1,j_z}_{j_x,j_y} + C^{j_o,j_z}_{j_x,j_y}}{2} ,
\end{aligned} \tag{12.10}$$

and for the C-component on $(j_x + 1/2, j_y + 1/2)$

$$\begin{aligned}
&\frac{C^{j_o+1,j_z}_{j_x+1/2,j_y+1/2} - C^{j_o,j_z}_{j_x+1/2,j_y+1/2}}{\Delta_o} + \frac{A^{j_o+1/2,j_z+1/2}_{j_x+1/2,j_y+1/2} - A^{j_o+1/2,j_z-1/2}_{j_x+1/2,j_y+1/2}}{\Delta_z} \\
&+ \frac{B^{j_o+1/2,j_z}_{j_x+1,j_y+1/2} - B^{j_o+1/2,j_z}_{j_x,j_y+1/2}}{\Delta_x} - i\frac{B^{j_o+1/2,j_z}_{j_x+1/2,j_y+1} - B^{j_o+1/2,j_z}_{j_x+1/2,j_y}}{\Delta_y} \\
&= \frac{1}{i\hbar c}(-mc^2 + V)^{j_o+1/2,j_z}_{j_x+1/2,j_y+1/2} \frac{C^{j_o+1,j_z}_{j_x+1/2,j_y+1/2} + C^{j_o,j_z}_{j_x+1/2,j_y+1/2}}{2} .
\end{aligned} \tag{12.11}$$

Finally, for the D component on the $(j_x + 1/2, j_y)$ sub-grid the update is

$$\begin{aligned}
&\frac{D^{j_o+1,j_z}_{j_x+1/2,j_y} - D^{j_o,j_z}_{j_x+1/2,j_y}}{\Delta_o} - \frac{B^{j_o+1/2,j_z+1/2}_{j_x+1/2,j_y} - B^{j_o+1/2,j_z-1/2}_{j_x+1/2,j_y}}{\Delta_z} \\
&+ \frac{A^{j_o+1/2,j_z}_{j_x+1,j_y} - A^{j_o+1/2,j_z}_{j_x,j_y}}{\Delta_x} + i\frac{A^{j_o+1/2,j_z}_{j_x+1/2,j_y+1/2} - A^{j_o+1/2,j_z}_{j_x+1/2,j_y-1/2}}{\Delta_y} \\
&= \frac{1}{i\hbar c}(-mc^2 + V)^{j_o+1/2,j_z}_{j_x+1/2,j_y} \frac{D^{j_o+1,j_z}_{j_x+1/2,j_y} + D^{j_o,j_z}_{j_x+1/2,j_y}}{2} ,
\end{aligned} \tag{12.12}$$

and, for $(j_x, j_y + 1/2)$,

$$\begin{aligned}
&\frac{D^{j_o+1,j_z}_{j_x,j_y+1/2} - D^{j_o,j_z}_{j_x,j_y+1/2}}{\Delta_o} - \frac{B^{j_o+1/2,j_z+1/2}_{j_x,j_y+1/2} - B^{j_o+1/2,j_z-1/2}_{j_x,j_y+1/2}}{\Delta_z} \\
&+ \frac{A^{j_o+1/2,j_z}_{j_x+1/2,j_y+1/2} - A^{j_o+1/2,j_z}_{j_x-1/2,j_y+1/2}}{\Delta_x} + i\frac{A^{j_o+1/2,j_z}_{j_x,j_y+1} - A^{j_o+1/2,j_z}_{j_x,j_y}}{\Delta_y} \\
&= \frac{1}{i\hbar c}(-mc^2 + V)^{j_o+1/2,j_z}_{j_x,j_y+1/2} \frac{D^{j_o+1,j_z}_{j_x,j_y+1/2} + D^{j_o,j_z}_{j_x,j_y+1/2}}{2} .
\end{aligned} \tag{12.13}$$

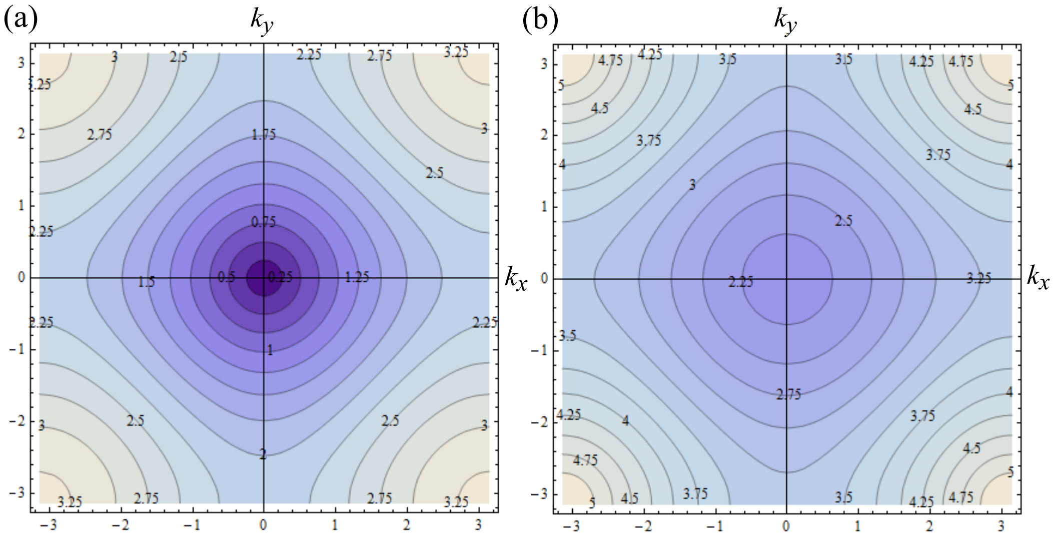

Figure 12.2: Dispersion relation of the leap-frog staggered-grid finite difference scheme for the (3+1)D Dirac equation. $\Delta_x = \Delta_y = \Delta_z = \hbar = 1$, $\Delta_o = 1/\sqrt{3}$, $m = 0$. (a) $k_z = 0$, (b) $k_z = \pi$.

12.2.1 Dispersion relation

There is no fermion doubling for this scheme. For constant coefficients (potential and mass), this can be shown by considering the equivalent to continuum plane-wave solutions for frequency ω and k-vector (k_x, k_y, k_z),

$$\vec{\psi}_{k_\mu}(x_\mu) = \begin{pmatrix} \tilde{A}(k_j) \\ \tilde{B}(k_j) \\ \tilde{C}(k_j) \\ \tilde{D}(k_j) \end{pmatrix} e^{-i\omega t} e^{i\sum_j k_j x_j} \; . \tag{12.14}$$

On the lattice, given by the scheme, plane-wave solutions take the form

$$\vec{\psi}_{k_\mu}(x_\mu) = \begin{pmatrix} \tilde{A}(k_j)e^{i\omega\Delta_t/2} \\ \tilde{B}(k_j)e^{i\omega\Delta_t/2}e^{ik_x\Delta_x/2}e^{ik_z\Delta_z/2} \\ \tilde{C}(k_j)e^{ik_z\Delta_z/2} \\ \tilde{D}(k_j)e^{ik_x\Delta_x/2} \end{pmatrix} e^{-i\omega j_t\Delta_t} e^{i\sum_j k_j j_j \Delta_j} \; , \tag{12.15}$$

where $\omega = ck_o$, $\Delta_o = c\Delta_t$, and $j_t = j_o$. [5] Insertion into the scheme above translates any discrete $x_o = ct$ derivative into a multiplication by

---

[5] The relative shift of the sub-grids e.g. in the x-y-plane can be established by a translation by one-half lattice spacing in x- or y-direction. In Eq. (12.15) the translation in x-direction is choosen. This does not induce an asymmetry in the scheme. In each of the four

$-\frac{2i}{\Delta_o}\sin(\frac{\omega\Delta_t}{2})$ and every discrete partial position $j = x, y, z$ derivative into a multiplication by a factor $\frac{2i}{\Delta_j}\sin(\frac{k_j\Delta_j}{2})$. A time average leads to a factor $\cos(\frac{\omega\Delta_t}{2})$.

For fixed Δ_μ, we therefore obtain the dispersion for the lattice from the continuum solution by the substitutions

$$E = \hbar\omega \to E(\omega) = \frac{2\hbar}{\Delta_o}\sin(\frac{\omega\Delta_t}{2})\;, \tag{12.16}$$

$$p_j = \hbar k_j \to P_j(k_j) = \frac{2\hbar}{\Delta_j}\sin(\frac{k_j\Delta_j}{2})\;, \tag{12.17}$$

and

$$mc^2 \to m(\omega)c^2 = mc^2\cos(\frac{\omega\Delta_t}{2})\;. \tag{12.18}$$

With these translation rules, the plane-wave solutions on the lattice can be obtained from the continuum solutions [34, 2]. In particular, the energy dispersion reads

$$E(\omega) = \pm\sqrt{m(\omega)^2c^4 + |c\mathbf{P}|^2}\;, \tag{12.19}$$

were $\mathbf{P} = (P_1, P_2, P_3)$ is the momentum vector with the components defined in Eq. 12.17. This establishes the dispersion relation between ω and k_j. Note that on the lattice the k_j's are restricted to the values $\big(-\frac{\pi}{\Delta_j}, +\frac{\pi}{\Delta_j}\big]$ and ω to $\big(-\frac{\pi}{\Delta_o}, +\frac{\pi}{\Delta_o}\big]$. Equation (12.19) can be solved for ω by taking the square and rearranging it to the final result for the dispersion relation

$$\hbar\omega = \pm\frac{2\hbar}{\Delta_t}\arcsin\big[X(k_j)\big] \quad \text{with} \quad X(k_j) = \sqrt{\frac{(mc^2)^2 + |c\mathbf{P}|^2}{(mc^2)^2 + (\frac{2\hbar}{\Delta_t})^2}}\;. \tag{12.20}$$

Moreover,

$$E(\omega) = \pm\frac{2\hbar}{\Delta_t}X(k_j) \tag{12.21}$$

and

$$m(\omega)c^2 = mc^2\sqrt{1 - X(k_j)^2}\;. \tag{12.22}$$

The spinor eigenket structure, as for the continuum model, is [2]

---

equations the common e-factor for the center position in space and time can be canceled. This neither changes the zeros of the characteristic determinant nor the spinor-component ratios of the eigensolutions.

$$\vec{\psi}(k_j)^{(1)} = N \begin{pmatrix} 1 \\ 0 \\ \frac{cP_z}{E(\omega)+m(\omega)c^2} \\ \frac{c(P_x+iP_y)}{E(\omega)+m(\omega)c^2} \end{pmatrix} , \qquad \vec{\psi}(k_j)^{(2)} = N \begin{pmatrix} 0 \\ 1 \\ \frac{c(P_x-iP_y)}{E(\omega)+m(\omega)c^2} \\ -\frac{cP_z}{E(\omega)+m(\omega)c^2} \end{pmatrix} ,$$

$$\vec{\psi}(k_j)^{(3)} = N \begin{pmatrix} \frac{-cP_z}{|E(\omega)|+m(\omega)c^2} \\ -\frac{c(P_x+iP_y)}{|E(\omega)|+m(\omega)c^2} \\ 1 \\ 0 \end{pmatrix} , \qquad \vec{\psi}(k_j)^{(4)} = N \begin{pmatrix} -\frac{c(P_x-iP_y)}{|E(\omega)|+m(\omega)c^2} \\ \frac{cP_z}{|E(\omega)|+m(\omega)c^2} \\ 0 \\ 1 \end{pmatrix} . \tag{12.23}$$

N depends on the choice of normalization.

12.2.2 Stability

A preliminary discussion of stability can be based on the dispersion relation associated with plane wave solutions (in absence of an external potential), Eq. (12.20). Instability occurs when $|X(k_j)|$ becomes larger than one, making the two solutions for ω to become a pair of complex conjugate numbers. Imposing

$$\left| \frac{(mc^2)^2 + (2\hbar c)^2 \sum_{j=x}^{z} \frac{1}{\Delta_j^2}}{(mc^2)^2 + (2\hbar c)^2 \frac{1}{\Delta_o^2}} \right| \leq 1 ,$$

one arrives at the condition

$$r_x^2 + r_y^2 + r_z^2 \leq 1 ,$$

for $r_j = \Delta_o/\Delta_j$. Thus, for equal spatial differences $\Delta_x = \Delta_y = \Delta_z = \Delta$ this gives the condition $r = \Delta_o/\Delta \leq 1/\sqrt{3}$.

In order to discuss stability of this scheme in more generality, we seek a quantity (norm) which is conserved under the discrete time evolution. For this purpose we introduce several definitions and abbreviations to simplify notation. Let us recall on which grid positions the spinor components are defined

$$\begin{aligned} A_j \text{ with } j &\in (j_x, j_y, j_z) \cup (j_x + 1/2, j_y + 1/2, j_z) , \\ B_j \text{ with } j &\in (j_x + 1/2, j_y, j_z + 1/2) \cup (j_x, j_y + 1/2, j_z + 1/2) , \\ C_j \text{ with } j &\in (j_x, j_y, j_z + 1/2) \cup (j_x + 1/2, j_y + 1/2, j_z + 1/2) , \\ D_j \text{ with } j &\in (j_x + 1/2, j_y, j_z) \cup (j_x, j_y + 1/2, j_z) , \end{aligned} \tag{12.24}$$

where j_x, j_y and j_z are integer numbers. In what follows we consider a time step Δ_t where spinor A and B are propagated from $j_o - 1/2$ to $j_o + 1/2$, and C and D are propagated from j_o to $j_o + 1$, using the short-hand notation $A_j^-, B_j^-, C_j^-, D_j^- \to A_j^+, B_j^+, C_j^+, D_j^+$. Furthermore we define a scalar product between spinor components $F_j^{j_o}$ and $G_{j+j'}^{j'_o}$ on the lattice in which a sum over all spatial sites j is performed

$$(F^{j_o}, G^{j'_o})_{j'} = \sum_j F_j^{j_o} G_{j+j'}^{j'_o *} = \sum_j F_{j-j'}^{j_o} G_j^{j'_o *}. \tag{12.25}$$

This short-hand notation involves a summation over all the spatial sublattice sites j on the time sheet j_o which belong to spinor component F. Also, j' is limited to spatial shifts which connect the spatial sublattice of F to the one associated with spinor component G. Note that this scalar product depends on j_o, j'_o, the relative position vector j', and the two spinor components involved. Here, however, we only need to consider products for up to nearest neighbor sites. For simplicity, we write $(F^{j_o}, G^{j'_o})_0 = (F^{j_o}, G^{j'_o})$.
$j_i^\pm$ is defined as the vector shifting in the spatial direction i by one half gridspacing. Eg. $j_x^\pm := (j_x \pm 1/2, j_y, j_z)$. Finally we define for any spinor component

$$(\delta_i F)_j := F_{j_i^+} - F_{j_i^-} \,. \tag{12.26}$$

Using the notation introduced above, a *quantity which is conserved under time propagation* is given by

$$\begin{aligned} E_r &= (A, A) + (B, B) + (C, C) + (D, D) \\ &\quad - r_z \Re\Big[(\delta_z C, A) - (\delta_z D, B)\Big] - r_x \Re\Big[(\delta_x D, A) + (\delta_x C, B)\Big] \\ &\quad + r_y \Re\Big[i(\delta_y D, A) - i(\delta_y C, B)\Big] \,. \end{aligned} \tag{12.27}$$

The proof can be given following the (1+1)D paper [25].

Proof. We begin by writing the scheme in short-hand notation using the definitions given above

$$\begin{aligned}
&A_j^+ - A_j^- + r_z(C^-_{j_z^+} - C^-_{j_z^-}) + r_x(D^-_{j_x^+} - D^-_{j_x^-}) - ir_y(D^-_{j_y^+} - D^-_{j_y^-}) \\
&= \frac{\Delta_o(mc^2+V)_j}{2i\hbar}(A_j^+ + A_j^-)\,, \qquad (12.28)\\
&B_j^+ - B_j^- - r_z(D^-_{j_z^+} - D^-_{j_z^-}) + r_x(C^-_{j_x^+} - C^-_{j_x^-}) + ir_y(C^-_{j_y^+} - C^-_{j_y^-}) \\
&= \frac{\Delta_o(mc^2+V)_j}{2i\hbar}(B_j^+ + B_j^-)\,, \qquad (12.29)\\
&C_j^+ - C_j^- + r_z(A^+_{j_z^+} - A^+_{j_z^-}) + r_x(B^+_{j_x^+} - B^+_{j_x^-}) - ir_y(B^+_{j_y^+} - B^+_{j_y^-}) \\
&= \frac{\Delta_o(-mc^2+V)_j^+}{2i\hbar}(C_j^+ + C_j^-)\,, \qquad (12.30)\\
&D_j^+ - D_j^- - r_z(B^+_{j_z^+} - B^+_{j_z^-}) + r_x(A^+_{j_x^+} - A^+_{j_x^-}) + ir_y(A^+_{j_y^+} - A^+_{j_y^-}) \\
&= \frac{\Delta_o(-mc^2+V)_j^+}{2i\hbar}(D_j^+ + D_j^-)\,, \qquad (12.31)
\end{aligned}$$

where $V = V^{j_o}$, $V^+ = V^{j_o+1/2}$, and analogous for m.
Each of the Eqs. (12.28) to (12.31) is used to obtain an identity for the real part of a scalar product. Eq. (12.28) is multiplied by $(A_j^+ + A_j^-)^*$ and summed over all lattice sites j. Similarly Eq. (12.29) is multiplied by $(B_j^+ + B_j^-)^*$ and so on. Adding up the real part of these four equations one obtains

$$\begin{aligned}
&(A^+,A^+) - (A^-,A^-) + (B^+,B^+) - (B^-,B^-) \\
&+ (C^+,C^+) - (C^-,C^-) + (D^+,D^+) - (D^-,D^-) \\
&+ \Re\Big\{ r_z\big[(A^+ + A^-, \delta_z C^-) + (C^+ + C^-, \delta_z A^+) \\
&\quad - (B^+ + B^-, \delta_z D^-) - (D^+ + D^-, \delta_z B^+)\big] \\
&\quad + r_x\big[(A^+ + A^-, \delta_x D^-) + (D^+ + D^-, \delta_x A^+) \\
&\quad + (B^+ + B^-, \delta_x C^-) + (C^+ + C^-, \delta_x B^+)\big]\Big\} \\
&- r_y \Im\Big\{(A^+ + A^-, \delta_y D^-) - (D^+ + D^-, \delta_y A^+) \\
&\quad - (B^+ + B^-, \delta_y C^-) + (C^+ + C^-, \delta_y B^+)\Big\} = 0\,. \qquad (12.32)
\end{aligned}$$

Whenever possible, terms have been grouped in pairs of the form $\Re\{(F^+ + F^-, \delta_k G^-) + (G^+ + G^-, \delta_k F^+)\}$ or $\Im\{(F^+ + F^-, \delta_k G^-) - (G^+ + G^-, \delta_k F^+)\}$. Each of the second terms in these pairs may be rewritten as follows (i. e.

summation by parts)

$$\begin{aligned}(G^+ + G^-, \delta_k F^+) &= \sum_j (G_j^+ + G_j^-)\,(F^+_{j_k^+} - F^+_{j_k^-})^* \\ &= -(\delta_k G^+, F^+) - (\delta_k G^-, F^+)\,, \end{aligned} \tag{12.33}$$

We now observe that the contribution arising from mixed terms in time $+$ and $-$ cancel when taking, respectively, the real and imaginary part, and Eq. (12.32) takes the form $E^+ - E^- = 0$ with E given in Eq. (12.27). □

In what follows, we utilize the conserved functional (12.27) to demonstrate stability for arbitrary space- and time-dependent mass and potential. The spinor elements stay finite, bounded by the estimate

$$(A, A) + (B, B) + (C, C) + (D, D) \le \frac{E_r^0}{1 - r_x - r_y - r_z}\,, \tag{12.34}$$

when $r_x + r_y + r_z < 1$ (e.g. using $r = r_x = r_y = r_z < 1/3$). E_r^0 is the norm (12.27) of the initial data $A^{-1/2}$, $B^{-1/2}$, C^0, and D^0.

Proof.

$$\begin{aligned}
E_r = E_r^0 &= (A,A) + (B,B) + (C,C) + (D,D)\\
&\quad - r_z \Re\Big[(\delta_z C, A) - (\delta_z D, B)\Big]\\
&\quad - r_x \Re\Big[(\delta_x D, A) + (\delta_x C, B)\Big]\\
&\quad + r_y \Re\Big[i(\delta_y D, A) - i(\delta_y C, B)\Big]\\
&\\
&\geq (A,A) + (B,B) + (C,C) + (D,D)\\
&\quad - r_z\Big|\Re\Big[(\delta_z C, A)\Big]\Big| - r_z\Big|\Re\Big[(\delta_z D, B)\Big]\Big|\\
&\quad - r_x\Big|\Re\Big[(\delta_x D, A)\Big]\Big| - r_x\Big|\Re\Big[(\delta_x C, B)\Big]\Big|\\
&\quad - r_y\Big|\Re\Big[(\delta_y D, A)\Big]\Big| - r_y\Big|\Re\Big[(\delta_y C, B)\Big]\Big|\\
&\\
&\geq (A,A) + (B,B) + (C,C) + (D,D)\\
&\quad - r_z\Big|\Re\Big[(C_{j_z^+}, A)\Big]\Big| - r_z\Big|\Re\Big[(D_{j_z^+}, B)\Big]\Big|\\
&\quad - r_x\Big|\Re\Big[(D_{j_x^+}, A)\Big]\Big| - r_x\Big|\Re\Big[(C_{j_x^+}, B)\Big]\Big|\\
&\quad - r_y\Big|\Re\Big[(D_{j_y^+}, A)\Big]\Big| - r_y\Big|\Re\Big[(C_{j_y^+}, B)\Big]\Big|\\
&\quad - r_z\Big|\Re\Big[(C_{j_z^-}, A)\Big]\Big| - r_z\Big|\Re\Big[(D_{j_z^-}, B)\Big]\Big|\\
&\quad - r_x\Big|\Re\Big[(D_{j_x^-}, A)\Big]\Big| - r_x\Big|\Re\Big[(C_{j_x^-}, B)\Big]\Big|\\
&\quad - r_y\Big|\Re\Big[(D_{j_y^-}, A)\Big]\Big| - r_y\Big|\Re\Big[(C_{j_y^-}, B)\Big]\Big|\\
&\\
&\geq (A,A) + (B,B) + (C,C) + (D,D)\\
&\quad - \big(r_x + r_y + r_z\big)\Big((A,A) + (B,B) + (C,C) + (D,D)\Big)\,. \qquad (12.35)
\end{aligned}$$

In the last line we use the inequality $2|\Re\{(a,b)\}| \leq \|a\|^2 + \|b\|^2$. □

By comparison with the result from the "reality condition" ($\Im\{\omega\} = 0$) of the dispersion (obtained for constant mass and potential), one observes that the condition derived here for arbitrary space- and time-dependent coefficients gives a narrower bound for stability (*i.e.* $r < 1/3$ vs. $r \leq 1/\sqrt{3}$). This is due to the coarse estimates in the short proof above. The proof of stability for the general case is more lengthy and is shown in 12.6 confirming the stability condition $r \leq 1/\sqrt{3}$ and $r = r_x = r_y = r_z$.

12.3 Numerical Scheme for the (2+1)D Dirac Equation

In some cases it is not necessary to solve the full (3+1)D Dirac equation. For example, under translational invariance in one spatial direction (when mass and potential terms are independent of this space coordinate) one can perform a partial Fourier transform within the scheme above, essentially leading to the substitution Eq. (12.17). The spin degree of freedom may be unimportant or it may be locked to the orbital motion, as is the case for the effective model for topological insulator (TI) surface states [15]. Then, a two component spinor in a (2+1)D model is adequate to capture the underlying physics. In some cases, low-dimensional models have been used simply because they are easier to handle.

Once more, we use the Schrödinger form of the (2+1)D Dirac equation

$$i\hbar c\partial_t \boldsymbol{\psi}(x,y,t) = \left[-i\hbar c\sigma_x \frac{\partial}{\partial x} - i\hbar c\sigma_y \frac{\partial}{\partial y} + \sigma_z m(x,y,t) + \mathbb{1}_2 V(x,y,t)\right]\boldsymbol{\psi}(x,y,t)\,, \tag{12.36}$$

where $\boldsymbol{\psi}(x,y,t) \equiv (u,v) \in \mathbb{C}^2$ is a 2-component spinor. For topological insulators, the two components are associated with spin$=1/2$, whereby the physical spin quantization axis is $\mathbf{S} \propto \hat{\mathbf{z}}\times\boldsymbol{\sigma}$. Here, $\hat{\mathbf{z}}$ is the unit-normal vector to the surface and c constitutes the effective velocity of the quasi-particles in the effective model. $V \in \mathbb{R}$ is the scalar potential.

Earlier on and mainly for the treatment of rectangular structures we have presented a scheme which shows perfect dispersion along the coordinate axes for the free mass-less case, but with a second Dirac cone equally shared by the four corners of the first Brillouin zone [26, 28]. It is therefore ideally suited for TI surface states with rectangular structuring. Here a different staggering of the grid in space is applied to the u- and v-component of the spinor $\boldsymbol{\psi} = (u,v)$ which eliminates the second cone. It is represented graphically in Fig. 12.3 and follows the procedure for the (3+1)D case: A progression in time by $\Delta_o = c\Delta_t$ involves two initial, $t = j_o - 1/2, j_o$, and two final time sheets, $t = j_o + 1/2, j_o + 1$. Spinor component u lives on a face-centered rectangular (fcr) lattice (fcr-u) on the half-integer time sheets.

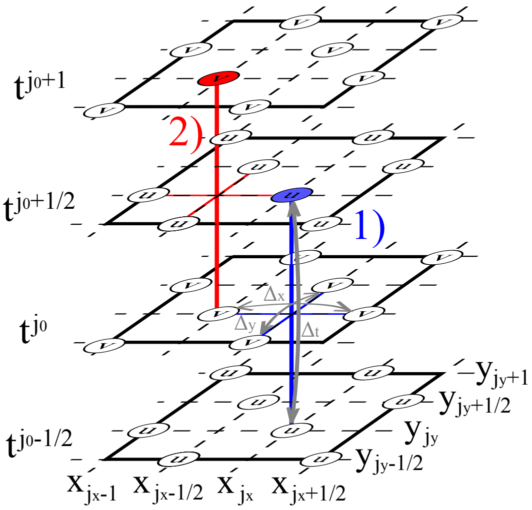

Figure 12.3: Leap-frog time stepping on a time and space staggered grid for the (2+1)D two component spinor Dirac equation. 1) In the first sub-step new u-components (blue/dark gray) are computed from old u and the spatial differences of the v values. 2) Then in the second sub-step (red/-light gray) the spatial differences of u are used together with the old v-components to update for the new v's.

Spinor component v lives on the fcr lattice (fcr-v) formed by the set of mid-point positions of lines connecting nearest neighbors of the simple rectangular sub-lattice of u, however, shifted vertically onto the integer time sheets. In other words, fcr-u is converted into fcr-y by a shift by $(i+1/2)\Delta_x\hat{e}_x$ (or $(i+1/2)\Delta_y\hat{e}_y$) followed by $\pm(j+1/2)\Delta_o\hat{e}_o, i, j \in \mathbb{Z}$, and vice versa.

The time progression by Δ_o is executed in two steps. First u is propagated from time sheet $j_o - 1/2$ to $j_o + 1/2$ (both supporting fcr-u) by forming symmetric x- and y-derivatives of v using fcr-v on time sheet j_o. In the second step, v on fcr-v on time sheet j_o is propagated to fcr-v on time sheet $j_o + 1$ using symmetric x- and y-derivatives of u living on fcr-u on time sheet $j_o + 1/2$. According to the discussion above, one has to propagate $u^{j_o-1/2}_{j_x,j_y}$, $u^{j_o-1/2}_{j_x+1/2,j_y+1/2}$, $v^{j_o}_{j_x+1/2,j_y}$, and $v^{j_o}_{j_x,j_y+1/2}$ for $j_\nu \in \mathbb{Z}$. Using second order accurate symmetric approximations for the derivatives one arrives at the following scheme for this grid

$$\begin{aligned}\frac{u^{j_o+1/2}_{j_x,j_y} - u^{j_o-1/2}_{j_x,j_y}}{\Delta_t} =& \left(\frac{m+V}{i\hbar c}\right)^{j_o}_{j_x,j_y} \frac{u^{j_o+1/2}_{j_x,j_y} + u^{j_o-1/2}_{j_x,j_y}}{2} \\ &- \frac{(v^{j_o}_{j_x+1/2,j_y} - v^{j_o}_{j_x-1/2,j_y})}{\Delta_x} \\ &+ i\frac{(v^{j_o}_{j_x,j_y+1/2} - v^{j_o}_{j_x,j_y-1/2})}{\Delta_y} ,\end{aligned} \tag{12.37}$$

$$\begin{aligned}\frac{v^{j_o+1}_{j_x-1/2,j_y} - v^{j_o}_{j_x-1/2,j_y}}{\Delta_t} =& - \left(\frac{m-V}{i\hbar c}\right)^{j_o+1/2}_{j_x-1/2,j_y} \frac{v^{j_o+1}_{j_x-1/2,j_y} + v^{j_o}_{j_x-1/2,j_y}}{2} \\ &- \frac{(u^{j_o+1/2}_{j_x,j_y} - u^{j_o+1/2}_{j_x-1,j_y})}{\Delta_x} \\ &- i\frac{(u^{j_o+1/2}_{j_x-1/2,j_y+1/2} - u^{j_o+1/2}_{j_x-1/2,j_y-1/2})}{\Delta_y} ,\end{aligned} \tag{12.38}$$

and analogous equations for the other sub-grid

$$\begin{aligned}&\frac{u^{j_o+1/2}_{j_x-1/2,j_y-1/2} - u^{j_o-1/2}_{j_x-1/2,j_y-1/2}}{\Delta_t} \\ &= \left(\frac{m+V}{i\hbar c}\right)^{j_o}_{j_x-1/2,j_y-1/2} \frac{u^{j_o+1/2}_{j_x-1/2,j_y-1/2} + u^{j_o-1/2}_{j_x-1/2,j_y-1/2}}{2} \\ &- \frac{(v^{j_o}_{j_x,j_y-1/2} - v^{j_o}_{j_x-1,j_y-1/2})}{\Delta_x} + i\frac{(v^{j_o}_{j_x-1/2,j_y} - v^{j_o}_{j_x-1/2,j_y-1})}{\Delta_y} ,\end{aligned} \tag{12.39}$$

$$\begin{aligned}\frac{v^{j_o+1}_{j_x,j_y-1/2} - v^{j_o}_{j_x,j_y-1/2}}{\Delta_t} =& -\left(\frac{m-V}{i\hbar c}\right)^{j_o+1/2}_{j_x,j_y-1/2} \frac{v^{j_o+1}_{j_x,j_y-1/2} + v^{j_o}_{j_x,j_y-1/2}}{2} \\ - \frac{(u^{j_o+1/2}_{j_x+1/2,j_y-1/2} - u^{j_o+1/2}_{j_x-1/2,j_y-1/2})}{\Delta_x} &- i\frac{(u^{j_o+1/2}_{j_x,j_y} - u^{j_o+1/2}_{j_x,j_y-1})}{\Delta_y} .\end{aligned} \tag{12.40}$$

Note that the u-component defined for the discrete time indices $j_o - 1/2 \in \mathbb{Z}$ 'lives' on the discrete space gridpoints $(j_x, j_y) \in \mathbb{Z}^2$ and on $(j_x - 1/2, j_y - 1/2) \in \mathbb{Z}^2$, whereas the v-component defined for $j_o \in \mathbb{Z}$ is defined for space indices $(j_x - 1/2, j_y) \in \mathbb{Z}^2$ and $(j_x, j_y - 1/2) \in \mathbb{Z}^2$.

For constant coefficients m and V von Neumann stability analysis reveals the stability of the finite difference scheme [36]. Moreover, the growth factor shows that an imaginary potential can be utilized to model an absorbing boundary layer. Fourier transformation in the spatial coordinates gives

$$\begin{aligned} &\underbrace{\begin{pmatrix} \frac{1}{\Delta_t} - \frac{m+V}{i\hbar c} & 0 \\ \frac{2i}{\Delta_x}\sin\frac{k_x\Delta_x}{2} + i\frac{2i}{\Delta_y}\sin\frac{k_y\Delta_y}{2} & \frac{1}{\Delta_t} + \frac{m-V}{i\hbar c} \end{pmatrix}}_{=:S} \begin{pmatrix} \tilde{u}^{+} \\ \tilde{v}^{+} \end{pmatrix} \\ &+ \underbrace{\begin{pmatrix} -\frac{1}{\Delta_t} - \frac{m+V}{i\hbar c} & \frac{2i}{\Delta_x}\sin\frac{k_x\Delta_x}{2} - i\frac{2i}{\Delta_y}\sin\frac{k_y\Delta_y}{2} \\ 0 & -\frac{1}{\Delta_t} + \frac{m-V}{i\hbar c} \end{pmatrix}}_{=:T} \begin{pmatrix} \tilde{u}^{-} \\ \tilde{v}^{-} \end{pmatrix} = 0\,. \end{aligned} \tag{12.41}$$

One defines the amplification matrix $G = -S^{-1}T = S^{-1}S^{*}$. Its eigenvalues are the growth factors (written for $\hbar = 1, c = 1$ and $\Delta_x = \Delta_y = \Delta$)

$$\lambda_{\pm} = P/2 \pm \sqrt{(P/2)^2 - Q}\,, \tag{12.42}$$

with

$$\begin{aligned} P = \mathrm{tr}[G] = -2\Big[&(m^2 - V^2)\Delta_t^2 - 4c^2(1 - \Delta_t^2) \\ &- 4c^2\Delta_t^2(\Delta_y^2\cos k_x\Delta_x + \Delta_x^2\cos k_y\Delta_y)/(\Delta_x\Delta_y)^2\Big]/N\,, \end{aligned} \tag{12.43}$$

$$Q = \det[G] = (4c^2 + (m^2 - V^2)\Delta_t^2 - 4icV\Delta_t)/N \tag{12.44}$$

and

$$N = 4c^2 + (m^2 - V^2)\Delta_t^2 + 4icV\Delta_t\,. \tag{12.45}$$

For $\Delta_t/\Delta \leq 1/\sqrt{2}$ and $m, V \in \mathbb{R}$ the absolute value of the growth factors is 1. Whereas for $V \in \mathbb{C}$ it depends on the sign of the imaginary part whether their absolute value is greater or lesser than 1. The latter can be used for *absorbing boundary layers*. The size of the absolute value of the growth (or in this case damping) factors is exemplified in Fig. 12.4.

The free-particle *dispersion relation* is revealed directly by using a plane wave ansatz $u^{j_o+1}_{j_x+1,j_y+1} = e^{i(\omega\Delta_t - k_x\Delta_x - k_y\Delta_y)}u^{j_o}_{j_x,j_y}$ (and similarly for v) leading to the substitutions Eqs. (12.16)-(12.18) and the dispersion relation

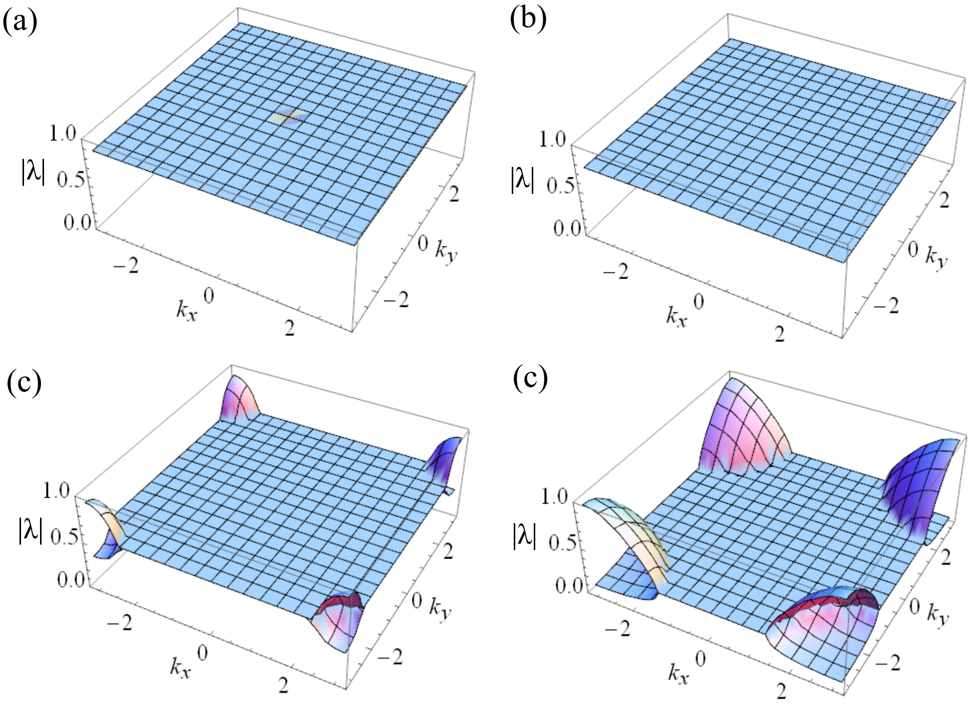

Figure 12.4: Absolute value of the eigenvalues $|\lambda_\pm|$ of the growth matrix G for $m = 0$ and $\Delta_t/\Delta = 0.99/\sqrt{2}$. (a) $V = 0.1i$, (b) $V = 0.2i$, (c) $V = 0.4i$ and (d) $V = 0.8i$.

$$\hbar\omega = \pm\frac{2\hbar}{\Delta_t}\arcsin\left\{\sqrt{\frac{1}{(mc^2)^2 + 2\hbar c/\Delta_t}\left[(mc^2)^2 + \left(\frac{2\hbar}{\Delta_x}\sin\frac{k_x\Delta_x}{2}\right)^2 + \left(\frac{2\hbar}{\Delta_y}\sin\frac{k_y\Delta_y}{2}\right)^2\right]}\right\}. \tag{12.46}$$

The naive discrete expression for the norm $\|\psi\| := \sqrt{\sum_{j_x,j_y}|u_{j_x,j_y}|^2 + |v_{j_x,j_y}|^2}$ in general oscillates around its mean value and is conserved in time only on average. We use a multiplication technique to identify an exactly *conserved functional* and prove stability for arbitrary space and time dependent coefficients, as for the (3+1)D case above. Let us again introduce a short-hand notation using

$$\begin{aligned} u_j \text{ with } j &\in (j_x, j_y) \cup (j_x + 1/2, j_y + 1/2) \; , \\ v_j \text{ with } j &\in (j_x + 1/2, j_y) \cup (j_x, j_y + 1/2) \; . \end{aligned} \tag{12.47}$$

We define spatial difference operators as $(\delta_x f^{j_o})_{j_x,j_y} = f^{j_o}_{j_x+1/2,j_y} - f^{j_o}_{j_x-1/2,j_y}$, $(\delta_y f^{j_o})_{j_x,j_y} = f^{j_o}_{j_x,j_y+1/2} - f^{j_o}_{j_x,j_y-1/2}$ and $(\delta_\pm f^{j_o})_{j_x,j_y} = (\delta_x f^{j_o})_{j_x,j_y} \pm i(\delta_y f^{j_o})_{j_x,j_y}$. We define the inner product $(u^{j_o}, v^{j'_o})_{j'} := \sum_j u^{j_o}_j v^{*j'_o}_{j+j'} = \sum_j u^{j_o}_{j-j'} v^{*j'_o}_j$ on $l^2(\mathbb{Z}^2;\mathbb{C})$ and the notation $\|u^{j_o}\|^2 := (u^{j_o}, u^{j_o})$, with the sum over j running over all spatial lattice points on the time sheet j_o. j' again denotes a displacement vector connecting the two spatial sublattices of u and v. The real part of the inner product of Eq. (39) with $(u^{j_o+1/2} + u^{j_o-1/2})$ gives

$$\left\|u^{j_o+1/2}\right\|^2 - \left\|u^{j_o-1/2}\right\|^2 + r\Re\Big[(\delta_+ v^{j_o}, u^{j_o+1/2} + u^{j_o-1/2})\Big] = 0 \; . \tag{12.48}$$

Analogously, Eq. (40) is multiplied by $(v^{j_o+1} + v^{j_o})^*$ and again the real part is taken to give

$$\left\|v^{j_o+1}\right\|^2 - \left\|v^{j_o}\right\|^2 + r\Re\Big[(\delta_- u^{j_o+1/2}, v^{j_o+1} + v^{j_o})\Big] = 0 \; . \tag{12.49}$$

Performing a summation by parts with vanishing "boundary terms" at infinity gives

$$\Re\Big[(\delta_x v^{j_o}, u^{j_o+1/2} + u^{j_o-1/2})\Big] = -\Re\Big[(\delta_x u^{j_o+1/2} + \delta_x u^{j_o-1/2}, v^{j_o})\Big] \; , \tag{12.50}$$

$$\begin{aligned} \Re\Big[(i\delta_y v^{j_o}, u^{j_o+1/2} + u^{j_o-1/2})\Big] &= \Re\Big[i\;(u^{j_o+1/2} + u^{j_o-1/2}, \delta_y v^{j_o})^*\Big] \\ &= \Re\Big[(i\delta_y u^{j_o+1/2} + i\delta_y u^{j_o-1/2}, v^{j_o})\Big] \; . \end{aligned} \tag{12.51}$$

Finally, adding Eq. (12.48) and Eq. (12.49) leads to

$$\begin{aligned} &\left\|u^{j_o+1/2}\right\|^2 + \left\|v^{j_o+1}\right\|^2 + r\Re\Big[(\delta_- u^{j_o+1/2}, v^{j_o+1})\Big] \\ &= \left\|u^{j_o-1/2}\right\|^2 + \left\|v^{j_o}\right\|^2 + r\Re\Big[(\delta_- u^{j_o-1/2}, v^{j_o})\Big] \end{aligned} \tag{12.52}$$

and one immediately identifies the conserved functional using $r = r_x = r_y$

$$E^{j_o}_r := \left\|u^{j_o+1/2}\right\|^2 + \left\|v^{j_o+1}\right\|^2 + r\Re\Big[(\delta_- u^{j_o+1/2}, v^{j_o+1})\Big] = \text{const} = E^0_r \; . \tag{12.53}$$

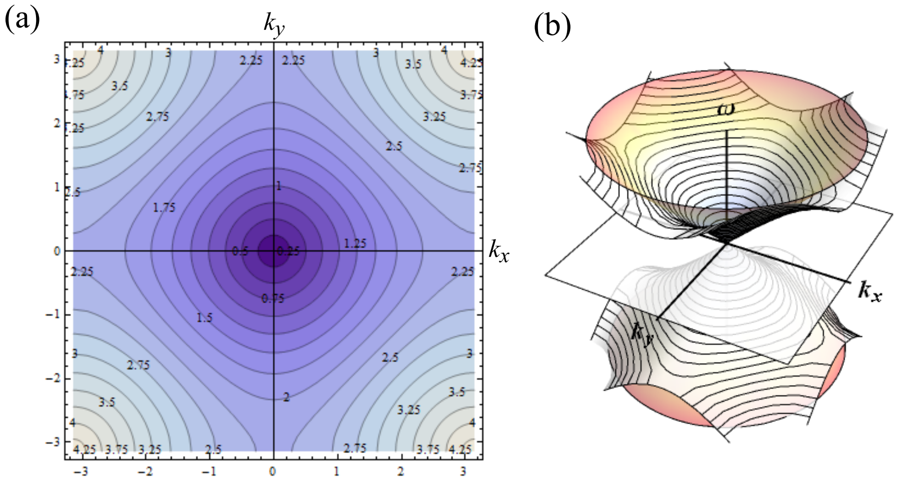

Figure 12.5: Dispersion relation of the leap-frog staggered-grid finite difference scheme for the (2+1)D Dirac equation. $\Delta_x = \Delta_y = \hbar = 1$, $\Delta_o = 1/\sqrt{2}$, $m = 0$. (a) Contour plot of the positive energy dispersion relation. (b) Comparison of the numerical dispersion relation with the exact Dirac cone dispersion.

Similar to the (3+1)D case in Section 12.2.2, we can use this result and give a *proof of stability* for an arbitrary space- and time-dependent mass and potential.

Proof.

$$\begin{aligned}
E_r^0 = E_r^{j_o} = &\left\|u^{j_o+1/2}\right\|^2 + \left\|v^{j_o+1}\right\|^2 \\
&+ r_x \Re\left[\left(\delta_x u^{j_o+1/2}, v^{j_o+1}\right)\right] - r_y \Re\left[\left(i\delta_y u^{j_o+1/2}, v^{j_o+1}\right)\right] \\
\\
&\geq \left\|u^{j_o+1/2}\right\|^2 + \left\|v^{j_o+1}\right\|^2 \\
&- r_x \left|\Re\left[\left(\delta_x u^{j_o+1/2}, v^{j_o+1}\right)\right]\right| - r_y \left|\Re\left[\left(i\delta_y u^{j_o+1/2}, v^{j_o+1}\right)\right]\right| \\
\\
&\geq \left\|u^{j_o+1/2}\right\|^2 + \left\|v^{j_o+1}\right\|^2 \\
&- \left(r_x + r_y\right)\left(\left\|u^{j_o+1/2}\right\|^2 + \left\|v^{j_o+1}\right\|^2 \right) .
\end{aligned}$$

Here we have used the inequality $2|\Re\left\{(a, b)\right\}| \leq \|a\|^2 + \|b\|^2$. With this one gets the result

$$\left\|u^{j_o+1/2}\right\|^2 + \left\|v^{j_o+1}\right\|^2 \leq \frac{E_r^0}{1 - r_x - r_y} \,, \tag{12.54}$$

proving stability for $r_x + r_y < 1$ (e.g. using $r_x = r_y < 1/2$) and arbitrary space- and time-dependence of the mass and potential terms. □

Again, this condition is too restrictive for constant mass and potential. From the reality condition for the free-particle dispersion, one has $r_x^2 + r_y^2 \leq 1$. For the special case $r = r_x = r_y$ this less restrictive stability condition reads $r \leq 1/\sqrt{2}$.

We use the special value $r = 1/\sqrt{2}$ in Eq. (12.53), i.e.

$$\begin{aligned} E = \sum_{j_x,j_y} &|u_{j_x,j_y}|^2 + |v_{j_x+1/2,j_y}|^2 \\ &+ \frac{1}{\sqrt{2}} \Re\Big[\big(u_{j_x+1,j_y} - u_{j_x,j_y} - iu_{j_x+1/2,j_y+1/2} + iu_{j_x+1/2,j_y-1/2}, v_{j_x+1/2,j_y}\big)\Big] \end{aligned} \tag{12.55}$$

to show that this is the stability condition for the general case. Here and in the following equations the summation runs over $j = (j_x, j_y) \in \mathbb{Z}^2 \cup (\mathbb{Z} + 1/2)^2$. We use the same strategy as in the (1+1)D version of the scheme [25].

Proof. We first define the auxiliary quantity

$$
\begin{aligned}
\tilde{E} :=& \frac{1}{2}\sum_{j_x,j_y}\left|\frac{u_{j_x+1,j_y}-iu_{j_x+1/2,j_y+1/2}}{\sqrt{2}}+v_{j_x+1/2,j_y}\right|^2 \\
&+\frac{1}{2}\sum_{j_x,j_y}\left|\frac{u_{j_x,j_y}-iu_{j_x+1/2,j_y-1/2}}{\sqrt{2}}-v_{j_x+1/2,j_y}\right|^2 \\
=& \sum_j |u_j|^2+|v_j|^2 \\
&+\frac{1}{2\sqrt{2}}\sum_{j_x,j_y}\Bigg[\left(u_{j_x+1,j_y}-iu_{j_x+1/2,j_y+1/2}\right)v^*_{j_x+1/2,j_y} \\
&\qquad+\left(u_{j_x+1,j_y}-iu_{j_x+1/2,j_y+1/2}\right)^* v_{j_x+1/2,j_y} \\
&\qquad-\left(u_{j_x,j_y}-iu_{j_x+1/2,j_y-1/2}\right)v^*_{j_x+1/2,j_y} \\
&\qquad-\left(u_{j_x,j_y}-iu_{j_x+1/2,j_y-1/2}\right)^* v_{j_x+1/2,j_y}\Bigg] \\
&+\frac{i}{4}\sum_{j_x,j_y}\Bigg[u_{j_x+1,j_y}u^*_{j_x+1/2,j_y+1/2}-u^*_{j_x+1,j_y}u_{j_x+1/2,j_y+1/2} \\
&\qquad+u_{j_x,j_y}u^*_{j_x+1/2,j_y-1/2}-u^*_{j_x,j_y}u_{j_x+1/2,j_y-1/2}\Bigg]\,, \qquad (12.56)
\end{aligned}
$$

where the last summation equals zero because the terms cancel, e.g. the first term with $j_x = j_y = 0$ cancels with the last one having $j_x = j_y = 1/2$. Thus, one gets $\tilde{E} = E$.

Using $\frac{1}{4}\|a_1+a_2\|^2 \le \frac{1}{4}\big(\|a_1+b\|+\|a_2-b\|\big)^2 \le \frac{1}{2}\|a_1+b\|^2+\frac{1}{2}\|a_2-b\|^2$ gives

$$
\|\tilde{u}\|^2 := \sum_{j_x,j_y}\left|\frac{u_{j_x+1,j_y}-iu_{j_x+1/2,j_y+1/2}}{2\sqrt{2}}+\frac{u_{j_x,j_y}-iu_{j_x+1/2,j_y-1/2}}{2\sqrt{2}}\right|^2 \le \tilde{E} = E_0\,. \qquad (12.57)
$$

The symmetry of the scheme and of E in u and v yields also: $\|\tilde{v}\|^2 \le \tilde{E} = E_0$. □

We remark that $\|\tilde{u}\|^2$ is a norm on $l^2\big[\mathbb{Z}^2 \cup (\mathbb{Z}+1/2)^2\big]$.

Proof. Assume $\|\tilde{u}\|^2 = 0$, which leads to

$$
u_{j_x+1,j_y}-iu_{j_x+1/2,j_y+1/2}+u_{j_x,j_y}-iu_{j_x+1/2,j_y-1/2}=0\,. \qquad (12.58)
$$

This is a leap-frog scheme $u_{j_x+1/2,j_y-1/2}, u_{j_x,j_y} \rightarrow u_{j_x+1,j_y}, u_{j_x+1/2,j_y+1/2}$. To show that is has no non-trivial solution in l^2 we observe that the real part of $u\big|_{\mathbb{Z}^2}$ is only coupled to the imaginary part of $u\big|_{(\mathbb{Z}+1/2)^2}$:

$$\begin{aligned} \Re u_{j_x,j_y} + \Im u_{j_x+1/2,j_y-1/2} &= -(\Re u_{j_x+1,j_y} + \Im u_{j_x+1/2,j_y+1/2}) \\ &= \Re u_{j_x+1,j_y+1} + \Im u_{j_x+3/2,j_y+1/2} = \cdots \end{aligned} \tag{12.59}$$

The l^2-summabilty of u implies Eq. (12.59) $= 0$ giving

$$\Re u_{j_x,j_y} = -\Im u_{j_x+1/2,j_y-1/2} \; . \tag{12.60}$$

Now we shift (12.58) by $(\frac{1}{2}, -\frac{1}{2})$ and take the imaginary part:

$$\begin{aligned} \Im u_{j_x+1/2,j_y-1/2} - \Re u_{j_x+1,j_y-1} &= -(\Im u_{j_x+3/2,j_y-1/2} - \Re u_{j_x+1,j_y}) \\ &= \Im u_{j_x+3/2,j_y+1/2} - \Re u_{j_x+2,j_y} = \cdots = 0 \; , \end{aligned} \tag{12.61}$$

again due to the l^2-summabilty. Combining (12.60) and (12.61) with their integer grid-shifts yields

$$\Re u_{j_x,j_y} = -\Im u_{j_x+1/2,j_y-1/2} = \Re u_{j_x+1,j_y-1} = -\Im u_{j_x+3/2,j_y-3/2} = \cdots \; . \tag{12.62}$$

By the l^2-summabilty, Eq. (12.62)$= 0$.

Analogously, the imaginary part of $u\big|_{\mathbb{Z}^2}$ is only coupled to the real part of $u\big|_{(\mathbb{Z}+1/2)^2}$. The same arguments as before lead to

$$\Im u_{j_x,j_y} = \Re u_{j_x+1/2,j_y-1/2} = \Im u_{j_x+1,j_y-1} = \Re u_{j_x+3/2,j_y-3/2} = \cdots = 0 \; . \tag{12.63}$$

Hence $\tilde{u} = 0$. ☐

Thus, the stability condition $r \leq 1/\sqrt{2}$ is confirmed.

12.4 Gauge-Invariant Introduction of a Vector Potential

In the previous exposition, only the presence of a scalar potential has been considered. The treatment of a Dirac fermion under the influence of a general electromagnetic field, however, calls for the use of the electromagnetic four-vector potential, *i.e.* both scalar and vector potential. The incorporation of the vector potential $\mathcal{A}(x, y, z, t)$ poses no problem for the two schemes presented above. It can be accomplished in the same fashion as discussed recently in conjunction with our (1+1)D and (2+1)D schemes, following the standard Peierls substitution for the spinor components ψ on the lattice [37, 38, 25, 26],

$$\psi^{t_j,z_j}_{x_j,y_j} \to \hat{\psi}^{t_j,z_j}_{x_j,y_j} := \psi^{t_j,z_j}_{x_j,y_j} \exp\{-ia^{t_j,z_j}_{x_j,y_j}\} \,. \tag{12.64}$$

Here ψ denotes a spinor component and the real phase $a^{t_j,z_j}_{x_j,y_j}$ is defined as the line integral of the vector potential $\mathcal{A}$, starting at an arbitrary, but fixed position (x_o, y_o, z_o) and ending on the lattice point (x_j, y_j, z_j),

$$a^{t_j,z_j}_{x_j,y_j} = \frac{q}{\hbar c} \int_{(x_o,y_o,z_o)}^{(x,y,z)} d\mathbf{s} \cdot \mathcal{A}(\mathbf{s}, t) \mid_{x=x_j,y=y_j,z=z_j,t=t_j} \,.$$

q is the fermion electric charge. Here the grid notation for the more general (3+1)D case has been adopted. The (2+1)D case can be handled analogously, as discussed in detail for our earlier (2+1)D scheme [26].

The implications of the insertion of the Peierls phase-shifted wave functions into the respective numerical schemes can be summarized as follows [26]:

- Since the connectivity of grid points is determined by the structure of the $\alpha-$ or, respectively, the $\sigma-$ matrices, requirements on the grid structure are not affected.
- Since every spinor component is multiplied merely by a phase factor, all stability and convergence estimates, as well as the definition of the norm, can be carried over simply by replacing spinor components by their Peierls transformed $\psi \to \hat{\psi}$.
- The effect of the substitution on difference quotients (derivative terms)

  $$\frac{\psi_1 - \psi_2}{\Delta} \to \frac{e^{-ia_1}\psi_1 - e^{-ia_2}\psi_2}{\Delta} \,.$$

  can be implemented by using the product rule for "differentiation on the lattice"

  $$\frac{e^{-ia_1}\psi_1 - e^{-ia_2}\psi_2}{\Delta} = f_+(a_1, a_2)\frac{\psi_1 - \psi_2}{\Delta} + \frac{e^{-ia_1} - e^{-ia_2}}{\Delta}\frac{\psi_1 + \psi_2}{2} \,,$$

  with the definition $f_\pm(a_1, a_2) := (e^{-ia_1} \pm e^{-ia_2})/2$. For the case of slow variation of the vector potential over the grid, the difference quotient for the exponential may be approximated by using the "chain rule" for the derivative on the grid

  $$\frac{e^{-ia_1} - e^{-ia_2}}{\Delta} = f_+(a_1, a_2)\frac{i(a_2 - a_1)}{\Delta} + \frac{1}{\Delta}O((a_1 - a_2)^3) \,. \tag{12.65}$$

- All symmetric averages of the structure

$$\frac{\psi_1 + \psi_2}{2} \to \frac{e^{-ia_1}\psi_1 + e^{-ia_2}\psi_2}{2} \ .$$

  may be rewritten into

$$\begin{aligned} \frac{e^{-ia_1}\psi_1 + e^{-ia_2}\psi_2}{2} &= f_+(a_1, a_2)\frac{\psi_1 + \psi_2}{2} + f_-(a_1, a_2)\frac{\psi_1 - \psi_2}{2} \\ &\approx f_+(a_1, a_2)\frac{\psi_1 + \psi_2}{2} \ , \end{aligned} \tag{12.66}$$

  whereby the f_- term may be neglected for vector potentials which are sufficiently smooth on the grid.

For such smooth vector potentials, approximations Eqs. (12.65) and (12.66) lead us to the following simple rules:

- Every partial time-derivative renormalizes the associated scalar potential term (which occurs in the same equation) according to

$$V_{x_j,y_j}^{t_j(,z_j)} \to V_{x_j,y_j}^{t_j(,z_j)} - \frac{q}{c}\int_{x_o,y_o(,z_o)}^{x_j,y_j(,z_j)} d\mathbf{s} \cdot \frac{\mathcal{A}(\mathbf{s}, t_j + \Delta_t/2) - \mathcal{A}(\mathbf{s}, t_j - \Delta_t/2)}{\Delta_t} \ .$$

- Every spatial j-derivative term transforms according to

$$\frac{\psi_{j+1/2} - \psi_{j-1/2}}{\Delta_j} \to \frac{\psi_{j+1/2} - \psi_{j-1/2}}{\Delta_j} - \frac{iq}{\hbar c}\mathcal{A}_j\frac{\psi_{j+1/2} + \psi_{j-1/2}}{2} \ .$$

The substitutions into the schemes above are straight-forward [25, 26]. Since the resulting expressions at the various stages of approximation are rather lengthy they are not given here in more detail.

12.5 Summary and Conclusions

We have presented a real-space finite-difference method for both the four-component (3+1)D and the two-component (2+1)D Dirac equation. In both cases, the scheme is capable of handling general time-dependent electromagnetic potential and mass terms. Stability is proven for this general case and an exactly conserved functional is identified. It can be interpreted as a probability density.

The proposed schemes share and combine several decisive advantages over previous methods. Most importantly, the fermion doubling problem is avoided by staggering the spinor components symmetrically both in space and time. The strictly monotonic dispersion relation features a single Dirac cone. The scheme is second order accurate and, because it is explicit, shows an optimal linear scaling behavior. It lends itself to a convenient introduction of absorbing boundary conditions via boundary regions with imaginary scalar potential contributions, following a strategy discussed elsewhere [26]. Furthermore, this scheme which we have developed explicitly for one, two, and three spatial dimensions can be extended to higher dimensions.

The code readily is parallelized. This can be achieved, for example, by dividing the problem into spatial sub-domains, each computed on one CPU and communicating only the boundary grid-points. Although Maxwell's equations have a different structure, the method presented here for the Dirac equation has much in common with the finite difference time domain (FDTD) method. Today it is applied with great success in computational electromagnetics [21, 22]. This close relationship also allows for the use of tools, initially developed for the FDTD time domain method, like the perfectly matched layer (PML), in its various variants, acting as an absorbing (open) boundary for finite-domain simulations [23, 24].

Since the presented schemes allow for the incorporation of the full electromagnetic four-vector potential, self-consistent dynamics (e.g., self-energy corrections) mediated by the electromagnetic interaction is readily achieved by solving the electromagnetic potential equations in parallel. This allows the utilization of all of the advantages associated with the present approach and eliminates the need for the discretization of non-linear extensions of the Dirac equation. On the other hand, the present method may prove to be useful also for the discretization of such nonlinear Dirac equations, in particular, where nonlinearities arise from other types of interaction [39].

In summary, the combination of these favorable properties makes this approach highly suitable for the numerical treatment of Dirac fermion dynamics in space- and time-dependent external fields. As such, it should be useful to a variety of fields in physics, ranging from elementary particle, atomic, molecular, to condensed matter and astro-physics.

Acknowledgment: This work has been supported by the Austrian Science

Foundation under Project No. I395-N16.

12.6 APPENDIX A: Stability condition for the (3+1)D leap-frog staggered-grid scheme

In this appendix we show that the stability condition for the (3+1)D scheme is $r \leq 1/\sqrt{3}$. We use Eq. 12.27

$$E = \sum_j |A_j|^2 + |B_{j+(\frac{1}{2},0,\frac{1}{2})}|^2 + |C_{j+(0,0,\frac{1}{2})}|^2 + |D_{j+(\frac{1}{2},0,0)}|^2 \tag{12.67}$$

$$- \frac{1}{\sqrt{3}} \Re \Big[\Big(C_{j+(0,0,\frac{1}{2})} - C_{j-(0,0,\frac{1}{2})} + D_{j+(\frac{1}{2},0,0)} - D_{j-(\frac{1}{2},0,0)} - iD_{j+(0,\frac{1}{2},0)} + iD_{j-(0,\frac{1}{2},0)}, A_j \Big) \Big] \tag{12.68}$$

$$- \frac{1}{\sqrt{3}} \Re \Big[\Big(- D_{j+(\frac{1}{2},0,1)} + D_{j+(\frac{1}{2},0,0)} + C_{j+(1,0,\frac{1}{2})} - C_{j+(0,0,\frac{1}{2})} + iC_{j+(\frac{1}{2},\frac{1}{2},\frac{1}{2})} - iC_{j+(\frac{1}{2},-\frac{1}{2},\frac{1}{2})}, B_{j+(\frac{1}{2},0,\frac{1}{2})} \Big) \Big] , \tag{12.69}$$

with $j \in \mathbb{Z}^3 \cup (\mathbb{Z} + 1/2)^2 \times \mathbb{Z}$ in the sum.

Proof. Let us define the auxiliary quantity

$$\begin{aligned}\tilde{E} := {} & \frac{1}{2} \sum_j \left| \frac{C_{j+(0,0,\frac{1}{2})} + D_{j+(\frac{1}{2},0,0)} - iD_{j+(0,\frac{1}{2},0)}}{\sqrt{3}} - A_j \right|^2 \\ & + \frac{1}{2} \sum_j \left| \frac{C_{j-(0,0,\frac{1}{2})} + D_{j-(\frac{1}{2},0,0)} - iD_{j-(0,\frac{1}{2},0)}}{\sqrt{3}} + A_j \right|^2 \\ & + \frac{1}{2} \sum_j \left| \frac{D_{j+(\frac{1}{2},0,1)} - C_{j+(1,0,\frac{1}{2})} - iC_{j+(\frac{1}{2},\frac{1}{2},\frac{1}{2})}}{\sqrt{3}} + B_{j+(\frac{1}{2},0,\frac{1}{2})} \right|^2 \\ & + \frac{1}{2} \sum_j \left| \frac{D_{j+(\frac{1}{2},0,0)} - C_{j+(0,0,\frac{1}{2})} - iC_{j+(\frac{1}{2},-\frac{1}{2},\frac{1}{2})}}{\sqrt{3}} - B_{j+(\frac{1}{2},0,\frac{1}{2})} \right|^2\end{aligned} \tag{12.70}$$

$$\tilde{E} = \sum_j |A_j|^2 + |B_{j+(\frac{1}{2},0,\frac{1}{2})}|^2 + |C_{j+(0,0,\frac{1}{2})}|^2 + |D_{j+(\frac{1}{2},0,0)}|^2 \tag{12.71}$$

$$\begin{aligned}
&+ \frac{1}{2\sqrt{3}} \sum_j \Big[- \big(C_{j+(0,0,\frac{1}{2})} + D_{j+(\frac{1}{2},0,0)} - iD_{j+(0,\frac{1}{2},0)}\big) A_j^* \\
&\qquad - \big(C_{j+(0,0,\frac{1}{2})} + D_{j+(\frac{1}{2},0,0)} - iD_{j+(0,\frac{1}{2},0)}\big)^* A_j \\
&\qquad + \big(C_{j-(0,0,\frac{1}{2})} + D_{j-(\frac{1}{2},0,0)} - iD_{j-(0,\frac{1}{2},0)}\big) A_j^* \\
&\qquad + \big(C_{j-(0,0,\frac{1}{2})} + D_{j-(\frac{1}{2},0,0)} - iD_{j-(0,\frac{1}{2},0)}\big)^* A_j \\
&\qquad + \big(D_{j+(\frac{1}{2},0,1)} - C_{j+(1,0,\frac{1}{2})} - iC_{j+(\frac{1}{2},\frac{1}{2},\frac{1}{2})}\big) B^*_{j+(\frac{1}{2},0,\frac{1}{2})} \\
&\qquad + \big(D_{j+(\frac{1}{2},0,1)} - C_{j+(1,0,\frac{1}{2})} - iC_{j+(\frac{1}{2},\frac{1}{2},\frac{1}{2})}\big)^* B_{j+(\frac{1}{2},0,\frac{1}{2})} \\
&\qquad - \big(D_{j+(\frac{1}{2},0,0)} - C_{j+(0,0,\frac{1}{2})} - iC_{j+(\frac{1}{2},-\frac{1}{2},\frac{1}{2})}\big) B^*_{j+(\frac{1}{2},0,\frac{1}{2})} \\
&\qquad - \big(D_{j+(\frac{1}{2},0,0)} - C_{j+(0,0,\frac{1}{2})} - iC_{j+(\frac{1}{2},-\frac{1}{2},\frac{1}{2})}\big)^* B_{j+(\frac{1}{2},0,\frac{1}{2})} \Big] \\
&+ \frac{1}{6} \sum_j \Big[C_{j+(0,0,\frac{1}{2})} \big(D^*_{j+(\frac{1}{2},0,0)} + iD^*_{j+(0,\frac{1}{2},0)}\big) \\
&\qquad + C^*_{j+(0,0,\frac{1}{2})} \big(D_{j+(\frac{1}{2},0,0)} - iD_{j+(0,\frac{1}{2},0)}\big) \\
&\qquad + C_{j-(0,0,\frac{1}{2})} \big(D^*_{j-(\frac{1}{2},0,0)} + iD^*_{j-(0,\frac{1}{2},0)}\big) \\
&\qquad + C^*_{j-(0,0,\frac{1}{2})} \big(D_{j-(\frac{1}{2},0,0)} - iD_{j-(0,\frac{1}{2},0)}\big) \\
&\qquad + D_{j+(\frac{1}{2},0,1)} \big(- C^*_{j+(1,0,\frac{1}{2})} + iC^*_{j+(\frac{1}{2},\frac{1}{2},\frac{1}{2})}\big) \\
&\qquad + D^*_{j+(\frac{1}{2},0,1)} \big(- C_{j+(1,0,\frac{1}{2})} - iC_{j+(\frac{1}{2},\frac{1}{2},\frac{1}{2})}\big) \\
&\qquad + D_{j+(\frac{1}{2},0,0)} \big(- C^*_{j+(0,0,\frac{1}{2})} + iC^*_{j+(\frac{1}{2},-\frac{1}{2},\frac{1}{2})}\big) \\
&\qquad + D^*_{j+(\frac{1}{2},0,0)} \big(- C_{j+(0,0,\frac{1}{2})} - iC_{j+(\frac{1}{2},-\frac{1}{2},\frac{1}{2})}\big) \Big] \\
&+ \frac{i}{6} \sum_j \Big[D_{j+(\frac{1}{2},0,0)} D^*_{j+(0,\frac{1}{2},0)} - D^*_{j+(\frac{1}{2},0,0)} D_{j+(0,\frac{1}{2},0)} \\
&\qquad + D_{j-(\frac{1}{2},0,0)} D^*_{j-(0,\frac{1}{2},0)} - D^*_{j-(\frac{1}{2},0,0)} D_{j-(0,\frac{1}{2},0)} \Big] \\
&+ \frac{i}{6} \sum_j \Big[- C_{j+(1,0,\frac{1}{2})} C^*_{j+(\frac{1}{2},\frac{1}{2},\frac{1}{2})} + C^*_{j+(1,0,\frac{1}{2})} C_{j+(\frac{1}{2},\frac{1}{2},\frac{1}{2})} \\
&\qquad - C_{j+(0,0,\frac{1}{2})} C^*_{j+(\frac{1}{2},-\frac{1}{2},\frac{1}{2})} + C^*_{j+(0,0,\frac{1}{2})} C_{j+(\frac{1}{2},-\frac{1}{2},\frac{1}{2})} \Big] \\
&= E \,,
\end{aligned} \tag{12.72}$$

since the last and the penultimate sum vanish because they are telescopic sums: In both sums the first (resp. second) term with $j = (0,0,0)$ cancels the forth (resp. third) term with $j = (\frac{1}{2}, \frac{1}{2}, 0)$. In the antepenultimate sum there occurs direct cancelation in two pairs of terms (involving $C_{j+(0,0,\frac{1}{2})} D^*_{j+(\frac{1}{2},0,0)}$ and $C^*_{j+(0,0,\frac{1}{2})} D_{j+(\frac{1}{2},0,0)}$) and the remaining terms are again telescopic sums.

Using $\frac{1}{4}\,\|a_1 + a_2\|^2 \;\leq\; \frac{1}{4}\big(\,\|a_1 + b\| + \|a_2 - b\|\,\big)^2 \;\leq\; \frac{1}{2}\,\|a_1 + b\|^2 + \frac{1}{2}\,\|a_2 - b\|^2$ gives

$$\begin{aligned}
\|(\tilde{C}, \tilde{D})\|^2 :=& \sum_j \Bigg| \frac{C_{j+(0,0,\frac{1}{2})} + D_{j+(\frac{1}{2},0,0)} - iD_{j+(0,\frac{1}{2},0)}}{2\sqrt{3}} \\
&\qquad + \frac{C_{j-(0,0,\frac{1}{2})} + D_{j-(\frac{1}{2},0,0)} - iD_{j-(0,\frac{1}{2},0)}}{2\sqrt{3}} \Bigg|^2 \\
&+ \sum_j \Bigg| \frac{D_{j+(\frac{1}{2},0,1)} - C_{j+(1,0,\frac{1}{2})} - iC_{j+(\frac{1}{2},\frac{1}{2},\frac{1}{2})}}{2\sqrt{3}} \\
&\qquad + \frac{D_{j+(\frac{1}{2},0,0)} - C_{j+(0,0,\frac{1}{2})} - iC_{j+(\frac{1}{2},-\frac{1}{2},\frac{1}{2})}}{2\sqrt{3}} \Bigg|^2 \\
\leq& \; \tilde{E} = E\,. \qquad\qquad (12.73)
\end{aligned}$$

The symmetry of the scheme and of E w.r.t. (C, D) and (A, B) yields also: $\|(\tilde{C}, \tilde{D})\|^2 \leq \tilde{E} = E$. $\square$

REFERENCES

[1] P. A. M. Dirac, The Quantum Theory of the Electron, Proc. R. Soc. Lond. A 117 (1928) 610-624.

[2] J. J. Sakurai, Advanced Quantum Mechanics, Pearson Education India (2006).

[3] L. H. Ryder, Quantum Field Theory, Cambridge University Press (1996).

[4] C. Itzykson and J. B. Zuber, Quantum Field Theory, Dover Publications Inc. New York (2005).

[5] M. Srednicki, Quantum Field Theory, Cambridge University Press (2007).

[6] I. I. Rabi, Das freie Elektron im homogenen Magnetfeld nach der Diracschen Theorie, Z. Phys. 49 (1928) 507-511.

[7] K. Nikolsky, Das Oszillatorproblem nach der Diracschen Theorie, Z. Phys. 62 (1930) 677-681

[8] D. M. Wolkow, Über eine Klasse von Lösungen der Diracschen Gleichung, z. Phys. 94 (1935) 250-260.

[9] H. A. Bethe, E. E. Salpeter, Quantum Mechanics of One- and Two-Electron Atoms, Plenum Publishing Corporation New York (1977) 63-71.

[10] Y. I. Salamin, S. X. Hu, K. Z. Hatsagortsyan, and C. H Keitel, Relativistic High-Power Laser-Matter Interactions, Phys. Rep. 427 (2006) 41-155, and references therein.

[11] A. Di Piazza, C. Müller, K. Z. Hatsagortsyan, and C. H. Keitel, Extremly High-Intensity Laser Interactions with Fundamental Quantum Systems, Rev. Mod. Phys. 84 (2012) 1177-1228, and references therein.

[12] G. R. Mocken and C. H. Keitel, FFT-Split-Operator Code for Solving the Dirac Equation in 2+1 Dimensions, Comp. Phys. Comm. 178 (2008) 868-882.

[13] F. Fillion-Gourdeau, E. Lorin, and A. D. Bandrauk, Numerical Solution of the Time-Dependent Dirac Equation in Coordinate Space without Fermion-Doubling, Comp. Phys. Comm. 183 (2012) 1403-1415.

[14] A. C. Neto, F. Guinea, N. M. R. Peres, K. S. Novoselov, and A. K. Geim, The Electronic Properties of Graphene, Rev. Mod. Phys. 81 (2009) 109-162, and references therein.

[15] X. L. Qi and S. C. Zhang, Topological Insulators and Superconductors, Reviews of Modern Physics 83 (2011) 1057-1110, and references therein.

[16] D. Hsieh, Y. Xia, D. Qian, L. Wray, F. Meier, J. H. Dil, J. Osterwalder, L. Patthey, A. V. Fedorov, H. Lin, A. Bansil, D. Grauer, Y. S. Hor, R. J. Cava, and M. Z. Hasan, Observation of Time-Reversal-Protected Single-Dirac-Cone Topological-Insulator States in Bi2Te3 and Sb2Te3, Phys. Rev. Lett. 103 (2009) 146401-1 - 146401-4.

[17] M. Z. Hasan and C. L. Kane, Colloquium: Topological Insulators, Rev. Mod. Phys. 82 (2010) 3045-3067, and references therein.

[18] Y. Xia, D. Qian, D. Hsieh, L. Wray, A. Pal, H. Lin, A. Bansil, D. Grauer, Y. S. Hor, R. J. Cava, and M. Z. Hasan, Observation of a Large-Gap Topological-Insulator Class with a Single Dirac Cone on the Surface, Nat. Phys. 5, (2009) 398-402.

[19] J. G. Analytis, J. H. Chu, Y. Chen, F. Corredor, R. D. McDonald, Z. X. Shen, and Ian R. Fisher, Bulk Fermi Surface Coexistence with Dirac Surface State in Bi2Se3: A Comparison of Photoemission and Shubnikov-de Haas Measurements, Phys. Rev. B 81 (2010) 204507-1 - 204507-5.

[20] H. B. Nielsen and M. Ninomiya, A No-Go Theorem for Regularizing Chiral Fermions, Physics Letters B 105 (1981) 219-223.

[21] K. S. Yee, Numerical Solution of Initial Boundary Value Problems Involving Maxwell's Equations in Isotropic Media, IEEE Transactions on Antennas and Propagation 14 (1966) 302-307.

[22] A. Taflove and S. C. Hagness, Computational Electrodynamics: The Finite-Difference Time-Domain Method, Artech House Norwood, (2005).

[23] J. P. Berenger, A Perfectly Matched Layer for the Absorption of Electromagnetic Waves, J. of Comp. Phys. 114 (1994) 185-200.

[24] S. G. Johnson, Notes on Perfectly Matched Layers (PMLs), Lecture notes, Massachusetts Institute of Technology, Massachusetts (2008).

[25] R. Hammer, W. Pötz, and A. Arnold, A Dispersion and Norm Preserving Finite Difference Scheme with Transparent Boundary Conditions for the Dirac Equation in (1+1)D, accepted in Journal of Computational Physics, preprint available at arXiv:1302.5587

[26] R. Hammer and W. Pötz, Staggered-Grid Leap-Frog Scheme for the (2+1)D Dirac Equation, accepted in Computer Physics Communications, preprint available at arXiv:1306.5895

[27] R. Hammer and W. Pötz, Dynamics of Domain-Wall Dirac Fermions on a Topological Insulator: A Chiral Fermion Beam Splitter, arXiv:1306.6139

[28] R. Hammer, C. Ertler, and W. Pötz, Solitonic Dirac Fermion Wave Guide Networks on Topological Insulator Surfaces, Appl. Phys. Lett. 102, (2013) 193514-1 - 193514-4.

[29] R. Stacey, Eliminating Lattice Fermion Doubling, Phys. Rev. D 26 (1982) 468-472.

[30] F. Alouges, F. De Vuyst, G. Le Coq, and E. Lorin, The Reservoir Technique: A Way to Make Godunov-Type Schemes Zero or Very Low Diffuse. Application to Colella-Glaz Solver - B/Fluids 27 (2008) 643-664.

[31] J. Kogut und L. Susskind, Hamilton Formulation of Wilson's Lattice Gauge Theories, Phys. Rev. D 11 (1975) 395-408.

[32] P. H. Ginsparg and K. G. Wilson, A Remnant of Chiral Symmetry on the Lattice, Phys. Rev. D 25 (1982) 2649-2657.

[33] D. B. Kaplan, A Method for Simulating Chiral Fermions on the Lattice, Phys. Lett. B 288, (1992) 342-347.

[34] W. Greiner, Relativistic Quantum Mechanics: Wave Equations, Springer Berlin (2000).

[35] A. Borzì and E. Decker, Analysis of a Leap-Frog Pseudospectral Scheme for the Schrödinger Equation, Journal of Computational and Applied Mathematics 193 (2006) 65-88.

[36] J. C. Strikwerda, Finite Difference Schemes and Partial Differential Equations, SIAM Philadelphia (2004).

[37] R. Peierls, Zur Theorie des Diamagnetismus von Leitungselektronen, Z. Phys. 80 (1933) 763-791.

[38] M. Graf and P. Vogl, Electromagnetic fields and dielectric response in empirical tight-binding theory, Phys. Rev. B 51 (1995) 4940-4949, and references therein.

[39] J. Xu, S. Shao, and H. Tang, Numerical Methods for the Non-Linear Dirac Equation, J. Comp. Phys. 245 (2013) 131-149.

Chapter 13

SUMMARY AND OUTLOOK

13.1 Summary

After a brief introduction to the short history of topological matter, the Dirac equation was introduced and its emergence in solid state systems was shown. The history of 3D topological insulators and their promises for future device applications were discussed.

A pedagogical introduction to finite-difference modeling and to transparent boundary conditions was given using the prototypical case of a simple (1+1)D advection equation. Various finite difference schemes for the (1+1)D Dirac equation were shown and their properties were discussed. The numerical treatment of the Dirac equation, using finite-difference methods, suffers from the fermion doubling problem. This issue was solved by developing a new algorithm which uses a special staggering of the spinor components in space and time. The scheme is dispersion preserving for the massless case and has very good dispersive properties for a finite mass. A functional which is conserved by the scheme was identified. Stability, for arbitrary space and time dependent mass and potential terms, could be proven.

Perfect absorbing, so-called discrete transparent, boundary conditions were derived. For their derivation, the infinite domain was divided in a computational domain and the exterior domains. In the latter, constant mass and potential terms were assumed. By application of the finite difference scheme and then using the Z-transform in the discrete time variable a constant coefficient difference equation was obtained. The latter was solved exactly on the exterior domains. Transparent boundary conditions were obtained by allowing only solutions which vanish at infinity.

The scheme was extended to (2+1) in two different ways. The first one preserves the exact $m = 0$ properties of the dispersion relation along the coordinate axes, but shows a second cone at the corner of the "Brillouin" zone. The second scheme, which was also extended to the full four spinor component (3+1)D Dirac equation, shows a single Dirac cone. The fermion doubling problem could also be avoided for this general case. As for the (1+1)D scheme a conserved functional could be identified and stability, for arbitrary space and time dependent mass and potential terms, could be proven. The electromagnetic vector potential was introduced in a gauge-invariant fashion in the (1+1)D, the (2+1)D and the (3+1)D scheme.

The (3+1)D Dirac scheme should be useful to a variety of fields, ranging form elementary particle, atomic, molecular to condensed matter and astro physics. For example it should allow for an efficient numerical simulation of the wave-packet dynamics of electrons in strong laser fields.

Using the (2+1)D scheme, the dynamics of Dirac fermion wave packets on the topological insulator surface was demonstrated under the influence of a variety of elementary mass and potential textures. Among them are the Klein step, Landau orbits, mass vortices, and domain-wall fermions. At the boundary an absorbing layer with imaginary potential was used.

The splitting behavior of Dirac fermion wave packets at domain-wall intersections was investigated. A parameter study, varying for example the angle of intersection, the localization length of the domain-wall fermion, and the width of the domain-wall was performed. We can conclude that for the splitting ratio depends strongly on the angle of intersection. For non-rectangular intersections the ratio of the localization length to the domain-wall with is the dominant quantity. When the domain-wall width is small compared to the confinement width of the wave packet, the outgoing channel at the acute angle is favored. This is due to tunneling because of spatial overlap. Otherwise the channel lying at the obtuse angle is preferred.

Finally, this spin polarized, dissipation-less, one-way propagating channels, together with beam-splitters, were proposed to build complex electronic networks. Exploiting these principles a electric-gate controlled fermion interferometer device was proposed and its working principle was shown numerically.

13.2 Outlook

The aim of this last section is to inspire future work by giving an outlook of what possibly can be done, using the numerical scheme and the ideas developed in this thesis.

The explicit single cone discretization scheme for the (2+1)D Dirac equation can be used within a dynamical potential and mass background. The dynamics of the latter can be solved self-consistently in parallel, using e.g. the Poisson and Landau-Lifschitz-Gilbert equation [1].

Mixed state physics can be described by an extension of the coherent wave packet approach to a stochastic wave packet, density matrix or Greens function formalism [2, 3, 4].

The perfect open boundary conditions (transparent boundary conditions) derived for the (1+1)D scheme [5], can (in principle) also be derived for the (2+1)D and (3+1)D system, but one must balance between costs and benefits. The perfectly matched layer, as used successfully in the FDTD method, could be an alternative way to improve the absorbing boundary conditions [6, 7].

The effective model, for the surface states on the topological insulator, and the numerical code can be extended in order to represent the energy dispersion relation away from the Dirac point more realistically, as for example to take into account hexagonal warping [8].

In combination with a discretization of the Bogoliubov-de-Gennes equation, topological insulator/superconductor heterostructures can be investigated, including novel fermion to Majorana splitting devices [9].

Finally, the (3+1)D Dirac scheme should be useful to a variety of fields, ranging from elementary particle, atomic, molecular to condensed matter and astrophysics. In particular, an efficient numerical simulation of the wave packet dynamics of electrons in strong laser fields would be a potential application [10].

REFERENCES

[1] M. Kurzke, C. Melcher, and R. Moser, Domain-walls and Vortices in Thin Ferromagnetic Films, Analysis, Modeling and Simulation of Multiscale Problems, Springer Berlin Heidelberg (2006) 249-298.

[2] P. Saalfrank, Stochastic Wave Packet vs. Direct Density Matrix Solution of Liouville-von Neumann Equations for Photodesorption Problems, Chem. Phys. 211 (1996) 265-276.

[3] T. Kramer, E. J. Heller and R. E. Parrott, An Efficient and Accurate Method to Obtain the Energy-Dependent Green Function for General Potentials, J. Phys.: Conf. Ser. 99 (2008) 1-12.

[4] C. Ertler, M. Raith, J. Fabian, Gate-Defined Coupled Quantum Dots in Topological Insulators, arXiv:1310.1463

[5] R. Hammer, W. Pötz, and A. Arnold, A Dispersion and Norm Preserving Finite Difference Scheme with Transparent Boundary Conditions for the Dirac Equation in (1+1)D, accepted in Journal of Computational Physics, preprint available at arXiv:1302.5587

[6] J. P. Berenger, A Perfectly Matched Layer for the Absorption of Electromagnetic Waves, J. of Comp. Phys. 114 (1994) 185-200.

[7] S. G. Johnson, Notes on Perfectly Matched Layers (PMLs), Lecture notes, Massachusetts Institute of Technology, Massachusetts (2008).

[8] X. L. Qi and S. C. Zhang, Topological Insulators and Superconductors, Reviews of Modern Physics 83 (2011) 1057-1110.

[9] A. R. Akhmerov, J. Nilson, and C. W. J. Beenakker, Electrically Detected Interferometry of Majorana Fermions in a Topological Insulator, Phys. Rev. Lett. 102 (2009) 216404-1 - 216404-1.

[10] A. Di Piazza, C. Müller, K. Z. Hatsagortsyan, and C. H. Keitel, Extremly High-Intensity Laser Interactions with Fundamental Quantum Systems, Rev. Mod. Phys. 84 (2012) 1177-1228, and references therein.

Chapter A

APPENDIX

A.1 Order of accuracy of the leap-frog staggered-grid scheme

In this appendix the order of accuracy of the leap-frog staggered-grid scheme for the Dirac equation in (1+1D) CHAPTER 8 is shown. Therefore, a Taylor expansion at the points in the center of the space and time finite difference approximation is applied. Then, rewriting the indices for the scheme Eq.: (8.23) (first for the fist half-step) gives:

$$\frac{1}{\Delta t}\left(u_j^{n+1/2} - u_j^{n-1/2}\right) + \frac{i(m-V)}{2}\left(u_j^{n+1/2} + u_j^{n-1/2}\right) + \frac{1}{\Delta x}\left(v_{j+1/2}^{n} - v_{j-1/2}^{n}\right) = \\ = 0\,, \tag{A.1}$$

with:

$$u_j^{n\pm1/2} = u_j^n \pm (u_t)_j^n \frac{\Delta t}{2} + (u_{tt})_j^n \left(\frac{\Delta t}{2}\right)^2 \frac{1}{2!} \pm (u_{ttt})_j^n \left(\frac{\Delta t}{2}\right)^3 \frac{1}{3!} \\ + (u_{tttt})_j^n \left(\frac{\Delta t}{2}\right)^4 \frac{1}{4!} + \mathcal{O}\left(\Delta t^5\right), \tag{A.2}$$

and

$$v_{j\pm1/2}^n = v_j^n \pm (u_x)_j^n \frac{\Delta x}{2} + (v_{xx})_j^n \left(\frac{\Delta x}{2}\right)^2 \frac{1}{2!} \pm (v_{xxx})_j^n \left(\frac{\Delta x}{2}\right)^3 \frac{1}{3!} + (v_{xxxx})_j^n \left(\frac{\Delta t}{2}\right)^4 \frac{1}{4!} + \mathcal{O}(\Delta x^5), \tag{A.3}$$

inserted in Eq.: (A.1) gives:

$$\frac{1}{\Delta t}\left(\Delta t u_t + \frac{\Delta t^3}{24} u_{ttt} + \mathcal{O}(\Delta t^5)\right) + \frac{i(m-V)}{2}\left(2u + \frac{\Delta t^2}{4} u_{tt} + \mathcal{O}(\Delta t^4)\right) + \frac{1}{\Delta x}\left(\Delta x v_x + \frac{\Delta x^3}{24} v_{xxx} + \mathcal{O}(\Delta x^5)\right) = 0\,. \tag{A.4}$$

Reshaping, to have the continuum expression of the first row of the Dirac equation gives the error terms on the right hand side:

$$u_t + (m-V)u + v_x = -\frac{\Delta t^2}{24} u_{ttt} - \frac{i(m-V)\Delta t^2}{8} u_{tt} - \frac{\Delta x^2}{24} v_{xxx} + (\text{higher orders})\,. \tag{A.5}$$

One can carry out the same procedure for the second half-step and obeys:

$$v_t - (m+V)v + u_x = -\frac{\Delta t^2}{24} v_{ttt} + \frac{i(m+V)\Delta t^2}{8} v_{tt} - \frac{\Delta x^2}{24} u_{xxx} + (\text{higher orders})\,. \tag{A.6}$$

This shows that the scheme converges to the continuum limit of the Dirac equation and is second order in its approximation of its time and space derivatives and its approximation of the mass and potential term. We can conclude, it has overall second order accuracy. But it is remarkable that for the case $m = 0, V = 0$ we have $u_t = -v_x$ and $v_t = -u_x$, therefor with the choice $\Delta t = \Delta x$ cancellation of all error terms in Eq.: (A.5) and (A.6) occurs:

$$u_t + (m-V)u + v_x = 0 \quad \text{and} \quad v_t - (m+V)v + u_x = 0 \tag{A.7}$$

This implies that for this case the numerical solution is identical to the analytical solution. The cancellation will also happen approximately for m, V small, and/or Δ small, leading to a effectively small coefficients of the error terms.

A.2 Matlab code for the (1+1)D single Dirac cone staggered-grid leap-frog scheme with TBC's

```

clear all
close all

%====================================================
%                   INITIALIZATION
%====================================================

% fundamental constants [in SI units]
h_planck = 1; %6.6260693e-34;
q_el = 1; %1.60217653e-19; %elementary charge
hbar = 1; %h_planck/(2*pi);
%material parameters
vf = 1; %6.2e5; %Fermi velocity

% ----- geometry -----
Lx = 40; %in normalized units

% ----- grid -----
Nx = 400;% # of grid points in x
Nt = 400; % # of time steps
dx = Lx/Nx; %step size
dt = 1*dx/vf; %CFL-condition dx ≥ vf dt for stability
Lt = Nt*dt;
xgrid = 1:Nx;

%--------------------------------------------------------------
% initialization of potential, mass gap in eV

%potential
VV = 2;
Vpot(1:Nx) = VV;
%mass gap
m_M = 1;
mgap(1:Nx) = m_M;

%--------------------------------------------------
%                 initial condition
%--------------------------------------------------

umat(1:Nt,1:Nx) = 0;
vmat(1:Nt,1:Nx) = 0;
psimat(1:Nt,1:Nx)=0;
```

```

%gaussian wave packet

Ex = 10; % energy of wavepacket
pd = 1; %direction of propagation

disp(' ')
disp(sprintf('%s %0.5g %s %0.5g %s',...
     'energy center of wavepacket (Ex,Ey): (',Ex,') normalized units' ))

kx0 = Ex*q_el/(hbar*vf); %wavevector E = hbar*vf*k for massless Dirac

x0 = floor(0.5*Nx);% in units of dx,dy, wave packet at center
bx = 0.05*Nx; %half width of Gaussian

disp(sprintf('%s %0.5g %s %0.5g %s',...
    'k-center of wave packet kx = ('...
,kx0/(pi/dx)*100,') % of half Brillouin zone (BZ)  (pi/dx)'))
disp(sprintf('%s %0.5g %s %0.5g %s',...
    'Half Gaussian width  real space bx = ('...
     ,bx*dx,') normalized units'))
disp(sprintf('%s %0.5g %s %0.5g %s',...
    'Half Gaussian width in k-space dkx = (',...
     1/(bx*dx)/(pi/dx)*100,') % of half BZ'))

%Gaussian wavepacket at x0, y0; width/2 = bx, by;  momentum = kx0, ky0
umat(1,:) = 1/sqrt(2)*exp(-(xgrid-x0).^2./(2*bx^2)+i*(xgrid-x0)*dx*kx0);
if pd>0
 vmat(1,:) = kx0/(Ex+mgap(x0))*pd*umat(1,:);
else
 for k = 1:Nx-1
 vmat(1,k) = kx0/(Ex-mgap(x0))*pd*umat(1,k+1);
 end
end
norm0 = sum(abs(umat(1,:)).^2+abs(vmat(1,:)).^2); %L2 norm of psi0
umat(1,:) = umat(1,:)/norm0;
vmat(1,:) = vmat(1,:)/norm0;
norm0 = sum(abs(umat(1,:)).^2+abs(vmat(1,:)).^2); %norm is 1 at start
%----------------------------------------


%====================================================
%         COEFFICIENTS FOR THE TBCs
%====================================================

s(1:Nt) = 0;
alpha = 1/4*(mgap(Nx)^2-Vpot(Nx)^2)*dx^2 + dx^2/dt^2 ...
    - (i*Vpot(Nx)*dx^2/dt);
beta = 1/2*(mgap(Nx)^2-Vpot(Nx)^2)*dx^2 - 2*dx^2/dt^2;
```

```
gamma = 1/4*(mgap(Nx)^2-Vpot(Nx)^2)*dx^2 + dx^2/dt^2 ...
    + (i*Vpot(Nx)*dx^2/dt);
s(2) = 1/alpha;
s(3) = -(beta+2)/alpha^2;
s(4) = (beta^2 + 4* beta + 5 - alpha*gamma)/alpha^3;
s(5) = -(beta+2)/alpha^4 *(beta^2 + 4*beta + 7 - 2*alpha*gamma);
for n = 6:Nt
    s(n) = -1/(n*alpha^2)*((2*n-3)*alpha*(beta+2)*s(n-1)...
        + (n-3)*(beta^2+4*beta+2*alpha*gamma)*s(n-2)...
        + (2*n-9)*(beta+2)*gamma*s(n-3) + (n-6)*gamma^2*s(n-4));
end


%====================================================
%          ITERATIVE SOLUTION CORE PROGRAMM
%====================================================

c1 = dt*q_el/(2*hbar); %dimless parameters q_el[J]= 1 eV
c2 = vf*dt/dx;

phip = (mgap+Vpot)*i*c1; % phip = phi+
phim = (mgap-Vpot)*i*c1; % phim = phi-

AA = (1-phim)./(1+phim); %matrix coefficients for iterative solution
BB = c2./(1+phim);
CC = (1+phip)./(1-phip);
DD = c2./(1-phip);

norm(1) = 1;

%--------------------------------------------------------------------
% start iteration
tic
for k = 1:Nt-1
    %next step for u
    v = vmat(k,:);
    % shifted v-matrices
    v_r = circshift(v,[0,1]); % shift one column to the right
    v_r(1) = 0;
    % calculate u(t+dt)
    umat(k+1,:) = AA.*umat(k,:)+BB.*(-v+v_r);
    %right TBC
    for n = 0:k %right
        if n == 0
            umat(k+1,Nx) = s(k-n+1)*umat(n+1,Nx-1);
        else
            umat(k+1,Nx) = umat(k+1,Nx) + s(k-n+1)*umat(n+1,Nx-1);
        end
    end
```

```
    u = umat(k+1,:);
    % shifted u-matrices
    u_l = circshift(u,[0,-1]); % shift to the left
    u_l(Nx) = 0;
    %calculate v(t+dt)
    vmat(k+1,:) = CC.*vmat(k,:)+DD.*(-u_l+u);
    %left TBC
    for n = 0:k %left
        if n == 0
            vmat(k+1,1) = s(k-n+1)*vmat(n+1,2);
        else
            vmat(k+1,1) = vmat(k+1,1) + s(k-n+1)*vmat(n+1,2);
        end
    end
    %calculate norm with conserved functional
    if k == 1
     psimat(k,:)=abs(umat(k,:)).^2+abs(vmat(k,:)).^2+real(...
         (circshift(umat(k,:),[0,-1])-umat(k,:)).*conj(vmat(k,:)));
     norm0 = sum(psimat(k,:));
    else
     psimat(k,:)=abs(umat(k,:)).^2+abs(vmat(k,:)).^2+real(...
         (circshift(umat(k,:),[0,-1])-umat(k,:)).*conj(vmat(k,:)));
     norm(k)=sum(psimat(k,:))/norm0;
    end
end

psi = abs(umat/dx).^2+abs(vmat/dx).^2; % probability of wave function
reu = real(umat/dx); % calculate real-part of u component
imu = imag(umat/dx); % of wave function to reveal phase information
absu = abs(umat/dx);
rev = real(vmat/dx);
absv = abs(umat/dx);

%====================================
% output
%====================================

fig1=figure(1);
%nulll= zeros(1,Nx);
set(0,'DefaultAxesLineStyleOrder','-|:|-.|-.','DefaultAxesColorOrder',...
    [0 0 1])
ah1=axes;
for k=1:Nt-1
   p1=plot(xgrid,3000*psimat(k,:)+Ex,xgrid,20*reu(k,:)+Ex,...
       xgrid,Vpot-mgap,xgrid,Vpot+mgap,'LineWidth',1);
   ylim([-1*abs(Ex) 2*abs(Ex)+10])
   xlabel('x_j')
   ylabel(['E, ','Re(u), ', '|\psi(x_j)|^2'])
   text(180,-5,['|\psi(',int2str(k),')|^2 = ',num2str(norm(k))])
```

```
   set(ah1,'FontSize',12);
   getframe(fig1);
end

tgrid = 2:Nt-1;
figure %plot norm of wave packet
ah4=axes;
p3=semilogy(tgrid,norm(2:Nt-1)/max(max(norm)));
set(gca,'ylim',[0,1]);
set(ah4,'FontSize',12);
xlabel('timestep n')
ylabel('||\psi||^2')
```

A.3 Matlab code for the (2+1)D single Dirac cone staggered-grid leap-frog scheme

```

clear all
close all

%====================================================
%                   INITIALIZATION
%====================================================

%--------------------------------------------------
% initialization fundamental constants and grid
%--------------------------------------------------

% fundamental constants [in SI units]
h_planck = 6.6260693e-34;
q_el = 1.60217653e-19; % elementary charge
hbar = h_planck/(2*pi);
% material parameters
vf = 6.2e5; % [m/s] Fermi velocity

% ----- geometry -----
Lx = 500e-9; % [m];
Ly = 500e-9; % [m];

% ----- grid -----
Nx = 500;% # of grid points in x
Ny = 500;
Nt = 200; % # of time steps
dx = Lx/Nx; %[nm/step] step size (dx=dy is recommended)
dy = Ly/Ny; % butcode is general, also for dy not equal dx
%CFL-condition  sqrt(2)*vf*dt ≤ dx,dy for stability
dt = 0.999/sqrt(2)*min([dx/vf,dy/vf]);
Lt = Nt*dt;
xgrid = 1:Nx; ygrid = 1:Ny;
[X,Y] = meshgrid(xgrid,ygrid);

% ----- potential and mass landscape-----
V(1:Ny,1:Nx) = 0;
mx(1:Ny,1:Nx) = 0; % [ev]
my(1:Ny,1:Nx) = 0; % [eV]
mz(1:Ny,1:Nx) = 0.1; % [eV]

% + imaginary potential as absorbing layer
Vimag = 0.5*i; % [eV]
```

```
layer_width = 5;
cutoff = 0.05;
Vimat(1:Ny,1:Nx) = + Vimag./(1+exp(-(X-Nx)/layer_width))...
        + Vimag./(1+exp(+(X)/layer_width))...
        + Vimag./(1+exp(-(Y-Ny)/layer_width))...
        + Vimag./(1+exp(+(Y)/layer_width));
Vimat(1:Ny,1:Nx) = Vimat(1:Ny,1:Nx) - cutoff*Vimag;
Vimat(imag(Vimat)≤0)=0;
V = V+Vimat;

%--------------------------------------------------
%                  initial condition
%--------------------------------------------------

%gaussian wave packet

Ex = 0.2; % [eV] "energy" of wavepacket
Ey = 0;

kx0 = Ex*q_el/(hbar*vf); % wavevector E = hbar*vf*k for massless Dirac
ky0 = Ey*q_el/(hbar*vf);

x0 = floor(0.2*Nx);% center of wave packet
y0 = floor(0.5*Ny);
bx = 20/(dx*10^9); % [nm] half width of Gaussian in x-direction
by = 20/(dy*10^9); % [nm] half width of Gaussian in y-direction

kabs = sqrt(kx0^2+ky0^2);
%four-quadrant inverse tangent y/x = tan(phi)
phi = atan2(sign(kx0)*kx0/kabs,ky0/kabs);

umat(1:Ny,1:Nx) = 0; %upper component of the spinor
vmat(1:Ny,1:Nx) = 0; %lower component of the spinor
%Gaussian initial:
umat = 1/sqrt(2)*exp(-(X-x0).^2./(2*bx^2)+i*(X-x0)*dx*kx0).*...
     exp(-(Y-y0).^2./(2*by^2)+i*(Y-y0)*dy*ky0);
vmat = umat(:,:)*exp(i*phi);

%upper comonent for t_{n-1/2} and lower component for for t_n
uv(1:Ny,1:Nx) = 0; %can be stored in one common array
uv(1:2:end,1:2:end) = umat(1:2:end,1:2:end);
uv(2:2:end,2:2:end) = umat(2:2:end,2:2:end);
uv(1:2:end,2:2:end) = vmat(1:2:end,2:2:end);
uv(2:2:end,1:2:end) = vmat(2:2:end,1:2:end);


%=====================================================
%          ITERATIVE SOLUTION CORE PROGRAMM
%=====================================================
```

```

c1 = dt*q_el/hbar; %dimless parameters
c2 = vf*dt/dx;

mp = i*(mz+V)*c1;
mm = i*(mz-V)*c1;

%matrix coefficients for iterative solution
AA = (1-mm)./(1+mm);
BB = c2./(1+mm);
CC = (1+mp)./(1-mp);
DD = c2./(1-mp);
BBMx = mx/2*c1./(1+mm);
DDMx = mx/2*c1./(1-mp);
BBMy = my/2*c1./(1+mm);
DDMy = my/2*c1./(1-mp);


fig1=figure(1);
winsize = get(fig1,'Position');
set(fig1,'NextPlot','replacechildren');
ah = axes;
reu(1:Ny,1:Nx)=0;
psi2(1:Ny,1:Nx)=0;
correction(1:Ny,1:Nx)=0;
for k = 1:Nt-1

    uv_r = circshift(uv,[0,-1]); % shift one column to the right
    uv_l = circshift(uv,[0,1]); % shift to the left
    uv_u = circshift(uv,[1,0]); % shift up
    uv_d = circshift(uv,[-1,0]); % shift one row down

    % calculate u(t+dt)
    uv(1:2:end,1:2:end) = AA(1:2:end,1:2:end)...
        .*uv(1:2:end,1:2:end)+BB(1:2:end,1:2:end)...
        .*(uv_u(1:2:end,1:2:end)-uv_d(1:2:end,1:2:end)...
        +i*(uv_r(1:2:end,1:2:end)-uv_l(1:2:end,1:2:end)))...
        +i*BBMx(1:2:end,1:2:end).*(uv_u(1:2:end,1:2:end)...
        +uv_d(1:2:end,1:2:end))-BBMy(1:2:end,1:2:end)...
        .*(uv_r(1:2:end,1:2:end)+uv_l(1:2:end,1:2:end));
    uv(2:2:end,2:2:end) = AA(2:2:end,2:2:end).*uv(2:2:end,2:2:end)...
        +BB(2:2:end,2:2:end).*(uv_u(2:2:end,2:2:end)...
        -uv_d(2:2:end,2:2:end)+i*(uv_r(2:2:end,2:2:end)...
        -uv_l(2:2:end,2:2:end)))+i*BBMx(1:2:end,1:2:end)...
        .*(uv_u(2:2:end,2:2:end)+uv_d(2:2:end,2:2:end))...
        -BBMy(2:2:end,2:2:end).*(uv_r(2:2:end,2:2:end)...
        +uv_l(2:2:end,2:2:end));

    uv_r = circshift(uv,[0,-1]); % shift one column to the right
```

```
    uv_l = circshift(uv,[0,1]); % shift to the left
    uv_u = circshift(uv,[1,0]); % shift up
    uv_d = circshift(uv,[-1,0]); % shift one row down

    % calculate v(t+dt)
    uv(1:2:end,2:2:end) = CC(1:2:end,2:2:end).*uv(1:2:end,2:2:end)...
        +DD(1:2:end,2:2:end).*(uv_u(1:2:end,2:2:end)...
        -uv_d(1:2:end,2:2:end)-i*(uv_r(1:2:end,2:2:end)...
        -uv_l(1:2:end,2:2:end)))+i*DDMx(1:2:end,2:2:end)...
        .*(uv_u(1:2:end,2:2:end)...
        +uv_d(1:2:end,2:2:end))+DDMy(1:2:end,2:2:end)...
        .*(uv_r(1:2:end,2:2:end)+uv_l(1:2:end,2:2:end));
    uv(2:2:end,1:2:end) = CC(2:2:end,1:2:end).*uv(2:2:end,1:2:end)...
        +DD(2:2:end,1:2:end).*(uv_u(2:2:end,1:2:end)...
        -uv_d(2:2:end,1:2:end)-i*(uv_r(2:2:end,1:2:end)...
        -uv_l(2:2:end,1:2:end)))+i*DDMx(2:2:end,1:2:end)...
        .*(uv_u(2:2:end,1:2:end)+uv_d(2:2:end,1:2:end))...
        +DDMy(2:2:end,1:2:end).*(uv_r(2:2:end,1:2:end)...
        +uv_l(2:2:end,1:2:end));

    uv_r = circshift(uv,[0,-1]); % shift one column to the right
    uv_l = circshift(uv,[0,1]); % shift to the left
    uv_u = circshift(uv,[1,0]); % shift up
    uv_d = circshift(uv,[-1,0]); % shift one row down

    % norm (conserved functional)
    psi2(1:2:end,1:2:end) = abs(uv(1:2:end,1:2:end)).^2; % |u|^2
    psi2(2:2:end,2:2:end) = abs(uv(2:2:end,2:2:end)).^2; % |u|^2
    psi2(1:2:end,2:2:end) = abs(uv(1:2:end,2:2:end)).^2; % |v|^2
    psi2(2:2:end,1:2:end) = abs(uv(2:2:end,1:2:end)).^2; % |v|^2
    correction(1:2:end,1:2:end)=-vf*dt/dx*imag(conj(uv(1:2:end,1:2:end))...
        .* (uv_r(1:2:end,1:2:end) - uv_l(1:2:end,1:2:end)))...
        + vf*dt/dx*real(conj(uv(1:2:end,1:2:end))...
        .*(uv_u(1:2:end,1:2:end)-uv_d(1:2:end,1:2:end)));
    correction(2:2:end,2:2:end)=-vf*dt/dx*imag(conj(uv(2:2:end,2:2:end))...
        .* (uv_r(2:2:end,2:2:end) - uv_l(2:2:end,2:2:end)))...
        + vf*dt/dx*real(conj(uv(2:2:end,2:2:end))...
        .*(uv_u(2:2:end,2:2:end)-uv_d(2:2:end,2:2:end)));
    normmath=psi2 + correction;
    normmat=(normmath+circshift(normmath,[1,0]))/2;
    % real-part of u component of wave function to reveal phase information
    reu(1:2:end,1:2:end) = real(uv(1:2:end,1:2:end));
    reu(2:2:end,2:2:end) = real(uv(2:2:end,2:2:end));
    reu(1:2:end,2:2:end) = real(uv(1:2:end,1:2:end));
    reu(2:2:end,1:2:end) = real(uv(2:2:end,2:2:end));

    if k == 1
        norm0=sum(sum(normmat));
    end
```

```
    norm(k)=sum(sum(normmat))/norm0;
    surf(ah,X,Y,(reu+max(max(reu)))/2,'EdgeColor','none'...
        ,'FaceAlpha','flat','AlphaData',normmat);
    set(ah,'XLim', [0,Nx],'YLim', [0,Ny],'ZLim', [-1,1]);
    view(0, 90);
    axis square
    %title(['norm = ',num2str(sum(sum(norm(k))))])
    getframe(fig1,winsize);
end
```

LIST OF FIGURES